

**Investigation on foam-assisted chemical flooding for enhanced oil recovery  
An experimental and mechanistic simulation study**

Janssen, Martijn

**DOI**

[10.4233/uuid:f98bca0e-5ee8-4fd3-8a60-d0e624e525d6](https://doi.org/10.4233/uuid:f98bca0e-5ee8-4fd3-8a60-d0e624e525d6)

**Publication date**

2020

**Document Version**

Final published version

**Citation (APA)**

Janssen, M. (2020). *Investigation on foam-assisted chemical flooding for enhanced oil recovery: An experimental and mechanistic simulation study*. [Dissertation (TU Delft), Delft University of Technology]. <https://doi.org/10.4233/uuid:f98bca0e-5ee8-4fd3-8a60-d0e624e525d6>

**Important note**

To cite this publication, please use the final published version (if applicable).  
Please check the document version above.

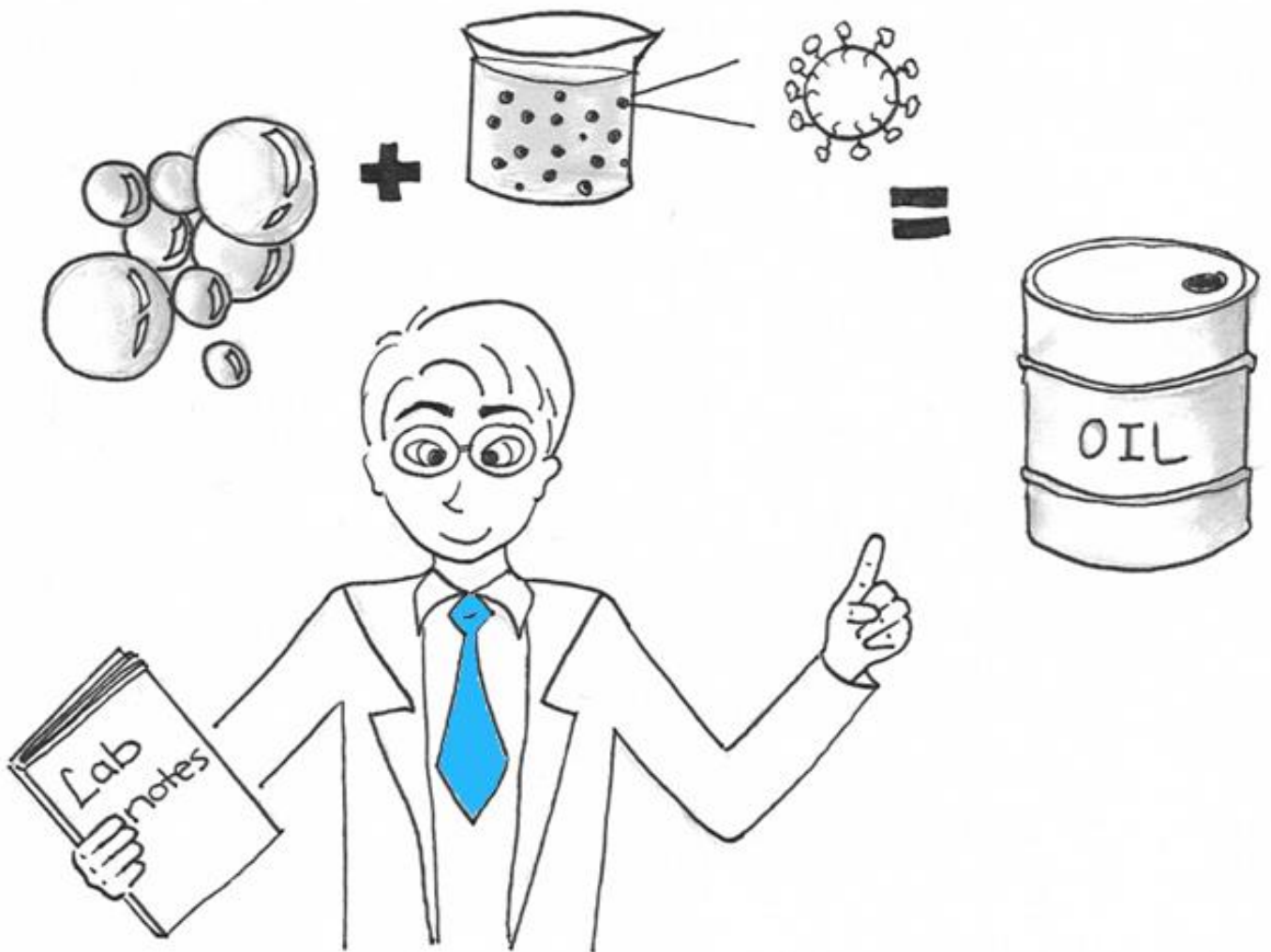
**Copyright**

Other than for strictly personal use, it is not permitted to download, forward or distribute the text or part of it, without the consent of the author(s) and/or copyright holder(s), unless the work is under an open content license such as Creative Commons.

**Takedown policy**

Please contact us and provide details if you believe this document breaches copyrights.  
We will remove access to the work immediately and investigate your claim.

# Investigation on Foam-Assisted Chemical Flooding for Enhanced Oil Recovery



**Martijn Janssen**

# **INVESTIGATION ON FOAM-ASSISTED CHEMICAL FLOODING FOR ENHANCED OIL RECOVERY**

AN EXPERIMENTAL AND MECHANISTIC SIMULATION STUDY



# **INVESTIGATION ON FOAM-ASSISTED CHEMICAL FLOODING FOR ENHANCED OIL RECOVERY**

AN EXPERIMENTAL AND MECHANISTIC SIMULATION STUDY

## **Proefschrift**

ter verkrijging van de graad van doctor  
aan de Technische Universiteit Delft,  
op gezag van de Rector Magnificus prof. dr. ir. T.H.J.J. van der Hagen,  
voorzitter van het College voor Promoties,  
in het openbaar te verdedigen op  
dinsdag 7 januari 2020  
om 10.00 uur

door

**Martijn Theodorus Gerardus JANSSEN**

Master of Science in Earth Sciences,  
Universiteit Utrecht, Utrecht, Nederland,  
geboren te Arnhem, Nederland.

Dit proefschrift is goedgekeurd door de

promotor: prof. dr. ir. P.L.J. Zitha

Samenstelling promotiecommissie:

Rector Magnificus, Prof. dr. ir. P.L.J. Zitha,	voorzitter Technische Universiteit Delft, promotor
---	---

Onafhankelijke leden:

Dr. ir. J. Groenenboom	Shell
Dr. D.V. Voskov	Technische Universiteit Delft
Prof. dr. W.R. Rossen	Technische Universiteit Delft
Dr. ir. F.J. Vermolen	Technische Universiteit Delft
Prof. dr. ir. H.E.J.G. Schlangen	Technische Universiteit Delft
Prof. dr. ir. S.M. Hassanizadeh	Universiteit Utrecht

The work presented in this thesis was conducted in the Department of Geoscience and Engineering, Delft University of Technology, Delft, The Netherlands. This doctoral research is the result of a collaboration between Delft University of Technology, University Teknologi Petronas, Petronas, and Shell. The research was funded by Petronas and Shell.



Key words: Alkaline, Surfactant, Foam, Oil, Immiscible gas injection, Water-alternating-gas, Enhanced oil recovery, Core-flood, Computed tomography, Mechanistic simulation

Cover design: Cover art design by Gulbin Uysal

Printed by: Ipskamp Printing, The Netherlands

Copyright © 2019 by M.T.G. Janssen ([mjanssen2@outlook.com](mailto:mjanssen2@outlook.com))

All rights reserved. No part of the material protected by this copyright notice may be reproduced or utilized in any form or by any means, electronic or mechanical, including photocopying, recording or by any information storage and retrieval system, without written permission of the author.

ISBN: 978-94-6384-099-6

An electronic version of this dissertation is available at

<http://repository.tudelft.nl/>

*To*

*My dear parents*

*Theodorus Gerardus Bonifatius Janssen and Hendrina Johanna Wilhelmina Maria Janssen-Joosten*

*My dear brothers*

*Jeroen Petrus Theodorus Janssen and Bas Theodorus Petrus Janssen*

*My beloved partner*

*Gulbin Uysal*

*In memory of my dear grandparents*

*Petrus Gerardus Janssen and Theodora van Aalten*

*Petrus Antonius Joosten and Theodora Johanna Maria Joosten-Melchers*



# Table of contents

1. Introduction.....	1
1.1. Enhanced oil recovery.....	1
1.2. Gas injection schemes.....	2
1.3. Sweep efficiency: gas foaming.....	3
1.3.1. Foam generation.....	5
1.3.2. Foam stability.....	5
1.3.3. Foam flow.....	6
1.4. Displacement efficiency: surfactants.....	6
1.5. Foam-assisted chemical EOR.....	7
1.6. Research questions and study objectives.....	8
1.7. Thesis outline.....	10
2. Immiscible gas injection schemes: continuous gas and water-alternating-gas injection.....	13
2.1. Introduction.....	14
2.2. Materials and methods.....	15
2.2.1. Chemicals.....	15
2.2.2. Core samples.....	16
2.2.3. Experimental set-up.....	16
2.2.4. CT scan.....	17
2.2.5. Experimental procedure.....	18
2.3. Results and discussion.....	19
2.3.1. Primary drainage and forced imbibition.....	19
2.3.1.1. Pressure drop.....	19
2.3.1.2. CT images.....	20
2.3.2. N <sub>2</sub> flooding at S <sub>wc</sub> .....	22
2.3.2.1. Pressure drop.....	22
2.3.3. N <sub>2</sub> flooding at S <sub>or_WF</sub> .....	23
2.3.3.1. Pressure drop.....	23
2.3.4. WAG injection at S <sub>wc</sub> .....	23
2.3.4.1. Pressure drop.....	24
2.3.5. Oil recovery.....	25
2.4. General discussion.....	25
2.5. Conclusions.....	28
3. Foam-assisted chemical flooding: effect of drive foam quality on oil bank propagation.....	29
3.1. Introduction.....	30
3.2. Materials and methods.....	31
3.2.1. Chemicals.....	31
3.2.2. Core samples.....	31
3.2.3. Experimental set-up.....	32
3.2.4. CT scan.....	33
3.2.5. Experimental procedure.....	33
3.2.5.1. Phase behaviour and IFT measurements.....	33

3.2.5.2. Core-flood experiments.....	33
3.3. Results and discussion.....	35
3.3.1. Phase behaviour and IFT measurements.....	35
3.3.2. Core-flood experiments.....	35
3.3.2.1. Primary drainage and forced imbibition.....	36
3.3.2.1.1. Pressure drop.....	37
3.3.2.1.2. CT images and oil saturation profiles.....	37
3.3.2.2. Mobilization of residual oil.....	39
3.3.2.2.1. Pressure drop.....	39
3.3.2.2.2. CT images and oil saturation profiles.....	40
3.3.2.3. Displacement of mobilized oil by foam.....	40
3.3.2.3.1. Pressure drops and MRFs.....	40
3.3.2.3.2. CT images and oil saturation profiles.....	44
3.3.2.3.3. Gas saturation profiles.....	46
3.3.2.4. Oil recovery.....	47
3.4. General discussion.....	49
3.4.1. Saturation paths.....	49
3.4.2. Oil mobilization.....	50
3.4.3. Oil displacement by foam.....	51
3.5. Conclusions.....	53
4. Foam-assisted chemical flooding: effect of surfactant slug salinity.....	55
4.1. Introduction.....	56
4.2. Materials and methods.....	56
4.2.1. Chemicals.....	56
4.2.2. Core samples.....	57
4.2.3. Experimental set-up.....	57
4.2.4. CT scan.....	57
4.2.5. Experimental procedure.....	58
4.2.5.1. Phase behaviour and IFT measurements.....	58
4.2.5.2. Bulk foam stability.....	58
4.2.5.3. Core-flood experiments.....	58
4.2.5.4. CT data post-processing.....	59
4.3. Results and discussion.....	59
4.3.1. Phase behaviour and IFT measurements.....	59
4.3.2. Bulk foam stability.....	59
4.3.3. Core-flood experiments.....	60
4.3.3.1. Mobilization of residual oil.....	61
4.3.3.1.1. Pressure drop.....	61
4.3.3.1.2. CT images and oil saturation profiles.....	62
4.3.3.2. Displacement of mobilized oil by foam.....	64
4.3.3.2.1. Pressure drop.....	64
4.3.3.2.2. CT images and oil saturation profiles.....	65
4.3.3.2.3. Gas saturation profiles.....	66
4.3.3.3. Oil recovery.....	67
4.4. General discussion.....	68

4.4.1.	Sectional saturation paths.....	68
4.4.2.	Gas flooding and WAG vs. FACF.....	70
4.5.	Conclusions.....	70
5.	Foam-assisted chemical flooding at reservoir conditions.....	71
5.1.	Introduction.....	72
5.2.	Materials and methods.....	72
5.2.1.	Chemicals.....	72
5.2.2.	Core samples.....	74
5.2.3.	Experimental set-up: bulk foam experiments.....	74
5.2.4.	Experimental set-up: core-flood experiments.....	75
5.2.5.	Experimental procedure.....	77
5.2.5.1.	Phase behaviour.....	77
5.2.5.2.	Bulk foam stability.....	77
5.2.5.3.	Core-flood experiments.....	77
5.3.	Results and discussion.....	78
5.3.1.	Phase behaviour and bulk foam experiments.....	78
5.3.2.	Foam quality scan.....	79
5.3.3.	FACF.....	81
5.3.3.1.	Mobilization of residual oil.....	81
5.3.3.2.	Displacement of mobilized oil by foam.....	84
5.3.3.3.	Oil recovery.....	87
5.4.	General discussion.....	88
5.5.	Conclusions.....	89
6.	Mechanistic modelling of water-alternating-gas injection and foam-assisted chemical flooding..	91
6.1.	Introduction.....	92
6.2.	Materials and methods.....	92
6.2.1.	WAG injection.....	92
6.2.2.	Foam-assisted chemical flooding.....	93
6.2.3.	UTCHEM simulator.....	93
6.3.	Results and discussion.....	94
6.3.1.	Geochemical reactions.....	94
6.3.2.	Model set-up: grid size, porosity, permeability, and initial water saturation.....	95
6.3.3.	Primary drainage and forced imbibition.....	96
6.3.4.	WAG injection.....	99
6.3.5.	Surfactant phase behaviour simulation.....	99
6.3.6.	Surfactant adsorption, ME viscosity, and IFT parameters.....	101
6.3.7.	Relative permeabilities surfactant flooding.....	102
6.3.8.	Oil mobilization by surfactant slug injection.....	103
6.3.9.	Displacement of mobilized oil by foam.....	105
6.4.	Conclusions.....	106
7.	Conclusions and recommendations.....	109
7.1.	Conclusions.....	109
7.2.	Recommendations.....	111
Appendix A.	CT imaging of two- and three-phase saturations using single- and dual-energy CT data.....	113

Appendix B. Pressure drop vs. oil bank shape during surfactant slug injection.....	115
Appendix C. Simulation parameters used per injection stage per experiment.....	117
Appendix D. Relative permeability curves: primary drainage and forced imbibition.....	121
Appendix E. Pressure drops, oil saturation profiles, and phase cuts: primary drainage and forced imbibition.....	127
Appendix F. Relative permeability curves: WAG injection.....	131
Appendix G. Relative permeability curves: surfactant slug injection.....	135
Appendix H. Pressure drops and oil saturation profiles: surfactant slug injection.....	137
Bibliography.....	141
Nomenclature.....	151
Summary.....	153
Samenvatting.....	155
Scientific contributions.....	159
Acknowledgements.....	161
About the author.....	163

# 1. Introduction

## 1.1 Enhanced oil recovery

Oil is the world's primary energy resource, accounting for nearly 33% of the global primary energy consumption by fuel in 2017 (BP Energy Outlook, 2019). In 2040, as predicted by the BP Energy Outlook (2019), oil and natural gas will still provide more than 50% of the world's primary energy consumption; regardless of the speed at which the energy transition, towards more sustainable energy resources, takes place. In all models forecasting primary energy consumption by fuel in 2040, the increase in renewables is by far most significant (**Figure 1.1**).

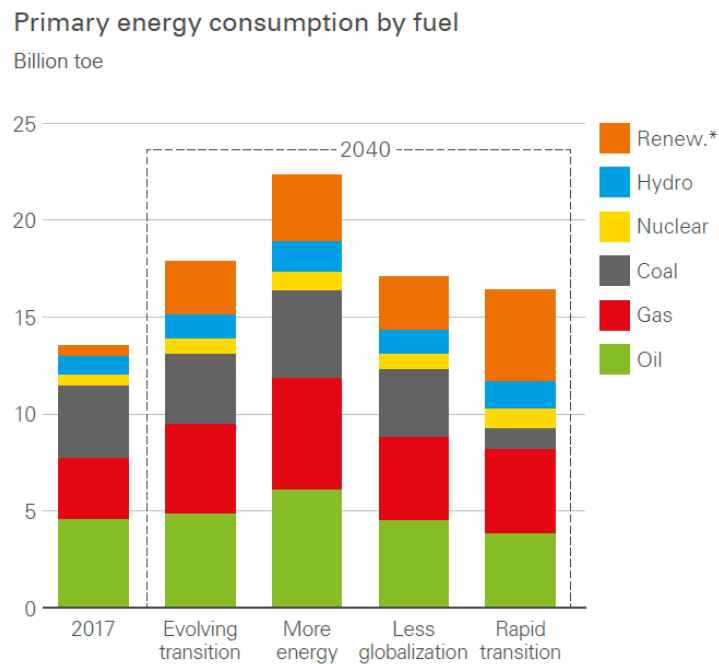


**Figure 1.1:** Global primary energy consumption by fuel in tonne of oil equivalent (toe): 2017 and multiple 2040 predictions. The 2040 scenarios mainly differ in terms of policy, i.e. the speed at which the energy transition takes place. Statistical data and analysis from BP Energy Outlook (2019).

\*Renewables includes wind, solar, geothermal, biomass, and biofuels.

The various predictive models prepared by the BP Energy Outlook (2019) for 2040, as shown in **Figure 1.1**, indicate that in the next 20 years the global demand for oil will remain high. Today's concern is that the world's oil demand will outrun the global oil production in the near future as the global oil demand continues to remain high whilst oil production from many giant, mature, oil fields worldwide is declining (Höök *et al.*, 2009). Together with the expectation that the probability of discovering new large oil fields becomes less, this underlines the importance of developing novel techniques that enhance oil production from mature oil fields: enhanced oil recovery (EOR) methods.

Oil field development can be separated into three main phases: primary, secondary, and tertiary recovery (Lake, 1989). Primary recovery covers the production of oil that is driven by natural mechanisms, leading to pressure depletion in the reservoir (e.g. gas cap drive). Secondary recovery

techniques involve water and gas injection to displace the oil to the production well and subsequent to the surface. These techniques are often used for reservoir pressure maintenance. Recovery techniques applied after secondary recovery belong to the tertiary recovery phase. *EOR* methods are mostly placed in the latter, tertiary, production phase and is defined by Lake (1989) as oil being recovered through the injection of external materials originally not present in the reservoir. Three primary *EOR* techniques can be distinguished: gas injection, thermal injection (mostly applied to heavy oils and tar sands), and chemical injection (Stahl *et al.*, 1987; Lake, 1989; Thomas, 2008; Shah, 2012). For light oil reservoirs a typical *EOR* target is approximately 45% of the oil initially in place (*OIIP*), as roughly 55% of the *OIIP* is targeted using primary and secondary recovery methods. However, for heavy oil reservoirs, bulk of the oil production comes from *EOR* methods, reaching an *EOR* target of approximately 90% of the *OIIP* (Thomas, 2008). Primarily reservoir fluid properties and geology control the suitability of an *EOR* process for a specific reservoir.

According to Sandrea and Sandrea (2007), the average oil recovery from mature oil fields worldwide, due to conventional primary and secondary recovery methods, varies between 20% and 40% of the *OIIP*. The oil recovery factor can be expressed as follows (Lake, 1989):

$$R_F = E_V \times E_D \quad (1.1)$$

where  $R_F$  is the recovery factor which represents the fraction of the volume of *OIIP* that is produced, measured at surface conditions.  $E_V$  is the volumetric sweep efficiency. It describes the volume fraction of the reservoir that is contacted by the injected fluid. The volumetric sweep efficiency mainly depends on the mobility and density ratios between the injected agent and the oil in place (*OIP*), reservoir heterogeneity, injection rate, and the total volume of fluid injected (Smalley *et al.*, 2009).  $E_D$  is the pore-scale displacement efficiency and refers to the ratio of the amount of oil being mobilized to the amount of oil that is contacted by the injected fluid.  $E_D$  is a strong function of rock-fluid and fluid-fluid properties (e.g. relative permeabilities, capillary pressures, wettability, and interfacial tensions) (Melrose and Brandner, 1974). The goal of applying *EOR* methods to existing oil fields is to improve both the macroscopic volumetric sweep and microscopic displacement efficiency. Volumetric sweep efficiencies may be increased by adjusting the mobility ratio ( $M$ ), between the injected agent and the *OIP*, in a favourable way. The pore-scale displacement efficiency might be improved by either reducing the oil-water ( $o/w$ ) interfacial tension (*IFT*), altering the rock wettability, or by reducing the oil viscosity (Dake, 1983).

## 1.2 Gas injection schemes

Gas injection is a widely used *EOR* technique which covers more than 50% of the total number of *EOR* projects in the U.S. in 2008 (Orr, 2007; Manrique *et al.*, 2010). In this process natural or non-natural gas (e.g. nitrogen ( $N_2$ ) or carbon dioxide ( $CO_2$ )) is injected into a mature oil field to increase the oil recovery factor over water flooding (Lake, 1989). A distinction is made between miscible and immiscible gas flooding. During miscible flooding the injected gas will form a single fluid phase with the displaced oil whereas the injected gas dissolves only partly in the oil during immiscible gas flooding. Miscibility requires sufficiently high reservoir pressures, an injected gas that contains a relatively low minimum miscibility pressure (*MMP*) (e.g.  $CO_2$ ), and light hydrocarbon components within the in-situ oleic phase. For miscible *EOR* methods, oil swelling, oil viscosity reduction, and/or  $o/w$  *IFT* reduction play a predominant role in oil displacement (Johns and Orr, 1996). When the injected gas is fully miscible with the *OIP*, locally  $E_D$  can approach 100%. For immiscible gas *EOR*

methods instead, oil swelling and viscosity reduction are limited compared to miscible conditions due to a significant reduction in mass transfer between the injected gas and the *OIP*. Here rock-fluid and fluid-fluid interactions control oil displacement.

For any continuous gas injection scheme, unfavourable mobility ratios, between the injected gas and the displaced fluids, is a major concern as it results in an unstable displacement (i.e. unfavourable  $E_v$ ). The mobility ratio between the injected and displaced phases can be calculated as follows:

$$M = \frac{\lambda_{inj}}{\lambda_{dis}} = \frac{\frac{k_{r\ inj}}{\mu_{inj}}}{\frac{k_{r\ dis}}{\mu_{dis}}} \quad (1.2)$$

where  $\mu_{inj}$ ,  $\mu_{dis}$ ,  $k_{r\ inj}$ , and  $k_{r\ dis}$  represent the viscosities of the injected and displaced phases, the relative permeability to the injectant, and the relative permeability to the displaced phase, respectively. The mobility of the injected and displaced phase are denoted as  $\lambda_{inj}$  and  $\lambda_{dis}$ , respectively. A favourable  $M (\leq 1)$  is reached when the displaced phase has a higher mobility than the injectant. Due to a high gas mobility, unfavourable mobility ratios, and hence unfavourable  $E_v$ , are often seen during gas injection projects. Viscous fingering as a result of viscous instabilities, gas channelling in high permeability streaks, and gravity segregation, triggered by the density difference between the injected gas and the fluids in place, are common phenomena in gas flooding, leading to early gas breakthrough (Zhu *et al.*, 2004; Rossen *et al.*, 2010; Farajzadeh *et al.*, 2009; Farajzadeh *et al.*, 2010; Andrianov *et al.*, 2011).

For controlling gas mobility and improving gas sweep efficiency, Parrish (1966) proposed the injection of gas slugs alternated by water slugs: water-alternating-gas (WAG) injection. WAG might delay gas breakthrough considerably, and increase the hydrocarbon contact time, leading to a substantial improvement in oil recovery (Hallam *et al.*, 1995). Skauge and Stensen (2003) reviewed 72 WAG field applications and they stated an average incremental oil recovery of 10% of the *OIP* due to WAG injection. Nevertheless, similar to a continuous gas injection scheme, gravity segregation may also occur during WAG yielding a reduced sweep efficiency (Andrianov *et al.*, 2011; Talebian *et al.*, 2014). Poor fluid injectivity, i.e. extremely high pressure drops due to the establishment of trapped gas, is another major management challenge concerning WAG field applications (Rogers and Grigg, 2001).

### 1.3 Sweep efficiency: gas foaming

Foaming of the gas is another, potentially more effective, way for improving gas sweep efficiency. Foam reduces gas mobility greatly by trapping gas in a discontinuous form, i.e. separated gas bubbles, within a continuous liquid phase (Kovscek and Radke, 1994; Rossen, 1996; Mannhardt *et al.*, 2000; Zitha *et al.*, 2006; Du *et al.*, 2007; Zitha and Du, 2010; Simjoo, 2012). Previous work concluded that the gas-mobility-reducing capacity of a foam is strongly related to its texture, i.e. gas bubble size, where gas mobility reduces with decreasing bubble size (Hirasaki and Lawson, 1985; Ettinger and Radke, 1992). The liquid phase mobility, on the other hand, does not depend on whether the gas has been foamed or not (Bernard *et al.*, 1965; Holm, 1968; Lawson and Reisberg, 1980). Foam stability is primarily a function of the thickness of thin liquid films, i.e. lamellae, that separate the gas bubbles within the foam texture (Lake, 1989; Gauglitz *et al.*, 2002; Farajzadeh *et al.*, 2010). The lamellae are stabilized by surfactants present in the aqueous phase. Its stability depends mainly on

the type of gas used and on the chemical formulation of the continuous aqueous phase (Aronson *et al.*, 1994; Shabib-asl *et al.*, 2014). For instance, higher aqueous solubility of CO<sub>2</sub> compared to N<sub>2</sub> might result in an increased diffusion of CO<sub>2</sub> from smaller to larger bubbles within the bulk foam texture, compared to a N<sub>2</sub> foam, which promotes foam decay. Throughout this work, foam quality ( $f_g$ ) is defined as the gas volumetric fractional flow in foam as follows:

$$f_g = \frac{u_g}{u_g + u_w} \quad (1.3)$$

where  $u_g$  and  $u_w$  represent the Darcy velocity for the gas and water phase, respectively. **Figure 1.2** presents a schematic comparison between the displacement fronts expected during continuous gas injection, WAG injection, and foam flooding.

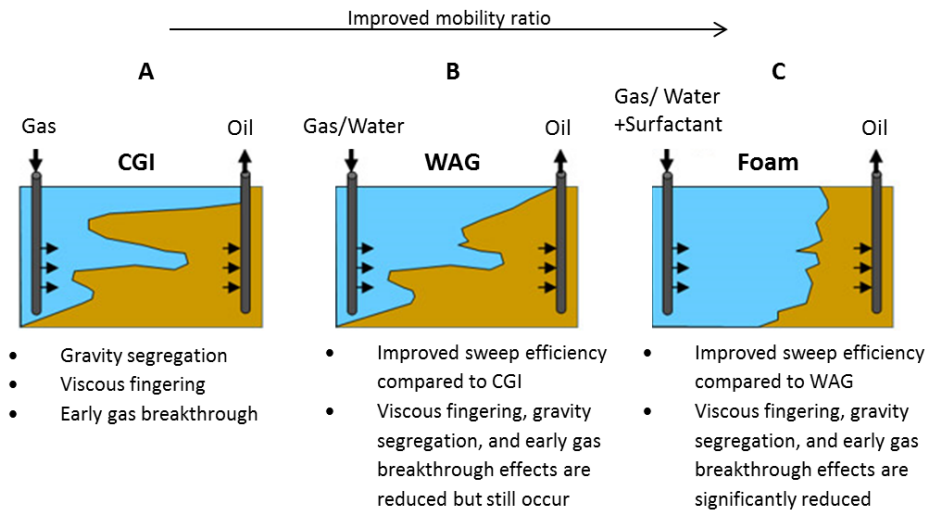


**Figure 1.2:** Schematic comparison between A) continuous gas injection (CGI), B) water-alternating-gas injection (WAG), and C) foam injection (Foam). The injectants are represented in blue and the oil in place is shown in brown. Note the improvement in sweep efficiency during foam injection compared to continuous gas and WAG injection. This figure has been modified after The EOR Alliance (2019).

Besides using foam for reducing gas mobility, hence improving its  $E_v$  in gas EOR processes, foam can also be used for conformance control in extremely heterogeneous reservoirs (Fuseni *et al.*, 2018). Since stronger, more viscous, foams are observed in high permeability layers (e.g. thief zones) compared to low permeability layers (Rossen, 1996; Boeije and Rossen, 2018), foam might be used as a blocking agent to divert the flow from high permeable areas to low permeable regions within the reservoir (Schramm and Smith, 1996; Fuseni *et al.*, 2018). The latter yielding again an improved  $E_v$  of the applied flooding process. Besides enhancing  $E_v$ , by reducing gas mobility and/or blocking high permeability streaks, foam might also contribute to the reduction of the  $o/w$  IFT, thus reducing capillary forces, hence increasing  $E_D$  (Equation 1.1) (Romero-Zeron and Kantzas, 2003; Farajzadeh *et al.*, 2010). Whether the reduction in  $o/w$  IFT is sufficient enough to increase  $E_D$  depends on the specific foaming surfactant(s) used and the characteristics of the OIP.

### 1.3.1 Foam generation

In order to generate foam in-situ in the reservoir, two methods are often used: co-injection of gas and surfactant solution and surfactant-alternating-gas (SAG) injection (Schramm and Smith, 1996; Turta and Singhal, 1998; Farajzadeh *et al.*, 2009). In the former injection strategy gas and an aqueous surfactant solution are co-injected at a fixed ratio which determines  $f_g$  (Equation 1.3). The latter technique implies injection of gas and surfactant solution in alternating slugs; similar to WAG. In addition to the abovementioned injection techniques, one may decide to inject supercritical CO<sub>2</sub> in which the surfactant is dissolved (Le *et al.*, 2008; Xing *et al.*, 2010). This strategy does not require the injection of a liquid slug as foam can be formed as soon as the injected supercritical CO<sub>2</sub> meets the water in place.

Foams, i.e. lamellae, are generated in porous media by three different mechanisms: snap-off, lamella division, and leave-behind (Falls *et al.*, 1988; Ransohoff and Radke, 1988; Chambers and Radke, 1990; de Vries and Wit, 1990; Rossen, 1996). The capillary snap-off mechanism was first described by Roof (1970) for explaining oil entrapment during water flooding. When gas is the non-wetting phase, the same mechanism is able to create foam lamellae, thus generating foam (Mast, 1972). According to Kovscek and Radke (1993), snap-off is the dominant foam generation mechanism in porous media. Figure 1.3 presents schematics illustrating the three aforementioned foaming mechanisms. Stable lamellae are only formed when there is a sufficient amount of surfactant present within the aqueous liquid phase.

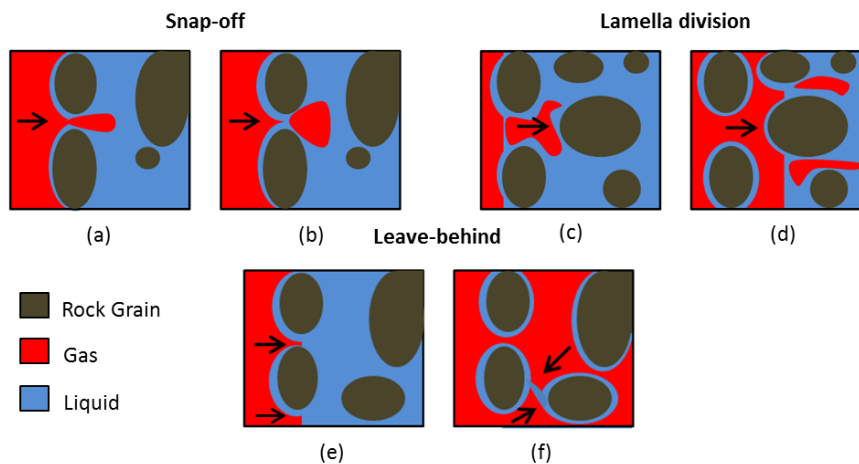


**Figure 1.3:** Schematic representation of the three foam generation mechanisms during drainage: Snap-off, Lamella division, and Leave-behind. Snap-off: gas jumps out of the pore throat (a), leading to a reduction in capillary pressure which allows the aqueous phase to flow towards the throat and form a lamella (b). Lamella division: a moving lamella encounters a branched point (c) which leads to its division (d). Leave-behind: two gas fronts flow into the same pore space (e) and squeeze the liquid phase (f).

### 1.3.2 Foam stability

Foam is a metastable phenomenon and its longevity depends on the lamellae stability (lake, 1989; Farajzadeh *et al.*, 2012). Some factors that control lamellae stability are surfactant concentration, type of oleic phase, brine salinity, capillary pressure, and bubble size (Aronson *et al.*, 1994; Shabib-asl *et al.*, 2014). Simjoo (2012) showed, in agreement with Aronson *et al.* (1994), that an increase in surfactant concentration enhanced bulk foam stability significantly in the presence of oil, whilst in the absence of oil this effect was considerably lower. Several experimental studies have shown that

oil might be detrimental to foam stability, lowering its apparent viscosity, hence increasing its mobility (Schramm *et al.*, 1993; Schramm and Smith, 1996). The general consensus is that oils with shorter carbon chains have a more destabilizing effect on foam stability compared to oils with longer carbon chains (Vikingstad *et al.*, 2005; Simjoo, 2012). Lamellae, i.e. foam, stability is also related to the salinity of the continuous aqueous phase, where lamellae stability increases with decreasing salinity (Klitzing *et al.*, 1999; Zhu *et al.*, 2004). In order for the main foam generation mechanism, i.e. snap-off, to occur and to generate stable foams, the capillary pressure needs to be sufficiently low; lower than the so-called limiting capillary pressure (Falls *et al.*, 1988; Khatib *et al.*, 1988; Farajzadeh *et al.*, 2015).

### 1.3.3 Foam flow

The flow of foam, at constant total superficial velocity ( $u_t = u_g + u_w$ ), through porous media in the absence of oil reveals two flow regimes, depending on foam quality (**Equation 1.3**): the low- and high-quality regimes (Osterloh and Jante, 1992). Foam flow in the low-quality regime is essentially a function of gas bubble trapping, and the foam apparent viscosity here is mainly controlled by the gas flow rate: increasing foam strength with increasing  $f_g$ . On the other hand, in the high-quality regime, gas bubble coalescence regulates foam flow behaviour and here the foam apparent viscosity is mostly dependent on the liquid superficial velocity: decreasing foam strength with increasing  $f_g$ . In the high-quality regime a limiting water saturation, corresponding to the limiting capillary pressure, exists below which foam collapses abruptly (Alvarez *et al.*, 2001). A sharp transition between the high- and low-quality regimes occurs at a critical foam quality ( $f_g^*$ ).

## 1.4 Displacement efficiency: surfactants

Besides obtaining a favourable  $E_V$  (e.g. by gas foaming),  $E_D$  needs to be sufficiently large as well in order to have a successful chemical EOR process (**Equation 1.1**). In extensively water-flooded reservoirs with good pore connectivity, residual oil remain trapped in the pore network, in the form of disconnected clusters and/or oil fragments because of the dominance of capillary forces (Howe *et al.*, 2015; Yang *et al.*, 2019). Capillary pressure is the discontinuity in pressure across an interface between two immiscible fluids. It is controlled by the IFT, pore size distribution, and contact angle between rock and *o/w* interface ( $\theta$ ) (Falode and Manuel, 2014). Rock wettability is defined as the tendency of one fluid to spread on, or adhere to, the rock's surface in the presence of another immiscible fluid (Craig, 1971). By altering  $\theta$ , from oil-wet ( $\theta > 90^\circ$ ) conditions toward a water-wet ( $\theta < 90^\circ$ ) system, one may promote a rock that has a stronger attraction towards brine than oil, which might favour oil mobilization, thus improving  $E_D$ . In this case, the resulting capillary pressure yields water to imbibe more easily, compared to the oil-wet conditions (Hu *et al.*, 2014; Liang *et al.*, 2016; Pan *et al.*, 2019). A significant reduction of the *o/w* IFT would directly lead to a lower capillary pressure which increases the ratio of viscous forces over capillary forces that promotes oil mobilization during a flooding process; thus increasing  $E_D$  (Lake, 1989).

Part of the trapped residual oleic phase may be mobilized through the injection of specially designed surfactants by a combined effect of rock wettability alteration towards more water-wet conditions (Wang *et al.*, 2011; Hou *et al.*, 2015), valid for mixed- or oil-wet reservoirs, and the reduction of the *o/w* IFT to ultralow values (Hirasaki *et al.*, 2011; Guo *et al.*, 2012; Jong *et al.*, 2016; Janssen *et al.*, 2019a; Janssen *et al.*, 2019b; Janssen *et al.*, 2019c). Surfactants, i.e. surface active agents, are amphiphilic molecules: they possess both hydrophilic (its head) and hydrophobic (its tail) properties. When dissolved in the water phase, surfactants absorb at the gas-water (*g/w*) or *o/w* interface; with

its hydrophilic head in water and its hydrophobic tail in the gas or oil phase (Myers, 2006). By doing so, the surfactant molecules replace some of the water molecules at the interface, reducing the  $IFT$  as the attractive forces between water and surfactant molecules are less than between two water molecules (Farn, 2008). Each surfactant type has its own critical micelle concentration ( $CMC$ ): the concentration at which surfactant micelles start to form (Kuhlman *et al.*, 1992). The main goal of utilizing surfactants is to decrease the  $IFT$ , i.e. increasing  $E_D$ , and to stabilize the interface.

To which extent a constant surfactant concentration, at fixed pH, can lower the  $o/w$   $IFT$  is essentially controlled by the aqueous phase salinity (Winsor, 1954). An oil-in-water micro-emulsion ( $ME$ ) is in equilibrium with excess oil (Type II- system) at under-optimum salinity conditions, whereas at over-optimum salinity a water-in-oil  $ME$  co-exists with excess water (Type II+ system). In between the Type II- and Type II+ systems, an optimum salinity range can be identified (Type III system) where a distinct  $ME$  is in equilibrium with excess oil and water. The Type III system reveals ultralow  $o/w$   $IFT$ s. **Figure 1.4** shows a schematic overview of the aforementioned Winsor Type systems.

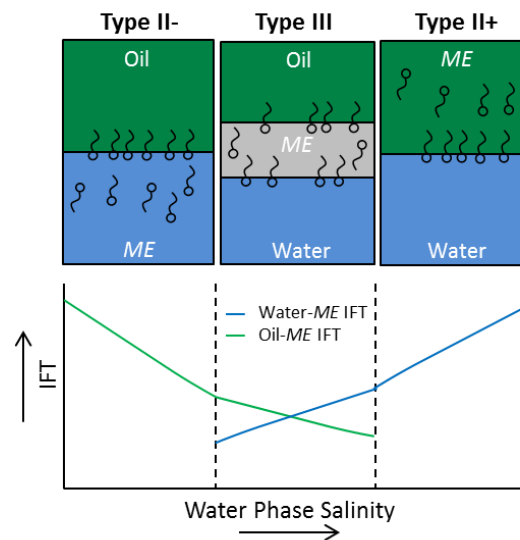


**Figure 1.4:** Schematic overview of Winsor (1954) Type surfactant systems: under-optimum (Type II-) system, optimum (Type III) system, and over-optimum (Type II+) system. Its relationship with both the water- $ME$  and oil- $ME$   $IFT$  is shown as well. Ultralow  $IFT$  is reached when aforementioned  $IFT$ s overlap, i.e. in the Type III system.

## 1.5 Foam-assisted chemical EOR

Foam-assisted chemical flooding ( $FACF$ ) combines the injection of a surfactant slug, for increasing  $E_D$ , with foam generation for drive mobility control; enhancing  $E_V$  (**Sections 1.3 and 1.4**) (Guo *et al.*, 2012; Hosseini-Nasab and Zitha, 2015; Janssen *et al.*, 2019a; Janssen *et al.*, 2019b; Janssen *et al.*, 2019c). In a well-designed  $FACF$ , the surfactant slug provides an ultralow  $o/w$   $IFT$ , mobilizing previously trapped residual oil leading to the development of an oil bank. Subsequently, the injection of a foam drive ensures good mobility control for displacement of the oil bank (**Figure 1.5**).

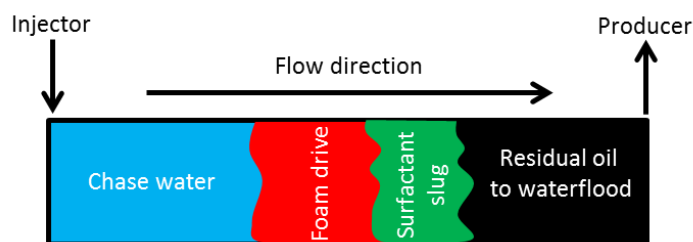


**Figure 1.5:** Foam-assisted chemical flooding. The surfactant slug ensures mobilization of residual oil to waterflood. The mobilized oil is subsequently displacement by a foam drive that provides good mobility control.

Several names were proposed for the process, including alkaline-surfactant-foam (ASF) flooding (Guo *et al.*, 2012; Hosseini-Nasab and Zitha, 2015), low-tension-gas (LTG) flooding (Szlendak *et al.*, 2013; Tang *et al.*, 2014; Jong *et al.*, 2016) and alkaline-surfactant-gas (ASG) flooding (Srivastava *et al.*, 2009). Here the term *FACF* is used as it provides a more general terminology for the chemical *EOR* process. The surfactant slug in *FACF* might contain an alkaline and a co-solvent in addition to the surfactant, all dissolved in injection water. The alkaline converts naphthenic acids, commonly present in crude oils, into soaps (i.e. natural surfactants) through a saponification process (Chatterjee and Wasan, 1998). The synergistic action of these natural surfactants in combination with the added surfactant can lead to the reduction of the *o/w* *IFT* to ultralow values. The alkaline also reduces anionic surfactant adsorption on charged clay sites within sandstones (Hirasaki and Zhang, 2004). A co-solvent might be added to the chemical slug formulation to ensure a stable slug solution, preventing precipitation and/or phase separation (Hirasaki *et al.*, 2011).

The *FACF* process bears analogies with the more conventional alkaline-surfactant-polymer (ASP) flooding. However, *ASP* uses polymers for mobility control instead of foam (Liu *et al.*, 2008). Unlike *FACF*, *ASP* suffers from limitations regarding the use of polymers in high-temperature, high-salinity, and low-permeability regions (Shupe, 1981). Polymer injectivity might be extremely challenging in low-permeable rocks, potentially yielding clogging of the formation and/or undesirable fractures (Zechner *et al.*, 2013; Delamaide *et al.*, 2014).

Previous studies have shown that *FACF* is a viable *EOR* process that can significantly enhance oil recovery factors over water flooding (Srivastava *et al.*, 2009; Guo *et al.*, 2012; Szlendak *et al.*, 2013; Tang *et al.*, 2014; Jong *et al.*, 2016). However, bulk of the existing literature essentially use observed pressure and effluent data to describe related oil mobilization and displacement processes within the porous medium. Hence, they only provide limited clues about oil mobilization and displacement mechanisms in a *FACF* process and more dedicated research is needed.

## 1.6 Research questions and study objectives

The central scope of this work is to gain understanding of oil mobilization and displacement mechanisms in a *FACF* process by studying the key physical phenomena. Results of this research will enable new predictive tools of *FACF* to be developed. More specifically, each of the next sections will describe one of the sub-questions the PhD dissertation intends to answer.

In order to fully grasp the advantages of the novel *EOR* methodology of *FACF*, the first goal of this thesis is to perform a base case study on immiscible continuous gas and *WAG* injection. The aim of the base case project is to conduct core-flood experiments to gain insight in related oil displacement

mechanisms: *which oil displacement mechanisms are responsible for oil recovery during immiscible continuous gas injection and WAG?* Under immiscible conditions, rock-fluid and fluid-fluid interactions, as described by relative permeabilities and capillary pressures, control oil displacement. It is believed that the so-called three-phase flow effect (i.e. by introducing gas to the system, the oleic phase becomes the intermediate-wetting phase) plays a dominant role in oil displacement during continuous gas injection and WAG. Moreover, for WAG, the introduction of a trapped gas saturation could increase the sweep efficiency of the injected gas and water slugs.

The second objective of this study is to assess under-optimum salinity FACF at model-like conditions, using a model brine, model oil, and model porous media, and to define the merits of under-optimum FACF compared to gas injection/WAG. This is done by performing dedicated computed-tomography (CT-) assisted core-flood experiments. More specifically, we investigate the effect of drive foam quality on oil bank displacement by foam: *how does the drive foam quality effects the oil bank displacement during under-optimum salinity FACF in a model-like setting?* The drive foam quality, i.e. gas fractional flow in foam, is one of the main controlling parameters of oil displacement by foam as it regulates the amount of surfactants, that stabilize foam lamellae, present.

The third goal is to investigate the effect of surfactant slug salinity, thus the impact of ultralow *o/w IFT*, on oil mobilization and displacement mechanisms in FACF in a model-like setting using CT-assisted core-floods: *how does the surfactant slug salinity, i.e. under-optimum versus (near-)optimum salinity, effects the FACF efficiency in terms of oil mobilization and displacement in a model-like setting?* The salinity of the surfactant slug, which directly controls the *o/w IFT*, is one of the key parameters that determine the amount of oil being mobilized by the slug. Moreover, it might also have an impact on drive foaming, and thus on oil displacement by foam, since it regulates the oil saturation distribution that is present once drive foam injection is initiated.

Subsequent to studying a model-like setting, the fourth objective of this PhD thesis is to evaluate FACF at reservoir conditions, again focussing on its oil mobilization and displacement processes. Attention is paid to the effect of slug salinity and drive foam strength: *what is the effect of surfactant slug salinity and drive foam strength, i.e. pre-generated drive foam versus in-situ foam generation, on oil mobilization and its displacement in FACF at reservoir conditions?* Equivalent to model-like conditions, the surfactant slug salinity directly regulates the amount of oil being mobilized as a result of *o/w IFT* reduction. It is likely that the drive foam strength mainly determines the stability of the oil bank displacement by foam.

The final goal of this study is to develop a mechanistic model, using a three-dimensional research simulator for multiphase and multicomponent systems, to history-match performed WAG/FACF experiments and, subsequently, identify the main mechanisms controlling oil recovery in those processes: *by developing a mechanistic model, can we history-match previously performed experiments and predict which parameters are crucial for a successful WAG/FACF process?* Once successful models have been built for the purpose of history-matching, we can use the same models to make predictions of the most crucial parameters in a WAG/FACF process. We expect trapped gas saturation (WAG), aqueous phase salinity (FACF), and drive foam strength (FACF) to be the most essential parameters in the related processes.

## 1.7 Thesis outline

The content of this thesis is based upon several published journal articles, and one soon to be published, by the author, all concerning *FACF* for *EOR*. The dissertation consists of seven chapters with **Chapter 1** being the introduction.

**Chapter 2** examines oil displacement mechanisms that are responsible for oil recovery during immiscible continuous gas injection and *WAG*. To this end, several well-controlled core-flood experiments are conducted using these injection schemes. Obtained pressure drop, effluent and, if available, CT scan data are used to elaborate on the related displacement processes. The results obtained in this chapter provide a baseline against which the outcomes of *FACF* will be compared to identify its benefits.

**Chapter 3** presents an experimental investigation of *FACF* at model-like conditions focussing on the impact of drive foam quality on oil bank displacement during under-optimum salinity *FACF*. At first surfactant slug phase behaviour is assessed in bulk, leading to the surfactant slug formulation to be used in succeeding core-floods. Once the surfactant slug and drive formulations were selected, CT-assisted core-flood experiments are performed in a 1 meter Bentheimer sandstone core, varying the foam quality of the drive foam. True dual-energy CT data are used to construct three-phase saturation profiles over the course of the core-flood experiments. Related novel results shed light on mechanisms responsible for oil mobilization and its displacement by foam.

**Chapter 4** proceeds with the theme of **Chapter 3** and provides an elaborated study on the effect of surfactant slug salinity on oil mobilization and displacement processes in *FACF* applied at model-like conditions. First, bulk foam experiments are conducted, highlighting the effect of surfactant concentration and salinity on foam stability in bulk. Next, CT-assisted *FACF* core-flood experiments, both at (near-)optimum and under-optimum salinity, are conducted and lead to the construction of three-phase saturation paths presented in ternary diagrams. While the main focus is on oil bank formation and displacement mechanisms, special attention is paid to the effect of slug salinity on the produced clean oil-solubilized oil ratio. The *FACF* saturation paths are compared with the ones for gas injection/*WAG* (**Chapter 2**) to clarify the beneficial effect of *FACF* over continuous immiscible gas injection/*WAG*.

**Chapter 5** serves as a full extension of **Chapters 3** and **4**, where *FACF* was studied in a model-like setting, and reports on an extensive laboratory study that addresses the feasibility of *FACF* to reservoir conditions. It includes surfactant stability, crude oil-surfactant phase behaviour, and drive foam stability in bulk tests that yield various surfactant formulations to be used in the ensuing core-floods. Core-flood experiments include a foam quality scan, where one surfactant drive formulation is used to generate foam at varying gas fractional flows in the absence of oil, and a series of CT-scanned *FACF* core-floods. Novel qualitative and quantitative analyses of the oil bank formation and its displacement during *FACF* at reservoir conditions are presented; focussing on the effects of surfactant slug salinity and drive foam strength.

**Chapter 6** discusses simulating *WAG* and *FACF* experiments at the model-like conditions imposed in **Chapters 2, 3** and **4**. Through the development of several mechanistic models, using a three-dimensional research simulator for multiphase and multicomponent systems, history-matching of the related core-flood experiments is done. The models, and related simulations, aim at exploring

## Chapter 1 – Introduction

and identifying the main mechanisms, and their controlling parameters, that determine incremental oil recovery in *WAG* and *FACF*.

**Chapter 7** presents the main conclusions of this thesis and gives recommendations for related future research.



## 2. Immiscible gas injection schemes: continuous gas and water-alternating-gas injection

---

### Abstract

*Gas injection is a widely applied enhanced oil recovery method. However, poor vertical and areal sweep efficiency result in inefficient oil displacement. For improving gas mobility control, water-alternating-gas injection has often been applied. The goal of this study was to compare several immiscible nitrogen injection schemes and to investigate how rock-fluid and fluid-fluid interactions control the immiscible flooding process. Well-controlled core-flood experiments were performed in Bentheimer sandstone cores. Nitrogen was injected into a core saturated with n-hexadecane at connate water saturation at constant pressure. Nitrogen was also injected at residual oil to waterflood and a water-alternating-gas injection scheme was evaluated. Core-flood results clearly demonstrated the beneficial effects of water-alternating-gas injection over continuous gas injection. The findings in this study suggest that a) residual oil saturation for immiscible nitrogen flooding is lower under three-phase flow compared to two-phase flow, and b) the relatively high oil recovery, i.e. lower ultimate residual oil saturation, by water-alternating-gas injection is most likely related to an increase in trapped gas saturation during the first few WAG cycles.*

---

The content of this chapter is based on the following publications:

Janssen, M.T.G., Pilus, R.M., and Zitha, P.L.J. 2019. A Comparative Study of Gas Flooding and Foam-Assisted Chemical Flooding in Bentheimer Sandstones. *Transport in Porous Media*. DOI: 10.1007/s11242-018-01225-3.

Janssen, M.T.G., Azimi, F., and Zitha, P.L.J. 2018. Immiscible Nitrogen Flooding in Bentheimer Sandstones: Comparing Gas Injection Schemes for Enhanced Oil Recovery. Society of Petroleum Engineers. DOI: 10.2118/190285-MS.

## 2.1 Introduction

This chapter elaborates on the base case study which scrutinizes oil displacement mechanisms that are responsible for oil recovery during immiscible continuous gas injection and WAG, as they form the basis for understanding the incremental effect of *FACF*. As previously discussed in **Section 1.2**, during immiscible gas injection it is expected that rock-fluid and fluid-fluid interactions, as described by relative permeabilities and capillary pressures, control oil displacement (Bear and Bachmat, 1990). One potential oil displacement mechanism that may play a pre-dominant role in immiscible gas floods is the drainage of oil films that lie between the water and gas phases within the pore space: film flow (Oren *et al.*, 1992; Vizika, 1993; Kalaydjian, 1992; Blunt *et al.*, 1995; Khorshidian *et al.*, 2016). Whether the oleic phase will spread out over the *g/w* interface in a water-wet porous medium is controlled by the spreading coefficient (Rowlinson and Widom, 1982):

$$C_s = \sigma_{gw} - \sigma_{go} - \sigma_{ow} \quad (2.1)$$

where  $\sigma_{gw}$ ,  $\sigma_{go}$ , and  $\sigma_{ow}$  are the *g/w*, gas-oil (*g/o*), and *o/w* IFTs, respectively. Only if  $C_s > 0$  (i.e.  $\sigma_{gw} > \sigma_{go} + \sigma_{ow}$ ) oil tends to spread over the *g/w* interface forming a thin liquid film (Hirasaki, 1993). If  $C_s < 0$ , stable three-phase contacts are expected and the oil blob most likely will keep its original structure; no tendency for the oleic phase to move towards the *g/w* interface. Note that the IFTs mentioned in **Equation 2.1** refer to internal equilibrium conditions. Examples for the latter condition, i.e. non-spreading oils, involve long-chain alkanes like dodecane (Blunt *et al.*, 1995). Although the abovementioned rule has been supported by many studies, some studies have reported the presence of continuous oil films for non-spreading oils (Dong *et al.*, 1995; Keller *et al.*, 1997). In order for the film flow phenomena to contribute to the incremental oil recovery observed in the laboratory during immiscible gas flooding experiments (when  $C_s > 0$ ), the film thickness needs to be sufficiently large (Blunt *et al.*, 1995). As very thin oil films yield slow drainage rates, thick oil films are required to provide pathways for speeding up the drainage, improving the oil relative permeability.

Several experimental studies focussing on displacement processes during immiscible gas flooding were reported (Blunt *et al.*, 1995; Vizika and Lombard, 1996; Dicarolo *et al.*, 2000; Grattoni and Dawe, 2003). Grattoni and Dawe (2003) demonstrated the significance of oil film flow in terms of oil recovery in water-wet sintered packs of glass beads. They observed a substantial increase in oil production in the case of spreading oils compared to non-spreading oils. This is due to the transition of residual, i.e. immobile, oil ganglia's into mobile continuous oil films (when  $C_s > 0$ ) which can be transported by the injected gas. On the other hand, if  $C_s < 0$ , oil may be produced in smaller amounts and in a discontinuous form (e.g. small slugs) by the push-pull process of the injected gas. They observed that in the latter case the majority of the non-spreading oil remained trapped due to discontinuity of the oleic phase. Although most experimental studies showed the effect of oil film flow in gravity assisted immiscible gas floods, Oren *et al.* (1992) revealed that oil recovery by film flow might also be an important displacement mechanism in horizontal immiscible gas floods where gravity effects are negligible.

Unfavourable mobility ratios between injected gas and the displaced fluids result in a poor  $E_v$  for any continuous gas injection process. For controlling gas mobility, WAG injection might be applied (**Section 1.2**). By periodically shifting between slugs of gas and water, part of the mobile gas present becomes trapped yielding a reduced gas relative permeability, thus an improved  $E_v$  of the injected gas (**Equation 1.2**). Shandrygin *et al.* (2015) performed WAG core-flood experiments in a water-wet

sandstone core at residual oil to waterflood ( $S_{or\_WF}$ ). They observed that, as soon as gas injection was initiated in the first WAG cycle, the discontinuous oleic phase started to redistribute. Reason for this is that the injected non-wetting gas phase occupied the larger pores of the system, moving out part of the previously trapped oil globules (now intermediate-wetting phase). The oil droplets that were mobilized by gas invading the larger pores could now be transported by the injected water and gas. Eventually, this three-phase flow effect led to an increasing  $E_D$  (**Equation 1.1**), thus a reduction in residual oil saturation ( $S_{or}$ ). This effect was also observed in various micromodel studies (Sohrabi *et al.*, 2000; Dong *et al.*, 2002; Feng *et al.*, 2004; van Dijke *et al.*, 2010).

Multiple studies in the past have addressed oil displacement mechanisms in immiscible gas/WAG injection. However, this was mainly done on pore-scale level using micromodels and capillary tubes. Bulk of these studies focused on either gravity assisted immiscible gas floods or at WAG floods individually. The aim of this study was to provide a complete comparison study on core-scale utilizing several immiscible nitrogen injection schemes. To this end numerous well-controlled core-flood experiments were conducted using various injection schemes: a) continuous nitrogen injection and b) WAG injection. X-ray CT images were taken during the flooding process to map the phase saturation distributions over time. Three-phase saturation paths are used to interpret core-scale results in the light of potential oil displacement mechanisms on pore-level. This chapter serves as a baseline for assessing the merits of the novel chemical EOR methodology of FACF.

## 2.2 Materials and methods

### 2.2.1 Chemicals

**Table 2.1** presents the physical properties of the various chemical components used in this study. The oleic phase, *n*-hexadecane, was doped with a red colorant (Oil Red O) for visualization purposes. Sodium chloride was dissolved in demineralized water for brine preparation. Demineralised water was produced using an ELGA PURELAB Prima120 water treatment device. It purifies water by using several stages of membrane filtration, to remove most of the mineral and salt ions present, until a water conductivity of 1.0  $\mu\text{S}/\text{cm}$  or lower is reached. The gas used to perform immiscible gas flooding and WAG core-flood experiments was nitrogen. In two experiments the oleic and aqueous phases were doped with 1-iododecane and potassium-iodide, respectively, for enhancing the CT contrast (see **Appendix A** for additional information regarding CT processing). **Table 2.2** gives an overview of the brine and oil types, including their physical properties, utilized in the various core-flood experiments.

**Table 2.1:** Physical properties of the chemicals utilized.

Chemical	Formula	Molecular weight (g/mol)	Density ( $\text{g}/\text{cm}^3$ ) <sup>a</sup>	Viscosity ( $\text{mPa}\cdot\text{s}$ ) <sup>a</sup>	Supplier	Purity (%)
<i>n</i> -hexadecane	$\text{CH}_3(\text{CH}_2)_{14}\text{CH}_3$	226.45	$0.775 \pm 0.001$	$3.37 \pm 0.06$	Merck	$\geq 99$
Oil Red O	$\text{C}_{26}\text{H}_{24}\text{N}_4\text{O}$	408.49	-	-	Sigma-Aldrich	$\geq 75$
Sodium chloride <sup>b</sup>	NaCl	58.44	$2.160 \pm 0.001$	-	Merck	$\geq 99$
1-iododecane	$\text{CH}_3(\text{CH}_2)_9\text{I}$	268.18	$1.257 \pm 0.001$	-	Sigma-Aldrich	$\geq 98$
Potassium iodide <sup>b</sup>	KI	166.00	$3.120 \pm 0.001$	-	Sigma-Aldrich	$\geq 99$
Nitrogen <sup>b</sup>	$\text{N}_2$	28.01	$1.165 \pm 0.001 \times 10^{-3}$	$1.76 \pm 0.50 \times 10^{-2}$	-	100

<sup>a</sup>All densities and viscosities mentioned are at 20°C and atmospheric pressure.

<sup>b</sup>Lide (2012).

**Table 2.2:** Brine and oil physical properties.

Exp.	Brine type	Brine density (g/cm <sup>3</sup> ) <sup>a</sup>	Brine viscosity (mPa*s) <sup>a</sup>	Oil type	Oil density (g/cm <sup>3</sup> ) <sup>a</sup>	Oil viscosity (mPa*s) <sup>a</sup>
1	3.0 wt% NaCl	1.020 ± 0.001	1.07 ± 0.05	<i>n</i> -hexadecane <0.006 wt% Oil Red O	0.775 ± 0.001	3.37 ± 0.06
2	3.0 wt% NaCl 7.5 wt% KI	1.078 ± 0.001	0.97 ± 0.08	<i>n</i> -hexadecane <0.006 wt% Oil Red O 7.5 wt% 1-iododecane	0.798 ± 0.001	3.19 ± 0.06
3	3.0 wt% NaCl 15.0 wt% KI	1.142 ± 0.001	1.01 ± 0.06	<i>n</i> -hexadecane <0.006 wt% Oil Red O 5.0 wt% 1-iododecane	0.790 ± 0.001	3.22 ± 0.07

<sup>a</sup>All densities and viscosities mentioned were measured at 20°C and atmospheric pressure.

### 2.2.2 Core samples

Bentheimer sandstones were used in this study as a model reservoir owing to its high permeabilities ( $2.6 \pm 1.2$  Darcy) and fairly homogeneous mineralogy [ $> 91$  weight percent (wt%) quartz] (Peksa *et al.*, 2015). Newly cored sandstone samples were dried in an oven at 60 °C for 48 h before they were cast into an epoxy resin, to avoid any bypassing flow alongside the core. The resin penetrated approximately 1.00 mm radially into the sandstone, reducing its effective diameter to  $3.80 \pm 0.10$  cm. Multiple equidistant holes were drilled in the glued cores for pressure(drop) measurements. **Table 2.3** gives an overview of the physical properties of the Bentheimer sandstone cores used in this study. Porosities were determined by using an Ultra Pycnometer 1000 (Quantachrome Corporation). The experiments were conducted under stable gravity conditions by placing the core-holder vertically on the couch of the CT scanner.

**Table 2.3:** Properties of Bentheimer sandstone cores used in this study.

	Experiment		
	1	2	3
Porosity (%)	22.70 ± 0.10	23.10 ± 0.10	23.60 ± 0.10
Permeability (Darcy)	2.68 ± 0.08	1.94 ± 0.14	2.30 ± 0.18
Length (cm)	17.00 ± 0.10	17.00 ± 0.10	17.00 ± 0.10
Diameter (cm)	3.90 ± 0.10	3.90 ± 0.10	3.90 ± 0.10
Pore volume (cm <sup>3</sup> )	46.10 ± 2.89	46.91 ± 2.94	47.93 ± 3.00

### 2.2.3 Experimental set-up

**Figure 2.1** presents the schematic of the experimental set-up used to conduct the core-flood experiments. The sandstone cores were placed in a core-holder made of polyether ether ketone (PEEK), that exhibits low X-ray attenuation, and were exposed to a confining pressure that equalled the inlet pressure. The core-holder was placed in line with either a single cylinder syringe pump (1000D Syringe Pump, Teledyne ISCO series) or, for the WAG experiment, with a dual cylinder liquid pump (Quizix QX-1500 HC). The ISCO pump was used for injecting both the aqueous and oleic phases, whereas the Quizix pump was only used for injecting aqueous solutions. N<sub>2</sub> was supplied from a 200 bar cylinder. A mass flow controller (Bronkhorst, EL-FLOW) was used to regulate the gas flow rate. A backpressure regulator (DEMO-TU Delft) was connected to the outlet to control the outlet pressure during the experiments. CO<sub>2</sub>, used for initial flushing of the cores, was provided by a 200 bar cylinder. A fraction collector (GE Akta Frac-920) was used to sample the effluents at the outlet at

predetermined time intervals. A total of four differential and two absolute pressure transducers were installed to monitor the pressure(drop) along the core. A thermocouple was used to record the temperature in the laboratory. The pressure transducers, and one thermocouple, were connected to a data acquisition system (National Instruments) which recorded pressure and temperature data at a 10 second time interval. Since the experiments were performed under gravity stable conditions, i.e. core-holder placed vertically, two sets of valves were installed which allows for changing the injection direction (from top to bottom and vice versa). The experiments were performed at room temperature ( $20 \pm 2$  °C).

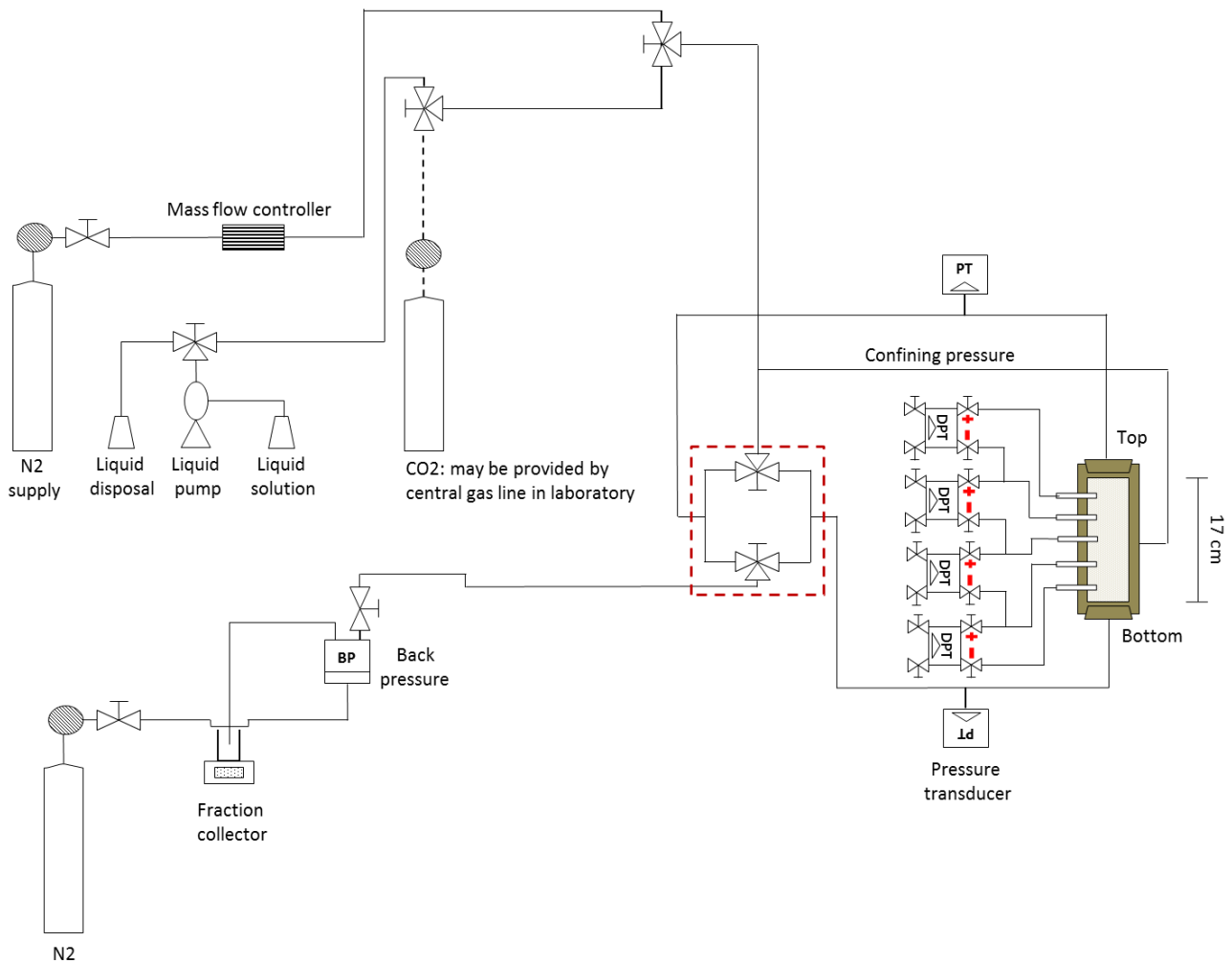


**Figure 2.1:** Schematic of the experimental set-up. The set of valves marked by the red dashed lines was used to switch injection direction from top-down (for oil and gas injection) to bottom-up (for water injection).

### 2.2.4 CT scan

In Exp. 2 and 3 the sandstone cores were CT scanned using a Siemens SOMATOM Definition CT scanner to gain insight into phase saturation distributions during the displacement processes. Each CT scan contained 12 slices of 4 mm thick, each containing 512×512 pixels with a pixel size of 0.2×0.2 mm. Scanning was done in sequential mode using an energy of 140 kV (250 mA). The acquired data was analysed using both ImageJ and Matlab™ software. See **Appendix A** for additional information regarding CT processing.

### 2.2.5 Experimental procedure

**Table 2.4** presents an overview of the gas injection schemes investigated in this study. In Exp. 1 immiscible N<sub>2</sub> flooding was applied at initial oil saturation ( $S_{oi}$ ), at connate water saturation ( $S_{wc}$ ). In Exp. 2, N<sub>2</sub> was injected in a continuous manner after water flooding (i.e. at  $S_{or\_WF}$ ) in order to study the effect of three-phase flow conditions versus two-phase flow. WAG injection was initiated at  $S_{oi}$ , thus at  $S_{wc}$ , in Exp. 3.

**Table 2.4:** Overview of core-flood experiments conducted.

Exp.	Procedure	Gas flow rate (cm <sup>3</sup> /min)	Liquid flow rate (cm <sup>3</sup> /min)	WAG ratio (water-gas ratio)	Backpressure (bar)	CT
1	N <sub>2</sub> flooding	0.5	-	-	10	No
2	Water flooding + N <sub>2</sub> flooding	0.5	2.0	-	5	Yes Oil – 7.5 wt% dopant Brine – 7.5 wt% dopant
3	water-alternating-gas injection	0.5	2.0	1:6	5	Yes Oil – 5.0 wt% dopant Brine – 15.0 wt% dopant

Note that for Exp. 2 and 3 there is a difference in the added amounts of dopant to both the oleic and aqueous phases. Based on the results of the dopant calibration and the CT imaging observations made during Exp. 2, it was decided to use dopant concentrations of 5.0 and 15.0 wt% for the oleic and aqueous phases, respectively, in Exp. 3. The applied change in dopant concentrations revealed better contrasts between the various phases on CT images.

The experimental procedure (**Table 2.5**) started with flushing the core with CO<sub>2</sub> for two hours at an injection pressure of 5 bar to remove all the air inside the system. Afterwards, approximately 10 pore volumes to liquid (PV) of 3.0 wt% NaCl brine was injected. During brine saturation the backpressure was increased to 25 bar to ensure complete dissolution of CO<sub>2</sub> in brine. By varying brine injection rates the average permeability of the core used was derived using Darcy's law (Darcy, 1856). Subsequently, primary drainage was initiated by injecting approximately 6 PV of *n*-hexadecane. To obtain the oil end-point relative permeability ( $k_{ro}^0$ ), the flow rates were varied during the last PV of oil injection. At this point  $S_{wc}$  was reached; starting point for N<sub>2</sub> flooding and WAG injection in Exp. 1 and 3, respectively. In Exp. 1 N<sub>2</sub> was injected, at  $S_{oi}$ , at a constant backpressure of 10 bar. In Exp. 3, a total of 12 WAG cycles [each cycle consisted of injecting a N<sub>2</sub> slug (1.30 PV) followed by a water slug (0.22 PV)] were injected at  $S_{oi}$ . Subsequent to primary drainage, in Exp. 2, water flooding (6 PV) was initiated to reach  $S_{or\_WF}$  and continuous N<sub>2</sub> injection took place afterwards. Similar to obtaining  $k_{ro}^0$ , the water end-point relative permeability ( $k_{rw}^0$ ) was calculated at the end of water flooding. In order to operate under gravity stable conditions, the core was placed vertically and water was injected from bottom to top whilst oil and gas were injected from top to bottom (for WAG, i.e. Exp. 3, both water and gas were injected top-down). For each experiment, gas flooding/WAG injection continued until no more oil was produced. The core-floods conducted are analysed in terms of oil recovery, pressure data, CT images (if available), and saturation profiles.

**Table 2.5:** Sequence of experimental procedure.

Step	Exp.	Description	Backpressure (bar)	Flow rate (cm <sup>3</sup> /min)	Injection pressure (bar)	Flow direction
1	All	CO <sub>2</sub> flushing	-	-	5	Down
2	All	Brine saturation	0, 25	2.0	-	Up
3	All	Oil injection	0	Exp. 1, 3: 2.0 Exp. 2: 5.0	-	Down
4	2	Water flooding <sup>a</sup>	0	2.0	-	Up
5	1 and 2	Gas flooding	Exp. 1: 10 Exp. 2: 5	0.5	-	Down
6	3	WAG injection <sup>a</sup>	5	Gas: 0.5 Water: 2.0	-	Down

<sup>a</sup>For water flooding and WAG injection, the same model brine was used as for brine injection in the specific experiment.

## 2.3 Results and discussion

The main results of the performed core-flood experiments are shown in **Table 2.6**. The obtained  $k_{rw}^0$  and  $k_{ro}^0$  are in good agreement with the data reported by Treiber et al. (1972) for consolidated water-wet porous media, although slight differences between individual experiments (i.e. cores) were observed. The relatively low value for  $k_{ro}^0$  found in Exp. 1 might be a result of the true  $S_{wc}$  not being reached ( $S_{wc}$  equalled  $0.30 \pm 0.02$  in Exp. 1 versus  $0.25 \pm 0.03$  in Exp. 2 and 3). This section proceeds with the following subsections: primary drainage and forced imbibition, N<sub>2</sub> flooding at  $S_{wc}$ , N<sub>2</sub> flooding at  $S_{or\_WF}$ , WAG injection at  $S_{wc}$ , and oil recovery. Pressure drop profiles, oil recovery plots, and CT data are analysed in order to assess the various injection schemes. Reported pressure drop values throughout the entire thesis are averaged values together with their standard deviations.

**Table 2.6:** Summary of the core-flood experiments conducted.  $S_{or\_GF}$ ,  $R_{FWF}$ ,  $R_{FGF}$ , and  $OIIP$  represent the residual oil saturation to N<sub>2</sub> flooding/WAG, recovery factor corresponding to water flooding, recovery factor corresponding to N<sub>2</sub> flooding/WAG, and oil initially in place, respectively.

Exp.	$k_{ro}^0$	$k_{rw}^0$	$S_{wc}$	$S_{oi}$	$S_{or\_WF}$	$R_{FWF}$ (% of OIIP)	$S_{or\_GF}$	$R_{FGF}$ (% of OIIP)
1	$0.48 \pm 0.05$	-	$0.30 \pm 0.02$	$0.70 \pm 0.02$	-	-	$0.35 \pm 0.02$	$50 \pm 4$
2	$0.65 \pm 0.07$	$0.14 \pm 0.01$	$0.24 \pm 0.02$	$0.76 \pm 0.02$	$0.49 \pm 0.02$	$36 \pm 4$	$0.36 \pm 0.02$	$53 \pm 4$
3	$0.60 \pm 0.05$	-	$0.26 \pm 0.02$	$0.74 \pm 0.02$	-	-	$0.30 \pm 0.02$	$59 \pm 4$

### 2.3.1 Primary drainage and forced imbibition

This subsection discusses the pressure drop readings and corresponding oil saturation ( $S_o$ ) profiles for the primary drainage and forced imbibition injection stages in Exp. 2 and Exp. 3, which are representative for Exp. 1 as well.

#### 2.3.1.1 Pressure drop

The pressure drop profiles obtained during primary drainage (Exp. 2 and 3) and forced imbibition (Exp. 2) are shown in **Figure 2.2**. Despite the difference in oil injection rate (5.0 cm<sup>3</sup>/min in Exp. 2 and 2.0 cm<sup>3</sup>/min in Exp. 3), both pressure drop profiles for primary drainage are very similar. Once the oleic phase reached the core inlet, a sharp increase in pressure drop was observed due to the capillary entry pressure; equivalent to approximately  $55 \pm 10$  mbar in both experiments. Next, the pressure drop increased gradually, reflecting the propagating oil front, until it reached a maximum

value of  $543 \pm 5$  mbar (Exp. 2) and  $200 \pm 5$  mbar (Exp. 3) at their respective oil breakthrough times of  $0.76 \pm 0.02$  PV (Exp. 2) and  $0.78 \pm 0.02$  PV (Exp. 3) oil injected. After oil breakthrough, the pressure drops decreased towards a value of  $370 \pm 10$  mbar (Exp. 2) and  $140 \pm 10$  mbar (Exp. 3), which corresponds to oil flow at  $S_{wc}$ . Note that the difference in absolute pressure drop readings between Exp. 2 and 3 corresponds roughly with a factor 2.5; the difference in oil injection rate.

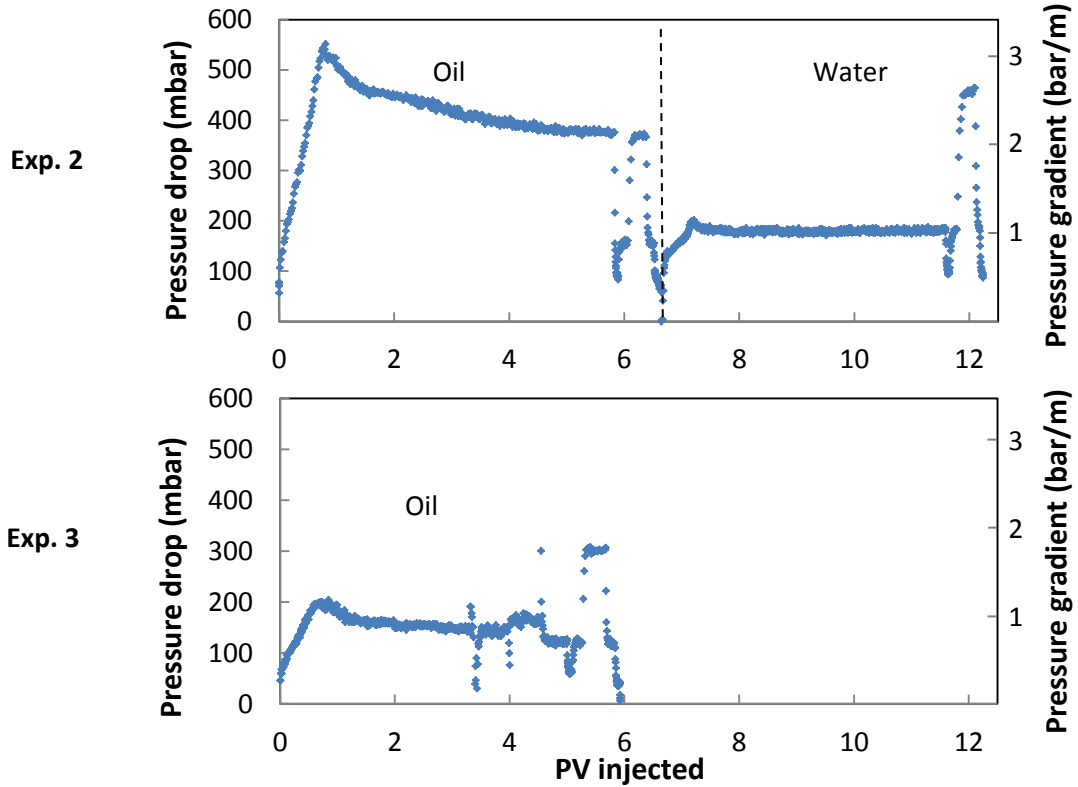


**Figure 2.2:** Total pressure drop profiles and pressure gradients for Exp. 2 (top) and Exp. 3 (bottom) prior to gas injection. Oil represents the primary drainage stage whereas Water refers to water flooding. Oil injection, at  $5.0 \text{ cm}^3/\text{min}$  (Exp. 2) or at  $2.0 \text{ cm}^3/\text{min}$  (Exp. 3), was continued for several pore volumes before varying the flow rate to obtain  $k_{ro}^0$ . Next, in Exp. 2, water flooding was initiated (at  $2.0 \text{ cm}^3/\text{min}$ ) after approximately 6.71 PV of oil injected. Once 5.0 PV of water was injected, the flow rate was varied in order to compute  $k_{rw}^0$ .

After injecting oil for approximately  $6.71 \pm 0.02$  PV, water flooding was initiated in Exp. 2 at  $2.0 \text{ cm}^3/\text{min}$ . Firstly, the pressure drop increased until it reached a maximum value of  $202 \pm 5$  mbar at water breakthrough ( $0.45 \pm 0.02$  PV after water flooding started). Subsequently, pressure drop declined slightly to a steady-state value of  $180 \pm 5$  mbar (pressure gradient of  $1.06 \pm 0.03$  bar/m), corresponding to solely water production from the core at  $S_{or\_WF}$ .

### 2.3.1.2 CT images

The CT images and analogous  $S_o$  profiles for both primary drainage and water flooding, in Exp. 2, are presented in **Figure 2.3**. **Figure 2.4** shows related CT images and  $S_o$  profiles during primary drainage in Exp. 3. Note that, due to the vertical position of the core-holder on the couch of the CT scanner, X-shaped artefacts of a significant magnitude were present in all CT images taken. The artefacts originate from the fact that the length of a diagonal X-ray path is greater than the length of X-ray paths coming from the sides; varying the amount of material encountered by different ray paths (Mees *et al.*, 2003). The acquired CT data was corrected in order to obtain two-phase saturation distributions. For each timestep, the center slice was loaded into Matlab<sup>TM</sup>, cropped, and averaged.

Subsequently, the averaged slice was corrected for the artefacts present before calculating two-phase saturation distributions (see **Appendix A**).

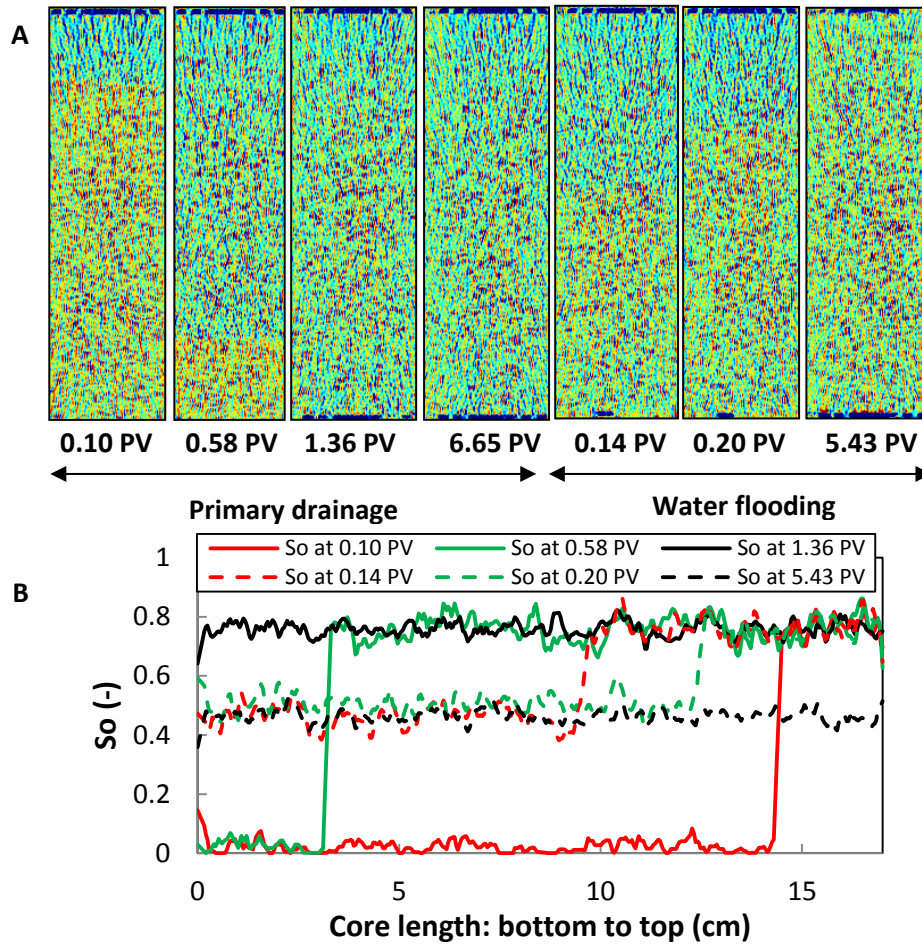


**Figure 2.3:** Displacement profiles during primary drainage and water flooding in Exp. 2: A) CT images and B) oil saturation profiles. PV=0 corresponds to the start of the particular injection phase. A: water (red/green) is displaced by oil (blue) during primary drainage and during water flooding oil (blue) is produced by water (red/green). B: continuous profiles present primary drainage injection phase whilst dashed lines correspond to water flooding. Note that oil was injected from the top and water/brine from the bottom.

During primary drainage water (red/green) was displaced by oil (blue) in a piston-like manner (**Figure 2.3A**). At the end of primary drainage, the relatively low  $S_o$  near the outlet region (i.e. bottom) is most likely a consequence of the capillary end effect. It implies the accumulation of water (wetting phase) near the outlet in order to try to satisfy the zero capillary pressure condition at the outlet boundary. When scanning the core horizontally (i.e. no X-shaped artefacts correction applied), this accumulation of the wetting phase is more distinctly recognizable on CT images. Corresponding  $S_o$  profiles (continuous lines in **Figure 2.3B**) show a sharp shock front region. However, most probably due to the correction applied, a typical rarefaction wave upstream of the shock front is hard to observe. Eventually, an averaged  $S_{oi}$  of  $0.76 \pm 0.02$  was reached.

CT scan images taken during water flooding show the displacement of the oleic phase (blue) by water (red/green) (**Figure 2.3A**). Corresponding  $S_o$  profiles show a similar trend compared to those for primary drainage. Nonetheless, the displacement front is less sharp due to capillary forces. After 5.43 PV water injected, a  $S_{or\_WF}$  of  $0.46 \pm 0.04$  was achieved, which is slightly lower than the value

obtained through material balance (**Table 2.6**). The displacement of oil by water is assumed to be piston-like with an end-point mobility ratio ( $M^0$ ) [ $= (k_{rw}^0/\mu_w)/(k_{ro}^0/\mu_o)$ ] of 0.71.

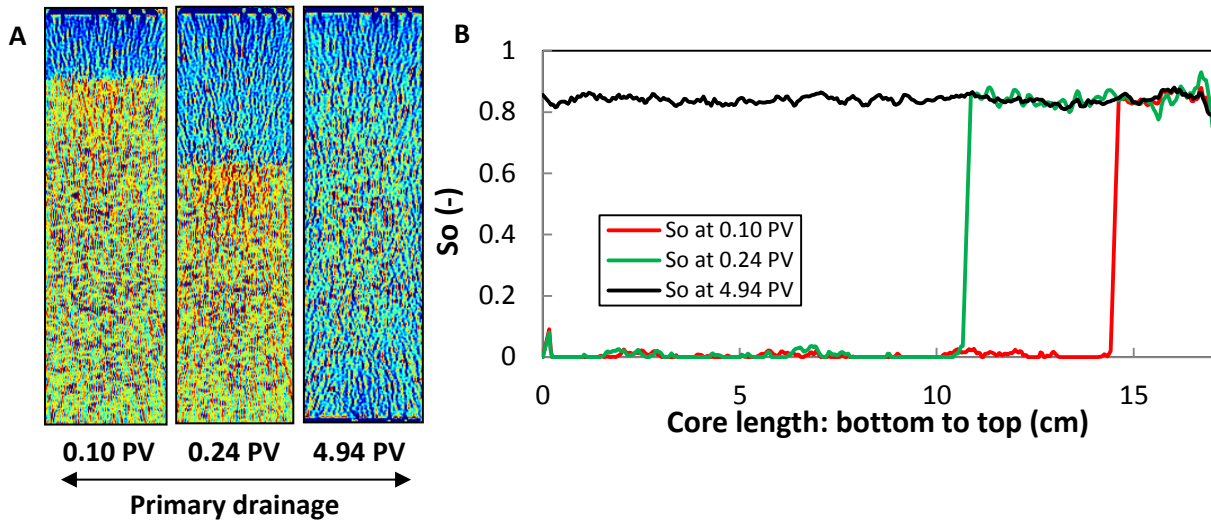


**Figure 2.4:** A: CT images taken during primary drainage in Exp. 3. PV=0 corresponds with the start of oil injection. Water (red/green) is displaced by oil (blue) in a stable manner. B: Related oil saturation profiles. Note that oil was injected from the top.

The CT images and  $S_o$  profiles related to primary drainage in Exp. 3 (**Figure 2.4**) are very similar to those presented in **Figure 2.3**. However, due to the changes in dopant concentrations added (**Table 2.4**), the difference between the oil and water attenuation coefficients increased, thus improving the CT contrast between the aqueous and oleic phases. Due to the correction applied, for removing X-shaped artefacts, the expected relatively low  $S_o$  at the core outlet and rarefaction wave upstream of the shock front are not observable. Eventually, an averaged  $S_{oi}$  of  $0.84 \pm 0.01$  was reached, which is nearly 10% higher than the  $S_{oi}$  obtained through material balance (**Table 2.6**).

### 2.3.2 $N_2$ flooding at $S_{wc}$

After primary drainage,  $N_2$  was injected under gravity stable conditions, i.e. from top to bottom (Exp. 1 in **Table 2.6**). In this subsection the pressure drop profile during  $N_2$  flooding at  $S_{wc}$  in Exp. 1 is discussed in more detail.

#### 2.3.2.1 Pressure drop

**Figure 2.5** presents the total pressure drop profile during immiscible  $N_2$  flooding in Exp. 1. As aforementioned, continuous gas injection was done under gravity stable conditions (i.e. from the top of the core). The estimated critical injection velocity, i.e. the maximum velocity at which the  $g/o$  contact remains stable/horizontal, was approximately 2.0 ft/day, which equals the used injection rate (Dietz, 1953). As soon as gas entered the core, oil was displaced and produced from the outlet (i.e. bottom side). Due to the production of oil by the moving gas front, the total pressure drop increased gradually to a maximum value of  $97 \pm 3$  mbar and then it decreased to steady-state values of approximately  $85 \pm 5$  mbar. This steady-state value is equivalent to a pressure gradient of  $0.50 \pm 0.03$  bar/m. Gas breakthrough was observed after injecting  $0.51 \pm 0.02$  PV of gas, evident from the fluctuations in pressure drop due to gas leaving the backpressure (**Figure 2.1**). The observed breakthrough time for secondary gas flooding is consistent with those found by Naylor and Frørup (1989), who studied gravity stable oil displacement by  $N_2$  (using a superficial velocity of approximately 1.0 ft/day) in fairly clean water-wet Aeolian sandstones.

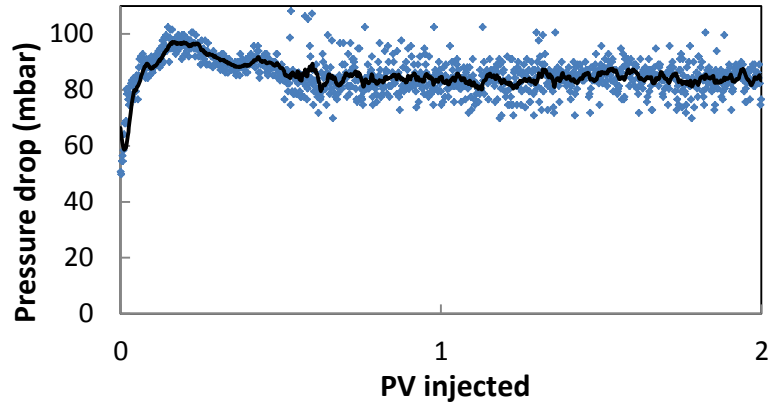


**Figure 2.5:** Total pressure drop profile during gas injection at gravity stable conditions in Exp. 1. A trend line (moving average with period equal to 14) is added to the data series.

### 2.3.3 N<sub>2</sub> flooding at $S_{or\_WF}$

In Exp. 2 first the core was brought to  $S_{or\_WF}$ , then N<sub>2</sub> was injected from the top in a continuous manner. This subsection elaborates on the related pressure drop profile during gas flooding in Exp. 2.

#### 2.3.3.1 Pressure drop

**Figure 2.6** shows the total pressure drop profile over the entire core during gas flooding for the first two PV injected. As soon as gas touched the core, a gradually increasing trend in total pressure drop was observed, indicating downward movement of the gas front through the core. During this stage both oil and water were produced. Once gas breakthrough occurred, at  $0.51 \pm 0.02$  PV, the total pressure drop reached a maximum of  $91 \pm 5$  mbar after which it slightly reduced to  $82 \pm 7$  mbar (equivalent to a pressure gradient of  $0.48 \pm 0.04$  bar/m).

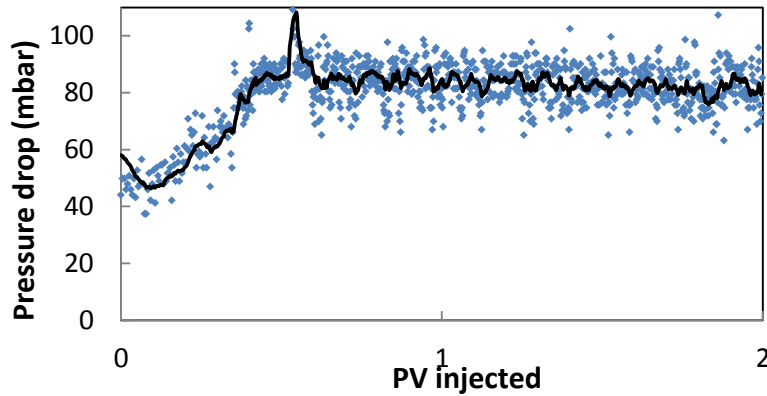


**Figure 2.6:** Total pressure drop profile during gas injection at gravity stable conditions in Exp. 2. A trend line (moving average with period equal to 14) is added to the data series.

### 2.3.4 WAG injection at $S_{wc}$

In Exp. 3 gas was injected at  $S_{oi}$  through a WAG scheme to investigate gas mobility control and displacement efficiency related to WAG. In this core-flood, both gas and water were injected from the top. The water that was injected in the various WAG cycles is similar to the model brine (**Table 2.2**). A total of 12 WAG cycles were injected. Each cycle started with injecting  $1.30 \pm 0.02$  PV of N<sub>2</sub> followed by  $0.22 \pm 0.02$  PV of water. The WAG ratio selected (1:6) may be considered to be dry, i.e. continuous gas injection in which small slugs of water were injected to improve mobility control (Dyer and Farouq Ali, 1994). In this subsection, the related pressure drop profile during WAG injection at  $S_{wc}$  is discussed in more detail. Unfortunately, CT scans acquired during WAG injection suffered from excessive artefacts and provide no meaningful insights.

### 2.3.4.1 Pressure drop

**Figure 2.7** presents the total pressure drop profile during WAG injection in Exp. 3. Each cycle started with the injection of  $N_2$  at  $0.5 \text{ cm}^3/\text{min}$  followed by water injection at  $2.0 \text{ cm}^3/\text{min}$ . Gas injection in the first WAG cycle shows a similar pressure drop profile compared to the one shown in **Figure 2.5**: an increase from  $62 \pm 2$  to  $103 \pm 2$  mbar followed by a slight decrease to  $80 \pm 5$  mbar. Gas breakthrough occurred at  $0.49 \pm 0.02$  PV. Subsequently, the shift from gas to water injection yielded a sharp increase in pressure drop to  $363 \pm 2$  mbar. This is most probably due to a combination of the increased injection rate and the development of a trapped (i.e. non-movable) gas saturation ( $S_{gt}$ ). It can be explained by considering Darcy's law for multi-phase flow in one dimension (Darcy, 1856):

$$\Delta P = u_t \left( \frac{f_o \mu_o}{k_{ro} k} + \frac{f_w \mu_w}{k_{rw} k} + \frac{f_g \mu_g}{k_{rg} k} \right) L \quad (2.2)$$

where  $\Delta P$ ,  $u_t$ ,  $\mu_a$ ,  $k_{ra}$ ,  $k$ ,  $f_a$ , and  $L$  represent the pressure drop, total superficial velocity, viscosity of phase  $a$ , relative permeability of phase  $a$ , absolute permeability to brine, fractional flow of phase  $a$ , and the core length, respectively. Subscripts  $o$ ,  $w$ , and  $g$  refer to the oil, water, and gas phase, respectively. The increase in  $u_t$  by a factor 4, upon switching from gas to water injection, alone cannot explain the increase in pressure drop from  $80 \pm 5$  to  $363 \pm 2$  mbar. This is due to changes in  $\frac{\mu_o}{k_{ro} k}$  and  $\frac{\mu_w}{k_{rw} k}$ . As soon as water injection started, water ( $S_w$ ) and oil ( $S_o$ ) saturations, respectively, increased and decreased, implying an enlarged  $k_{rw}$  while  $k_{ro}$  most probably decreased only slightly due to a relatively small shift in  $S_o$  (effluent analysis revealed only limited amounts of oil being produced during the injection of the first water slug). The above entails that the reduction of  $\frac{\mu_w}{k_{rw} k}$  was of a larger magnitude than the increase of  $\frac{\mu_o}{k_{ro} k}$ , suggesting that  $\frac{\mu_g}{k_{rg} k}$  should increase to be consistent with the observed increase in pressure drop when shifting from gas to water injection in the first WAG cycle. It required a reduction of  $k_{rg}$  due to lowering of the free (i.e. flowing) gas saturation ( $S_{gf}$ ) by production of gas and the formation of  $S_{gt}$ .

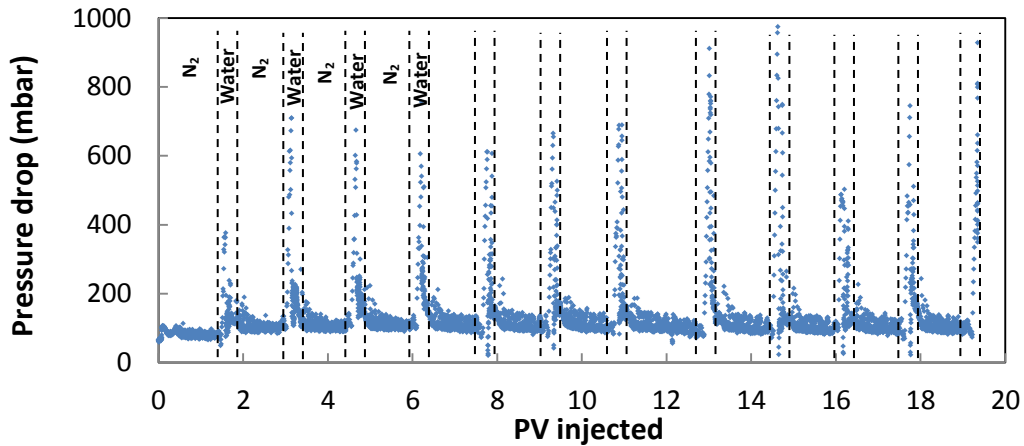


**Figure 2.7:** Total pressure drop profile during WAG injection at  $S_{wc}$  in Exp. 3. Note that for the first four WAG cycles the gas and water injection phases are shown.

During injection of the second gas slug, the total pressure drop decreased to a steady-state value of  $102 \pm 10$  mbar; pressure gradient of  $0.60 \pm 0.06$  bar/m. The higher steady-state pressure drop for gas injection, compared to the first WAG cycle, is most likely due to the presence of  $S_{gt}$  in combination with the introduced water phase in the previous cycle. Water injection at the end of the second cycle

resulted in a peak pressure drop of  $709 \pm 2$  mbar. The relatively high pressure drops during water injection in all succeeding WAG cycles are consistent with earlier work of Dong et al. (2005). Most likely  $S_{gf}$  decreased, whereas  $S_{gt}$  increased, yielding reduced  $k_{rg}$ . The increment in  $S_{gt}$  can furthermore restrict water flow through the pores, reducing  $k_{rw}$ .

### 2.3.5 Oil recovery

**Figure 2.8** shows the oil cut, water cut, and cumulative oil recovery profiles for Exp. 1, 2, and 3. The recovery profile for Exp. 1 shows that roughly half of the ultimate oil recovery was achieved before gas breakthrough occurred. Eventually, after 16 PV of gas injected, a final recovery factor of  $50 \pm 4\%$  of the *OIIP* was reached ( $R_{FGF}$  in **Table 2.6**). During water flooding in Exp. 2, bulk of the oil was produced prior to water breakthrough ( $0.45 \pm 0.02$  PV). After water breakthrough occurred, limited amounts of oil were produced, increasing the recovery factor ( $R_{FWF}$  in **Table 2.6**) from  $31 \pm 4$  to  $36 \pm 4\%$  of the *OIIP*. The relatively low  $R_{FWF}$  (Simjoo, 2012; Janssen *et al.*, 2019c) might be affected by the low absolute permeability of the core used; smaller pore sizes yield higher capillary forces that may keep the oil in place. Including immiscible gas flooding, the ultimate  $R_F$  reached  $53 \pm 4\%$  of the *OIIP* ( $R_{FGF}$  in **Table 2.6**), which implies an incremental oil recovery of  $17 \pm 8\%$  of the *OIIP*. However, it should be noticed that the incremental recovery might be an overestimation due to the suspected low  $R_{FWF}$ . Oil swelling and oil viscosity reduction are negligible displacement mechanisms during immiscible gas injection (Exp. 1 and 2), since the system operated well below the expected *MMP* of roughly 350 bar (Sebastian and Lawrence, 1992).

During WAG injection at  $S_{oi}$  (Exp. 3), in the first cycle, only oil was produced until gas breakthrough occurred. The plot clearly shows that most of the oil was produced in the first two WAG cycles ( $R_{FCycle2}$  equalled  $53 \pm 4\%$  of the *OIIP*). This can be explained by a good contact between the *OIP* and the injected phases. Finally, after successfully injecting 12 WAG cycles, a  $R_{FGF}$  of  $59 \pm 4\%$  of the *OIIP* was reached; equivalent to a  $S_{or\_GF}$  of  $0.30 \pm 0.02$  (**Table 2.6**).

## 2.4 General discussion

In this section the results of our study are re-examined in the light of a conceptual model for the immiscible oil displacement by gas. We shall develop our arguments relying upon the ternary saturation diagrams as they provide a schematic way to depict the different gas injection schemes investigated. All saturation paths presented in this section were determined by volumetric material balance calculations and they represent averaged phase saturations over the entire core length. Before discussing potential oil displacement mechanisms of the gas injection strategies assessed,  $C_s$  of the gas-oil-water system utilized in this work needs to be known. Using the measured  $g/w$ ,  $g/o$ , and  $o/w$  IFTs of  $40.8 \pm 0.1$ ,  $27.3 \pm 0.1$ , and  $10.7 \pm 1.0$  mN/m, respectively, and apply them to **Equation 2.1** (which is valid for our water-wet porous medium), a positive  $C_s$  of  $2.8 \pm 1.2$  was achieved in Exp. 1. The latter suggesting that the oil used is spreading on  $g/w$  interfaces.

**Figure 2.9** shows the saturation paths for Exp. 1, 2, and 3. First let us discuss the one for Exp. 1, i.e. continuous  $N_2$  flooding at  $S_{oi}$ .  $N_2$  injection took place at practically constant  $S_{wc}$ , indicating that gas injection essentially resulted in two-phase  $g/o$  flow. However, since the used gas was not humidified, it is possible that a small amount of water was vaporized into the gas phase; this seems to be negligible though. Oil recovery during continuous  $N_2$  flooding at  $S_{oi}$  shows characteristic features of an immiscible displacement of oil by the propagating gas front. Bulk of the oil was most likely displaced and produced by the advancing  $g/o$  interface, accounting for approximately 60% of the

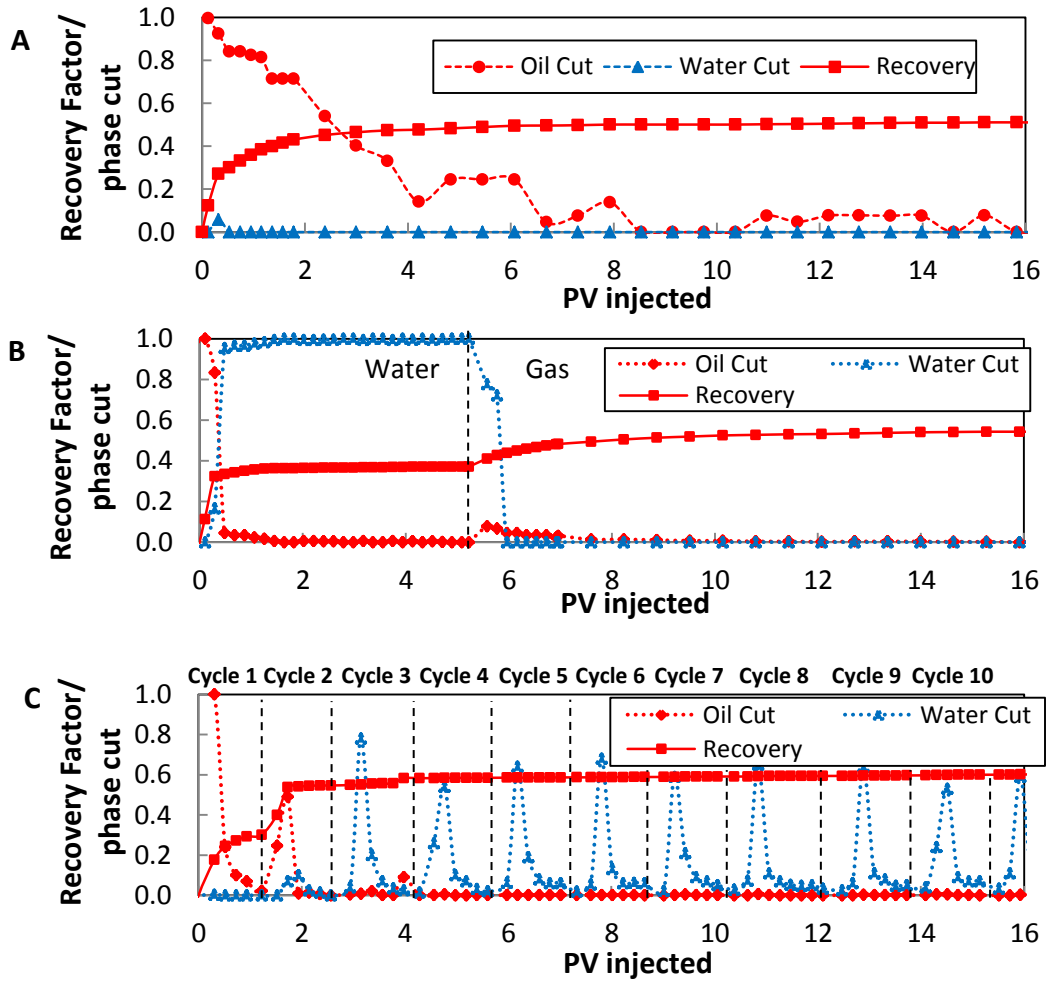


**Figure 2.8:** Oil cut, water cut, and recovery profiles for core-floods 1 (A), 2 (B), and 3 (C). Water, gas, and cycle X refer to water flooding, gas flooding, and injection of WAG cycle X, respectively. All values shown are with respect to the OIIP. Note that only the first 10 WAG cycles are presented.

total oil recovery. Due to the expected positive  $C_s$ , it is unlikely that a  $g/w$  interface exists as the continuous oleic phase might separate the gas and water phases. After the advanced  $g/o$  interface reached the core outlet, at  $0.51 \pm 0.02$  PV, we propose that oil was mainly produced by the film flow mechanism (Oren *et al.*, 1992; Vizika, 1993; Kalaydjian, 1992; Blunt *et al.*, 1995; Khorshidian *et al.*, 2016). For film flow to occur, not only the gas-oil-water system should reveal a positive  $C_s$ , the non-wetting gas phase should be able to enter a pore throat as well, i.e. the capillary pressure should be sufficiently high. If the injected gas fill all neighbouring pores, oil may be drained out from the pore throat corners by flow through oil films. At  $S_{or\_GF}$  in Exp. 1, the continuous film of oil was presumably too thin to support the drainage further.

After reaching a  $S_{oi}$  of  $0.76 \pm 0.02$  in Exp. 2, water flooding reduced  $S_o$  to  $0.49 \pm 0.02$  ( $S_{or\_WF}$  in **Table 2.6**). The injection of  $N_2$  reveals oil displacement that follows a saturation path consisting of two segments. After a small reduction in  $S_w$  and  $S_o$  due to the introduction of  $S_g$ , the displacement process follows a path of roughly constant  $S_{or}$ , and here mainly water was produced. Afterwards, a similar saturation path can be observed as in Exp. 1: gas displacing the oil at a fairly constant  $S_w$  somewhat higher than  $S_{wc}$ . Reason why continuous  $N_2$  injection was not able to reduce  $S_w$  further might be the formation of so-called gas loops (Oren *et al.*, 1992). Once gas loops are formed, the wetting water phase might become trapped, allowing the water to only leave the system through continuous

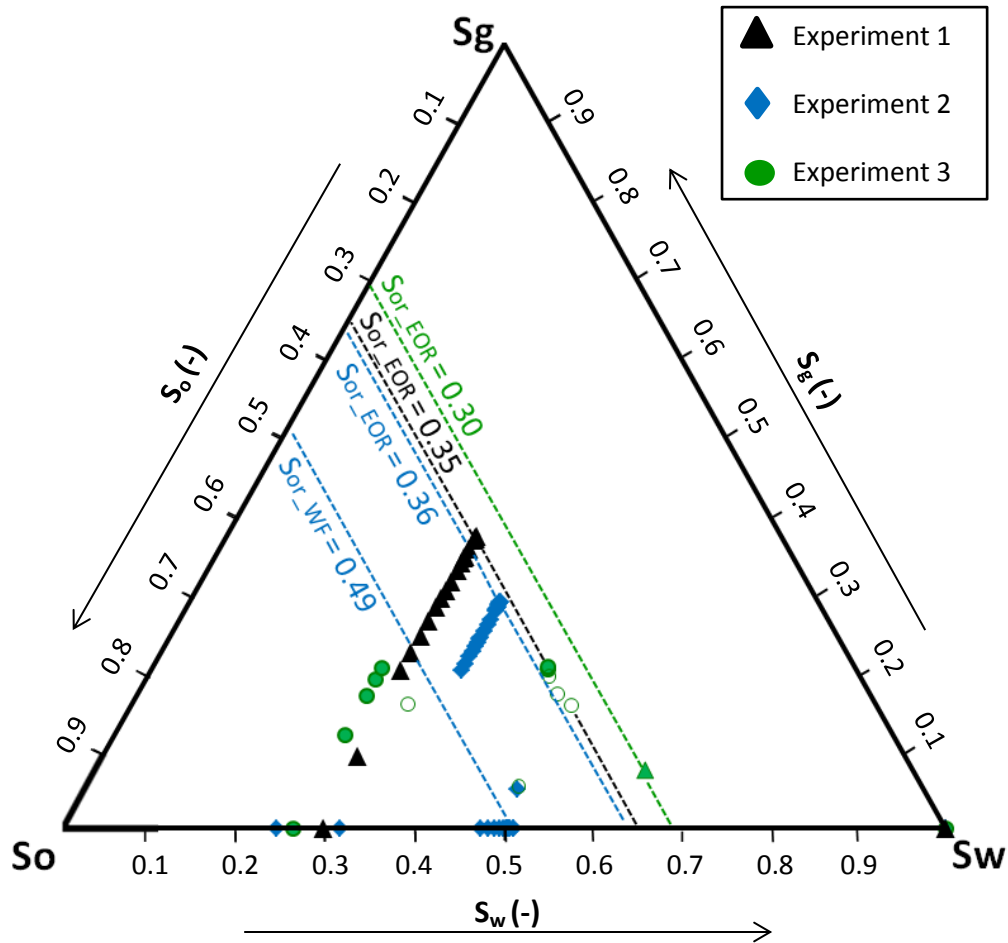


**Figure 2.9:** Saturation paths for Exp. 1, 2, and 3.  $S_w$ ,  $S_o$ ,  $S_g$ ,  $S_{or\_WF}$ , and  $S_{or\_EOR}$  represent the water, oil, gas, residual oil to waterflood, and residual oil to immiscible gas/WAG, respectively. Three-phase saturations shown were averaged over the entire core and calculated using material balance calculations. The closed and open circles in Exp. 3 represent the gas and water injection during the first two WAG cycles, respectively. The green triangle indicates the saturation distribution after successfully injecting 12 full WAG cycles.

water-wetting films; which is a high resistance path. The rather high incremental oil recovered by  $N_2$  flooding over water flooding might be influenced by the idea that water flooding did not reach true  $S_{or\_WF}$  but a slightly higher saturation. These observations advocate that  $R_{FGF}$  is higher under three-phase flow conditions (Exp. 2) compared to two-phase flow conditions (Exp. 1).

The saturation path for Exp. 3 supports the aforementioned concept that  $S_{or\_GF}$  is lower under three-phase flow conditions compared to two-phase flow conditions. We propose that the newly introduced gas, non-wetting, phase occupies larger pores in the system. It might push out part of the previously present oil globules, which is now the intermediate-wetting phase, that could finally be transported by the injected water and gas (Shandrygin *et al.*, 2015). The subsequent injected water, i.e. wetting phase, most probably propagated through a different flow path compared to the injected gas, displaced oil that was present in that flow path and allowed gas pockets to become trapped (Dong *et al.*, 2005). Most likely  $S_{gt}$  increased drastically during water injection in the first two WAG cycles, as reflected by both the increase in averaged  $S_g$  at the end of the cycles and the spikes in pressure drops observed (**Figure 2.7**). The establishment of a  $S_{gt}$  might improve the volumetric sweep efficiency of the injected gas because it reduces gas mobility overall. Moreover, trapped gas pockets could potentially force the injected water to flow through new, still oil bearing, pore channels and

hence increase oil production during WAG injection. As more cycles were injected, the trapped gas saturation increased which resulted in a lower  $S_o$ . The substantial reduction in oil production in later WAG cycles is most probably due to the presence of a more discontinuous oleic phase. The findings for the  $N_2$  WAG scheme are in accord with the studies of Zhang et al. (2010) and Fatemi et al. (2013).

## 2.5 Conclusions

An experimental study of immiscible  $N_2$  flooding was conducted using Bentheimer sandstone cores and a light model oil. Three gas injection schemes were investigated in controlled core-flood experiments including: 1) continuous  $N_2$  injection at connate water saturation, 2) continuous  $N_2$  injection at residual oil to waterflood, and 3) water-alternating-gas injection at connate water saturation. This work forms the basis for understanding the relevance of *FACF*.

By constructing ternary saturation diagrams, we find that the injection of nitrogen at connate water saturation reveals characteristics of a two-phase gas-oil displacement at constant water saturation. When injecting nitrogen at residual oil to waterflood, we identified a saturation path consisting of two main segments. At first, water is displaced at a roughly constant oil saturation. Finally, similar to injection at connate water saturation, nitrogen displaces the oil at a fairly constant water saturation.

We find that water-alternating-gas injection provides the largest ultimate oil recovery factor of  $59 \pm 4\%$  of the *OIP*. The establishment of trapped gas, reducing gas mobility, is most likely a key factor for the incremental oil recovered; increasing its volumetric sweep efficiency.

The obtained results are consistent with the hypothesis that an increment in oil recovery arises mostly from the fact that the residual oil to gas flooding is lower under three-phase flow conditions compared to two-phase flow.

### 3. Foam-assisted chemical flooding: effect of drive foam quality on oil bank propagation

---

#### Abstract

*Foam-assisted chemical flooding is a novel enhanced oil recovery process that increases oil recovery over water flooding by combining foaming with a decrease in the oil-water interfacial tension by two to three orders of magnitude. We conducted an experimental study regarding the formation of an oil bank and its displacement by foam drives with foam qualities within the range of 57 to 97%. The experiments included bulk phase behaviour tests using n-hexadecane and a single internal olefin sulfonate surfactant, and a series of CT-scanned core-flood experiments using Bentheimer sandstone cores. The main goal of this study was to investigate the effect of drive foam quality on oil bank displacement. The surfactant formulation was found to lower the oil-water interfacial tension by at least two orders of magnitude. Core-flood results, at under-optimum salinity conditions, yielding an oil-water interfacial tension in the order of  $10^{-1}$  mN/m, showed similar ultimate oil recovery factors for the range of drive foam qualities studied. A more distinct frontal oil bank displacement was observed at lower drive foam qualities investigated, yielding an increased oil production rate. The findings in this study suggest that a) dispersive characteristics at the leading edge of the generated oil bank in this work were strongly related to the surfactant slug size used, b) the lowest drive foam quality assessed yielded the highest apparent foam viscosity (and, thus, the most stable oil bank displacement), and c) drive foam generation increased upon touching the oil bank when using drive foam qualities of 57 and 77%.*

---

The content of this chapter is based on the following publications:

Janssen, M.T.G., Zitha, P.L.J., and Pilus, R.M. 2019. Oil Recovery by Alkaline/Surfactant/Foam Flooding: Effect of Drive-Foam Quality on Oil-Bank Propagation. *SPE Journal*. DOI:10.2118/190235-PA.

Janssen, M.T.G., Zitha, P.L.J., and Pilus, R.M. 2018. Oil Recovery by Alkaline-Surfactant-Foam (ASF) Flooding: Effect of Drive Foam Quality on Oil Bank Propagation. Society of Petroleum Engineers. DOI:10.2118/190235-MS.

### 3.1 Introduction

Once we have an understanding about the main mechanisms that play a predominant role in oil recovery through immiscible gas injection and WAG (**Chapter 2**), we shift our attention to FACF. Here we present a laboratory investigation on FACF at model-like conditions. Acquired novel CT-based information allows us to clearly visualize, and quantify, the oil bank formation and its displacement during FACF. The introduction section continues with a short recap of the theoretical background.

In **Section 1.2** we discussed gas flooding and its major drawback: poor  $E_V$  as a result of an unfavourable density and mobility contrast between the injected gas and the fluids in place (**Equation 1.2**). Besides applying WAG, for controlling gas mobility, gas foaming is a highly effective method for improving  $E_V$  of the injected gas (**Section 1.3**).

Besides a good  $E_V$ , mobilization of trapped oil, i.e. sufficiently large  $E_D$ , is another critical requirement for a successful chemical EOR process, as discussed in **Sections 1.1** and **1.4**. Carefully formulated surfactants are able to reduce the  $o/w$  IFT, thus inducing mobilization of  $S_{or}$ , yielding a drastic increase in capillary number ( $N_c$ ):

$$N_c = \frac{\mu * u}{\sigma} \quad (3.1)$$

where  $\mu$ ,  $u$ , and  $\sigma$  represent the viscosity of the injectant, injection velocity, and the  $o/w$  IFT, respectively. For a given water-surfactant-oil system at constant surfactant concentration, two or three phases co-exist in equilibrium, depending on salinity (**Figure 1.4**).

In **Section 1.5** we introduced the novel EOR methodology of FACF. FACF combines the injection of a surfactant slug (for increasing  $E_D$ ) with foam generation for drive mobility control (improving  $E_V$ ). The surfactant used has a dual role, if a single surfactant type is used: a) to ensure that a sufficiently low  $o/w$  IFT is achieved and, thereby, induce the mobilization of  $S_{or\_WF}$  and b) to promote foaming of the injected gas, thus improving mobility control and  $E_V$ .

Past studies clearly support the idea that FACF is a viable EOR process (Srivastava *et al.*, 2009; Guo *et al.*, 2012; Jong *et al.*, 2016). Nevertheless, several important aspects concerning the underlying mechanisms are far from being well-understood—for instance, how an oil bank is formed and, more importantly, how it is displaced by foam. While existing literature has mainly used obtained pressure and effluent data to gain insight into related physical processes within the porous media, in this study we present novel results and insights which could only be obtained by CT scanning. When scanning with true dual-energy, we were able to assess and visualize oil bank formation and its displacement by foam during a FACF process on core-scale. A single surfactant with the ability to lower the  $o/w$  IFT by two to three orders of magnitude and to stabilize foam was used to conduct the CT-assisted core-flood experiments along with a model oil. Core-floods were performed using Bentheimer sandstone, a natural outcrop rock that is often used for modelling sandstone reservoirs (Peksa *et al.*, 2015). Slug phase behaviour in bulk was assessed separately. Drive foam quality (i.e., gas fractional flow) was varied (57, 77, and 97%) during the core-floods to shed light on its effect on the oil bank displacement during an FACF process.

## 3.2 Materials and methods

### 3.2.1 Chemicals

An Internal Olefin Sulfonate, IOS2024, surfactant (ENORDET O242) was selected for the experiments (Barnes *et al.*, 2010). The surfactant was supplied in aqueous solution with an active matter (AM) content of 19 wt% and used without further treatment. Its CMC in the presence of 1 wt% sodium carbonate ( $\text{Na}_2\text{CO}_3$ ), 0.5 wt% sec-butanol ( $\text{C}_4\text{H}_{10}\text{O}$ ), and 0.4 wt% sodium chloride (NaCl) was determined from surface tension measurements (KSV Sigma 700/701 tensiometer) using the Du Noüy ring method (Du Noüy, 1925). It equalled approximately  $3.0 \times 10^{-3}$  wt% AM IOS2024. The alkaline used in the experiments was  $\text{Na}_2\text{CO}_3$  ( $\geq 99\%$  purity from Sigma-Aldrich). Although no naphthenic acids were added to the oleic phase, avoiding any saponification processes (**Section 1.5**), still alkaline was used to minimize surfactant adsorption (Southwick *et al.*, 2014). NaCl ( $\geq 99\%$  purity from Merck) was used for brine preparation and the co-solvent that was used is  $\text{C}_4\text{H}_{10}\text{O}$  ( $\geq 99\%$  purity from Merck). The co-solvent was added to ensure a stable slug solution, preventing precipitation and/or phase separation. Hirasaki *et al.* (2011) concluded that the use of alcohol as a co-solvent is not necessary when working with IOS2024 below  $60^\circ\text{C}$ , as the presence of branches in its molecular structure ensures sufficient stability. The co-solvent was therefore added as a precautionary measure and for consistency with future experiments at reservoir conditions ( $>60^\circ\text{C}$ ). Dissolved NaCl in demineralized water (2 wt%) was used as a model brine. Its density and viscosity at  $20^\circ\text{C}$  were  $1.013 \pm 0.001 \text{ g/cm}^3$  and  $1.03 \pm 0.05 \text{ cP}$ , respectively. The model oil used in this work was *n*-hexadecane [ $\text{CH}_3(\text{CH}_2)_{14}\text{CH}_3$ ,  $\geq 99\%$  purity from Merck] with viscosities of  $3.38 \pm 0.03 \text{ cP}$  (doped with 25 wt% dopant) and  $3.31 \pm 0.03 \text{ cP}$  (doped with 20 wt% dopant) at  $20^\circ\text{C}$ . Its densities at  $20^\circ\text{C}$  were  $0.867 \pm 0.001 \text{ g/cm}^3$  (doped with 25 wt% dopant) and  $0.841 \pm 0.001 \text{ g/cm}^3$  (doped with 20 wt% dopant). A red colorant (Oil Red O,  $\text{C}_{26}\text{H}_{24}\text{N}_4\text{O}$ , from Sigma-Aldrich) was added to the oleic phase ( $<0.006 \text{ wt}\%$ ) for its better visualization. The oil used in the core-flood experiments was doped either with 25 wt% 1-iododecane [ $\text{CH}_3(\text{CH}_2)_9\text{I}$ , 98% purity from Sigma-Aldrich] or with 20 wt% 1-iododecane for CT contrast enhancement. Nitrogen gas ( $\text{N}_2$ ), with a density and viscosity (at  $20^\circ\text{C}$  and atmospheric pressure) of  $1.165 \pm 0.001 \times 10^{-3} \text{ g/cm}^3$  and  $1.76 \pm 0.50 \times 10^{-2} \text{ cP}$ , respectively, was co-injected with the surfactant drive solution for foam generation. All liquid solutions were degassed under vacuum to remove dissolved oxygen and nitrogen before injection into cores.

### 3.2.2 Core samples

**Table 3.1** shows the physical properties of the Bentheimer sandstone cores used to conduct the experiments. The outcrop sandstones were fairly clean ( $> 91 \text{ wt}\%$  quartz) and had high permeabilities (Peksa *et al.*, 2015). After cutting and drying for 48 hours in an oven at  $60^\circ\text{C}$ , the cores were cast in an epoxy resin to avoid bypassing flow alongside the core. The resin penetrated approximately 2 mm inside the porous media. Multiple holes were drilled into the core sample for pressure drop measurements. The porosities reported in **Table 3.1** represent averaged values that were calculated using measured CT data (**Appendix A**), with errors corresponding to standard deviations. The porosity of one representative rock sample was also measured using an Ultrapycnometer 1000 (Quantachrome Corporation) and yielded a porosity of  $24.10 \pm 0.10\%$ . A core length of approximately 1 m proved to be a sufficient length to assess oil bank formation and its displacement. It also reduced the significance of the capillary entry/end effect. Its small diameter ( $3.80 \pm 0.10 \text{ cm}$ ) minimized gravity effects.

**Table 3.1:** Properties of the Bentheimer cores used in the experiments conducted.

	Experiment			
	1	2	3	4
Porosity (%)	24.00 ± 0.40	24.00 ± 0.40	24.00 ± 0.50	23.00 ± 0.40
Permeability (Darcy)	3.14 ± 0.11	3.20 ± 0.11	3.11 ± 0.15	3.32 ± 0.10
Length (cm)	96.80 ± 0.10	96.20 ± 0.10	96.90 ± 0.10	97.00 ± 0.10
Diameter (cm)	3.80 ± 0.10	3.80 ± 0.10	3.80 ± 0.10	3.80 ± 0.10
Pore volume (cm <sup>3</sup> )	263.48 ± 18.97	261.84 ± 18.85	263.75 ± 20.14	253.02 ± 18.41

### 3.2.3 Experimental set-up

A schematic overview of the experimental set-up used to conduct the core-flood experiments is shown in **Figure 3.1**. The set-up consisted of a core-holder in line with a dual-cylinder liquid pump (Quizix QX-6000), which was used for injecting aqueous solutions. A backpressure regulator (DEMO-TU Delft) was connected to the core-end to control the outlet pressure during the experiments. Fluids were collected in a measuring cup placed on a digital balance, where images were taken at fixed time intervals of 15 minutes. N<sub>2</sub> was supplied from a 200 bar cylinder, connected to the inlet through a mass flow controller (Bronkhorst, EL-FLOW). For primary drainage, we used a transfer vessel connected to the liquid pump. A Coriolis meter (Bronkhorst, CORI-FLOW) was placed at the outlet for measuring effluent densities and mass flow to accurately determine breakthrough times. Several differential- and absolute-pressure transducers were placed to monitor the pressure behaviour in the system. A thermocouple was used to keep track of potential temperature fluctuations. A data acquisition system (National Instruments) was connected to the PC and recorded pressure and temperature data using a 10 second time interval. The experiments were conducted at room temperature (21 ± 1°C).

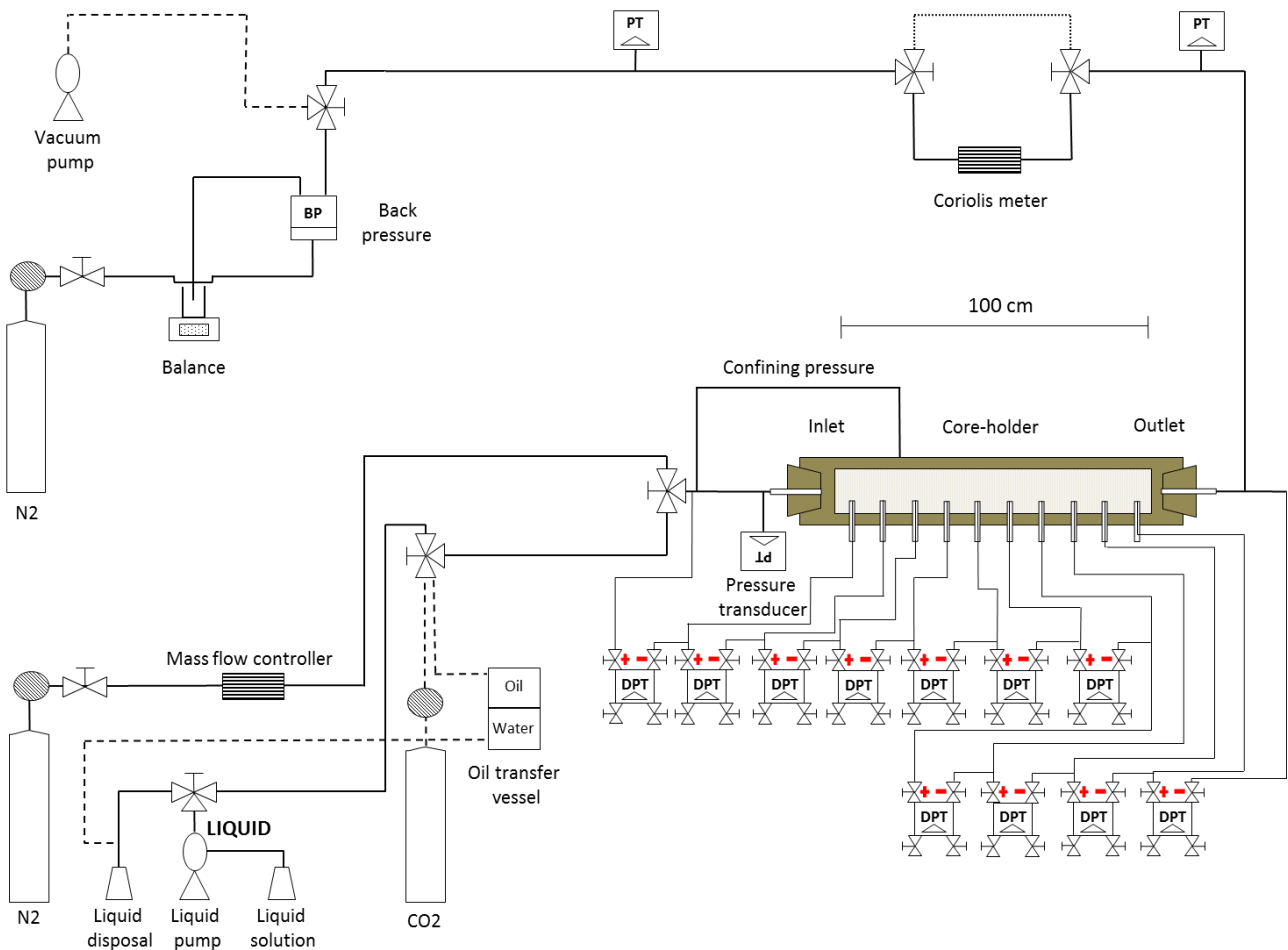


**Figure 3.1:** Experimental set-up used to perform the core-flood experiments. DPT = differential pressure transducer.

### 3.2.4 CT scan

CT scans were taken using a Siemens SOMATOM Definition CT scanner having full dual-energy scanning capabilities. The core-holder was placed on the bed of the CT scanner in a fixed horizontal position. The CT scanner operated using two X-ray tubes simultaneously: a) 80 kV and 550 mA current and b) 140 kV and 250 mA current. Dual-energy scans were used for quantifying three-phase saturation distributions during the course of various injection stages. One single scan consisted of 490 slices of each 2 mm thick. One slice contained 512×512 pixels with a pixel size of 0.2×0.2 mm. Note that the circular core only occupied part of the square slice surface. Scanning was done in spiral mode. The acquired data was analysed using ImageJ software. See **Appendix A** for additional information regarding CT processing.

### 3.2.5 Experimental procedure

#### 3.2.5.1 Phase behaviour and IFT measurements

An elaborate salinity scan was conducted to assess the systems phase behaviour in the under-optimum salinity regime. Nine *n*-hexadecane/alkaline/surfactant (AS) combinations were prepared with 0.3 wt% AM IOS2024, 1 wt% Na<sub>2</sub>CO<sub>3</sub>, 0.5 wt% sec-butanol, and NaCl concentrations in the range of 0.0 to 2.5 wt% present in the aqueous AS phase. The *n*-hexadecane/AS solutions were mixed using an *o/w* ratio of 1:2. After manually shaking the samples for 2 minutes and placing them on a shaking roller for 10 hours, they were stored in an oven at 90°C for 4 weeks. This temperature was used to speed up the equilibration process. The effect of temperature on the *o/w* IFT measured was studied for a system containing the same chemicals, except for the oil type, and showed a small, within measurement error, decrease in *o/w* IFT at optimum salinity when switching from 25 ± 1°C to 90 ± 1°C.

After 4 weeks, equilibrium was reached and *o/w* IFT measurements were performed. A spinning drop tensiometer (SVT20N, Dataphysics) was used to measure the *o/w* IFT for each *n*-hexadecane/AS system at 90 °C using extracted excess brine as a continuous phase and excess oil in the form of a droplet. The software uses the Young-Laplace equation (Young, 1805; Laplace, 1806) to fit the shape of the oil droplet as a function of revolutions per minute (*rpm*). As soon as the applied centrifugal forces reach equilibrium with the interfacial forces, the droplet's shape is fixed and unique for a specific *o/w* IFT. IFTs were measured at rotational speeds of 1,000 to 5,000 *rpm*.

#### 3.2.5.2 Core-flood experiments

An overview of the core-flood experiments performed is given in **Table 3.2**. Exp. 1 served as a baseline to study the performance of AS slug injection in the absence of drive foam mobility control. In Exp. 2, 3, and 4, 0.46 PV liquid AS slug was injected prior to the co-injection of an AS drive solution with N<sub>2</sub> for drive foam generation. The gas fractional flow (i.e., foam quality) during drive co-injection varied from 57% (Exp. 2), to 77% (Exp. 3), to 97% (Exp. 4).

**Table 3.3** presents the sequence that was used to conduct the experiments. The basic sequence started with the removal of air by flushing the core with CO<sub>2</sub> for 2 hours at an injection pressure of 5 bar. Subsequently, after vacuuming the system, 2 wt% NaCl brine (approximately 10 PV) was injected while keeping the pressure at the outlet at 25 bar (the latter was done to ensure complete CO<sub>2</sub> dissolution in brine). By varying the flow rates, the absolute permeability to brine was determined using Darcy's law (Darcy, 1856). Next, primary drainage was performed by injecting approximately 3 PV of *n*-hexadecane. By varying the oil injection rate at the end of the injection phase,  $k_{ro}^0$  was

obtained. Then, water flooding was initiated by injecting approximately 7 PV of 2 wt% NaCl brine. In order to establish  $S_{or\_WF}$  and to overcome the capillary end effect, a bump flood of 4.00 cm<sup>3</sup>/min was applied. Similar to obtaining  $k_{ro}^0$ ,  $k_{rw}^0$  was calculated using Darcy's law. Following water flooding, a liquid AS slug (0.46 PV) was injected at 0.15 cm<sup>3</sup>/min to mobilize  $S_{or\_WF}$ . In the baseline flood (Exp. 1), the AS slug injection was extended to 3.3 PV and no co-injection followed. Finally, in Exp. 2, 3, and 4, a liquid AS drive solution was co-injected with N<sub>2</sub> (at a total injection rate of 1.1 cm<sup>3</sup>/min; equivalent to 4.6 ft/day) to generate foam for mobility control. The co-injection continued until no more oil was produced. Foam quality was defined as the gas fractional flow in the centre of the core. The core-flood experiments performed were analysed in terms of pressure data, mobility reduction factor (*MRF*), (incremental) oil recovery, CT scan images, and corresponding saturation profiles. *MRF* is defined as the ratio of pressure drops for AS drive and N<sub>2</sub> co-injection to pressure drops corresponding to single-phase brine flow in a brine-saturated core at the same superficial velocity.

**Table 3.2:** Overview of core-flood experiments performed in this study. AS slug composition for all experiments contained 0.4 wt% NaCl, 1 wt% Na<sub>2</sub>CO<sub>3</sub>, 0.5 wt% sec-butanol, and 0.3 wt% AM IOS2024 and was injected at 0.15 cm<sup>3</sup>/min. Drive composition was co-injected with N<sub>2</sub> for mobility control and consisted of 0.4 wt% NaCl, 1 wt% Na<sub>2</sub>CO<sub>3</sub>, and 0.3 wt% AM IOS2024 for Exp. 2, 3, and 4. The liquid slug and drive solutions were prepared by mixing an NaCl/Na<sub>2</sub>CO<sub>3</sub> solution with an IOS2024/sec-butanol solution, both prepared at concentrations that were twice as high as the desired concentrations. Drive foam quality was set as the variable.

Exp.	Procedure	Gas flow rate (cm <sup>3</sup> /min)	Liquid flow rate (cm <sup>3</sup> /min)	Foam quality (%)	CT
1	AS	-	0.150	-	Yes - Oil with 20wt% dopant
2	FACF	0.627	0.473	57	Yes - Oil with 25wt% dopant
3	FACF	0.847	0.253	77	Yes - Oil with 20wt% dopant
4	FACF	1.067	0.033	97	Yes - Oil with 20wt% dopant

**Table 3.3:** Sequence of experimental procedure.

Step	Description	Back pressure (bar)	Flow rate (cm <sup>3</sup> /min)	Injection pressure (bar)
1	CO <sub>2</sub> flushing	-	-	5
2	Vacuuming	-	-	-
3	Brine saturation (2 wt% NaCl)	25	0.25 (Exp. 3,4) 0.50 (Exp. 1,2)	-
4	Oil injection	20	0.20 (Exp. 1) 0.50 (Exp. 2,3,4)	-
5	Water flooding (2 wt% NaCl)	20	0.25	-
6	AS slug (0.46 PV)	20	0.15	-
7	AS drive + N <sub>2</sub> co-injection	20	Liquid: 0.473 (Exp. 2) 0.253 (Exp. 3) 0.033 (Exp. 4) Gas: 0.627 (Exp. 2) 0.847 (Exp. 3) 1.067 (Exp. 4)	-

In Exp. 2, the core was first saturated with 4 wt% NaCl brine and water flooding took place using the same brine. Because a brine-slug salinity gradient was avoided and the AS slug with a total ionic strength equivalent to 4 wt% NaCl appeared to be slightly hazy, we decided to proceed with water

flooding using 2 wt% NaCl brine. Afterwards, an AS slug having a total ionic strength equivalent to 2 wt% NaCl (clear solution) was injected. In the other core-flood experiments, 2 wt% NaCl brine was used immediately (**Table 3.3**).

### 3.3 Results and discussion

#### 3.3.1 Phase behaviour and IFT measurements

The ability of a given surfactant concentration to lower the *o/w* IFT depends greatly on the salinity of the system. The goal of the salinity scan was to examine the phase behaviour of the oil/AS slug system in the under-optimum salinity [i.e. Type II(-)] regime at a constant surfactant concentration of 0.3 wt% AM IOS2024 and to measure the related *o/w* IFTs. **Figure 3.2** shows the measured *o/w* IFTs (at 90°C) of the nine salinity conditions examined in this study. The IFTs exhibited a decreasing trend as a function of increasing salinity, reaching the lowest *o/w* IFT of  $5 \pm 1 \times 10^{-2}$  mN/m at a salinity of  $2.0 \pm 0.1$  wt% NaCl. The highest *o/w* IFT was found at 0 wt% NaCl and equalled  $31 \pm 5 \times 10^{-2}$  mN/m. The decreasing trend of the measured *o/w* IFTs with increasing salinity confirmed that the conducted scan successfully captured the phase behaviour in the Type II(-) region. Moreover, results showed that the selected AS slug formulation in this study, 0.4 wt% NaCl in **Figure 3.2**, operated at under-optimum conditions [i.e. Winsor Type II(-) system]. The related *o/w* IFT equalled  $19 \pm 2 \times 10^{-2}$  mN/m. The used surfactant concentration of 0.3 wt% AM IOS2024 was able to lower the *o/w* IFT by a factor of approximately 130. The more extended phase behaviour scan, shown later on in **Section 6.3.5**, reveals the optimum salinity range ( $3.0 \pm 0.5$  wt% NaCl).

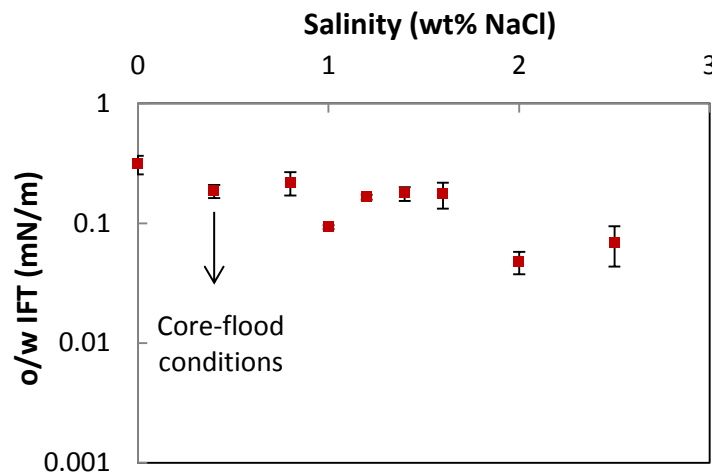


**Figure 3.2:** IFT measurements conducted with the spinning drop tensiometer of the systems prepared: X wt% NaCl, 1 wt% Na<sub>2</sub>CO<sub>3</sub>, 0.5 wt% sec-butanol, and 0.3 wt% AM IOS2024 with *n*-hexadecane. The error bars correspond to the standard deviation of the specific dataset.

#### 3.3.2 Core-flood experiments

As discussed above, the AS slug formulation used in the core-floods (0.4 wt% NaCl, 1 wt% Na<sub>2</sub>CO<sub>3</sub>, 0.5 wt% sec-butanol, and 0.3 wt% AM IOS2024) yielded an *o/w* IFT of  $19 \pm 2 \times 10^{-2}$  mN/m in bulk. The drive composition used in the core-flood experiments (0.4 wt% NaCl, 1 wt% Na<sub>2</sub>CO<sub>3</sub>, and 0.3 wt% AM IOS2024) showed good foaming characteristics in bulk in the absence of oil. Results of the core-flood experiments conducted are discussed next.

**Table 3.4** summarizes the main results of the core-flood experiments performed in this study. The measured  $k_{ro}^0$  and  $k_{rw}^0$  are also reported. They are in good agreement with those found by Treiber et al. (1972) for consolidated water-wet porous media. Averaged values for  $S_{wc}$ ,  $S_{oi}$ ,  $S_{or\_WF}$ , and  $R_{FWF}$ , all

determined on the basis of CT data, equalled  $0.22 \pm 0.05$ ,  $0.78 \pm 0.05$ ,  $0.42 \pm 0.02$ , and  $47 \pm 6\%$  of the *OIIP*, respectively. The values obtained prior to chemical *EOR* (**Table 3.4**) are in line with those reported in the literature (Guo *et al.*, 2012; Simjoo, 2012; Battistutta *et al.*, 2015). Note that, in Exp. 2 and 4, the drive foam quality was altered in a later stage of the experiment.

This section proceeds with the following subsections: primary drainage and forced imbibition, mobilization of residual oil, and displacement of mobilized oil by foam. Pressure drop profiles, oil recovery factors, and saturation profiles as function of core length are compared in order to study the effect of drive foam quality on oil bank displacement.

**Table 3.4:** Summary of the core-flood experiments performed. The parameters  $f_g$ ,  $k_{ro}^0$ ,  $k_{rw}^0$ ,  $S_{wc}$ ,  $S_{oi}$ ,  $S_{or\_WF}$ ,  $S_{or\_CEOR}$ ,  $R_{FWF}$ , and  $R_{FCEOR}$  represent the foam quality, oil end-point relative permeability, water end-point relative permeability, connate water saturation, initial oil saturation, residual oil saturation to waterflood, residual oil saturation to chemical *EOR*, recovery factor corresponding to water flooding, and recovery factor corresponding to chemical *EOR*, respectively. Data were obtained through material balance calculations and CT processing.

	Experiment							
	1		2		3		4	
$k_{ro}^0$	$0.53 \pm 0.06$		$0.51 \pm 0.02$		$0.57 \pm 0.09$		$0.56 \pm 0.11$	
$k_{rw}^0$	$0.14 \pm 0.02$		$0.13 \pm 0.01$		$0.14 \pm 0.01$		$0.15 \pm 0.02$	
	Material Balance	CT	Material Balance	CT	Material Balance	CT	Material Balance	CT
$S_{wc}$	$0.24 \pm 0.03$	$0.23 \pm 0.04$	$0.20 \pm 0.04$	$0.22 \pm 0.04$	$0.23 \pm 0.04$	$0.22 \pm 0.05$	$0.17 \pm 0.04$	$0.20 \pm 0.05$
$S_{oi}$	$0.76 \pm 0.03$	$0.77 \pm 0.04$	$0.80 \pm 0.04$	$0.78 \pm 0.04$	$0.77 \pm 0.04$	$0.78 \pm 0.05$	$0.83 \pm 0.04$	$0.80 \pm 0.05$
$S_{or\_WF}$	$0.39 \pm 0.05$	$0.42 \pm 0.01$	$0.43 \pm 0.06$	$0.41 \pm 0.02$	$0.39 \pm 0.05$	$0.42 \pm 0.01$	$0.42 \pm 0.06$	$0.42 \pm 0.02$
$R_{FWF}$ (% of <i>OIIP</i> )	$49 \pm 5$	$45 \pm 5$	$46 \pm 10$	$47 \pm 6$	$49 \pm 9$	$46 \pm 6$	$49 \pm 10$	$48 \pm 7$
$S_{or\_CEOR}$	$0.32 \pm 0.08$	$0.32 \pm 0.03$	$0.34 \pm 0.06$ ( $f_g$ 57%) $0.27 \pm 0.06$ ( $f_g$ 100%, 57%)	$0.31 \pm 0.03$ ( $f_g$ 57%) $0.20 \pm 0.03$ ( $f_g$ 100%, 57%)	$0.30 \pm 0.05$	$0.31 \pm 0.04$	$0.33 \pm 0.06$ ( $f_g$ 97%) $0.29 \pm 0.06$ ( $f_g$ 55%, 77%, 97%)	$0.32 \pm 0.04$ ( $f_g$ 97%) $0.27 \pm 0.04$ ( $f_g$ 55%, 77%, 97%)
$R_{FCEOR}$ (% of <i>OIIP</i> )	$57 \pm 11$	$58 \pm 6$	$58 \pm 8$ ( $f_g$ 57%) $66 \pm 8$ ( $f_g$ 100%, 57%)	$60 \pm 5$ ( $f_g$ 57%) $74 \pm 5$ ( $f_g$ 100%, 57%)	$61 \pm 9$	$60 \pm 7$	$60 \pm 9$ ( $f_g$ 97%) $65 \pm 9$ ( $f_g$ 55%, 77%, 97%)	$60 \pm 7$ ( $f_g$ 97%) $66 \pm 7$ ( $f_g$ 55%, 77%, 97%)
Incremental $R_F$ (%)	$8 \pm 16$	$13 \pm 11$	$12 \pm 18$ ( $f_g$ 57%) $20 \pm 18$ ( $f_g$ 100%, 57%)	$13 \pm 11$ ( $f_g$ 57%) $27 \pm 11$ ( $f_g$ 100%, 57%)	$12 \pm 18$	$14 \pm 13$	$11 \pm 19$ ( $f_g$ 97%) $16 \pm 19$ ( $f_g$ 55%, 77%, 97%)	$12 \pm 14$ ( $f_g$ 97%) $18 \pm 14$ ( $f_g$ 55%, 77%, 97%)

### 3.3.2.1 Primary drainage and forced imbibition

This subsection discusses the first preparatory stages of the core-flood experiments (i.e. primary drainage and forced imbibition). It provides the foundation for the interpretation of oil mobilization by surfactant slug injection and oil displacement by foam in a *FACF* process. Pressure drops, CT images, and corresponding  $S_o$  profiles are presented and discussed in more depth. We limit the discussion to one experiment (Exp. 2) because it is representative for all the core-flood experiments conducted.

## 3.3.2.1.1 Pressure drop

**Figure 3.3** shows the total pressure drop (i.e. pressure drop over the entire core length) obtained during drainage and imbibition for Exp. 2. As soon as the oil touched the core, the pressure drop increased until oil breakthrough occurred at  $0.75 \pm 0.02$  PV of oil injected. Afterwards, the pressure drop decreased, eventually reaching an averaged steady-state value of roughly  $188 \pm 10$  mbar, corresponding to oil flow at  $S_{wc}$ . Lower pressure drops were obtained during water flooding owing to lower flow rates and a lower water viscosity. Water breakthrough occurred at  $0.37 \pm 0.02$  PV of water injected. Oil and water breakthrough times for the other experiments equalled  $0.72 \pm 0.02$  and  $0.34 \pm 0.02$  (Exp. 1),  $0.75 \pm 0.02$  and  $0.39 \pm 0.02$  (Exp. 3), and  $0.77 \pm 0.02$  PV and  $0.41 \pm 0.02$  PV (Exp. 4), respectively.

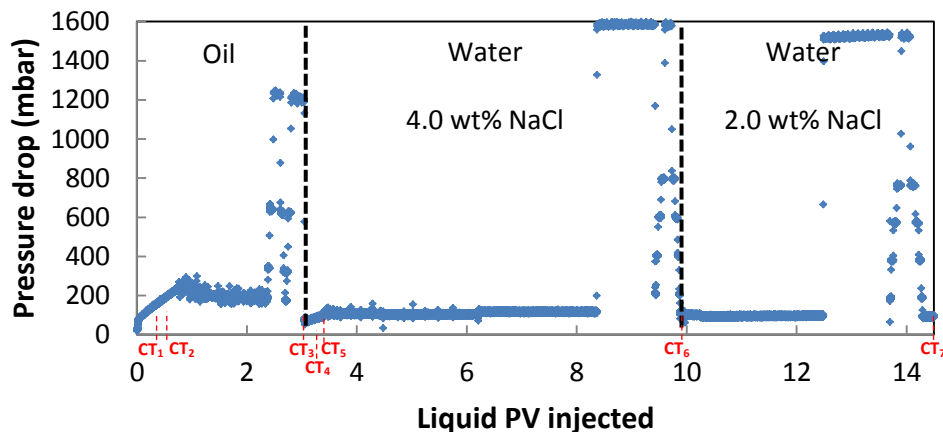


**Figure 3.3:** Total pressure drop profile for Exp. 2 prior to chemical EOR. Various injection steps are shown: oil injection (oil) and water flooding (water). After injecting approximately 2 PV of oil at  $0.50 \text{ cm}^3/\text{min}$ , the flow rate was set to 1, 2, 4, 2, 1, 0.5, 1, 2, and  $4 \text{ cm}^3/\text{min}$  to obtain  $k_{ro}^0$ . Water flooding was initiated using a flow rate of  $0.25 \text{ cm}^3/\text{min}$ . Next, after approximately 4 PV injected, the flow rate was set to 4, 0.5, 1, 1.5, 2, 4, 2, 1.5, 1, and  $0.5 \text{ cm}^3/\text{min}$  to determine  $k_{rw}^0$ . Note that, in Exp. 2, water flooding was performed twice to reduce brine salinity from 4 to 2 wt% NaCl. In both water flooding stages, the same changes in flow rate were applied. The markers in red denote the times at which CT scans were taken.

## 3.3.2.1.2 CT images and oil saturation profiles

**Figure 3.4** presents CT images and corresponding  $S_o$  profiles obtained at selected time intervals during the primary drainage and forced imbibition injection stages in Exp. 2 (red markers in **Figure 3.3**). During primary drainage, water (blue) was displaced by oil (red/orange) in a characteristic frontal manner (**Figure 3.4A**). The green/yellow color near the core outlet, at the end of primary drainage, indicates the accumulation of water. This is a consequence of the capillary end effect (**Section 2.3.1.2**). The wetting phase (water) needs to satisfy the zero capillary pressure condition at the outlet boundary; hence, water tends to accumulate near the outlet region (Huang and Honarpour, 1998). During water flooding, oil (red/orange) was displaced by water (blue) equally in a front-like manner but with a less sharp transition between high- and low- $S_w$  zones. The last CT scan image presents the condition after 2 wt% NaCl water flooding. No measurable amounts of oil were produced during this final water flooding stage.

During primary drainage, the  $S_o$  profiles show a typical Buckley-Leverett displacement behaviour (Buckley and Leverett, 1942), including a sharp shock front region and a rarefaction wave upstream of it (**Figure 3.4B**). Note the relatively low  $S_o$  near the outlet at the end of primary drainage caused by the capillary end effect. Averaged  $S_o$  values along the entire core at the end of primary drainage (i.e.

$S_{oi}$ ) are shown in **Table 3.4**. Note that these values are in good agreement with those obtained from material balance calculations. The  $S_o$  profiles during water flooding (dashed lines in **Figure 3.4B**) show a behaviour similar to that of primary drainage. However, the shock front region seems less sharp owing to the presence of capillary forces. With end-point mobility ratios [ $M^o = (k_{rw}^o/\mu_w)/(k_{ro}^o/\mu_o)$ ] of 0.85, 0.84, 0.79, and 0.86 for Exp. 1, 2, 3, and 4, respectively, the displacement of oil by water is seen as piston-like. Averaged  $S_{o_{WF}}$  values are presented in **Table 3.4** and are similar to material balance calculations.

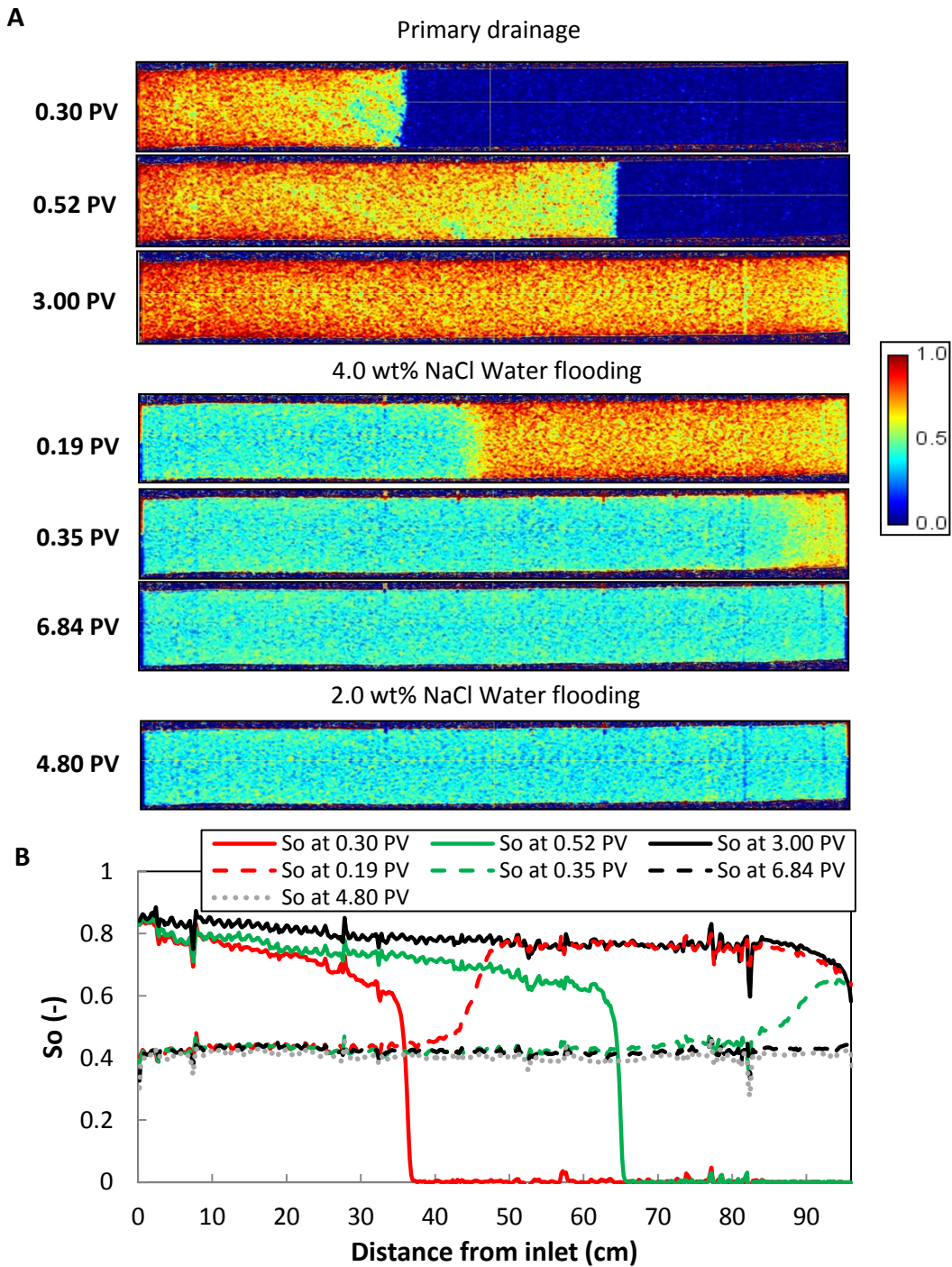


**Figure 3.4:** A: Oil saturation images during primary drainage and water flooding in Exp. 2. The scan shown has a X:Y ratio of 3:1. PV = 0 corresponds to the start of the particular injection phase. Red indicates oil, and blue represents brine. The purpose of the 2 wt% NaCl flooding was solely to lower brine salinity; no measurable amounts of oil were produced during this stage. B: Oil saturation profiles during primary drainage (continuous lines) and water flooding (dashed lines) for Exp. 2. The dotted grey line in the graph represents the  $S_o$  profile at the end of 2 wt% NaCl water flooding. The initial oil saturation corresponds to the  $S_o$  profile at 3.00 PV injected (continuous black line).

### 3.3.2.2 Mobilization of residual oil

The results of the AS slug injection and the ensuing mobilization of  $S_{or\_WF}$  for the four core-flood experiments conducted in this study are presented in this subsection. The discussion aims at Exp. 1, but the other experiments are scrutinized as well since they form the basis for the oil displacement by co-injection of  $N_2$  and AS drive to promote foam generation. Pressure drops are examined because they are a qualitative indicator for the formation of the oil bank. CT scans and corresponding  $S_o$  profiles are studied to directly visualize and quantitatively analyze the build-up of the oil bank.

#### 3.3.2.2.1 Pressure drop

**Figure 3.5** shows the total pressure drop profiles during AS slug injection for all four experiments performed. Initially, let us focus on the first 0.46 PV of injection (i.e. slug injection in full *FACF* core-floods). The trend during AS slug injection is similar in all four tests: an increase in pressure drop from approximately  $50 \pm 10$  mbar to roughly  $85 \pm 15$  mbar due to the formation and propagation of the oil bank. At first, pressure drops increased relatively rapidly, whereas, at later times, the rate at which pressure drops increased reduced; suggesting a more dispersed form of the oil bank at later times (i.e. a less sharp transition between high- and low- $S_o$  zones). From here on, our discussion focuses on the pressure drop profile for Exp. 1, which is the extended AS slug injection without foam drive, as it exhibits more revealing features. Corresponding pressure drop increased monotonically from  $63 \pm 3$  mbar to a maximum value of  $104 \pm 5$  mbar. This maximum value was reached at oil bank breakthrough time equal to  $0.72 \pm 0.02$  PV slug injected. After oil breakthrough occurred, the pressure drop diminished and eventually reached a steady-state value of  $59 \pm 5$  mbar. At  $1.20 \pm 0.02$  PV injected a *ME* broke through. The *ME* produced (droplet size  $<1 \mu\text{m}$ ) showed no evidence of coalescence of dispersed oil droplets over time, suggesting a thermodynamically stable system, which verifies that we are dealing with a *ME* instead of a macro-emulsion. At  $2.37 \pm 0.02$  PV injected the flow rate was increased from 0.15 to  $1.10 \text{ cm}^3/\text{min}$  to assess whether an increase in the amount of shear (i.e. mixing of oil and water) would yield stronger and/or greater emulsification. Both pressure drop and effluent data showed no evidence related to the formation of a new, more stronger, *ME*. Abovementioned results suggest that in the other experiments (Exp. 2, 3, and 4) *MEs* were formed during the AS slug injection stage.

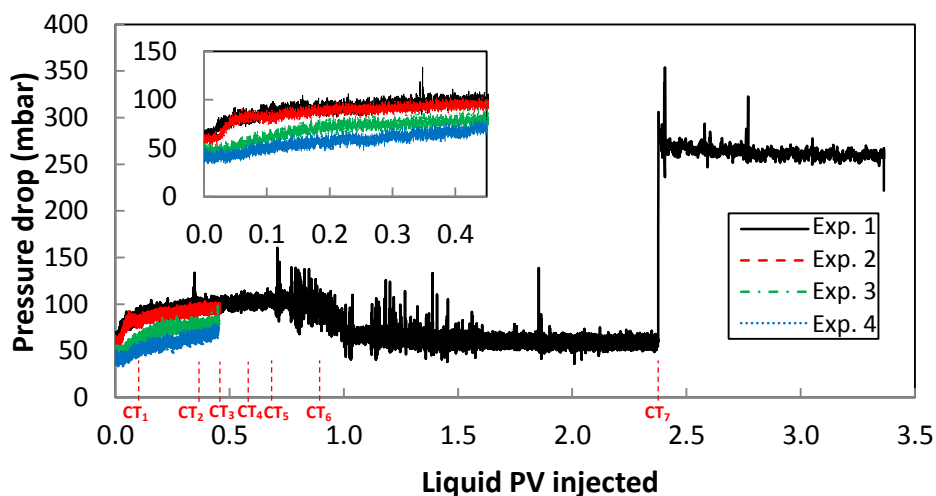


**Figure 3.5:** Total pressure drop profiles for all four tests conducted during AS slug injection. Exp. 1 presents a baseline case where, in total,  $3.36 \pm 0.02$  PV AS slug was injected. At  $2.37 \pm 0.02$  PV AS slug injected, the flow rate was increased from 0.15 to  $1.10 \text{ cm}^3/\text{min}$  (Exp. 1). In the other core-floods (Exp. 2, 3, and 4) only  $0.46 \pm 0.02$  PV AS slug was injected at  $0.15 \text{ cm}^3/\text{min}$ . The markers in red denote the times at which CT scans were taken during Exp. 1.

### 3.3.2.2.2 CT images and oil saturation profiles

**Figure 3.6** presents the  $S_o$  CT scan images and corresponding saturation profiles for the extended AS slug injection in baseline Exp. 1. The images and profiles for core-floods 2, 3, and 4 during AS slug injection are not shown here as they are similar to the first three scans and profiles presented in **Figure 3.6**. Let us first focus on the CT scans taken at 0.06, 0.38, and 0.46 PV slug injected as they are representative for the full *FACF* core-floods where only 0.46 PV AS slug was injected (**Table 3.3**). It is evident that a sharp oil bank was formed after 0.06 PV injection with a peak  $S_o$  of  $0.72 \pm 0.02$ ; consistent with the sharp increase in pressure drop (**Figure 3.5**). Scans taken at later time intervals (0.38 and 0.46 PV) reveal a more dispersed shape of the oil bank, mainly at its leading edge (i.e. downstream side) where  $S_o$  gradually reduced to  $S_{or\_wf}$ . Nonetheless, peak  $S_o$  remained rather constant, reaching  $0.70 \pm 0.02$  at 0.46 PV slug injected; suggesting a  $S_w$  close to  $S_{wc}$  within the oil bank (**Table 3.4**). Several oil remnants can be observed in the upstream area of the core, probably owing to an unfavourable  $M$  (**Equation 1.2**) between AS slug ( $1.07 \pm 0.06$  cP at 20 °C) and *n*-hexadecane ( $3.31 \pm 0.03$  cP at 20 °C) in combination with gravitational effects. The averaged  $S_o$  upstream of the oil bank at 0.46 PV equalled  $0.33 \pm 0.03$ ,  $0.33 \pm 0.04$ ,  $0.35 \pm 0.02$ , and  $0.33 \pm 0.02$  for Exp. 1, 2, 3, and 4, respectively. These values for  $S_{or}$  might be reduced when operating at optimum salinity conditions. For all full *FACF* core-flood experiments, a continuously growing oil bank was observed during slug injection, where oil tended to coalesce at its leading edge.

The first three profiles shown in **Figure 3.6** raise the question about how the oil bank would evolve and propagate if the injection of AS slug continued beyond 0.46 PV. This can be assessed by analysing the acquired CT data for injection times later than 0.46 PV slug injected. The profiles from 0.55 PV onwards in **Figure 3.6** reveal that, after 0.46 PV slug injected, a more uniform oil bank was formed at the leading edge. This suggests that the dispersion at the leading edge was a strong function of injection time where, at first, dispersion increased with time, whilst at later injection times, dispersion seems to reduce as function of PV injected. In spite of the expected unfavourable  $M$  (**Equation 1.2**) between the injected slug and the *OIP*, the newly formed oil bank was displaced in a stable manner. It propagated with an average velocity of  $97 \pm 3$  cm per PV slug injected. Peak  $S_o$  values in the oil bank remained constant over time and equalled  $0.71 \pm 0.03$ . Eventually, after  $2.37 \pm 0.02$  PV slug injected, even the oil remnants in the top part of the core (e.g. at 0.55 PV) were produced and an averaged  $S_{or}$  of  $0.32 \pm 0.03$  was achieved. Note that, near the core inlet, a  $S_{or}$  of  $0.06 \pm 0.02$  was reached.

### 3.3.2.3 Displacement of mobilized oil by foam

This subsection presents the results of the oil displacement by the co-injection of  $N_2$  and AS drive (formulation in caption **Table 3.2**) to support foam generation. It includes close examination of pressure drops and related *MRFs*, since they are qualitative indicators of foam generation and propagation. CT scans and corresponding  $S_o$  and  $S_g$  profiles are assessed to study and visualize the displacement of the oil bank by foam in core-floods 2, 3, and 4.

#### 3.3.2.3.1 Pressure drops and *MRFs*

**Figure 3.7** shows the total pressure drop profiles during co-injection of  $N_2$  and AS drive for foam generation and **Figures 3.8A** through **3.8C** present corresponding sectional *MRFs* as function of total PV injected for Exp. 2, 3, and 4, respectively. In the following subsections, when referring to PV injected, the sum of gas and liquid PV (i.e. total PV) is considered unless otherwise noted. Note that

*MRF* is defined as the ratio of pressure drop corresponding to foam flow to that for single-phase brine flow in a brine-saturated core at the same superficial velocity.

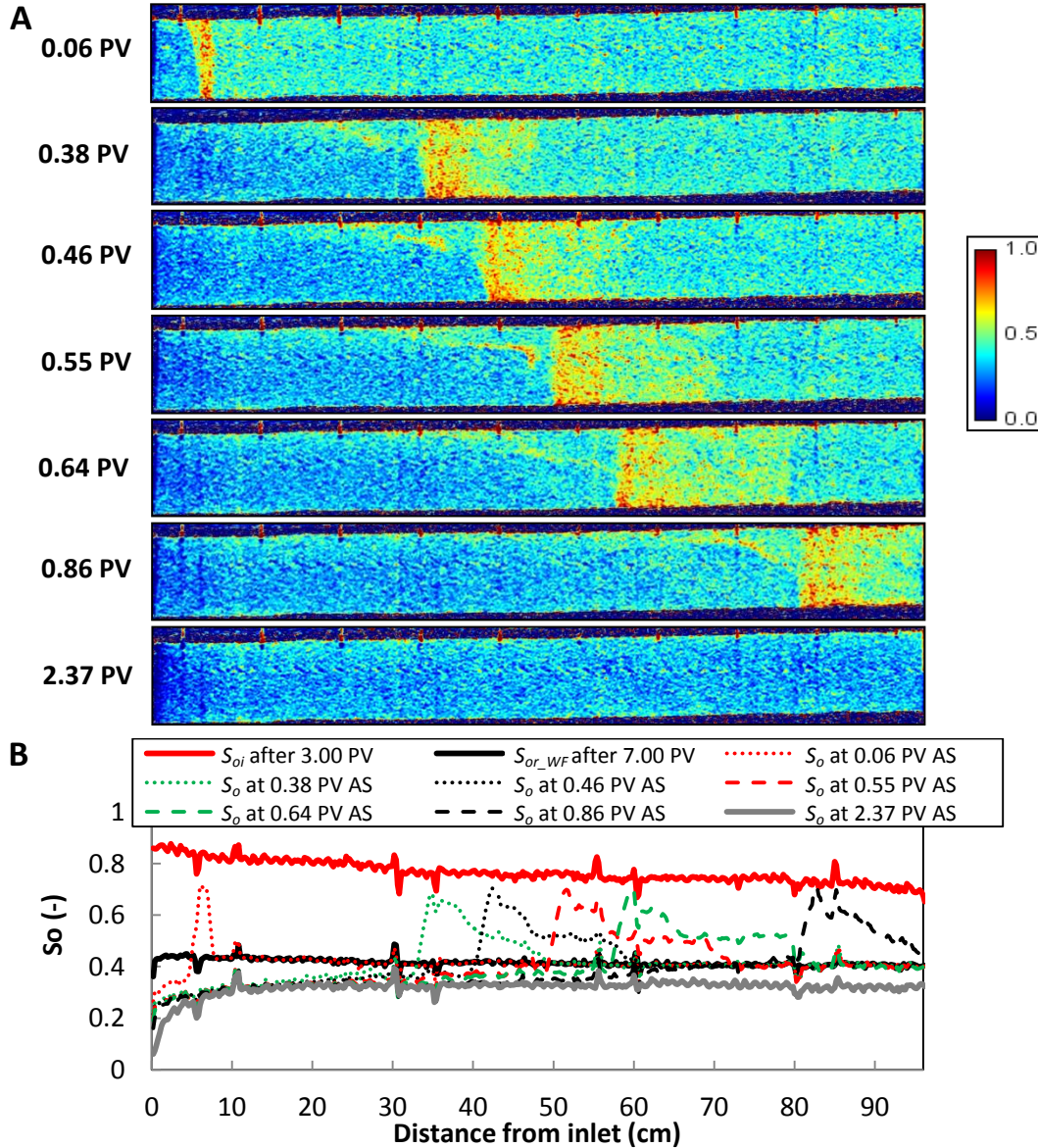


**Figure 3.6:** A: Oil saturation CT scan images, and B: oil saturation profiles during AS slug injection in baseline core-flood 1. The CT scan shown has an X:Y ratio of 4:1. PV = 0 corresponds to the start of slug injection. Red indicates oil and blue represents brine. Note the clear formation and the stable displacement of the oil bank.

The complete pressure drop profiles presented in **Figure 3.7** are the result of foam generation combined with displacement of the oil bank. First, let us consider core-flood 2 (**Table 3.2**). The initiation of co-injection resulted in a steep increase in total pressure drop to  $485 \pm 3$  mbar due to a combination of the increase in  $u_t$  from 0.15 to  $1.10 \text{ cm}^3/\text{min}$  and a reduction in water mobility. Afterwards, pressure drops slightly decreased before increasing again from  $0.59 \pm 0.02$  PV slug and drive injected onwards until a maximum of  $1040 \pm 61$  mbar was reached at  $0.95 \pm 0.02$  PV. The initial decline in pressure drop most likely indicates a modification of the oil bank's shape (i.e. reduction of its peak  $S_o$  may yield an enhanced water mobility), potentially leading to a reduction in total pressure drop. The latter can be explained by assuming a simplified 1D multiphase Darcy's law ( $\Delta P =$

$\frac{u_t}{\lambda_w + \lambda_o + \lambda_g} L$ , where  $\Delta P$ ,  $L$ ,  $\lambda_w$ ,  $\lambda_o$ , and  $\lambda_g$  represent the total pressure drop, core length, and mobility of the water phase, oil phase, and gas phase, respectively). If the increment in  $\lambda_w$ , and the introduction of  $\lambda_g$ , outweighs the reduction in  $\lambda_o$  (as a result of a lower peak  $S_o$ ), the total pressure drop reduces. After  $0.95 \pm 0.02$  PV, the pressure drop reduced marginally to  $702 \pm 34$  mbar at  $1.60 \pm 0.02$  PV. Once the oil bank was completely produced, breakthrough of a *ME* occurred at  $1.24 \pm 0.02$  PV. The abovementioned behaviour in pressure drop is expected to be related to weak foam generation downstream, which broke through at  $0.86 \pm 0.02$  PV ( $0.40 \pm 0.02$  total PV after co-injection started), as indicated by the sectional *MRFs* ( $\leq 1.46$  total PV) shown in **Figure 3.8A**. That figure shows a maximum *MRF* of  $86 \pm 3$  at  $0.96$  total PV near the core outlet, whereas *MRFs* remained negligible in the upstream area during the first  $1.46 \pm 0.02$  total PV of injection. Because of a failure of the liquid pump, only gas was injected for  $0.06 \pm 0.02$  PV, starting at  $1.68 \pm 0.02$  PV. Afterwards, co-injection continued with a gas fractional flow of 57%. As a result of the short, sharp increase in foam quality (i.e. from 57 to 100%), a new foam front was developed, indicated by the steep increase in pressure drop from  $1.80 \pm 0.02$  PV to  $2.90 \pm 0.02$  PV. The second (and stronger) foam front resulted in an increase in *MRF* more upstream in the core (**Figure 3.8A**). The figure also revealed a steep increase in *MRF* downstream (at  $2.86$  total PV injected), which was most likely caused by a combination of the propagating foam front and a *ME* that broke through at  $3.62 \pm 0.02$  PV. Finally, a total pressure drop of  $1127 \pm 20$  mbar was reached, equivalent to foam flow at  $S_{or}$ . Once no more oil was produced, the *MRF* near the outlet stabilized at  $43 \pm 5$  (**Figure 3.8A**).

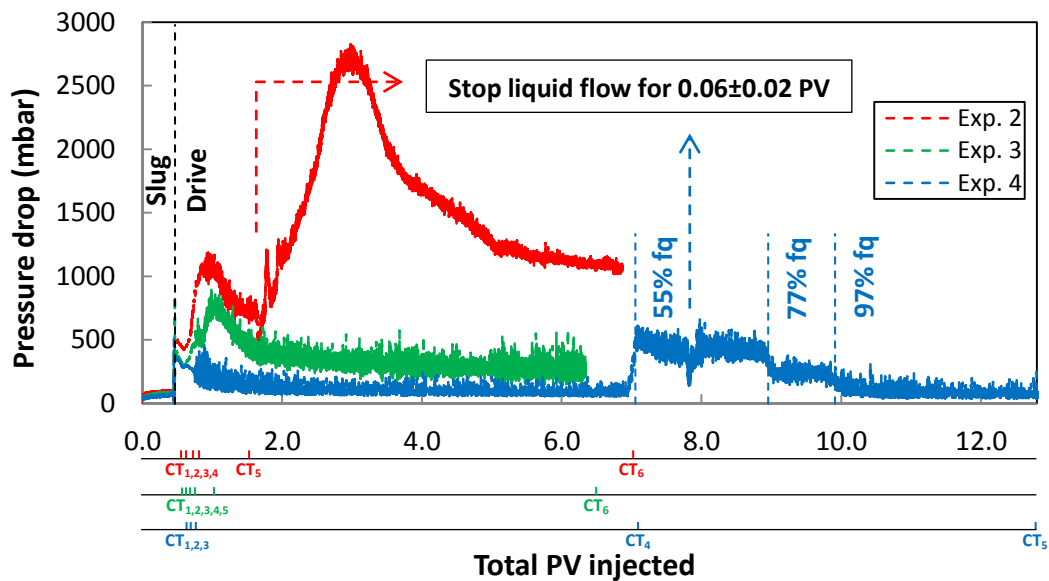


**Figure 3.7:** Total pressure drop profiles for Exp. 2, 3, and 4 during AS slug and AS drive co-injection as function of total (gas + liquid) PV injected. First,  $0.46$  PV AS slug was injected (discussed in previous subsection) followed by co-injection of  $N_2$  and AS drive solution, aiming at a foam quality of 57% (Exp. 2), 77% (Exp. 3), and 97% (Exp. 4). Due to failure of the liquid pump, only gas was injected for  $0.06 \pm 0.02$  total PV starting from  $1.68 \pm 0.02$  total PV in Exp. 2. Because of the observations made in Exp. 2, it was decided to change foam quality to 55% in Exp. 4 after  $7.03 \pm 0.02$  total PV and stop liquid injection for  $0.06 \pm 0.02$  total PV at  $7.87 \pm 0.02$  total PV. Subsequently, at  $8.96 \pm 0.02$  total PV, foam quality was set to 77% and finally to 97% at  $9.95 \pm 0.02$  total PV in Exp. 4. The markers in red, green, and blue denote the times at which CT scans were taken during Exp. 2, 3, and 4, respectively.

The pressure drop profile for Exp. 3 is similar to the pressure drop behaviour during the first  $1.60 \pm 0.02$  PV injected in Exp. 2 (**Figure 3.7**). At the start of the co-injection, a steep increase in pressure drop to  $383 \pm 5$  mbar was observed. Afterwards, it slightly decreased before it increased again to reach a maximum pressure drop at  $1.03 \pm 0.02$  PV injected. Again, we suggest that the decreasing

trend at the start of co-injection was caused by a reduction in the oil bank's peak  $S_o$ , enhancing the contribution of  $\lambda_w$  to the total pressure drop. Finally, a plateau value was reached of approximately  $293 \pm 60$  mbar. The described total pressure drop profile is related to the development of a weak foam front downstream in the core, yielding a maximum  $MRF$  at the core outlet of approximately  $89 \pm 5$  (at 1.48 total PV in **Figure 3.8B**). The foam front broke through at  $0.75 \pm 0.02$  PV ( $0.29 \pm 0.02$  total PV after co-injection started). A limited amount of  $ME$  was produced between  $1.69 \pm 0.02$  and  $4.38 \pm 0.02$  PV injected.

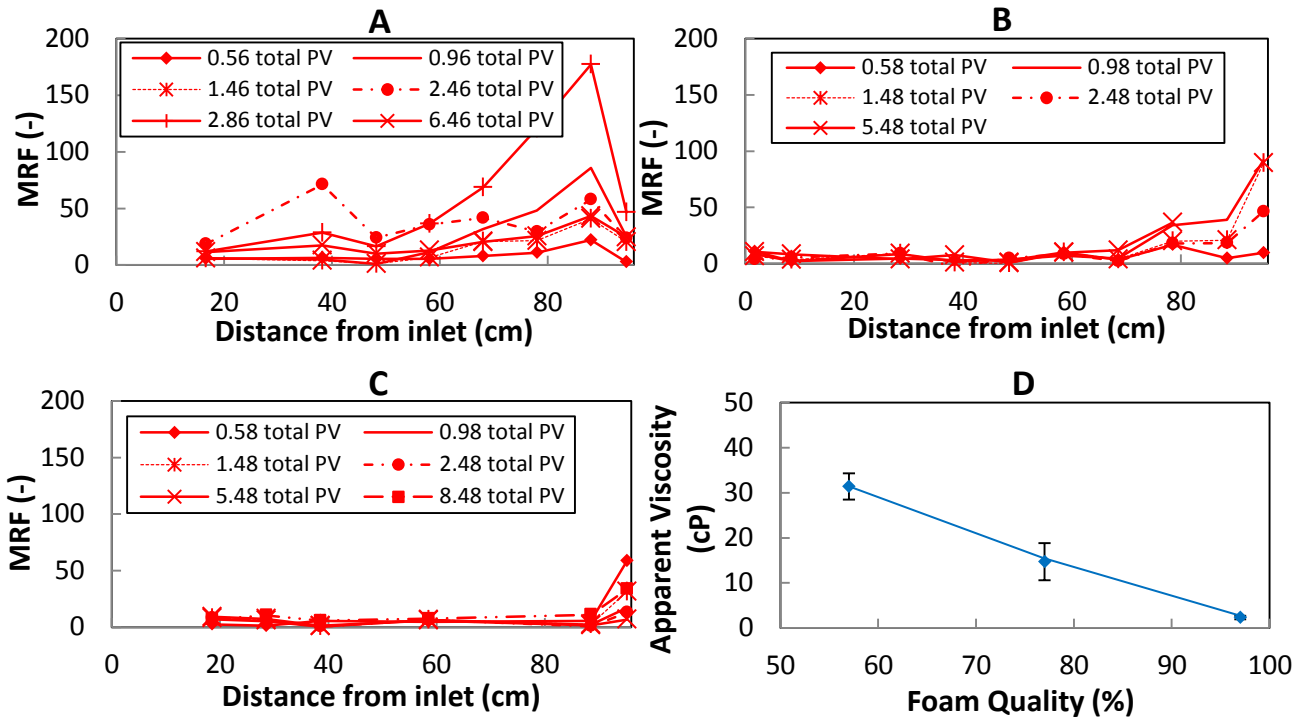


**Figure 3.8:** Sectional  $MRF$  as function of total PV injected during Exp. 2 (A), Exp. 3 (B), and Exp. 4 (C) and apparent foam viscosities at residual oil saturation for each drive foam quality studied (D). PV = 0 refers to the start of the slug injection in graphs A, B, and C. Note that the measured pressure drop (thus  $MRF$ ) over a specific core section is pinpointed to the centre of that particular section. The apparent foam viscosities (D) represent the foam strength at the end of  $FACF$  at constant drive foam qualities.

The profile corresponding to Exp. 4 differs from the two previously discussed core-flood experiments as no evidence of foam generation was found here (**Figure 3.7**). Once co-injection was initiated, a steep increase in pressure drop to  $390 \pm 5$  mbar was observed. Afterwards, it slowly decreased to a steady-state pressure drop of  $91 \pm 18$  mbar, corresponding with the fairly low  $MRF$  over the entire core length at 5.48 total PV (**Figure 3.8C**). Gas breakthrough happened at  $0.72 \pm 0.02$  PV ( $0.26 \pm 0.02$  total PV after co-injection started). During this stage no  $ME$  was produced, only clean oil by means of the oil bank. Though the baseline test (Exp. 1) indicated the presence of a  $ME$  during AS slug injection (**Section 3.3.2.2**), most likely, due to an unfavourable  $M$ , gas was not able to displace the  $ME$  and bypassed it instead. Since no foam was generated in core-flood 4 until this point, at  $7.03 \pm 0.02$  PV the foam quality was set to 55% and liquid injection stopped between  $7.87 \pm 0.02$  PV and  $7.93 \pm 0.02$  PV. The aim was to determine whether a strong foam front could be generated this way (as observed in Exp. 2). As seen in **Figure 3.7**, this had no significant effect on the observed pressure drop. Owing to the increase in liquid fractional flow, a  $ME$  broke through at  $7.72 \pm 0.02$  PV injected. Next, after  $8.96 \pm 0.02$  PV, the foam quality was changed to 77%, which yielded a pressure drop of  $249 \pm 50$

mbar. Eventually, the foam quality was set back to 97% again at  $9.95 \pm 0.02$  PV, corresponding to an average total pressure drop of  $87 \pm 20$  mbar, which is similar to the initial steady-state pressure drop at 97% foam quality. The *MRF* profile constructed for 8.48 total PV injected (**Figure 3.8C**) confirms the absence of foam generation upon changing the foam quality to 55% and temporarily shutting down liquid injection.

**Figure 3.8D** presents the apparent foam viscosities for each constant drive foam quality, i.e. before alterations applied in Exp. 2 and 4, at its  $S_{or}$ . The data show that apparent viscosities decreased linearly with increasing foam quality. Several authors (Lee and Heller, 1990; Osterloh and Jante, 1992) identified two foam-flow regimes: a) low-quality regime, where the apparent foam viscosity increases with increasing foam quality, and b) high-quality regime, where the apparent foam viscosity decreases as the foam quality increases (**Section 1.3.3**). The transition between both foam-flow regimes is characterized by the critical foam quality ( $f_g^*$ ), which exhibits the maximum apparent foam viscosity. The data corresponding to the conditions in this study (**Figure 3.8D**) suggest that  $f_g^*$  can be a) lower than 57%, b) equal to 57%, or c) in between 57% and 77%. The observed trend in **Figure 3.8D** is in good agreement with the findings of Guo et al. (2012), who studied IOS2024 foam strength as function of foam quality (55 to 91%) in Bentheimer sandstones in the absence of oil.

The baseline core-flood, Exp. 1, showed that, when injecting the liquid AS slug at  $0.15 \text{ cm}^3/\text{min}$ , a minimal amount of *ME* was produced (approximately 0.01 PV), which had no significant effect on pressure drop readings (**Figure 3.5**). Although these results are representative for the AS slug injection phase in Exp. 2, 3, and 4, one could debate what happened when co-injection started. During the co-injection, the total flow rate increased to  $1.10 \text{ cm}^3/\text{min}$ , while mobilized oil was still present in the core. The increase in total flow rate, thus in shear rate, yielded more *o/w* mixing, which might promote the emulsification process.

#### 3.3.2.3.2 CT images and oil saturation profiles

**Figure 3.9** presents the  $S_o$  CT scan images and profiles for experiments Exp. 2 (A), Exp. 3 (B), and Exp. 4 (C) during drive co-injection. First, we discuss the images and profiles related to Exp. 2. As soon as co-injection was initiated, the shape of the oil bank changed, reducing its peak  $S_o$ . Oil breakthrough occurred at  $0.19 \pm 0.02$  PV co-injected (i.e. excluding slug). At 1.08 total PV, the first oil bank was completely produced, resulting in a  $S_{or}$  of  $0.31 \pm 0.03$ . Eventually, due to the formation of a second foam front as a result of the sharp increase in foam quality, an additional oil bank was produced, reducing  $S_{or}$  further to  $0.20 \pm 0.03$  (**Table 3.4**). Note that, initially, by using a constant drive foam quality of 57%, only the downstream area in the core was properly swept (CT scan at 1.08 total PV). The generation of a new (and stronger) foam front near the inlet region resulted in oil also being produced from that section (CT scan at 6.35 total PV). Including an incremental recovery of  $14 \pm 10\%$ , the  $R_{FCEOR}$  equalled  $74 \pm 5\%$  of the *OIIP* (**Table 3.4**).

The CT scan images taken during core-flood 3 (**Figure 3.9B**) appeared very similar with those taken during Exp. 2. They clearly show the presence and propagation of the oil bank as well as its reducing peak  $S_o$  once co-injection started. Oil breakthrough occurred at  $0.25 \pm 0.02$  PV co-injected. The image at 5.91 total PV shows the situation after performing the co-injection with a constant foam quality of 77%. It looks analogous to the image taken at 1.08 total PV in Exp. 2; mainly the area downstream was swept. Similar to using a constant drive foam quality of 57%, a  $S_{or}$  of  $0.31 \pm 0.04$  and  $R_{FCEOR}$  of  $60 \pm 7\%$  of the *OIIP* were achieved by using a constant gas fraction of 77% in the drive (**Table 3.4**).

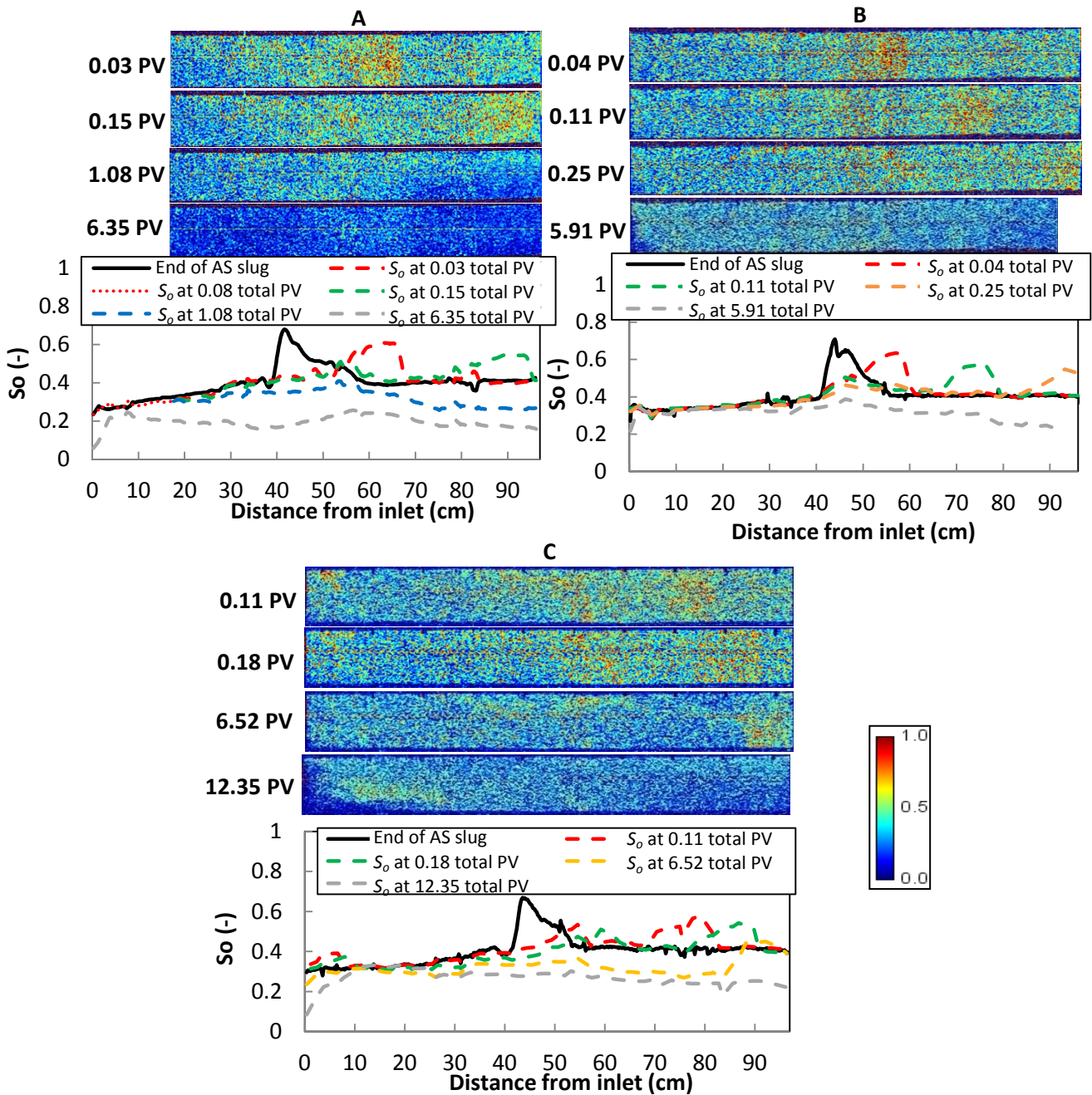


**Figure 3.9:** Oil saturation CT scan images (top) and profiles (bottom) during AS drive and  $N_2$  co-injection for Exp. 2 (A), Exp. 3 (B), and Exp. 4 (C). Total PV = 0 corresponds to the start of the co-injection. Red indicates oil and blue represents brine. Note that, due to CT limitations, only the last 79 cm of the core could be scanned in Exp. 2. The profile at 6.35 total PV was constructed from two separate scans, and the  $S_o$  profile at 0.08 total PV is the result of a distinct scan of the first 18 cm (Exp. 2). The scan taken at 5.91 total PV in Exp. 3 misses the last 6 cm of the core. The presented profiles were constructed by applying a moving average function with an interval of 6 to the processed data.

The CT scan images taken during Exp. 4 (**Figure 3.9C**) are comparable to the ones taken during Exp. 2 and 3. However, several differences were observed. CT data suggest a disintegrated oil bank in Exp. 4 once co-injection started, while in Exp. 2 and 3 the oil bank remained more distinctively present during co-injection. Nonetheless, oil breakthrough time was similar to that in the other two experiments ( $0.23 \pm 0.02$  PV co-injected). The CT scan image at 6.52 total PV shows the oil distribution after conducting co-injection with a constant foam quality of 97%. Because of the absence of foam generation, gas tended to override, leaving oil behind near the outlet section. Nevertheless, a  $S_{or}$  of  $0.32 \pm 0.04$  was found at this stage (**Table 3.4**). The CT scan image at 12.35 total

PV presents the  $S_o$  distribution at the end of the experiment, after the foam quality was altered (first to 55%, later to 77%, and finally back to 97%). The changes applied to the drive foam quality improved the sweep efficiency, yielding a final  $S_{or}$  of  $0.27 \pm 0.04$  ( $R_{FCEOR}$  of  $66 \pm 7\%$  of the  $OIIP$ ). All mobilized oil from the first 5 cm of the core was accumulated at 10-30 cm distance from the inlet.

The ultimate  $R_{FCEOR}$  corresponding to  $FACF$  at constant drive foam qualities of 57, 77, and 97% were all similar:  $60 \pm 7\%$  of the  $OIIP$ . Yet, the time required to reach this ultimate recovery was the longest (i.e. less efficient) in Exp. 4 and the shortest (i.e. most efficient) in Exp. 2. The latter being controlled by the apparent foam viscosity (**Figure 3.8D**) of each drive foam quality assessed.

### 3.3.2.3.3 Gas saturation profiles

**Figure 3.10** shows the  $S_g$  profiles during the co-injection of  $N_2$  and AS drive solution for the three  $FACF$  core-floods performed. First, we discuss the profiles related to Exp. 2. Until 1.08 total PV co-injected, i.e. excluding slug, the  $S_g$  profiles reveal the same trend:  $S_g$  remained low until it reached a distance of  $50 \pm 1$  cm from the core inlet. From that point on, gas started to divide more equally across the core cross-sectional area, shown by the cross-section at 56 cm at 0.15 total PV injected in **Figure 3.10**. This observation, together with the pressure drop and sectional  $MRF$  profiles in **Figures 3.7** and **3.8A**, respectively, is a qualitative indicator of foam generation. In the first  $50 \pm 1$  cm, gas was mainly overriding owing to gravitational effects, as illustrated by the cross-sections shown at 20 and 48 cm distance at 0.15 total PV injected. Foam breakthrough occurred at  $0.40 \pm 0.02$  PV co-injected, and the front propagated with an averaged velocity of  $144 \pm 10$  cm per PV injected. The profile at 6.35 total PV shows the  $S_g$  distribution after failure of the liquid pump (i.e. at the end of the experiment). The averaged  $S_g$  along the core at the end of the test equalled  $0.53 \pm 0.07$ .

The  $S_g$  profile behaviour in Exp. 3 is similar to the one in Exp. 2:  $S_g$  remained relatively low and started to increase from a distance of approximately  $50 \pm 1$  cm from the core inlet. Analogous to Exp. 2, the  $S_g$  profiles, together with the pressure drop and sectional  $MRF$  (**Figures 3.7** and **3.8B**), suggest foam generation in the downstream area. Foam breakthrough happened at  $0.29 \pm 0.02$  PV co-injected, and the front propagated with an averaged velocity of  $353 \pm 27$  cm per PV injected. Eventually, after 5.91 total PV injected, a  $S_g$  of approximately  $0.38 \pm 0.02$  was reached near the outlet.

The  $S_g$  profiles constructed for Exp. 4 differ from the profiles previously discussed in this subsection. Here, there was no characteristic increase in  $S_g$  to indicate foam generation.  $S_g$  profiles, sectional  $MRFs$  (**Figure 3.8C**), and the related total pressure drop profile (**Figure 3.7**) all suggest the absence of foam generation over the entire core. Gas breakthrough occurred at  $0.26 \pm 0.02$  PV co-injected. After injecting with a constant foam quality of 97% for 6.52 total PV, an average  $S_g$  of  $0.22 \pm 0.04$  along the core was achieved. This value increased to  $0.33 \pm 0.06$  after altering the foam quality (at 12.35 total PV injected). Averaged velocity of the propagating gas front equalled  $407 \pm 30$  cm per PV injected.

In all three aforementioned experiments, a propagating gas/foam front was identified. The front was least stable in Exp. 4 (i.e. early gas breakthrough) and most stable in Exp. 2 (i.e. delayed gas breakthrough), which was a direct consequence of the related apparent foam viscosities (**Figure 3.8D**). The breakthrough time of gas in Exp. 4 corresponds well with literature values for gas flooding in Bentheimer sandstones (Simjoo, 2012). The liquid fraction in Exp. 4 might be too low for foam to develop; insufficient amount of surfactant may support the oil to prevent stable foam generation.

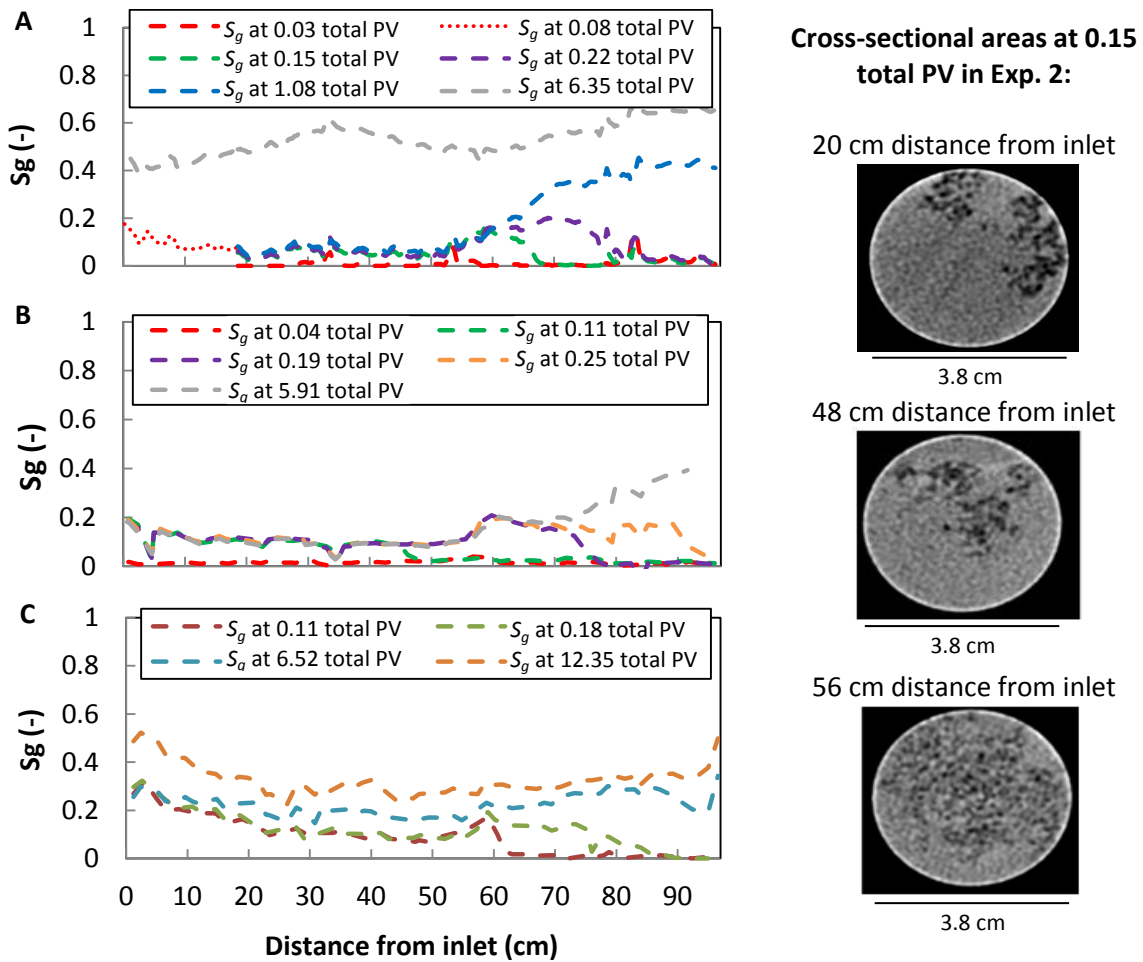


**Figure 3.10:** Gas saturation profiles during co-injection of AS drive and  $N_2$  for Exp. 2 (A), Exp. 3 (B), and Exp. 4 (C). For this purpose, true dual-energy (80 and 140 kV) scanning was applied. Note that, in Exp. 2, only the last 79 cm could be scanned due to CT scan limitations; the profile at 6.35 total PV was constructed from two separate scans, and the  $S_g$  profile at 0.08 total PV is the result of a distinct scan of the first 18 cm. PV = 0 corresponds to the start of the co-injection. On the right-hand side of the figure, three cross-sectional areas are shown for 0.15 total PV injected in Exp. 2. They represent the original CT data in Hounsfield units where the gas phase is shown in black.

### 3.3.2.4 Oil recovery

**Figure 3.11** presents the cumulative oil recovery and oil cut plots during AS slug injection and co-injection of  $N_2$  and AS drive for the four experiments conducted in this study. First, the baseline study, Exp. 1, will be discussed, followed by Exp. 2, 3, and 4.

**Figure 3.11A** shows the oil cut and cumulative oil recovery for the first two total PV of injection in Exp. 1; the increase in injection rate (**Figure 3.5**) did not yield additional oil production. Although the profile shows a sharp increase in oil cut at  $0.39 \pm 0.02$  PV, which was most probably caused by a small amount of oil that was produced from the core-holder end-cap, breakthrough of the oil bank occurred at  $0.72 \pm 0.02$  PV. It took  $0.38 \pm 0.02$  PV for the oil bank to be completely produced. Eventually, including oil production in the form of a ME, an ultimate recovery of 18% of the OIP after water flooding (equivalent to an overall  $R_{FCEOR}$  of  $57 \pm 11\%$  of the OIIP) was achieved (**Table 3.4**).

In Exp. 2, breakthrough of the first oil bank corresponds with the steep increase in oil cut from 0 to 30% (**Figure 3.11B**). Due to the formation of a second foam front, a second oil bank broke through, indicated by the increase in oil cut to 14% at  $3.29 \pm 0.02$  PV slug and drive injected. Subsequently, a

long tail-shaped production profile is noticed where oil was mainly produced in the form of a *ME*. Finally, after  $6.82 \pm 0.02$  PV injected, an ultimate recovery of 37% of the *OIP* after water flooding (corresponding to a  $R_{FCEOR}$  of  $66 \pm 8\%$  of the *OIIP*) was reached (**Table 3.4**). The oil recovery before altering the foam quality equalled 20% of the *OIP* after water flooding ( $R_{FCEOR}$  of  $58 \pm 8\%$  of the *OIIP*).

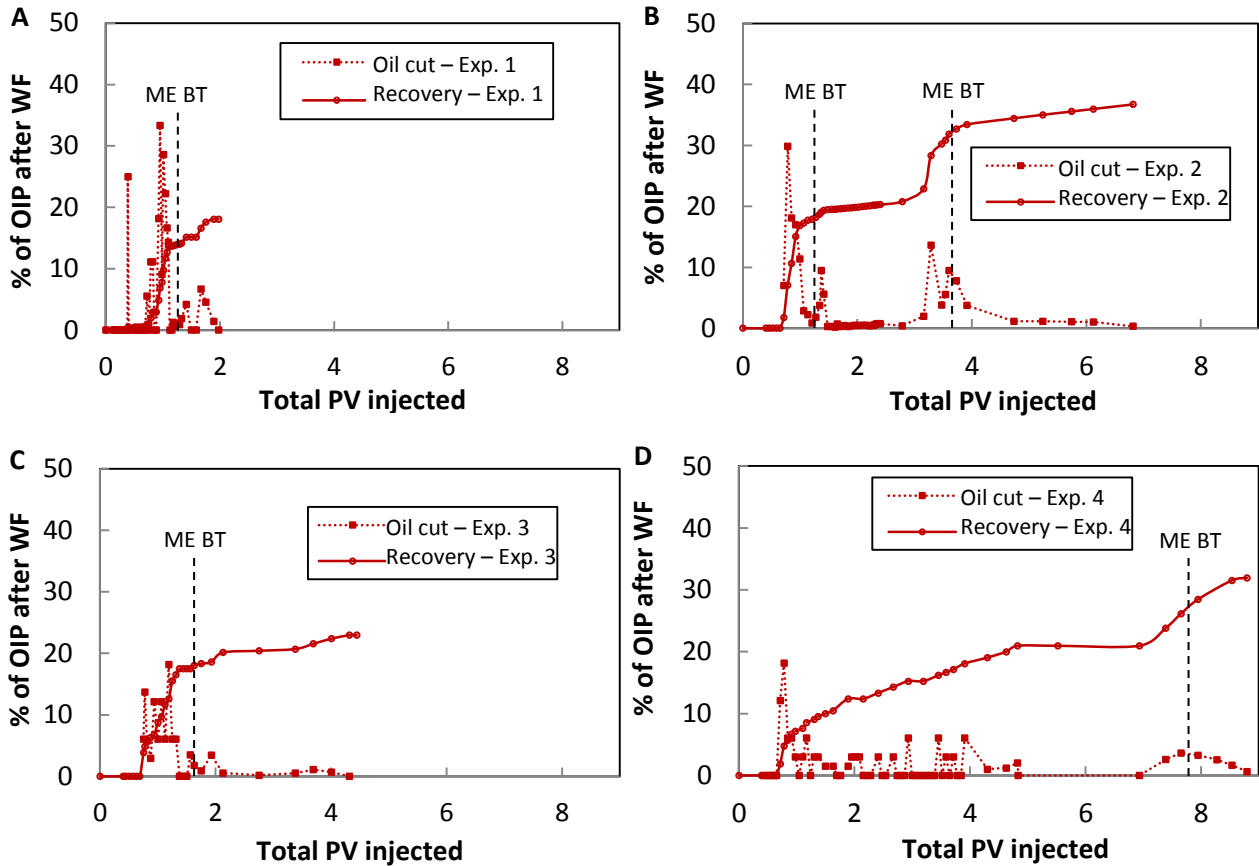


**Figure 3.11:** Oil cut and cumulative oil recovery for Exp. 1 (A), Exp. 2 (B), Exp. 3 (C), and Exp. 4 (D). Here, 0 PV injected corresponds with the start of the AS slug injection. Breakthrough of an oil bank happened at  $0.72 \pm 0.02$  total PV (Exp. 1),  $0.65 \pm 0.02$  total PV (Exp. 2),  $0.71 \pm 0.02$  total PV (Exp. 3), and at  $0.69 \pm 0.02$  total PV (Exp. 4). The y-axis uses the oil in place (*OIP*) after water flooding as a reference. Micro-emulsion (*ME*) breakthrough times (*BT*) are shown within each graph. For every foam quality studied, before altering the foam quality, final recovery factors were similar. All the values were calculated based on material balance.

The step increase in oil cut from 0 to 14% corresponds to the breakthrough of the oil bank in core-flood 3 (**Figure 3.11C**). Oil production after  $1.69 \pm 0.02$  PV was mainly in the form of a *ME*. Finally, after  $4.44 \pm 0.02$  PV injected, an ultimate recovery factor of 23% of the *OIP* after water flooding was achieved; consistent with a  $R_{FCEOR}$  of  $61 \pm 9\%$  of the *OIIP* (**Table 3.4**).

The recovery profile related to Exp. 4 (**Figure 3.11D**) shows a relatively slow increasing trend in oil recovery. The step increase in oil cut from 0 to 18% corresponds with the oil bank breakthrough. Only clean oil was produced here, and a 97% foam quality eventually resulted in a cumulative oil recovery of 21% of the *OIP* after water flooding ( $R_{FCEOR}$  of  $60 \pm 9\%$  of the *OIIP*). As a result of the changes applied to the drive foam quality (i.e. increasing its liquid fraction), the oil that was left behind near the core outlet (**Figure 3.9C**) broke through at  $6.93 \pm 0.02$  PV injected. Afterwards, oil was produced in the form of both clean and solubilized oil. Eventually, after  $8.80 \pm 0.02$  PV injected, a recovery factor of 32% of the *OIP* after water flooding was reached;  $R_{FCEOR}$  of  $65 \pm 9\%$  of the *OIIP* (**Table 3.4**).

Despite the expected unfavourable  $M$  between the AS slug ( $1.07 \pm 0.12$  cP) and the OIP ( $3.31 \pm 0.03$  cP), the recovery profile of the baseline experiment (Exp. 1) shows a relatively efficient displacement and production of the oil bank (similar to the recovery profile related to Exp. 2). Increasing drive foam quality (i.e. gas fractional flow) from 57 to 77 to 97% resulted in a more unstable displacement of the banked oil, because apparent foam viscosities decreased (**Figure 3.8D**). Hence, it gave rise to a recovery profile that advocates a more dispersed oil bank (**Figure 3.11B vs. 3.11C and 3.11D**). This is consistent with the corresponding  $S_o$  CT images shown in **Figure 3.9**. When injecting at constant drive foam qualities of 57, 77, and 97%, the amount of clean non-solubilized oil produced by the oil bank was similar in all core-floods performed:  $19 \pm 2\%$  of the OIP after water flooding. The latter suggesting that, at these conditions, the variation in drive chemicals (i.e. foam quality) injected did not significantly alter the amount of produced clean oil; only the rate at which it was produced. Moreover, approximately  $15 \pm 5\%$  of the total amount of oil produced, i.e. clean + solubilized oil, consists of solubilized oil (constant  $f_g$  in Exp. 2 and 3 only).

The FACF methodology is more efficient than continuous immiscible  $N_2$  flooding and WAG, in terms of oil being produced (**Section 2.3.5**). Though the ultimate  $R_{FGF}$  of WAG is similar to the final  $R_{FCEOR}$  of FACF (when flooding with a constant drive foam quality), WAG requires much more total PV to be injected to reach the same ultimate  $R_F$  (5.0 total PV vs. 1.6 total PV to reach a  $R_F$  of 57% of the OIIP). It is expected that the  $R_{FCEOR}$  of FACF would increase when operating at ultralow  $o/w$  IFT (i.e. optimum salinity).

### 3.4 General discussion

The results presented in this study will be analysed in view of oil mobilization and oil displacement mechanisms, as both are crucial aspects in studying the effect of drive foam quality on oil bank propagation. For assessing the displacement of oil by foam in a FACF process, ternary diagrams were constructed. They represent three-phase saturation evolutions during the course of FACF flooding, providing a schematic comparison between various saturation paths.

#### 3.4.1 Saturation paths

**Figure 3.12** presents the saturation paths for the three FACF core-flood experiments performed in this study. Using obtained CT data, averaged three-phase saturations were calculated over the entire core length. Since primary drainage, water flooding, and AS slug injection yielded very similar results in all three core-floods, we focus on the AS drive and  $N_2$  co-injection here. Though gas-liquid ratios differ per experiment during co-injection, the general trend in saturation path is very similar. As soon as co-injection was initiated, first only water was produced at a constant  $S_o$ . Afterwards, in Exp. 2 between 0.32 and 1.08 total PV co-injected (excluding slug), the foam front displaced both water and oil, hence the reduction in  $S_w$  and  $S_o$  and the increase in  $S_g$ . In Exp. 3, between 0.50 and 5.91 total PV co-injected,  $S_g$  remained more or less constant as foam breakthrough occurred prior to 0.50 total PV and the foam structure, most likely, had not changed significantly afterwards. Here, foam displaced oil and water, where water predominantly replaced the oil in previously oil bearing pores; decrease in  $S_o$  and an increase in  $S_w$ . During co-injection in Exp. 4, between 0.25 and 6.52 total PV, gas displaced both oil and water. This resulted in an increase in  $S_g$ , a decreasing  $S_o$ , and a  $S_w$  that remained roughly constant because gas was the main phase that replaced the oil from their bearing pores. All core-floods yielded similar  $S_{or}$  after co-injecting with a fixed drive foam quality (57, 77, and 97%);  $S_{or\_CEOR}$  in **Figure 3.12**. Though  $S_{or\_CEOR}$  values were similar in all core-flood experiments performed, oil was produced faster in Exp. 2 compared to Exp. 3 and 4. Oil bank displacement by a

stable drive foam (Exp. 2 and 3) features displacement of oil by foam where mainly water replaced oil in the pores whereas gas replaced oil from their bearing pores in the case of no stable drive foam (Exp. 4); all related to our experimental conditions. Because of the changes applied to the foam quality in Exp. 2 and 4,  $S_{or\_CEOR}$  was reduced further to  $S_{or\_CEOR}^*$ . The second, stronger, foam front generated in Exp. 2 resulted in a sharp increase in  $S_g$ .

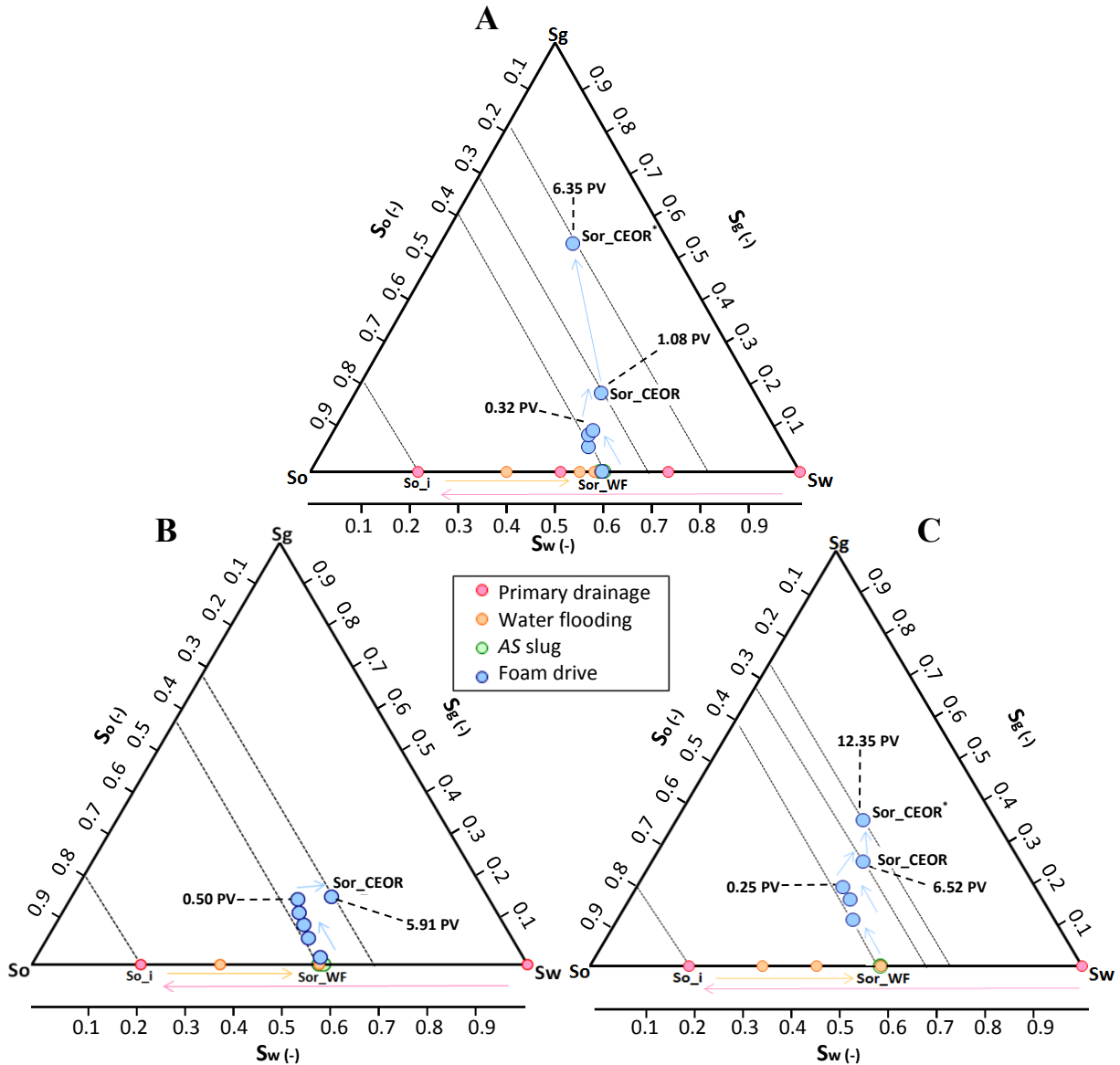


**Figure 3.12:** Saturation paths for Exp. 2 (A), Exp. 3 (B), and Exp. 4 (C).  $S_w$ ,  $S_o$ ,  $S_g$ ,  $S_{or\_WF}$ ,  $S_{or\_CEOR}$ ,  $S_{or\_CEOR}^*$ , and  $S_{o\_i}$  represent the water, oil, gas, residual oil to waterflood, residual oil to FACH at constant  $f_g$ , residual oil to FACH at varying  $f_g$ , and initial oil saturations, respectively. Saturation values shown were calculated using CT data and were averaged over the entire core length. Since in Exp. 2 dual-energy CT data was not available over the entire length of the core, for the first 18 cm it was assumed that the  $S_o$  profile equals the  $S_o$  profile constructed at 0.08 total PV injected (Figure 3.9A). This seems to be a reasonable assumption as the  $S_o$  profiles in the first 18 cm of Exp. 3 and 4 are more or less constant in time when flooding with a constant foam quality (Figures 3.9B and 3.9C). This was done for all the saturation profiles that required dual-energy data in Exp. 2 until 1.08 total PV injected.

### 3.4.2 Oil mobilization

To investigate the effect of drive foam quality on oil bank propagation, first we need to shed light on how oil is actually being mobilized, i.e. how an oil bank is being formed during AS slug injection under the conditions imposed in this work. The experiments presented in this study showed that the

designed AS slug was effective at mobilizing part of  $S_{or\_WF}$ . The pore level mechanism responsible for the partly mobilization of  $S_{or\_WF}$  included *o/w IFT* lowering, mobilizing ganglia, and solubilizing the remaining oil. A schematic of the proposed mechanism is shown in **Figure 3.13**. The middle figure presents the situation after water flooding, at  $S_{or\_WF}$ . It was expected that  $S_{or\_WF}$  consisted mainly of relatively big oil blobs and/or ganglia (Howe *et al.*, 2015). When the AS slug was injected, the *o/w IFT* and, correspondingly, the capillary pressure that kept the *OIP* were reduced (*o/w IFT* was reduced by a factor of approximately 130). Similarly,  $N_c$  (**Equation 3.1**) increased from  $10^{-7}$  (water flooding) to  $10^{-5}$  (AS slug injection).

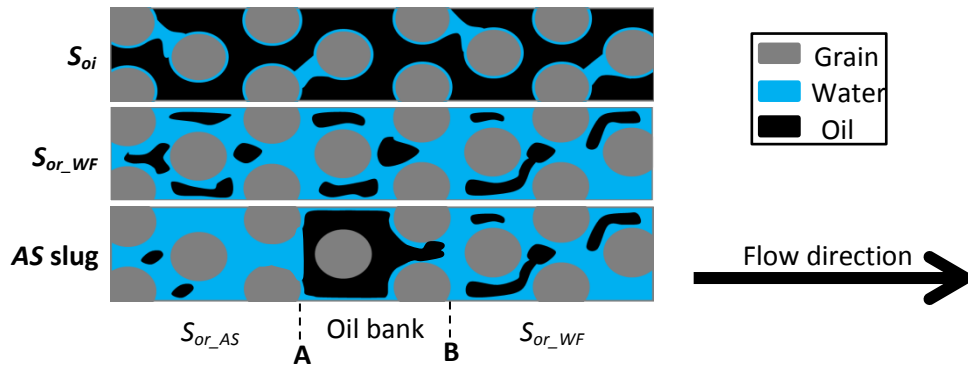


**Figure 3.13:** Schematic overview of the proposed oil mobilization mechanism by AS slug injection in this work. The top sketch presents the situation at initial oil saturation ( $S_{oi}$ ), the middle sketch shows the condition after water flooding (at  $S_{or\_WF}$ ), and the bottom one shows the situation during AS slug injection where the front reached approximately one-third of the core. A and B refer to the oil bank's trailing edge and leading edge, respectively.

The surfactant slug partly mobilized the oil blobs/ganglia, allowing them to propagate through narrow pore throats and, subsequently, might lead to their division into smaller droplets. At the slug front, coalescence among mobilized oil droplets or between mobilized and trapped oil droplets may occur, leading to the formation of a continuous oil bank. During its propagation, oil coalescence occurred at its leading edge, as verified by CT scans (**Figure 3.6**). The oil bank showed peak oil saturations close to  $1-S_{wc}$ . Upstream of the oil bank (i.e. at its trailing edge), remaining oil droplets were solubilized by the slug, forming a *ME*. The presence of the *ME* during AS slug injection was verified by the baseline core-flood, Exp. 1. It is likely that  $S_{or\_AS}$  consisted primarily of small oil droplets. The aforementioned proposed mobilization mechanism for AS slug injection in this study should be validated by experiments which allow one to assess pore-scale phenomena.

### 3.4.3 Oil displacement by foam

The effect of drive foam quality on oil bank propagation is strongly related to the occurrence of a potential foaming mechanism. The results presented in this study showed that stable IOS2024 foam could be generated at relatively low foam qualities in the presence of *n*-hexadecane, suggesting the existence of stable pseudo-emulsion films that permitted the transport of foam lamellae over oil droplets. For further analysis, we consider the schematic of the static averaged saturation distribution at the end of AS slug injection (**Figure 3.14**). The proposed mechanisms responsible for foam generation were snap-off, lamellae division, and leave-behind, as shown in **Figure 1.3** (Kovscek and Radke, 1994). Most likely, these physical processes yielded very coarse gas bubbles in the upstream area ( $S_{or\_AS}$  in **Figure 3.14**). Rossen and Gauglitz (1990) stated that, for foam generation to happen, the local pressure gradient needs to exceed a critical value. The local pressure drop in the  $S_{or\_AS}$  section was most probably too low for lamellae division to occur; hence, the absence of smaller, more equally divided, gas bubbles. However, when the co-injected gas/AS drive front reached a

distance of  $50 \pm 1$  cm from the inlet, foam started to generate in Exp. 2 and 3 (**Figure 3.10**). We suggest that the presence of a potential *ME*, in combination with temporary oil remnants upstream of the oil bank, might promote foam generation. Let us consider this proposed foaming mechanism in the light of Exp. 2. **Figure 3.15** presents both original and processed CT images at 0.15 total PV injected in Exp. 2. It is evident from **Figure 3.15** that the location where foaming characteristics occurred corresponded exactly with an area of relatively high  $S_o$ . Production data suggest the presence of a *ME* phase just upstream of this high  $S_o$  zone as *ME* breakthrough occurred after the oil from this area was produced. It is likely that once the co-injected gas/AS drive reached the distance of  $50 \pm 1$  cm from the inlet, this zone of relatively high  $S_o$  was already present (first two profiles in **Figure 3.9A**). We propose that, once the co-injected gas/AS drive met this zone with potentially predominantly oil and *ME* bearing pores, effective porosity reduced, gas and liquid interstitial velocities increased, and, consequently, local pressure drop increased. Considering an effective porosity reduction of 25% would increase local interstitial velocities by approximately 33%, proportional to the expected increase in local pressure drop. This might be the trigger for lamellae division to take place and to generate a gas bubble distribution that was smaller in size. To test this hypothesis (i.e. the presence of a zone with potentially *ME* and oil bearing pores controls foam generation), co-injection of AS drive solution and  $N_2$  at a foam quality of 57% was applied at the end of baseline Exp. 1. Since, at this moment, the complete oil bank and *ME* phase were already produced (**Figure 3.6**), no foam generation was expected. Results indicated the absence of any foam generation while, in Exp. 2, the same foam quality yielded the most stable foam. The aforementioned mechanism for foam generation at our experimental conditions needs to be validated by dedicated microfluidic experiments, thus enabling the study of pore-scale processes.

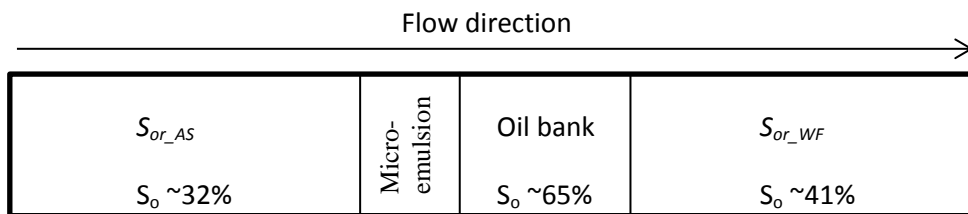


**Figure 3.14:** Schematic of the fluid distribution after AS slug injection (at the start of co-injection) for Exp. 2, 3, and 4.

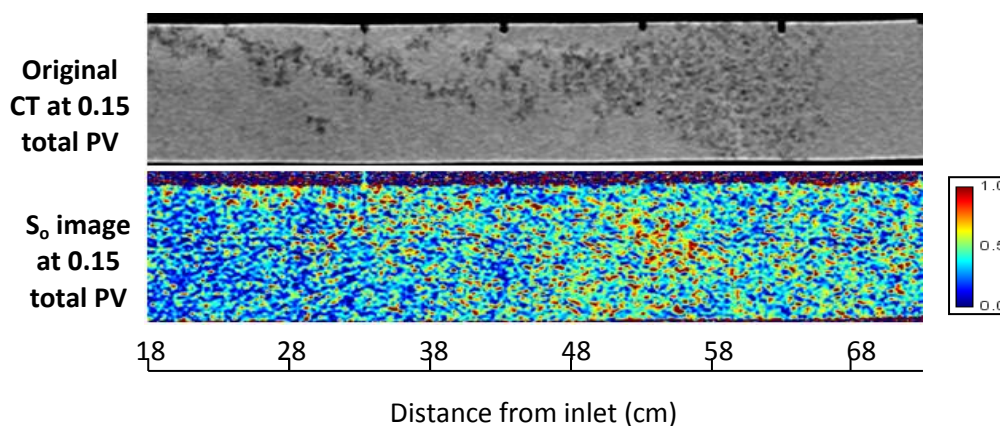


**Figure 3.15:** Original (top) and processed (bottom) CT scan images taken at 0.15 total PV injected during co-injection of AS drive with  $N_2$  in Exp. 2. PV = 0 corresponds with the start of the co-injection. The top image represents original CT data in Hounsfield units where the gas phase is shown in black. Red indicates oil in the bottom image.

Although all *FACF* core-floods conducted revealed a relatively high  $S_o$  zone at  $50 \pm 1$  cm from the inlet during early co-injection times (**Figure 3.9**), it appeared that the liquid *AS* drive fraction in Exp. 4 was too low for the suggested foaming mechanism to occur. The latter resulted in less favourable oil bank displacement. As a consequence of the absence of stable foam in the upstream area in Exp. 2 and 3, for constant drive foam qualities, mainly the downstream area was swept (**Figures 3.9A** and **3.9B**). This observation differs from the reported *FACF* experimental work of Guo et al. (2012). They observed stable foam generation near the inlet area as, in their experiments, almost all the remaining oil to waterflood was mobilized by the *AS* slug (ultralow o/w *IFT*), most likely yielding an  $S_o$  low enough for stable foam generation to occur. We suggest that the oil used in our core-floods may partially prevent foam generation in the  $S_{or\_AS}$  zone (**Figure 3.14**), but, if the oil together with the potential *ME* formed a zone with reduced effective porosity over a significant part of the cross-sectional area, it might also be the key that controls foam generation. The latter is linked to the oil bank shape generated during *AS* slug injection in this study, because it controls the oil bearing part of the core cross-sectional area. To extend the swept area by generating foam upstream in the core, it might be helpful to use another, more appropriate, chemical surfactant for foaming instead of IOS2024.

### 3.5 Conclusions

*FACF* was studied systematically using a model oil and porous media. Bulk phase behaviour tests were conducted to optimize the chemical slug formulation. CT scan assisted core-floods were performed to discern the main mechanisms for oil mobilization and oil displacement by a foam drive. Core-floods included the injection of an alkaline-surfactant (*AS*) slug at under-optimum salinity conditions into Bentheimer sandstone cores previously brought to residual oil saturation to waterflood and, in all cases except one, a foam drive (i.e. co-injection of  $N_2$  and *AS* drive solution). Drive foam quality was varied to examine its effect on the oil bank displacement.

The formation of the oil bank during *AS* slug injection was clearly visualized and quantified using CT scanning data. The designed surfactant slug operated at under-optimum salinity conditions and was able to lower the oil-water interfacial tension by a factor 130. Oil coalescence took place at the oil bank's leading edge, yielding expansion of the banked oil. Dispersion at its leading edge was a strong function of injection time as verified by the baseline core-flood. Peak oil saturations of  $0.67 \pm 0.02$  were found in the oil bank for all experiments performed.

The co-injection of  $N_2$  and *AS* drive solution at constant foam qualities of 57 and 77% yielded weak foam generation in the presence of residual oil. Foam strength increased upon touching the oil bank, leading to an effective oil bank displacement. The proposed mechanism responsible implies foaming behaviour being controlled by the presence of a zone with potentially micro-emulsion and oil bearing pores.  $N_2$  and *AS* drive co-injection at a constant foam quality of 97% did not result in foam generation. Presumably this resulted from an insufficient amount of surfactant present.

The displacement of the oil bank by foam was most stable (i.e. better mobility control) at the lowest foam quality investigated (57%) and least stable at the highest foam quality considered (97%). Ultimate oil recoveries of under-optimum *FACF* at constant drive foam qualities of 57, 77, and 97% were similar:  $60 \pm 7\%$  of the *OIIP*. Performing extended slug injection without a foam drive showed an equivalent ultimate oil recovery of  $58 \pm 6\%$  of the *OIIP*. When injecting at constant drive foam qualities of 57 and 77%, oil was produced in the form of clean oil ( $85 \pm 5$  vol.%) and solubilized oil (15

$\pm 5$  vol.%). Cumulative clean oil recovery was not affected by the constant drive foam qualities assessed.

## 4. Foam-assisted chemical flooding: effect of surfactant slug salinity

---

### Abstract

*A laboratory study on foam-assisted chemical flooding injection schemes is reported. Well-controlled foam-assisted chemical flooding CT-scanned core-flood experiments were conducted using n-hexadecane and Bentheimer sandstone cores. The impact of ultralow oil-water interfacial tension, an essential feature of the FACF scheme along with foaming, on oil mobilization and displacement of residual oil to waterflood, was studied. Incremental oil recoveries and related displacement mechanisms by FACF, at varying salinity, were compared to continuous gas injection and WAG. Under-optimum salinity FACF (oil-water interfacial tension of  $10^{-1}$  mN/m) showed a similar ultimate oil recovery as WAG:  $60 \pm 5\%$  of the OIIP. However, ultimate oil recovery for FACF at (near-)optimum salinity (oil-water interfacial tension of  $10^{-2}$  mN/m) reached  $74 \pm 8\%$  of the OIIP. FACF was able to enhance the oil recovery over WAG by effectively lowering the oil-water interfacial tension ( $<10^{-1}$  mN/m) for oil mobilization. FACF at (near-)optimum salinity increased the clean oil fraction in the production stream over under-optimum salinity FACF. At (near-)optimum FACF, the formed oil bank by the surfactant slug displayed uniform and elongated characteristics, whereas at under-optimum salinity FACF, the generated oil bank showed a highly dispersed behaviour.*

---

The content of this chapter is based on the following publication:

Janssen, M.T.G., Pilus, R.M., and Zitha, P.L.J. 2019. A Comparative Study of Gas Flooding and Foam-Assisted Chemical Flooding in Bentheimer Sandstones. *Transport in Porous Media*. DOI: 10.1007/s11242-018-01225-3.

## 4.1 Introduction

After obtaining a clear picture regarding the effect of the drive foam quality on oil bank propagation in a *FACF* process (**Chapter 3**), we now investigate the effect of surfactant slug salinity on oil mobilization and displacement processes in *FACF*, applied at the same model-like conditions. This section continues with a short synopsis of the theory.

In **Equation 1.1** we introduced  $E_V$  and  $E_D$ , both of which are essential parameters for any *EOR* process. The novel *EOR* method of *FACF* combines the injection of a surfactant slug (for promoting  $E_D$ ) with foam generation for drive mobility control, thus enhancing  $E_V$  (**Section 1.5**). For a fixed surfactant concentration, the magnitude of *o/w IFT* lowering (thus the increment in  $E_D$ ), through the injection of the surfactant slug, depends on various parameters of which the aqueous phase salinity is likely to be the most important (**Section 1.4**).

Variants of the *FACF* process were investigated by others in literature (Srivastava *et al.*, 2009; Szlendak *et al.*, 2013; Tang *et al.*, 2014; Jong *et al.*, 2016) but they did not provide clues about oil mobilization and displacement mechanisms. Recently, we have investigated the *FACF* process based upon the injection of an *AS* slug for oil mobilization followed by co-injection of gas and *AS* drive solution for foam generation (i.e. mobility control), at varying drive foam qualities (**Chapter 3**). This study is a detailed extension of **Chapter 3**. It focuses on a) the impact of surfactant slug salinity on oil bank formation, and b) the ability of generated foam to displace the mobilized oil bank at varying salinity. The study includes drive foam stability tests in bulk, *AS* slug phase behaviour tests, and a series of CT-scanned *FACF* core-flood experiments conducted in Bentheimer sandstones. *FACF* core-floods were performed both at under-optimum and at (near-)optimum salinity conditions to investigate its effect on oil bank formation and displacement by foam.

## 4.2 Materials and methods

### 4.2.1 Chemicals

**Table 4.1** presents the physical properties of the chemicals used in this study. The oil used to conduct the core-floods was *n*-hexadecane. A fat-soluble dye (Oil Red O) was added to the oleic phase for ease of visual inspection. The oleic phase was doped with 1-iododecane for enhancement of the CT contrast between the oleic and aqueous phases. Brine was prepared by dissolving sodium chloride in demineralized water. Demineralized water was produced by using an ELGA PURELAB Prima120 water treatment device. It purifies water by using several stages of membrane filtration, to remove most of the mineral and salt ions present, until a water conductivity of 1.0  $\mu\text{S}/\text{cm}$  or lower is reached. The *AS* slug solution was prepared by adding the required amounts of an Internal Olefin Sulfonate (IOS2024) surfactant, a co-solvent (sec-butanol), and an alkaline (sodium carbonate) to brine. The *CMC* of IOS2024, in the presence of the designed *AS* slug formulation, equalled approximately  $3.0 \times 10^{-3}$  wt% AM IOS2024. The alkali was added to the *AS* slug solely for minimizing surfactant adsorption. The co-solvent was used as a precautionary measure to guarantee stable *AS* slug solution, even though it is not strictly required when working with IOS2024 below 60°C (Hirasaki *et al.*, 2011). The defined *AS* drive formulation is similar to the *AS* slug composition without the addition of the co-solvent.  $\text{N}_2$  was used for co-injection with *AS* drive solution for drive foam generation. All liquid solutions were degassed under vacuum prior to injection.

### 4.2.2 Core samples

Bentheimer sandstones were used in this study as a model reservoir. The sandstones have high permeabilities ( $2.6 \pm 1.2$  Darcy) and a fairly homogeneous mineralogy ( $> 91$  wt% quartz) (Peksa *et al.*, 2015). More information regarding the preparation of the sandstone cores is given in **Sections 2.2.2** and **3.2.2**. **Table 4.2** gives an overview of the physical properties of the Bentheimer sandstone cores used in this work. Porosities reported were determined from CT scan data (**Appendix A**). The sandstone cores, having a length of roughly 1 m, were placed horizontally on the couch of the CT scanner. This core length proved to be sufficient for reducing the capillary entry/end effects and, more significantly, for accurate assessment of the oil bank formation and its displacement by foam in a FACF process.

**Table 4.1:** Physical properties of the chemicals used in this study.

Chemical	Formula	Molecular weight (g/mol)	Density (g/cm <sup>3</sup> ) <sup>a</sup>	Viscosity (mPa·s) <sup>a</sup>	Supplier	Purity (%)
<i>n</i> -hexadecane	CH <sub>3</sub> (CH <sub>2</sub> ) <sub>14</sub> CH <sub>3</sub>	226.45	0.775 ± 0.001	3.365±0.055	Merck	≥99
Oil Red O	C <sub>26</sub> H <sub>24</sub> N <sub>4</sub> O	408.49	-	-	Sigma-Aldrich	≥75
Sodium chloride <sup>b</sup>	NaCl	58.44	2.160 ± 0.001	-	Merck	≥99
Sodium carbonate <sup>b</sup>	Na <sub>2</sub> CO <sub>3</sub>	105.99	2.540 ± 0.001	-	Sigma-Aldrich	≥99
Sec-butanol	C <sub>4</sub> H <sub>10</sub> O	74.12	0.806 ± 0.001	-	Merck	≥99
1-iododecane	CH <sub>3</sub> (CH <sub>2</sub> ) <sub>9</sub> I	268.18	1.257 ± 0.001	-	Sigma-Aldrich	≥98
IOS2024	-	-	0.996 ± 0.001	-	Shell Global	19
Nitrogen <sup>b</sup>	N <sub>2</sub>	28.01	1.165 ± 0.001×10 <sup>-3</sup>	1.760 ± 0.500×10 <sup>-2</sup>	-	100

<sup>a</sup>All densities and viscosities mentioned are at 20°C and atmospheric pressure.

<sup>b</sup>Lide (2012).

**Table 4.2:** Properties of Bentheimer sandstone cores used in this study.

	Experiment	
	1	2
Porosity (%)	24.00 ± 0.40	24.00 ± 0.40
Permeability (Darcy)	3.20 ± 0.11	3.45 ± 0.15
Length (cm)	96.20 ± 0.10	97.10 ± 0.10
Diameter (cm)	3.80 ± 0.10	3.80 ± 0.10
Pore volume (cm <sup>3</sup> )	261.84 ± 18.85	264.29 ± 18.16

### 4.2.3 Experimental set-up

The same experimental set-up discussed earlier (**Section 3.2.3**) was used in this study to conduct the core-flood experiments, where we placed the sandstone cores in a specially designed core-holder made of polyether ether ketone (PEEK) characterized by low X-ray attenuation and high mechanical strength. During the course of the experiments, the sandstone cores were continuously exposed to a confining pressure equal to the inlet pressure. **Section 3.2.3** and **Figure 3.1** present more information regarding the experimental set-up used in this study.

### 4.2.4 CT scan

The CT scan settings applied are discussed in more detail in **Section 3.2.4** and the mathematical formulas used for CT processing can be found in **Appendix A**. The maximum percentage errors in obtained oil saturations ( $\frac{\delta S_o \times 100}{S_o}$ ) and porosities ( $\frac{\delta \phi \times 100}{\phi}$ ), using 140 kV data, equalled approximately 3.6 and 1.2%, respectively, assuming absolute errors in Hounsfield units (HU) measurements of  $\pm 2$  HU at all times (Castanier, 1988). The maximum percentage error in derived oil saturations for three-

phase conditions equalled roughly 6.9%. Note that in following parts of this study the errors shown corresponding to parameters obtained by CT data processing are related to standard deviations of the respective dataset and not to the error in CT measurements itself. The data was analysed and visualised using ImageJ software.

## 4.2.5 Experimental procedure

### 4.2.5.1 Phase behaviour and IFT measurements

The procedure for conducting phase behaviour tests and *o/w* IFT measurements was explained in detail in **Section 3.2.5.1**.

### 4.2.5.2 Bulk foam stability

Bulk foam experiments were conducted using the Foam Scan apparatus (I.T. Concept-TECLIS) to investigate foam stability of various AS drive formulations. The effect of surfactant concentration and salinity on foam stability in bulk were examined. Fixed volumes of surfactant solution ( $33.5 \pm 0.5 \text{ cm}^3$ ) were placed in the sample holder after which  $\text{N}_2$  was injected through the solution (at  $20 \text{ cm}^3/\text{min}$ ) until the foam column reached a volume of  $110 \pm 1 \text{ cm}^3$ . Subsequently,  $\text{N}_2$  injection was shut-off and the foam volume was monitored as function of time. The experiments were done at room temperature ( $21 \pm 1 \text{ }^\circ\text{C}$ ), atmospheric pressure, and in the absence of oil.

### 4.2.5.3 Core-flood experiments

An overview of the core-flood experiments conducted in this study is presented in **Table 4.3**. In the two *FACF* core-floods, first approximately 0.46 PV AS slug was injected at  $S_{or\_WF}$  prior to co-injection of AS drive with  $\text{N}_2$  for drive mobility control (identical to the core-flood procedure described in **Section 3.2.5.2**). The drive foam quality (i.e. gas fractional flow) was kept constant at 57%, as this quality proved to be able to generate stable drive foam in the presence of  $S_{or}$  (**Chapter 3**). Gas and liquid flow rates were adjusted to maintain a mid-core foam quality of 57%. AS slug injection in Exp. 1 and 2 was done at under-optimum and (near-)optimum salinity conditions, respectively. The experiments continued until no more measureable amounts of oil were produced. See **Section 3.2.5.2** and **Table 3.3** for more details regarding the core-flood procedure used in this study.

**Table 4.3:** Overview of core-flood experiments conducted. *FACF* was applied at residual oil to waterflood.

Exp.	Gas flow rate ( $\text{cm}^3/\text{min}$ )	Liquid flow rate ( $\text{cm}^3/\text{min}$ )	AS slug formulation (wt%)	AS drive formulation (wt%)	Drive foam quality (%)	Back-pressure (bar)	CT
1	0.627	0.473	NaCl (0.4) Na <sub>2</sub> CO <sub>3</sub> (1.0) sec-butanol (0.5) IOS2024 (0.3)	NaCl (0.4) Na <sub>2</sub> CO <sub>3</sub> (1.0) IOS2024 (0.3)	57	20	Yes – Oil with 25 wt% dopant
2	0.627	0.473	NaCl (2.0) Na <sub>2</sub> CO <sub>3</sub> (1.0) sec-butanol (0.5) IOS2024 (0.3)	NaCl (2.0) Na <sub>2</sub> CO <sub>3</sub> (1.0) IOS2024 (0.3)	57	20	Yes – Oil with 20 wt% dopant

**Table 4.4** presents the physical properties of the various types of brine, oil, AS slug, and AS drive solutions used in this study. In Exp. 1, water flooding was first done with 4.0 wt% NaCl brine. Afterwards, water salinity was reduced by extensively flooding the core with 2.0 wt% NaCl brine as a brine-slug salinity gradient was being avoided and the total ionic strength of the AS slug corresponded to 2.0 wt% NaCl dissolved in demineralized water. In Exp. 2, 3.6 wt% NaCl brine, total

ionic strength equivalent to the AS slug formulation used, was injected immediately. This procedure ensured the absence of a brine-slug-drive salinity gradient.

**Table 4.4:** Physical properties of the types of brine, oil, AS slug, and AS drive solutions used.

	Experiment	
	1	2
Brine type	4.0 wt% NaCl 2.0 wt% NaCl	3.6 wt% NaCl
Brine density (g/cm <sup>3</sup> ) <sup>a</sup>	1.027 ± 0.001 (4.0 wt%) 1.013 ± 0.001 (2.0 wt%)	1.024 ± 0.001
Brine viscosity (mPa*s) <sup>a</sup>	1.07 ± 0.05 (4.0 wt%) 1.03 ± 0.05 (2.0 wt%)	1.06 ± 0.06
Oil type	<i>n</i> -hexadecane <0.006 wt% Oil Red O 25.0 wt% 1-iododecane	<i>n</i> -hexadecane <0.006 wt% Oil Red O 20.0 wt% 1-iododecane
Oil density (g/cm <sup>3</sup> ) <sup>a</sup>	0.867 ± 0.001	0.841 ± 0.001
Oil viscosity (mPa*s) <sup>a</sup>	3.38 ± 0.03	3.31 ± 0.03
AS slug density (g/cm <sup>3</sup> ) <sup>a</sup>	1.013 ± 0.001	1.023 ± 0.001
AS slug viscosity (mPa*s) <sup>a</sup>	1.07 ± 0.06	1.15 ± 0.05
AS drive density (g/cm <sup>3</sup> ) <sup>a</sup>	1.012 ± 0.001	1.023 ± 0.001
AS drive viscosity (mPa*s) <sup>a</sup>	1.04 ± 0.05	1.10 ± 0.06

<sup>a</sup>All densities and viscosities mentioned are at 20°C and atmospheric pressure.

#### 4.2.5.4 CT data post-processing

The amount of dopant added to the oleic phase was reduced from 25 (Exp. 1) to 20 wt% (Exp. 2) 1-iododecane, because 25 wt% 1-iododecane resulted in CT responses of oil in bulk ( $CT_{oil,2}$  in **Equations A.7** and **A.8** in **Appendix A**) that exceeded the default CT scale (-1,024 HU to 3,072 HU). Consequently, for Exp. 1, the extended and, hence, less accurate CT scale (-10,000 HU to 30,000 HU) was used for determining  $CT_{oil,2}$ . In two-phase flow conditions, CT scan images were taken using one single energy beam of 140 kV, whilst for defining three-phase saturation distributions, scans were taken using simultaneously 140 and 80 kV energy beams (**Appendix A**).

### 4.3 Results and discussion

#### 4.3.1 Phase behaviour and IFT measurements

**Figure 4.1** presents the measured *o/w* IFTs of the nine *n*-hexadecane-AS slug combinations examined. It can be concluded that the surfactant concentration used in the AS slug (0.3 wt% AM IOS2024) was able to lower the *o/w* IFT with a factor of circa 130 and 540 for 0.4 and 2.0 wt% NaCl samples, respectively. The *FACF* core-flood experiments performed in this study were done at under-optimum salinity conditions, *o/w* IFT of  $1.9 \pm 0.2 \times 10^{-1}$  mN/m (0.4 wt% NaCl in **Figure 4.1**), and at assumed (near-)optimum salinity conditions, *o/w* IFT of  $4.8 \pm 1.0 \times 10^{-2}$  mN/m (2.0 wt% NaCl in **Figure 4.1**). More detailed information regarding the results of the phase behaviour scan can be found in **Section 3.3.1**.

#### 4.3.2 Bulk foam stability

Bulk foam experiments were performed in the absence of oil to assess foaming capacity and foam stability in bulk for various AS drive solutions. Both salinity and surfactant concentration were varied. Results are shown in **Figure 4.2**. It is found that increasing salinity had hardly any effect on foaming capacity, but reduced foam stability. Higher salt concentrations reduce the effective range of repulsive forces (i.e. Debye length), leading to earlier foam decay compared to lower salinities (Klitzing *et al.*, 1999). The increase in surfactant concentration showed no significant effect on foaming capacity and foam longevity. Recall that both surfactant concentrations assessed (0.3 and

0.6 wt% AM IOS2024) are well above its  $CMC$  ( $3.0 \times 10^{-3}$  wt% AM IOS2024). This implies that the surfactant adsorption density at the  $g/w$  interfaces barely changed upon varying surfactant concentration.

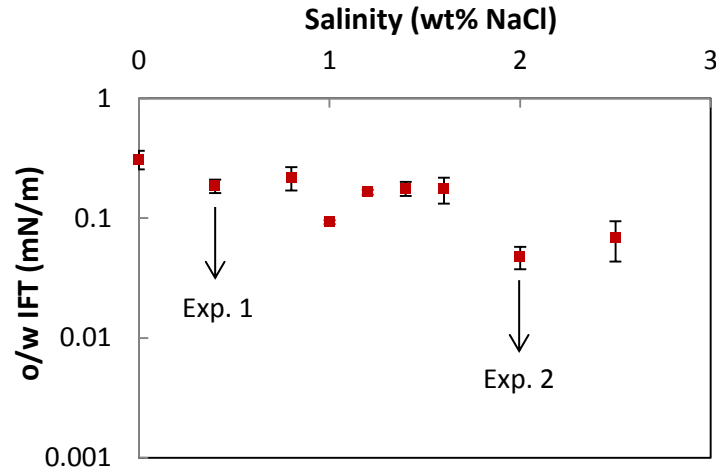


**Figure 4.1:** IFT measurements conducted with the spinning drop tensiometer of the systems prepared: X wt% NaCl, 1 wt%  $Na_2CO_3$ , 0.5 wt% sec-butanol, and 0.3 wt% AM IOS2024 with *n*-hexadecane. The error bars correspond to the standard deviation of the specific dataset.

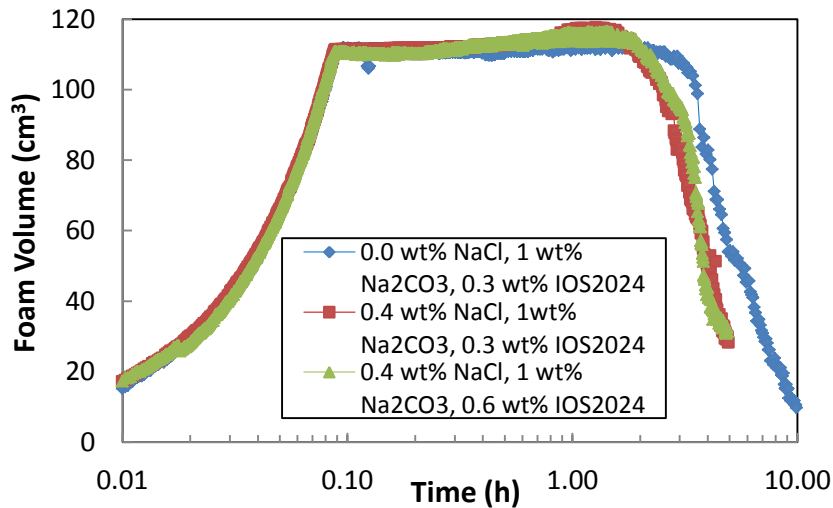


**Figure 4.2:** Development of foam volumes in bulk at different salinities and surfactant concentrations at ambient temperature and atmospheric pressure. A foam half decay time ( $t_{1/2}$ ) of 4.93 h was seen for the 0.0 wt% NaCl solution whilst both surfactant concentrations, in the presence of 0.4 wt% NaCl, showed half decay times of 3.70 h.

### 4.3.3 Core-flood experiments

A summary of the performed core-floods is presented in **Table 4.5**. The results of the preparatory part consisting of primary drainage (oil injection) and forced imbibition (water flooding) for Exp. 1 are described in detail in **Section 3.3.2.1** and are representative for Exp. 2 as well. **Table 4.6** gives an overview of the oil and water breakthrough times during primary drainage and water flooding for Exp. 1 and 2. This section continues with the following subsections: mobilization of residual oil and displacement of mobilized oil by foam. Oil recovery factors, pressure drop profiles, and  $S_o$  and  $S_g$  profiles as function of core length are analysed to investigate the effect of surfactant slug salinity on oil mobilization and displacement in a *FACF* process.

**Table 4.5:** Summary of core-floods conducted.  $k_{ro}^0$ ,  $k_{rw}^0$ ,  $S_{wc}$ ,  $S_{oi}$ ,  $S_{or\_WF}$ ,  $S_{or\_CEOR}$ ,  $R_{FWF}$ ,  $R_{FCEOR}$ , and  $OIIP$  represent the oil end-point relative permeability, water end-point relative permeability, connate water saturation, initial oil saturation, residual oil saturation to waterflood, residual oil saturation to *FACF*, recovery factor corresponding to water flooding, recovery factor corresponding to *FACF*, and the oil initially in place, respectively. Saturations and recovery factors shown are based on CT data processing.

Exp.	$k_{ro}^0$	$k_{rw}^0$	$S_{wc}$	$S_{oi}$	$S_{or\_WF}$	$R_{FWF}$ (% of <i>OIIP</i> )	$S_{or\_CEOR}$	$R_{FCEOR}$ (% of <i>OIIP</i> )
1	0.51 ± 0.02	0.13 ± 0.01	0.22 ± 0.04	0.78 ± 0.04	0.41 ± 0.02	47 ± 6	0.31 ± 0.03	60 ± 5
2	0.66 ± 0.09	0.15 ± 0.01	0.17 ± 0.05	0.83 ± 0.05	0.41 ± 0.02	51 ± 7	0.21 ± 0.06	74 ± 8

**Table 4.6:** Overview of oil and water breakthrough times during primary drainage (PD) and water flooding (WF). The end-point mobility ratios ( $M^0$ ) were calculated using  $M^0 = (k_{rw}^0/\mu_w)/(k_{ro}^0/\mu_o)$  where  $\mu_w$  and  $\mu_o$  represent the brine and oil viscosity, respectively.

Exp.	Oil BT (PD)	Water BT (WF)	$M^0$
1	0.75 ± 0.02 PV	0.37 ± 0.02 PV	0.84 ± 0.16
2	0.76 ± 0.02 PV	0.41 ± 0.02 PV	0.71 ± 0.23

#### 4.3.3.1 Mobilization of residual oil

In Exp. 1 and 2 an AS slug, at respectively under-optimum and (near-)optimum salinity conditions (**Figure 4.1**), was injected into the previously water-flooded cores to attempt the mobilization of  $S_{or\_WF}$ . This subsection presents related pressure drop and  $S_o$  profiles obtained during the injection of the surfactant slug in Exp. 1 and 2.

##### 4.3.3.1.1 Pressure drop

**Figure 4.3** presents the resulting pressure drop profiles obtained during slug injection in Exp. 1 and 2. As soon as the AS slug contacted the core in Exp. 1, the pressure drop increased sharply from 59 ± 7 to 83 ± 7 mbar at 0.07 ± 0.02 PV injected. Thereafter, pressure drops continued to increase, reaching 97 ± 7 mbar at the end of slug injection. The observed increase in pressure drop is due to the formation and propagation of the oil bank (**Section 3.3.2.2.1**). The slope of the pressure drop vs. PV injected decreased over time due to modifications of the oil bank shape. The pressure drop profile corresponding to Exp. 2 shows initially the same trend as Exp. 1: an increase from 59 ± 7 to 73 ± 7 mbar at 0.09 ± 0.02 PV injected. However, afterwards, pressure drops slightly reduced during slug injection in Exp. 2.

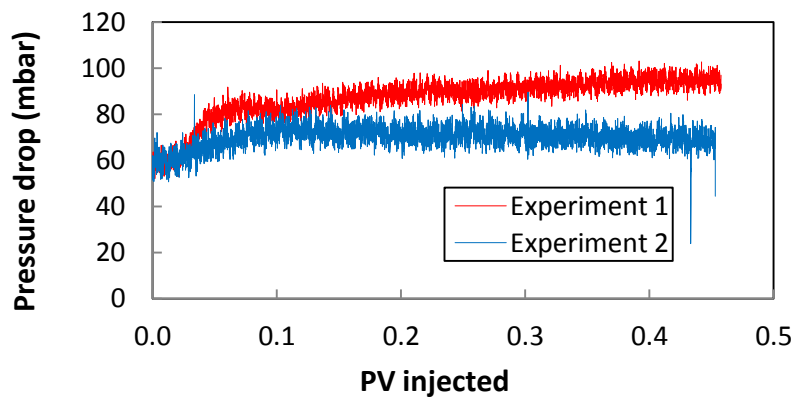


**Figure 4.3:** Total pressure drop profiles as function of PV injected during AS slug injection in Exp. 1 and 2. A total of 0.46 ± 0.02 PV AS slug was injected at 0.15 cm<sup>3</sup>/min (0.62 ft/day).

4.3.3.1.2 CT images and oil saturation profiles

The CT images and  $S_o$  profiles for Exp. 1 and 2 are presented in **Figure 4.4**. It is evident that a sharp oil bank, with peak  $S_o$  of  $0.64 \pm 0.02$  and  $0.69 \pm 0.02$  for Exp. 1 and 2, respectively, was formed after 0.06 PV (Exp. 1) and 0.07 PV (Exp. 2) injected. For further analysis, first Exp. 1 will be discussed. As injection continued, the oil bank became more dispersed as indicated by the gradual reduction of  $S_o$  on the leading edge (i.e. downstream side). Yet, peak  $S_o$  remained fairly constant around  $0.67 \pm 0.02$ ; suggesting average  $S_w$  slightly higher than  $S_{wc}$  within this part of the oil bank (**Table 4.5**). Due to an expected non-optimal sweep efficiency (i.e. unfavourable AS slug-oil mobility ratio; **Equation 1.2**), the upstream area of the core was not perfectly swept and various oil remnants can be seen. Finally, after 0.46 PV AS slug injection, an averaged  $S_o$  of  $0.33 \pm 0.04$  was observed upstream of the oil bank. The leading edge propagated with a velocity slightly higher than the trailing edge, i.e. upstream side, ( $128 \pm 5$  cm/PV vs.  $92 \pm 5$  cm/PV); implying a continuously growing oil bank.

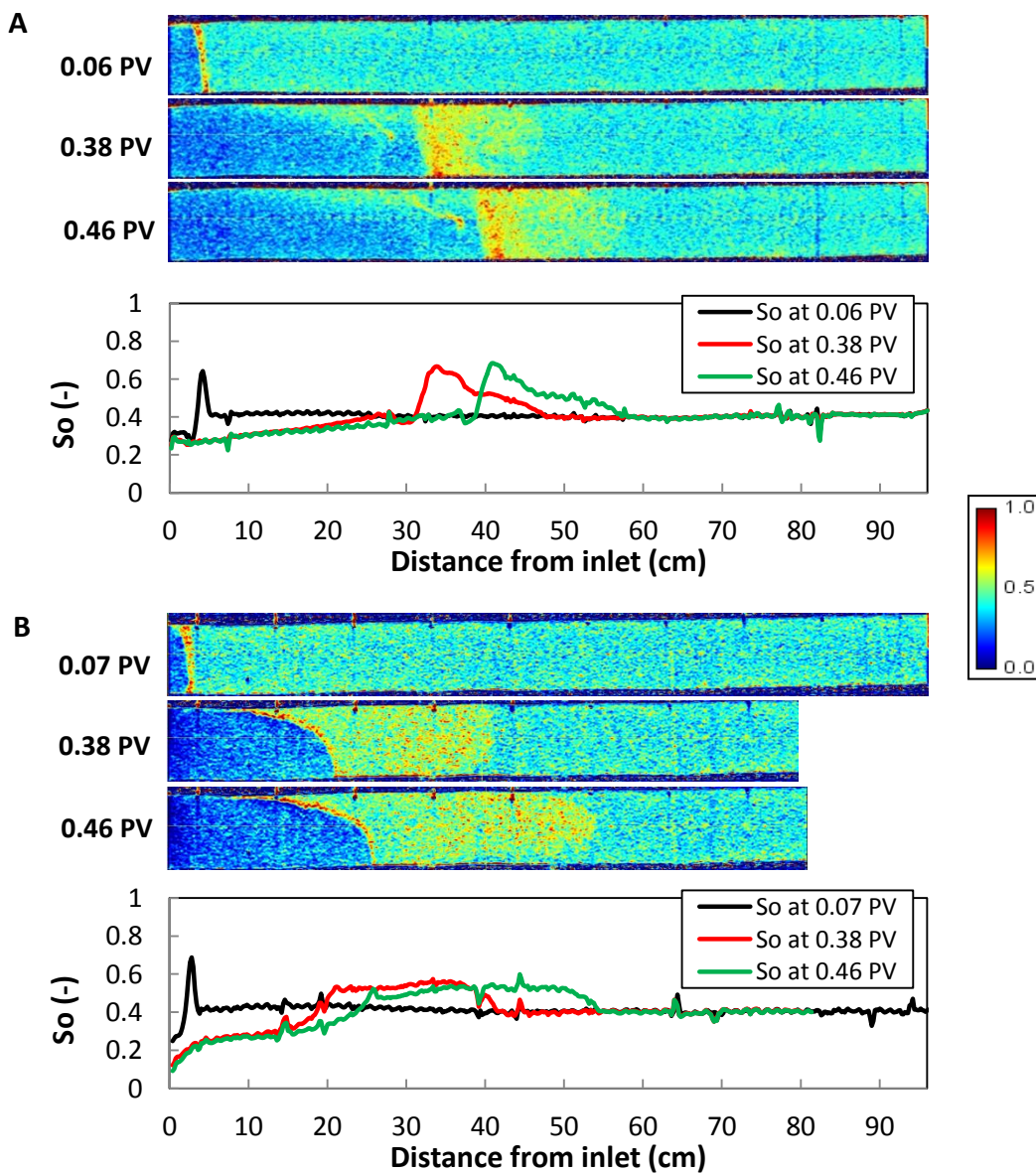


**Figure 4.4:** Oil saturation CT scan images and corresponding saturation profiles during AS slug injection for Exp. 1 (A) and 2 (B). Note that the last two scans taken during Exp. 2 do not include the full outlet section as  $S_o$  was not altered there ( $S_o = S_{o_{wf}}$ ). The images shown have X:Y ratios of 3:1. Red refers to oil and blue indicates water.

The oil bank formation in Exp. 2 reflects the fact that the AS slug operated at (near-)optimum salinity conditions. The oil bank is characterized by a more uniform  $S_o$  distribution. Due to a roughly four times lower  $o/w$  IFT compared to Exp. 1 (**Section 4.3.1**), mobilization of  $S_{or\_WF}$  improved, hence increasing the amount of oil that was available for oil coalescence. Most likely this caused a greatly diminished dispersion effect on the leading edge as well as a more extended oil bank (compared to Exp. 1). Furthermore, lower values for peak  $S_o$  were seen ( $0.60 \pm 0.02$ ). The latter might be a result of reduced capillary forces, that kept the oil trapped, when flooding at (near-)optimum slug salinity compared to under-optimum salinity conditions. Decreased capillary forces yield lower amounts of residual oil, reducing that part of peak  $S_o$  that is immobile. At the end of AS slug injection, the averaged  $S_o$  upstream of the oil bank equalled  $0.10 \pm 0.02$ . Lower estimated propagation velocities were found for the leading edge ( $93 \pm 5$  cm/PV) and the trailing edge ( $61 \pm 5$  cm/PV) compared to Exp. 1, suggesting an increase in the oil bank's expansion rate. It is evident from the CT scans shown in **Figure 4.4** that oil coalescence was substantial at the leading edge. It remains inconclusive how the  $o/w$  IFT reduction affects the coalescence of oil. Previous studies suggested that the rate of oil coalescence appears to be a function of interfacial viscosity rather than IFT; with lower interfacial viscosities promoting oil coalescence (Wasan *et al.*, 1978; Fayers, 1981; Aderangi and Wasam, 1995).

The relationship between the shape of the oil bank and related pressure drop was studied for a test case and is presented in **Appendix B**. The biggest contribution to the pressure drop came most likely from the relatively high  $S_o$  within the oil bank. At those locations, pressure drop significantly increased due to a substantial lowering of the water mobility ( $\lambda_w = \frac{k_{rw}k}{\mu_w}$ ). It is, most probably, for this reason that Exp. 1 revealed higher pressure drop values over the course of AS slug injection than Exp. 2 (**Figure 4.3**). The initial, relatively sharp, increasing trend in pressure drop during both Exp. 1 and 2 reflects the formation of a sharp oil bank. Subsequently, in Exp. 1, the more gradually increasing pressure drop (**Figure 4.3**) matches the continuously expansion of the oil bank while maintaining, or slightly increasing, its peak  $S_o$ . In Exp. 2, after the initial increase, total pressure drop reduced slightly due to a combination of the reduction in peak  $S_o$  (decreasing pressure drop) and the expansion of the banked oil (increasing pressure drop).

CT images taken during both experiments reveal gravity underriding effects of the injected aqueous AS slug. This effect seems to be more strongly present in Exp. 2 compared to Exp. 1. The end-point dimensionless gravity number ( $N_g^0$ ), calculated using **Equation 4.1**, characterizes the ratio of gravitational to viscous forces. The more obvious gravity underriding effect in Exp. 2 ( $N_g^0$  of 0.56) compared to Exp. 1 ( $N_g^0$  of 0.31) is mainly a result of the effective density difference at the trailing edge's interface. The end-point dimensionless gravity number is calculated as follows (Hagoort, 1980):

$$N_g^0 = \frac{k k_{ro}^0 \Delta \rho_{wo} g}{\mu_o u_t} \quad (4.1)$$

where  $k$ ,  $k_{ro}^0$ ,  $\Delta \rho_{wo}$ ,  $g$ ,  $\mu_o$ , and  $u_t$  represent the absolute horizontal permeability to brine, end-point relative permeability of the oil, density difference between the injected slug and the displaced oil, gravitational acceleration, viscosity of the oleic phase, and the total volumetric Darcy velocity, respectively.

### 4.3.3.2 Displacement of mobilized oil by foam

Following AS slug injection for oil mobilization, AS drive formulations (**Table 4.3**) were co-injected with  $N_2$  at a foam quality of 57% for promoting drive mobility control (**Equation 1.2**). This subsection presents related total pressure drop,  $S_o$ , and  $S_g$  profiles obtained during the co-injection in Exp. 1 and 2.

#### 4.3.3.2.1 Pressure drop

**Figure 4.5** shows corresponding total pressure drop profiles related to AS slug and drive co-injection. This subsection only focuses on the AS drive co-injection phase. Let us again first consider Exp. 1. The complete pressure drop profile is the result of a combination between displacing the oil bank and foam generation. As soon as co-injection was initiated, a steep increase in pressure drop to  $485 \pm 3$  mbar was observed, because of the increase in total flow rate. Afterwards, pressure drop slightly decreased to  $422 \pm 2$  mbar at  $0.59 \pm 0.02$  PV (PV refers to the sum of gas and liquid PV injected, i.e. total PV). The reduction in pressure drop most likely indicates a decrease of the oil bank's peak  $S_o$  (see **Appendix B** and **Section 4.3.3.1** for the effect of high  $S_o$  on pressure drop). From  $0.59 \pm 0.02$  PV onwards, the total pressure drop increased until it reached a maximum of  $1040 \pm 61$  mbar at  $0.95 \pm 0.02$  PV. Next, it slightly decreased to  $702 \pm 34$  mbar, corresponding to an averaged pressure gradient of  $1.25 \pm 0.08$  bar/m. The latter behaviour of the pressure drop is expected to be due to foam generation downstream (note the constant low pressure drop in the first 53.0 cm). Only data up to  $1.68 \pm 0.02$  PV injected is shown for Exp. 1 since afterwards, as a result of failure of the liquid pump, the applied foam quality changed (**Section 3.3.2.3.1** and **Figure 3.7**). Note that steady-state pressure conditions were already reached at  $1.68 \pm 0.02$  PV injected. Production of the oil bank started at  $0.65 \pm 0.02$  PV and foam breakthrough occurred at  $0.86 \pm 0.02$  PV ( $0.40 \pm 0.02$  PV since co-injection started).

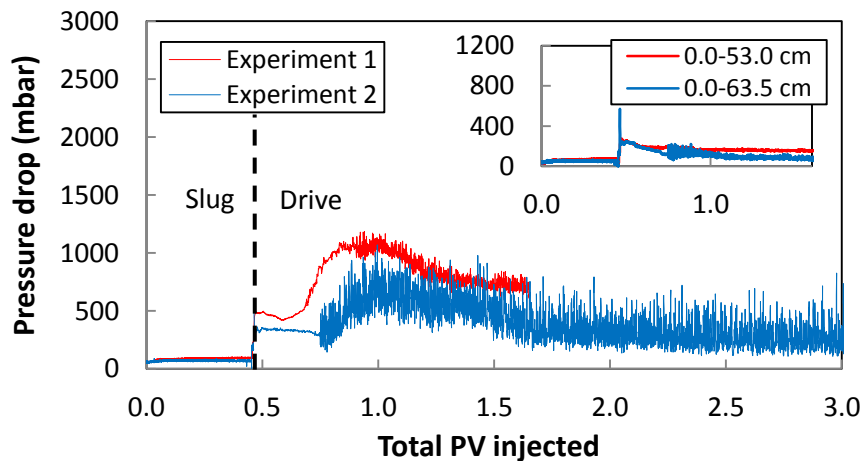


**Figure 4.5:** Total pressure drop profiles during AS slug injection and AS drive co-injection for Exp. 1 and 2. Co-injection of AS drive solution with  $N_2$  took place at a total injection rate of  $1.10 \text{ cm}^3/\text{min}$  ( $4.58 \text{ ft}/\text{day}$ ). The upper right graph presents the pressure drop over, respectively, the first 53.0 cm (Exp. 1) and 63.5 cm (Exp. 2).

During AS drive and  $N_2$  co-injection in Exp. 2, again a steep increase in pressure drop was observed due to the change in total flow rate. The sharp increase yields lower pressure drop values compared to Exp. 1, mainly due to the difference in saturation distribution. The oil bank formed in Exp. 2 exhibits a more uniform  $S_o$  distribution compared to Exp. 1, with relatively low peak  $S_o$  (**Figure 4.4**). The reduction in peak  $S_o$  (when compared to Exp. 1) most probably implies a substantial increase in water mobility, whereas oil mobility reduced slightly, resulting in a reduced pressure drop.

Subsequent to the sharp increase, a slight reduction in pressure drop to  $297 \pm 9$  mbar at  $0.74 \pm 0.02$  PV was observed. Afterwards, the pressure drop increased before starting to decline again to reach a steady-state value of  $303 \pm 103$  mbar; averaged pressure gradient of  $0.66 \pm 0.31$  bar/m. Similar to the previously discussed Exp. 1, this behaviour in pressure drop (i.e. increasing pressure drop followed by a slight decrease) is believed to be related to weak foam generation downstream, as low pressure drops were observed in the first 63.5 cm (**Figure 4.5**). Oil bank breakthrough occurred at  $0.71 \pm 0.02$  PV, causing the total pressure drop to fluctuate. Foam breakthrough was observed at  $0.90 \pm 0.02$  PV ( $0.44 \pm 0.02$  PV since co-injection started).

#### 4.3.3.2.2 CT images and oil saturation profiles

**Figure 4.6** presents CT images and  $S_o$  profiles related to the foam drive in Exp. 1 and 2. First the images and profiles related to Exp. 1 will be considered. As soon as co-injection started, the shape of the oil bank changed. Peak oil saturations were reduced, leading to a more uniform oil bank. Its breakthrough occurred after  $0.19 \pm 0.02$  PV of co-injection. After 1.08 PV injected, the complete oil bank was produced, yielding a  $S_{or,CEOR}$  of  $0.31 \pm 0.03$  (**Table 4.5**). It is clear from the CT images that mainly the downstream area of the core was properly swept.

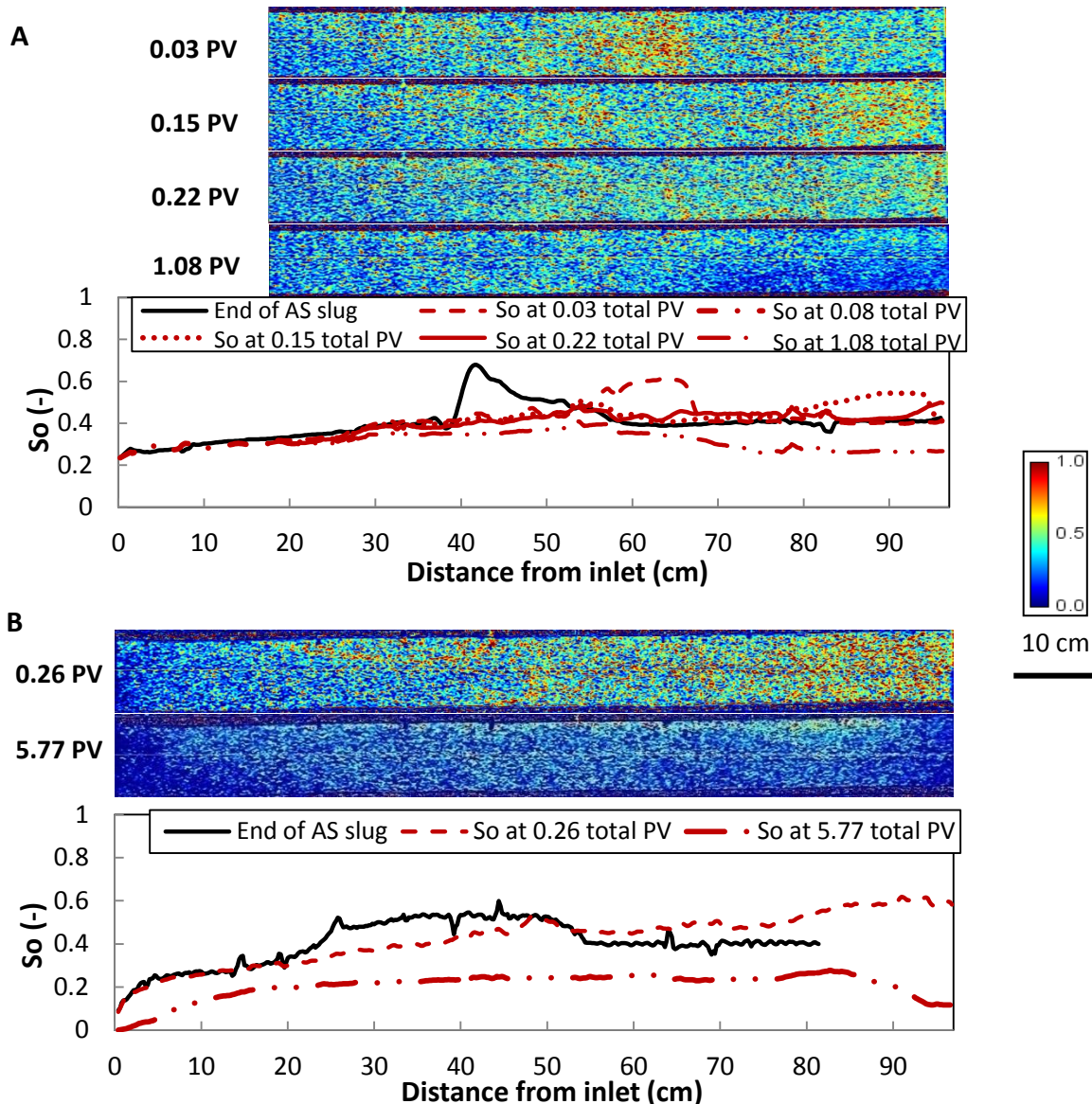


**Figure 4.6:** Oil saturation CT scan images and corresponding saturation profiles during foam drive co-injection for Exp. 1 (A) and 2 (B). PV = 0 corresponds to the start of the co-injection. Note that in Exp. 1 only the last 79 cm of the core could be scanned due to CT limitations; a separate scan of the inlet was taken at 0.08 PV. The presented profiles were constructed by applying a moving average function with an interval of 6 to the processed data.

The CT scan taken after 0.26 PV injected during Exp. 2 shows the situation just after oil bank breakthrough (occurred after  $0.25 \pm 0.02$  PV co-injection). The delayed oil bank breakthrough at (near-)optimum salinity compared to under-optimum salinity is expected to be controlled by a difference in accessible pore volume. Since at (near-)optimum salinity more residual oil was mobilized, and thus available for oil coalescence, consequently more pores were accessible for the oil bank to propagate through. Finally, after 5.77 PV of injection, no more oil was produced and a  $S_{or\_CEOR}$  of  $0.21 \pm 0.06$  was reached (**Table 4.5**). In contrast to *FACF* at under-optimum salinity conditions, here the entire core was equally swept.

#### 4.3.3.2.3 Gas saturation profiles

**Figure 4.7** shows the  $S_g$  profiles during co-injection of AS drive solution and  $N_2$  to form a foam drive for both Exp. 1 and 2. The constructed profiles for Exp. 1 show a clear trend where  $S_g$  remained rather low until a distance of  $50 \pm 1$  cm. From that point onwards,  $S_g$  increased, which is a qualitative indicator of foam generation (i.e. gas phase starts to divide equally across the rock's cross-sectional area; note the cross-sections shown in **Figure 4.7A**). The foam front propagated with an average velocity of  $144 \pm 10$  cm/PV and its breakthrough was observed at  $0.40 \pm 0.02$  PV. A more detailed description of the  $S_g$  profile in Exp. 1 is given in **Section 3.3.2.3.3** and **Figure 3.10A**.

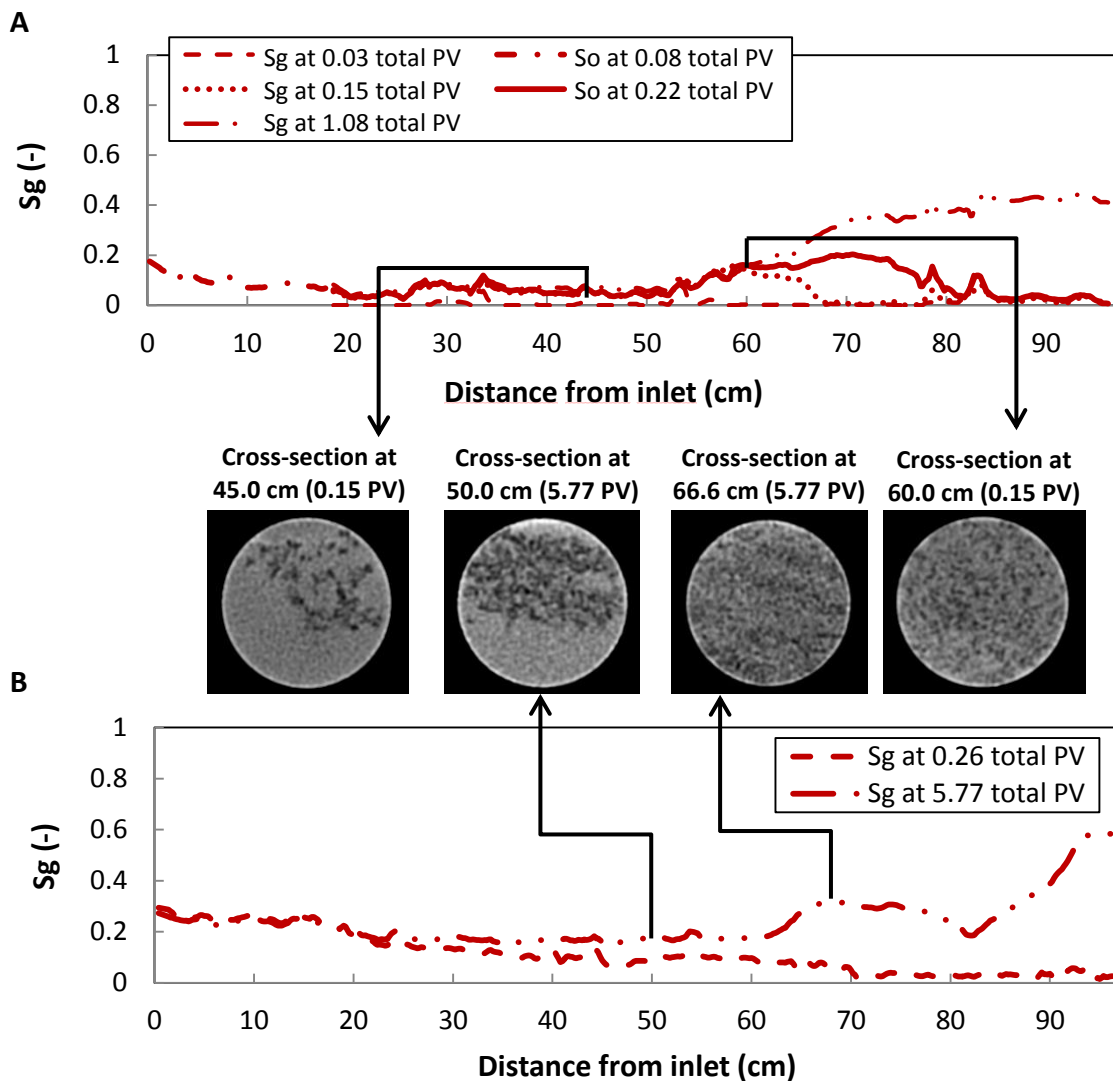


**Figure 4.7:** Gas saturation profiles during foam drive co-injection in Exp. 1 (A) and 2 (B). Note that in Exp. 1 only the last 79 cm of the core could be scanned due to CT limitations; a separate scan of the inlet was taken at 0.08 PV. The presented profiles were constructed by applying a moving average function with an interval of 6 to the processed data. The cross-sectional areas shown represent the original CT data in Hounsfield units where the gas phase is represented in black.

The  $S_g$  profiles corresponding to Exp. 2 reveal the same general trend: fairly low saturations before reaching a distance of  $62 \pm 1$  cm, where  $S_g$  started to increase. Again, similar to Exp. 1, as depicted by the two cross-sectional areas shown in **Figure 4.7B**, gas was partly overriding upstream of  $62 \pm 1$  cm, whereas a more uniform gas distribution (qualitative indicator of foam generation) was observed downstream. The averaged velocity of the foam front equalled  $156 \pm 5$  cm/PV and its breakthrough occurred at  $0.44 \pm 0.02$  PV. It remains unclear why gas seems to accumulate near the core outlet.

#### 4.3.3.3 Oil recovery

Cumulative oil recovery and oil cut plots for both *FACF* experiments are shown in **Figure 4.8**. First 0.46 PV of AS slug was injected, which did not produce any measurable amounts of oil. As aforementioned, oil bank breakthrough occurred slightly earlier in Exp. 1 compared to Exp. 2. Once breakthrough happened in Exp. 1, the oil cut increased progressively until it reached a peak value of  $30 \pm 5\%$  at  $0.78 \pm 0.02$  PV. Afterwards, it slightly reduced to zero. Clean oil production by the oil bank continued until a *ME* broke through at  $1.24 \pm 0.02$  PV. Its production lasted till  $1.41 \pm 0.02$  PV. Eventually, after  $1.63 \pm 0.02$  PV, the produced clean oil – solubilized oil ratio equalled approximately 10, and the oil recovery reached  $20 \pm 3\%$  of the *OIP* after water flooding (equivalent to a  $R_{FCEOR}$  of  $60 \pm 5$  of the *OIIP*; **Table 4.5**).

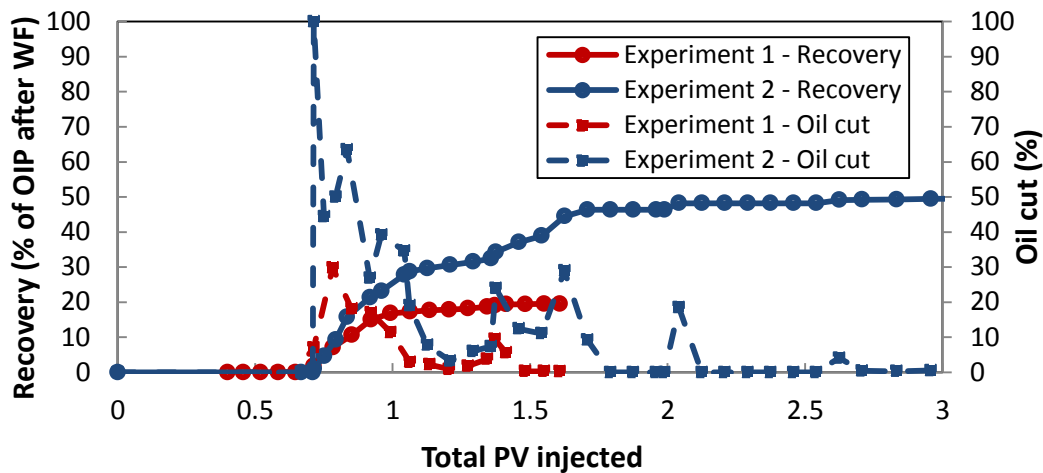


**Figure 4.8:** Oil cut and cumulative oil recovery for Exp. 1 (red) and 2 (blue). The recovery uses the oil in place after water flooding as a reference. PV = 0 corresponds with the start of AS slug injection; drive foam co-injection started at 0.46 PV. The profiles were constructed from material balance calculations.

Higher oil cuts were obtained for Exp. 2 [(near-)optimum salinity], after breakthrough of the oil bank, compared to Exp. 1 (under-optimum salinity), due to a larger volume of the continuous mobilized oil phase within the oil bank. Its profile is very similar to the one corresponding to Exp. 1: a sharp increase in oil cut followed by a more gradually decreasing trend. The latter implies diffusive behaviour of the trailing edge of the oil bank. Whereas in Exp. 1 it only took  $1.24 \pm 0.02$  PV for the oil bank to be completely produced, here clean oil production by the oil bank continued until  $2.62 \pm 0.02$  PV injected. Afterwards, very little amounts of *ME* were produced, yielding a clean oil – solubilized oil ratio of roughly 106 in the effluents. Key reason for producing significantly more clean oil than solubilized oil when flooding at (near-)optimum salinity conditions is that, due to the lower *o/w IFT*, larger quantities of mobilized oil were available for oil coalescence, and consequently, less oil was accessible for solubilisation. Finally, after  $2.96 \pm 0.02$  PV injected, an oil recovery of  $50 \pm 7\%$  of the *OIP* after water flooding was achieved;  $R_{FCEOR}$  of  $74 \pm 8$  of the *OIIP* (**Table 4.5**). In both experiments the rate of oil recovery was greatly diminished as soon as foam breakthrough occurred.

## 4.4 General discussion

Let us now examine the results presented in this chapter in the light of oil mobilization and displacement mechanisms. The evolutions of three-phase saturations during the course of *FACF*, both at under-optimum and (near-)optimum salinity, are displayed in ternary saturation diagrams. The diagrams provide a schematic way of comparison between various saturation paths, allowing us to develop mechanistic conceptual models for oil displacement. Furthermore, the results presented in study will be compared to continuous gas injection and *WAG* observations made in **Chapter 2**.

### 4.4.1 Sectional saturation paths

**Figure 4.9** presents the sectional saturation paths for the two *FACF* core-flood experiments reported in this study. Averaged three-phase saturations were calculated using acquired CT slices at, respectively, 40 and 75 cm distance from the inlet. Those specific locations were selected as they represent the area prior to and after the jump in  $S_g$  (**Figure 4.7**). Let us first consider the diagrams (40 vs. 75 cm) corresponding to under-optimum salinity *FACF* (Exp. 1). Since primary drainage and water flooding yielded uniform saturation distributions, the main difference between the two locations in space was seen during *AS* slug and *AS* drive co-injection. The oil bank formed by *AS* slug injection propagated to a distance of approximately 40 to 60 cm from the inlet (**Figure 4.4A**), yielding increased  $S_o$  at 40 cm distance while no saturation alterations were observed at a distance of 75 cm. During co-injection of *AS* drive solution and  $N_2$  (at 40 cm distance), first water displaced the oil bank, reducing  $S_o$ . Subsequently, the co-injected  $N_2$  with surfactant solution reduced  $S_w$  at a constant  $S_o$  before displacing a relatively small amount of oil in a way where  $S_w$  increased twice as fast as  $S_g$ . Most likely, the small amount of oil displaced is due to a lack of drive mobility control as foam was not generated yet (**Figure 4.7A**). At 75 cm distance from the inlet, foam was generated, hence the increase in  $S_g$ . During drive co-injection, at first  $S_o$  slightly increased due to propagation of the oil bank. Afterwards, similar to its saturation path at 40 cm distance,  $S_o$  remained constant whereas  $S_w$  diminished and  $S_g$  increased (0.22 total PV), suggesting water displacement by foam at this point. Finally, oil was produced by the foam front at a constant  $S_w$ . Eventually,  $S_{or\_CEOR}$  was lower at 75 cm distance compared to 40 cm distance from the inlet due to improved mobility control.

The sectional saturation paths constructed for Exp. 2 show similar primary drainage and water flooding behaviour as Exp. 1. *AS* slug injection resulted in an increase in  $S_o$  only at a distance of 40 cm, due to the position of the oil bank at the end of the injection phase (**Figure 4.4**). Note that  $S_o$  at the end of *AS* slug injection at 40 cm distance is lower compared to Exp. 1 because of the presence of a more uniform oil bank with lower peak  $S_o$  (**Section 4.3.3.1**). Oil was displaced by the co-injected  $N_2$  and surfactant solution at 40 cm distance (after 0.26 total PV), whereas at 75 cm distance, oil was replacing water as the oil bank propagated downstream. Afterwards, at 40 cm distance, a similar saturation path compared to Exp. 1 was seen (i.e. displacement of oil where  $S_w$  increased with a rate twice as high as  $S_g$ ). However, lower  $S_{or\_CEOR}$  was reached due to flooding at (near-)optimum salinity conditions ( $S_{or\_CEOR} = 0.22$  vs. 0.35). The diagram corresponding to a distance of 75 cm from the inlet shows similar features as the saturation path related to Exp. 1 at the same distance. Although only two data points are available here (due to the amount of CT scans taken), they suggest oil displacement by drive foam at a nearly constant  $S_w$  as well. Note that the final  $S_{or\_CEOR}$  at 75 cm distance for Exp. 2 (0.23) is very similar to the one observed for Exp. 1 (0.26).

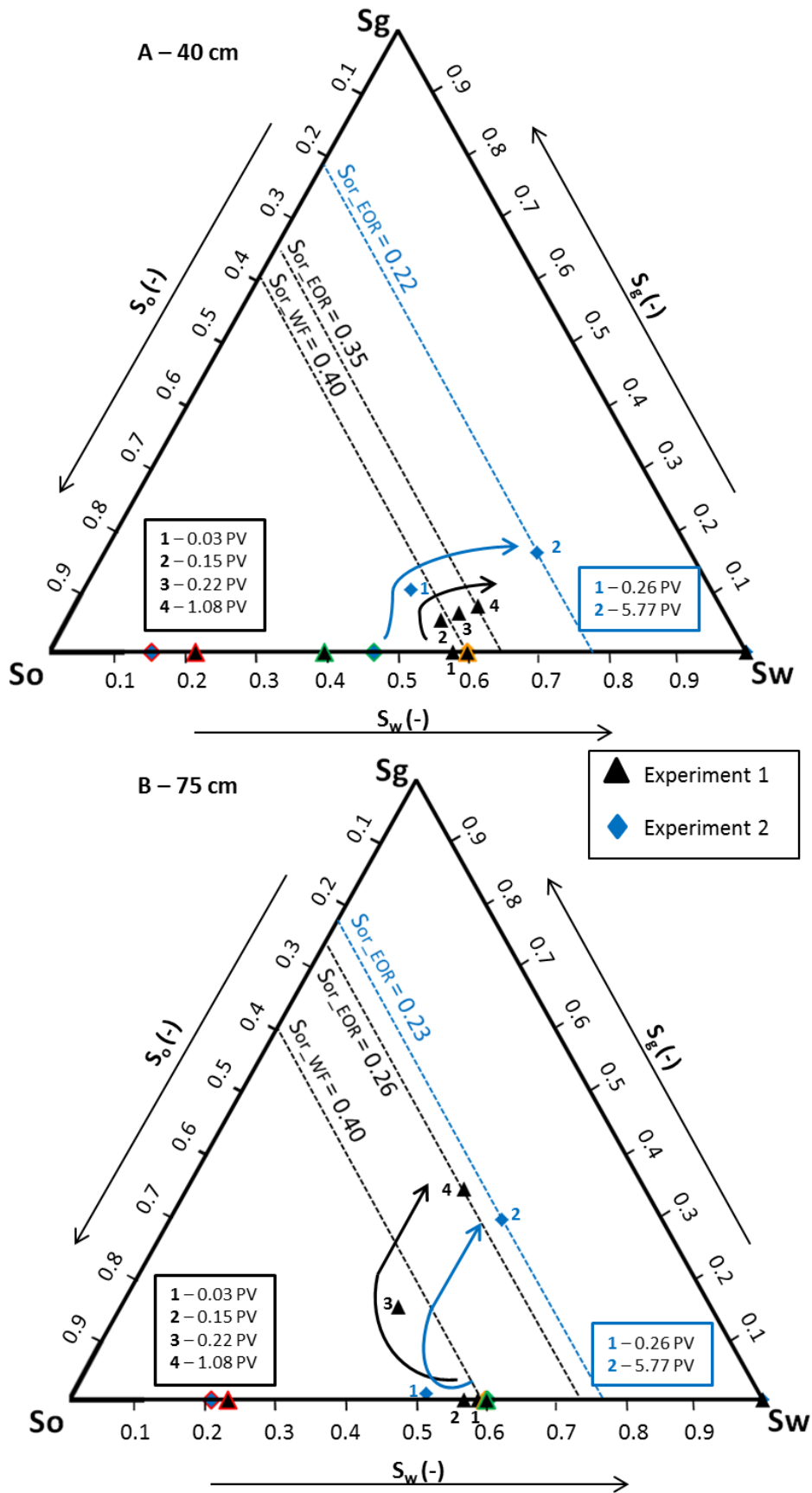


**Figure 4.9:** Sectional saturation paths constructed for Exp. 1 (black triangles) and 2 (blue diamonds) at a distance of 40 (A) and 75 cm (B) from the inlet.  $S_w$ ,  $S_o$ ,  $S_g$ ,  $S_{or\_WF}$ , and  $S_{or\_EOR}$  represent the water, oil, gas, residual oil to waterflood, and residual oil to chemical EOR saturations, respectively. Three-phase saturations shown were averaged and calculated using CT data. The data points outlined in red, orange, and green represent the initial oil saturation, residual oil to waterflood, and the condition at the end of AS slug injection, respectively. Co-injection times are shown for each experiment where PV = 0 corresponds to the initiation of co-injection.

#### 4.4.2 Gas flooding and WAG vs. FACF

Saturations paths for continuous gas injection at  $S_{oi}$  and at  $S_{or\_WF}$  (Exp. 1 and 2 in **Figure 2.9**) reveal similarities with saturation paths corresponding to oil being displaced by a stable drive foam in Exp. 1 and 2 (**Figure 4.9B**): the displacement of oil at a nearly constant  $S_w$ . However, due to the combining effect of lower  $o/w$  IFTs and more favourable mobility control, FACF was able to mobilize and displace significant more oil than continuous  $N_2$  injection. WAG showed a distinctive saturation path. It indicated that, when applying WAG for gas mobility control,  $S_{or\_WF}$  (Exp. 2 in **Figure 2.9**) and  $S_{or\_EOR}$  (Exp. 1 and 2 in **Figure 2.9**) could easily be reached after injecting the first and second WAG cycle, respectively. Although oil recoveries by WAG and under-optimum salinity FACF are very similar, FACF at (near-)optimum salinity conditions was able to enhance the oil recovery with approximately 15% of the OIIP with respect to WAG.

### 4.5 Conclusions

FACF was investigated by conducting well-controlled CT-assisted core-flood experiments using a model oil and Bentheimer sandstone cores. The core-flood experiments were done at both under-optimum and (near-)optimum salinity conditions.

We were able to clearly visualize the formation of the oil bank during surfactant slug injection at both salinities assessed. The composed AS slug formulation lowered the  $o/w$  IFT by a factor of 130 and 540 for under-optimum and (near-)optimum salinity conditions, respectively. Lowering of the  $o/w$  IFT favoured the mobilization of residual oil to waterflood, promoting the development of an oil bank. At (near-)optimum salinity, the oil bank formed was more uniform and elongated compared to the oil bank developed at under-optimum salinity conditions.

The AS drive formulation showed good foaming characteristics in bulk. Co-injection of AS drive solution and  $N_2$  in presence of  $n$ -hexadecane generated weak foams. Foam strength surged upon hitting the oil bank, leading to effective displacement of the banked oil. This is in agreement with the observations reported in **Chapter 3**.

Ultimate oil recovery at under-optimum FACF was rather similar to that for WAG ( $60 \pm 5\%$  of the OIIP). However, the ultimate recovery for FACF at (near-)optimum salinity was higher by  $15 \pm 5\%$  of the OIIP, proving the higher effectiveness of oil mobilization and displacement in a FACF process. Performing FACF at (near-)optimum salinity increased the produced clean oil – solubilized oil ratio over under-optimum flooding with roughly a factor 10.

# 5. Foam-assisted chemical flooding at reservoir conditions

---

## Abstract

*The novel enhanced oil recovery technique combining the reduction of oil-water interfacial tensions to ultra-low values and generation of a foam drive for mobility control is known as foam-assisted chemical flooding. We present a well-controlled laboratory study on the feasibility of FACF at reservoir conditions. Two specially selected chemical surfactants were screened on their stability in sea water at 90°C. The ability of both surfactants to generate stable foam in bulk was studied in presence and absence of crude oil. It led to the composition of the foam drive formulation for drive mobility control. Phase behaviour scan studies, for the two crude oil-surfactant-brine systems, yielded the design of the chemical slug capable of mobilizing residual oil by drastically lowering the oil-water interfacial tension. Core-flood experiments were performed in Bentheimer sandstones previously brought to a residual oil to waterflood of  $0.33 \pm 0.02$ . A surfactant slug at under-optimum or optimum salinity, showing oil-water interfacial tensions of  $10^{-2}$  and  $10^{-3}$  mN/m, respectively, was injected for mobilizing residual oil. It resulted in the formation of an unstable oil bank due to dominant gravitational forces at both salinities. Next, a foam drive was generated either in-situ, by co-injecting nitrogen gas and surfactant solution, or pre-generated ex-situ and then injected to displace the oil bank. We found that a) the presence of the crude oil used in this work had a detrimental effect on foam stability in bulk, b) optimum salinity FACF was able to increase the ultimate oil recovery with 5% of the OIP after water flooding compared with under-optimum FACF, and c) injection of pre-generated drive foam increased its ultimate oil recovery by 13% of the OIP after water flooding compared to in-situ drive foam generation at optimum salinity.*

---

The content of this chapter is based on the following publications:

Janssen, M.T.G., Mutawa, A.S., Pilus, R.M., and Zitha, P.L.J. 2019. Foam-Assisted Chemical Flooding for Enhanced Oil Recovery: Effects of Slug Salinity and Drive Foam Strength. *Energy & Fuels*, 33(6), 4951 – 4963.

Janssen, M.T.G., Mutawa, A.S., Pilus, R.M., and Zitha, P.L.J. 2019. Evaluation of Foam-Assisted Surfactant Flooding at Reservoir Conditions. Society of Petroleum Engineers. DOI:10.2118/195481-MS.

## 5.1 Introduction

After studying *FACF* in a model-like setting (**Chapters 3 and 4**), this chapter reports on an extensive experimental study that discusses the viability of *FACF* to reservoir conditions. The introduction proceeds with a brief overview of the theoretical background and existing literature.

In order to overcome the drawbacks related to continuous gas injection and *WAG* applications, one might foam the gas to reduce its mobility, and hence increase its  $E_V$  (**Section 1.2 and 1.3**). Besides obtaining a favourable  $E_V$ , any successful chemical *EOR* methodology should show a fairly large  $E_D$  as well (**Equation 1.1**). In **Section 1.4** we introduced the use of chemical surfactants. They might mobilize part of the trapped residual oleic phase by a combined effect of rock wettability alteration, towards a stronger water-wet system, and the reduction of the *o/w IFT* to ultralow values (**Section 1.4**). *FACF* entails the injection of a surfactant slug, for achieving sufficiently large  $E_D$ , combined with drive foam generation, for improving  $E_V$  (**Section 1.5**).

Earlier studies reported in literature showed that *FACF* is a viable *EOR* methodology (Srivastava *et al.*, 2009; Guo *et al.*, 2012; Jong *et al.*, 2016). However, since bulk of these studies used only obtained pressure and effluent data to make predictions regarding related physical processes within the porous media during *FACF*, they did not provide conceptual models for oil mobilization and its displacement during *FACF*. In **Chapters 3 and 4** we studied the effect of drive foam quality on oil bank propagation and the effect of surfactant slug salinity, respectively, during a *FACF* process at model-like conditions. We have presented novel insights related to oil mobilization and its displacement by a drive foam, in a *FACF* process, by the use of true dual-energy CT scanning. It allowed us to clearly visualize and quantitatively analyse oil bank formation and its displacement on core-scale.

The study reported in this chapter serves as a full extension of **Chapters 3 and 4**. Here we report on an elaborated laboratory study that addresses the feasibility of *FACF* to reservoir conditions instead of model-like settings. It includes surfactant stability, crude oil-surfactant phase behaviour, and drive foam stability in bulk tests that yielded various surfactant formulations to be used in the ensuing core-floods. Core-flood experiments include a foam quality scan, where one surfactant drive formulation was used to generate foam at varying gas fractional flows in the absence of crude oil, and a series of CT-scanned *FACF* core-floods conducted in Bentheimer sandstones. The effects of surfactant slug salinity and drive foam strength on the *FACF* efficiency were studied by performing *FACF* both at under-optimum and optimum salinity conditions and comparing in-situ drive foam generation, through co-injection, with the injection of pre-generated drive foam.

## 5.2 Materials and methods

### 5.2.1 Chemicals

In order to induce oil mobilization (by *o/w IFT* lowering) and gas foaming (achieving mobility control), two surfactants were selected: IOS2024 (ENORDET O242) and a proprietary surfactant which will be designated as Surfactant X. IOS2024 is an anionic surfactant, while Surfactant X contains both anionic and amphoteric surfactants, the latter carrying simultaneously anionic and cationic hydrophilic groups. Both surfactants were found to be unstable in the vicinity of injection water, that is, sea water, at 90 °C as the magnesium ( $Mg^{2+}$ ) and calcium ( $Ca^{2+}$ ) ions present yield complexation and, finally, precipitation of both surfactants. It was decided to remove corresponding salts (magnesium chloride hexahydrate,  $MgCl_2 \cdot 6H_2O$ , and calcium chloride dehydrate,  $CaCl_2 \cdot 2H_2O$ ) from the injection water composition and to compensate for its removal through the addition of sodium chloride (NaCl)

equal in total ionic strength (**Table 5.1**). The modified injection water formulation forms the basis for all aqueous solutions used throughout the entire study (**Table 5.2**).

**Table 5.1:** Original and modified injection water compositions. The removal of  $MgCl_2 \cdot 6H_2O$  and  $CaCl_2 \cdot 2H_2O$  was accounted for by adding an amount of NaCl equal in total ionic strength. Modified injection water contained 3.44 wt% NaCl, 0.37 wt%  $Na_2SO_4$ , 0.06 wt% KCl, and 0.03 wt%  $NaHCO_3$ . During the course of the various experiments, water salinity will be altered by changing NaCl and KCl concentrations.

Salt	Concentration (g/L)	
	Original	Modified
NaCl	25.21	35.71
$MgCl_2 \cdot 6H_2O$	10.15	0.00
$CaCl_2 \cdot 2H_2O$	1.47	0.00
$Na_2SO_4$	3.83	3.83
KCl	0.67	0.67
$NaHCO_3$	0.33	0.33

**Table 5.2:** Physical properties of all liquid phases used in the core-flood experiments. Densities and viscosities were measured at  $90 \pm 1^\circ C$

	Experiment				
	1	2	3	4	5
Brine type	1.72 wt% NaCl 0.37 wt% $Na_2SO_4$ 0.03 wt% KCl 0.03 wt% $NaHCO_3$	0.98 wt% NaCl 0.37 wt% $Na_2SO_4$ 0.02 wt% KCl 0.03 wt% $NaHCO_3$	0.98 wt% NaCl 0.37 wt% $Na_2SO_4$ 0.02 wt% KCl 0.03 wt% $NaHCO_3$	1.72 wt% NaCl 0.37 wt% $Na_2SO_4$ 0.03 wt% KCl 0.03 wt% $NaHCO_3$	1.72 wt% NaCl 0.37 wt% $Na_2SO_4$ 0.03 wt% KCl 0.03 wt% $NaHCO_3$
Brine viscosity (mPa·s)	$0.37 \pm 0.04$	$0.38 \pm 0.05$	$0.38 \pm 0.05$	$0.37 \pm 0.04$	$0.37 \pm 0.04$
Brine density ( $g/cm^3$ )	$0.983 \pm 0.001$	$0.976 \pm 0.001$	$0.976 \pm 0.001$	$0.983 \pm 0.001$	$0.983 \pm 0.001$
Oil type	-	Crude oil	Crude oil 20.0 wt% 1-iododecane	Crude oil 20.0 wt% 1-iododecane	Crude oil 20.0 wt% 1-iododecane
Oil viscosity (mPa·s)	-	$1.02 \pm 0.03$	$1.02 \pm 0.03$	$1.02 \pm 0.03$	$1.02 \pm 0.03$
Oil density ( $g/cm^3$ )	-	$0.774 \pm 0.001$	$0.830 \pm 0.001$	$0.830 \pm 0.001$	$0.830 \pm 0.001$
Slug type	-	0.98 wt% NaCl 0.37 wt% $Na_2SO_4$ 0.02 wt% KCl 0.03 wt% $NaHCO_3$ 1.00 wt% sec-butanol 0.30 wt% AM IOS2024	0.98 wt% NaCl 0.37 wt% $Na_2SO_4$ 0.02 wt% KCl 0.03 wt% $NaHCO_3$ 1.00 wt% sec-butanol 0.30 wt% AM IOS2024	1.72 wt% NaCl 0.37 wt% $Na_2SO_4$ 0.03 wt% KCl 0.03 wt% $NaHCO_3$ 1.00 wt% sec-butanol 0.30 wt% AM IOS2024	1.72 wt% NaCl 0.37 wt% $Na_2SO_4$ 0.03 wt% KCl 0.03 wt% $NaHCO_3$ 1.00 wt% sec-butanol 0.30 wt% AM IOS2024
Slug viscosity (mPa·s)	-	$0.40 \pm 0.05$	$0.40 \pm 0.05$	$0.41 \pm 0.03$	$0.41 \pm 0.03$
Slug density ( $g/cm^3$ )	-	$0.975 \pm 0.001$	$0.975 \pm 0.001$	$0.980 \pm 0.001$	$0.980 \pm 0.001$
Drive type	1.72 wt% NaCl 0.37 wt% $Na_2SO_4$ 0.03 wt% KCl 0.03 wt% $NaHCO_3$ 0.50 wt% AM Surfactant X	0.98 wt% NaCl 0.37 wt% $Na_2SO_4$ 0.02 wt% KCl 0.03 wt% $NaHCO_3$ 0.50 wt% AM surfactant X	0.98 wt% NaCl 0.37 wt% $Na_2SO_4$ 0.02 wt% KCl 0.03 wt% $NaHCO_3$ 0.50 wt% AM Surfactant X	1.72 wt% NaCl 0.37 wt% $Na_2SO_4$ 0.03 wt% KCl 0.03 wt% $NaHCO_3$ 0.50 wt% AM Surfactant X	1.72 wt% NaCl 0.37 wt% $Na_2SO_4$ 0.03 wt% KCl 0.03 wt% $NaHCO_3$ 0.50 wt% AM Surfactant X
Drive viscosity (mPa·s)	$0.38 \pm 0.04$	$0.40 \pm 0.05$	$0.40 \pm 0.05$	$0.38 \pm 0.04$	$0.38 \pm 0.04$
Drive density ( $g/cm^3$ )	$0.972 \pm 0.001$	$0.956 \pm 0.001$	$0.956 \pm 0.001$	$0.972 \pm 0.001$	$0.972 \pm 0.001$

An overview of the physical properties of the chemicals used in this study is presented in **Table 5.3**. Brine was prepared by dissolving sodium chloride, sodium sulphate, potassium chloride, and sodium bicarbonate in demineralized water. Surfactant slug solutions were prepared by adding required amounts of surfactant and sec-butanol, a co-solvent, to brine. The co-solvent was added to the surfactant slug formulation to guarantee its stability (Hirasaki *et al.*, 2011). Surfactant drive formulations were prepared by adding the necessary amounts of surfactant to brine. Nitrogen gas was used for co-injection with surfactant drive solution for in-situ foam generation and for creating pre-generated drive foam. A crude oil was used in the core-flood experiments. Its acid and base numbers were measured and equalled 0.17 and 0.32 mg KOH/g, respectively. In two *FACF* core-flood experiments the oleic phase was doped with 20 wt % 1-iododecane for enhancement of the CT contrast between the oleic and aqueous phases. Aqueous solutions were degassed under vacuum prior to injection.

**Table 5.3:** Properties of the used chemicals.

Chemical	Formula	Molecular weight (g/mol)	Density (g/cm <sup>3</sup> ) <sup>a</sup>	Viscosity (mPa·s) <sup>a</sup>	Supplier	Purity (%)
Sodium chloride <sup>b</sup>	NaCl	58.44	2.160 ± 0.001	-	Merck	≥99
Potassium Chloride <sup>b</sup>	KCl	58.44	1.980 ± 0.001	-	Merck	≥99
Sodium Bicarbonate <sup>b</sup>	NaHCO <sub>3</sub>	84.01	2.200 ± 0.001	-	VWR	≥99
Sodium Sulphate <sup>b</sup>	Na <sub>2</sub> SO <sub>4</sub>	142.04	2.660 ± 0.001	-	Sigma-Aldrich	≥99
Sec-butanol	C <sub>4</sub> H <sub>10</sub> O	74.12	0.806 ± 0.001	3.10 ± 0.01	Merck	≥99
1-iododecane	CH <sub>3</sub> (CH <sub>2</sub> ) <sub>9</sub> I	268.18	1.257 ± 0.001	3.00 ± 0.01	Sigma-Aldrich	≥98
IOS2024	-	-	0.996 ± 0.001	-	Shell Global	19
Surfactant X	-	-	1.020 ± 0.001	-	PETRONAS	20
Nitrogen <sup>b</sup>	N <sub>2</sub>	28.01	1.165 ± 0.001 × 10 <sup>-3</sup>	1.760 ± 0.500 × 10 <sup>-2</sup>	Linde Gas Benelux	100
Crude oil	-	-	0.843 ± 0.001	2.79 ± 0.04	PETRONAS	100

<sup>a</sup>All densities and viscosities mentioned are at 20°C and 1 atmosphere.

<sup>b</sup>Lide (2012).

### 5.2.2 Core samples

Reservoir rocks for the studied oil field are exclusively sandstones that exhibit good reservoir characteristics in terms of porosity (up to 25%) and permeability (up to 640 mD). Bentheimer sandstone cores were used in this study to mimic reservoir rocks because of its homogeneous mineralogy (>91 wt % Quartz) and high permeabilities (3.39 ± 0.91 Darcy) (Peksa *et al.*, 2015). Its physical properties are presented in **Table 5.4**. Porosities shown were either determined from CT scan data (**Appendix A**) or by using an Ultra Pycnometer 1000 (Quantachrome Corporation). Several equidistant holes were drilled in the cores for pressure drop measurements. All cores were placed horizontally. More details about the preparation of the sandstone samples are given elsewhere (**Sections 2.2.2** and **3.2.2**).

### 5.2.3 Experimental set-up: bulk foam experiments

Bulk foam stability experiments were performed using two surfactant formulations studied in this work: IOS2024 and Surfactant X. Experiments were conducted in the absence and presence of crude oil utilizing the Foam Scan instrument (I.T. Concept-TECLIS). The apparatus is designed to measure a)

the ability of a liquid to develop foam by sparging  $N_2$  through it, and b) the stability of the generated foam by monitoring its volume as function of time.

#### 5.2.4 Experimental set-up: core-flood experiments

Core-flood experiments were conducted utilizing the experimental set-up shown in **Figure 5.1**. Bentheimer sandstone cores were placed horizontally in a designed core-holder made of polyether ether ketone which exhibits low X-ray attenuation and high mechanical strength. The confining pressure, that is, the pressure in the core-holder surrounding the sandstone, was set equal to the inlet pressure in all experiments performed. Aqueous solutions were injected using a dual-cylinder liquid pump (Quizix QX-6000), placed in line with the core-holder. A separate transfer vessel was used for injecting the crude oil. Several absolute and differential pressure transducers were installed along the core for accurately monitoring pressure (drop) behaviour during the various injection stages. Thermocouples were connected to the set-up for temperature monitoring. The (differential) pressure transducers and thermocouples were linked to a USB data acquisition system (National Instruments, cDAQ-9174) that recorded the data using a 5 s time interval. The outlet pressure was set using a backpressure regulator (DEMO-TU Delft). For regulating the  $N_2$  fractional flow during drive foam injection, i.e. foam quality, a mass flow controller (Bronkhorst, EL-FLOW) was used. A Coriolis flowmeter (Bronkhorst, CORI-FLOW), which measured effluent densities and mass flow rates, was connected to the outlet for accurately determining phase breakthrough times. Effluent fluids were collected in a measuring cup placed on a digital balance.  $CO_2$ , used for initial flushing of the core, was supplied in a 200 bar cylinder. In one *FACF* core-flood, Exp. 5 in **Table 5.5**, a high-pressure static mixing tee (Health & Science, U-466), which features a 10  $\mu m$  stainless steel frit, was placed at the inlet section in order to pre-generate foam prior to injection. The frit pore size of 10  $\mu m$  corresponds well with averaged pore body and throat diameters reported for Bentheimer sandstones (Peksa *et al.*, 2015). All core-flood experiments were conducted at a reservoir temperature of  $90 \pm 1^\circ C$ . Temperature was either controlled by a) placing the core-holder in an oven (Exp. 1, 2, and 5 in **Table 5.5**), or by b) utilizing aluminium heating sleeves filled with silicon oil for CT-assisted core-floods (Exp. 3 and 4 in **Table 5.5**). Note that, because of the design of the core-holder, two separate aluminium sleeves were used which led a short section of the core holder uncovered by the heating sleeves (**Figure 5.1**).

**Table 5.4:** Properties of the Bentheimer sandstone cores used.

Parameter	Experiment				
	1	2	3	4	5
Porosity (%)	$23.0 \pm 0.1^b$	$23.0 \pm 0.1^b$	$21.8 \pm 0.3^a$	$22.4 \pm 0.4^a$	$23.0 \pm 0.1^b$
Permeability (D)	$3.42 \pm 0.20$	$2.48 \pm 0.50$	$3.58 \pm 0.30$	$3.73 \pm 0.30$	$3.76 \pm 0.20$
Length (cm)	$40.00 \pm 0.10$	$40.00 \pm 0.10$	$40.00 \pm 0.10$	$40.00 \pm 0.10$	$40.00 \pm 0.10$
Diameter (cm)	$3.80 \pm 0.10$	$3.80 \pm 0.10$	$3.80 \pm 0.10$	$3.80 \pm 0.10$	$3.80 \pm 0.10$
Pore volume ( $cm^3$ )	$104.34 \pm 6.32$	$104.34 \pm 6.32$	$98.89 \pm 6.98$	$101.62 \pm 7.60$	$104.34 \pm 6.32$

<sup>a</sup>Porosity values reported were calculated using obtained CT data.

<sup>b</sup>Porosity values shown were obtained from a representative measurement using the Ultra Pycnometer 1000.

In Exp. 3 and 4 (**Table 5.5**), a Siemens SOMATOM Definition CT scanner with true dual-energy scanning capabilities was utilized for quantifying three-phase saturation distributions during the various injection stages. It allowed for assessing and visualizing the oil bank formation and its displacement by a foam drive. A more detailed description of the apparatus is given elsewhere (**Sections 3.2.4** and **4.2.4**).

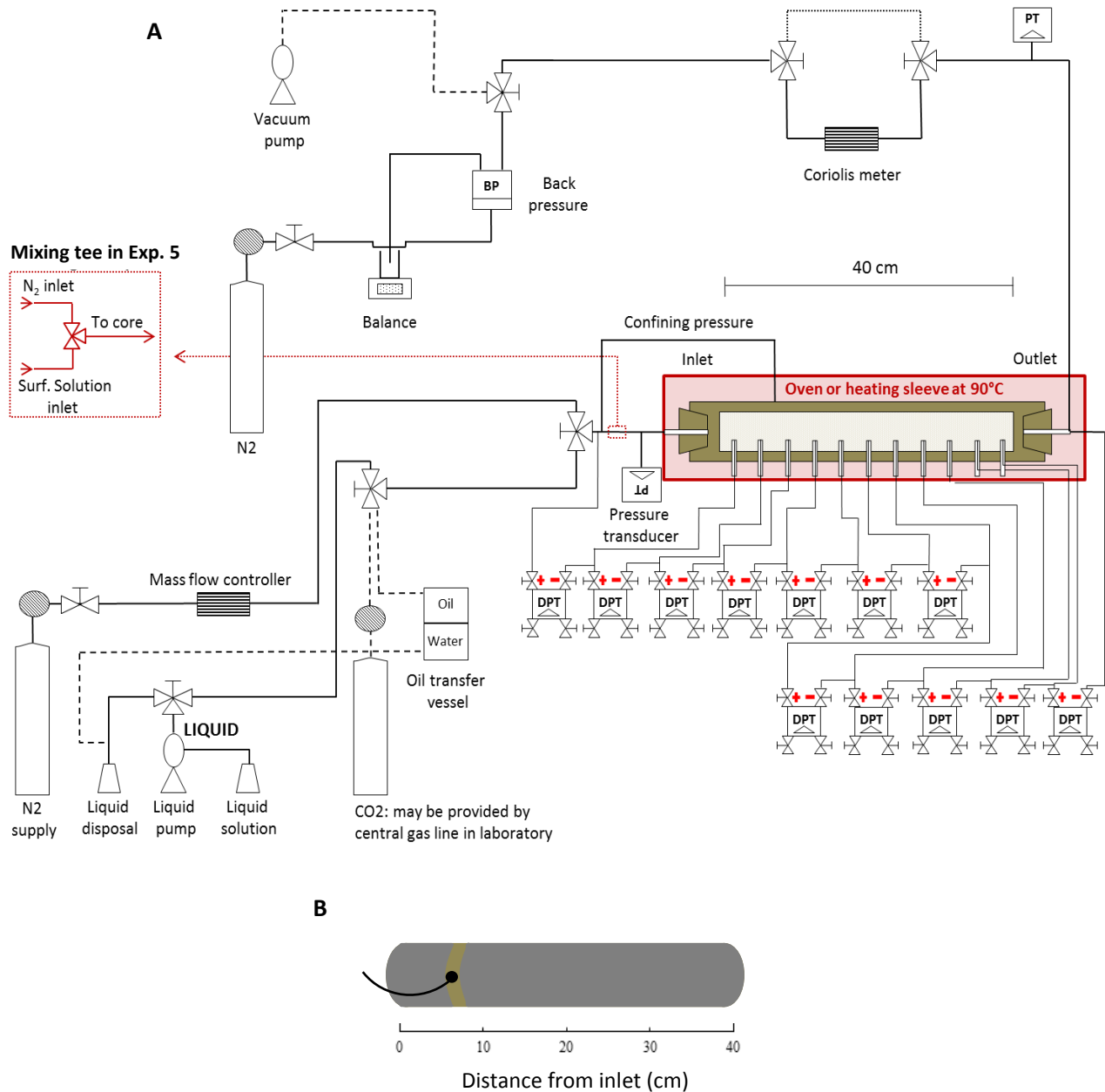


**Figure 5.1:** A: schematic of experimental set-up. B: for CT-assisted core-floods a heating sleeve (grey) was used instead of an oven. Due to the position of the inlet port of the confining pressure (black), two separate heating sleeves were used. It resulted in a small section (5.6-8.6 cm from inlet) of the core-holder (brown) being uncovered by the sleeves.

**Table 5.5:** Overview of core-flood experiments performed.

Exp.	Process	Salinity	Foam quality (%)	Liquid flow rate (cm <sup>3</sup> /min)	Gas flow rate (cm <sup>3</sup> /min)	Total injection velocity (ft/day)	CT	Method of drive foam generation
1	Foam quality scan	-	Multiple	Multiple	Multiple	2.1 ± 0.1	No	Co-injection
2	FACF	Under-optimum	57.5	0.2125	0.2875	2.1 ± 0.1	No	Co-injection
3	FACF	Under-optimum	57.5	0.2125	0.2875	2.1 ± 0.1	Yes	Co-injection
4	FACF	Optimum	57.5	0.2125	0.2875	2.1 ± 0.1	Yes	Co-injection
5	FACF	Optimum	57.5	0.2125	0.2875	2.1 ± 0.1	No	Pre-generated

## 5.2.5 Experimental procedure

### 5.2.5.1 Phase behaviour

Phase behaviour tests were conducted by preparing several crude oil-surfactant slug formulations where the surfactant slug contained X wt % NaCl, 0.37 wt % Na<sub>2</sub>SO<sub>4</sub>, X/53.3 wt % KCl, 0.03 wt % NaHCO<sub>3</sub>, 1.00 wt % sec-butanol, and 0.30 wt % AM IOS2024 or 0.30 wt % AM Surfactant X. Both NaCl and KCl concentrations were altered in order to vary slug salinity because we aimed to change solely the monovalent chloride ions. Crude oil-surfactant slug mixtures were prepared at a 1:2 oil-to-water ratio and subsequently placed on a shaking roller for 10 h to ensure adequate mixing. Afterwards, the samples were placed in an oven at 90 °C until equilibrium was reached (typically after 3 weeks). The oil and water solubilisation ratios, defined as the ratio of solubilized oil or water volume to the surfactant volume in the *ME* phase, were then estimated by assuming that all the surfactant is present in the *ME* phase and not in the excess oil or water phases (Lake, 1989). Optimum salinity was determined as the salinity at which the oil and water solubilisation ratios overlap. The goal of the phase behaviour study is to identify the surfactant slug formulation (IOS2024 or Surfactant X) that will be used in the *FACF* core-floods and to categorize the Winsor type systems (**Section 1.4**) of the final surfactant slug composition (Winsor, 1954). All phase behaviour tests were performed at ambient pressure and the core-floods were conducted using a backpressure of 20 bar. The potential pressure effect implies an increasing optimum salinity range (Type III system) with increasing pressure (Skauge and Fotland, 1990). However, this effect is expected to be insignificant when dealing with a pressure difference of only 20 bar.

### 5.2.5.2 Bulk foam stability

In order to assess drive foam stability in bulk for both IOS2024 and Surfactant X, bulk foam experiments were conducted in the absence of crude oil. The two surfactant drive solutions studied contained 3.44 wt % NaCl, 0.37 wt % Na<sub>2</sub>SO<sub>4</sub>, 0.06 wt % KCl, 0.03 wt % NaHCO<sub>3</sub>, and 0.50 wt % AM IOS2024 or 0.50 wt % AM Surfactant X. Surfactant solutions (40.0 ± 0.5 cm<sup>3</sup>) were placed in the sample holder. Then, N<sub>2</sub> was sparged into the surfactant solutions (at 20 cm<sup>3</sup>/min) until the volume of the generated foam column reached 110 ± 1 cm<sup>3</sup>. Next, N<sub>2</sub> gas supply was shut off and the foam volume was monitored over time. The bulk foam experiments were performed at 20 ± 1 °C and at atmospheric pressure. The goal of abovementioned tests is to select the surfactant drive solution that yielded the most stable foam in bulk; this drive formulation will be used in the succeeding *FACF* core-floods. Although core-flood experiments were conducted at 90 ± 1 °C, the anticipated temperature effect on foam stability in bulk (that is, earlier foam decay at higher temperatures because of reduction in liquid viscosity) is expected to be similar for both surfactant drive formulations (Kapetas *et al.*, 2015). The latter implies that comparing the results of the bulk foam tests performed at 20 ± 1 °C is still qualitatively valid for 90 ± 1 °C. Lastly, the impact of crude oil on the stability of the selected surfactant drive foam in bulk was studied by performing one additional bulk foam test. It included 5 volume percent (vol. %) crude oil to the initial amount of liquid surfactant solution placed in the sample holder.

### 5.2.5.3 Core-flood experiments

**Table 5.5** gives an overview of the core-flood experiments performed in this study. The sequence used for performing all five core-floods is presented in **Table 5.6**. After flushing the core with CO<sub>2</sub> and evacuated the system to -1 bar, to remove all the air inside the core, approximately 10.00 PV of brine were injected. During the last PV of brine injection, the backpressure was increased from

atmospheric pressure to 25 bar to ensure complete dissolution of remaining CO<sub>2</sub> in brine. Next, in Exp. 1, a surfactant drive pre-flush of approximately 10.00 PV was conducted in order to satisfy the surfactant adsorption capacity of the rock. Afterwards, drive foam was generated at various gas fractional flows in Exp. 1. This was done through co-injection of the selected surfactant drive formulation and N<sub>2</sub> at a constant superficial velocity of 2.1 ± 0.1 ft/day. Results obtained from Exp. 1 give an overview of steady-state foam strengths as a function of drive foam quality in the absence of crude oil. For all other core-flood experiments, subsequent to brine injection, crude oil was injected (circa 5.00 PV) for establishing S<sub>wc</sub>. Afterwards, the system was exposed to extensive water flooding (nearly 7.00 PV) in order to reach S<sub>or\_WF</sub>. At the end of brine injection, oil injection, and water flooding, injection rates were varied for determining the absolute permeability to brine and the  $k_{ro}^0$  and  $k_{rw}^0$ , respectively, by using Darcy's law (Darcy, 1856). Prior to changing injection rates for  $k_{ro}^0$  and  $k_{rw}^0$  estimation during primary drainage and water flooding, respectively, bump floods were applied by increasing the injection rate with a factor 8 (oil injection) or 16 (water flooding) in order to establish true S<sub>oi</sub> and S<sub>or\_WF</sub>. Next to water flooding, in Exp. 2, 3, 4, and 5, approximately 0.45 PV of surfactant slug was injected at 0.6 ± 0.1 ft/day, at either under-optimum (Exp. 2 and 3) or at optimum (Exp. 4 and 5) salinity, in order to mobilize S<sub>or\_WF</sub>. Consequently, for displacing the formed oil bank, drive foam was generated either in-situ through co-injection of N<sub>2</sub> and surfactant drive solution (Exp. 2, 3, and 4) or by injecting pre-generated foam (Exp. 5), all at a constant foam quality of 57.5% and a total superficial velocity of 2.1 ± 0.1 ft/day (**Table 5.5**). Drive foam injection continued until no more measurable amounts of oil were produced. Although Exp. 5 was not conducted with the assistance of a medical CT scanner, still the oleic phase was doped with 1-iododecane in order to allow for comparison of the results with Exp. 4. **Table 5.2** gives an overview of the physical properties of the various types of brine, oil, surfactant slug, and drive solutions utilized in this study. In order to avoid any brine-slug-drive salinity gradient, the total ionic strength of each aqueous solution within one experiment was kept constant. More detailed information on the CT data processing is given in **Appendix A**.

**Table 5.6:** Core-flood procedure.

Step	Exp.	Process	Back pressure (bar)	Pore volumes injected	Flow rate (cm <sup>3</sup> /min)
1	All	CO <sub>2</sub> flushing	-	-	-
2	All	Vacuuming	-	-	-
3	All	Brine saturation	25	10.00	0.25
4	1 <sup>b</sup>	Surfactant drive pre-flush	20	10.00	0.50
5	2, 3, 4, 5	Oil injection	20	5.00	0.50
6	2, 3, 4, 5	Water flooding <sup>a</sup>	20	7.00	0.25
7	2, 3, 4, 5	Surfactant slug injection	20	0.45	0.15
8	1 <sup>b</sup> , 2, 3, 4	Surfactant drive co-injection	20	-	Liquid: 0.2125 Gas: 0.2875
9	5	Pre-generated foam injection	20	-	Liquid: 0.2125 Gas: 0.2875

<sup>a</sup>For water flooding the same synthetic brine was used as for brine saturation in the respective experiment.

<sup>b</sup>In Exp. 1 foam flooding was assessed at fully surfactant drive solution saturated conditions using various foam qualities whilst maintaining a superficial velocity of 2.1 ± 0.1 ft/day.

## 5.3 Results and discussion

### 5.3.1 Phase behaviour and bulk foam experiments

The phase behaviour study for the crude oil-Surfactant X system did not reveal a distinct ME phase for the entire range of salinities investigated (0.0–5.0 wt % NaCl + KCl). It showed that Surfactant X

was not able to reduce the *o/w* IFT to ultralow values. Hence, the discussion of the salinity scan will be restricted to the crude oil/IOS2024 system. Note that, unless otherwise stated, salinities refer to wt % NaCl + KCl. **Figure 5.2** presents the oil and water solubilisation ratios ( $V_o/V_s$  and  $V_w/V_s$ , respectively) as function of salinity for the crude oil/IOS2024 phase behaviour study. The Winsor Type III system, characterized by a distinct *ME* phase in equilibrium with clean excess oil and water, was found at salinities ranging from 1.50 to 1.75 wt %. The oil/*ME* (*o/m*) and water/*ME* (*w/m*) IFTs at these optimum salinities were estimated using Huh's empirical correlation and varied from  $6.0 \times 10^{-4}$  to  $1.0 \times 10^{-2}$  mN/m, respectively (Sheng, 2010). The under-optimum salinity regime, i.e. Winsor Type II- system, was observed for salinities below 1.50 wt %, whereas a Winsor Type II+ system, that is, over-optimum regime, was found at salinities larger than 1.75 wt %. Exp. 2 and 3 were conducted at an under-optimum salinity of 1.00 wt %, whereas Exp. 4 and 5 were done at an optimum salinity of 1.75 wt % (**Figure 5.2** and **Table 5.2**). The addition of 20 wt % 1-iododecane to the crude oil did not alter the phase behaviour.

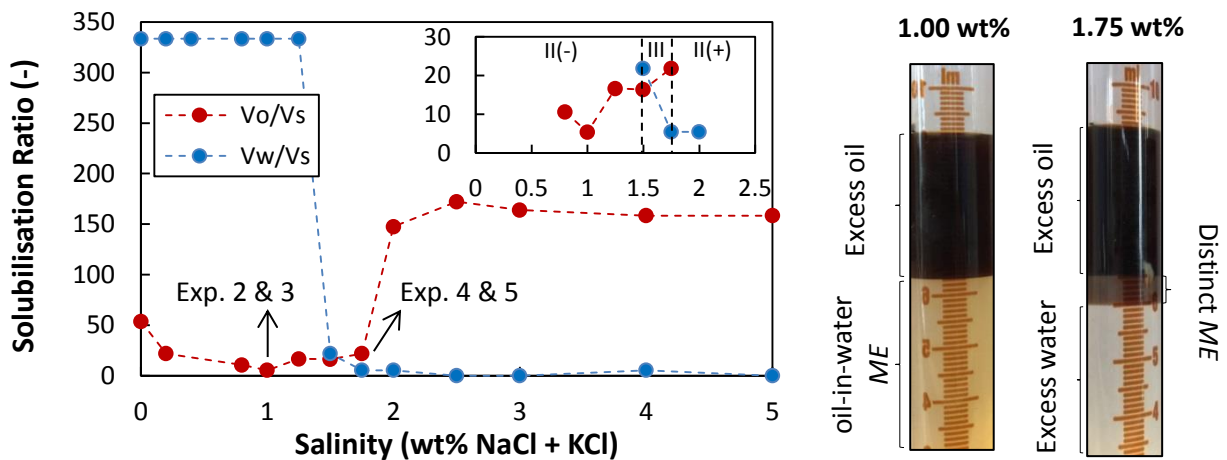


**Figure 5.2:** Solubilisation ratios as function of salinity for the IOS2024 phase behaviour study. Aqueous phase compositions consist of X wt% NaCl, 0.37 wt%  $\text{Na}_2\text{SO}_4$ , (X/53.3) wt% KCl, 0.03 wt%  $\text{NaHCO}_3$ , 1.00 wt% sec-butanol, and 0.30 wt% AM IOS2024. The top right diagram covers the optimum salinity range (Type III system) which is found in between 1.50-1.75 wt% NaCl + KCl, the under-optimum range, Type II(-) system (<1.50 wt% NaCl + KCl) and the over-optimum salinity conditions, Type II(+) system (>1.75 wt% NaCl + KCl). Experiments 2 and 3 were performed at under-optimum salinity whereas experiments 4 and 5 were done at optimum salinity conditions. The right-hand side presents the two crude oil-surfactant slug mixtures, after being placed in an oven at 90°C for three weeks, representative for the experimental conditions. Note the presence of a clear, distinct, *ME* at optimum salinity.

The foam half-decay times ( $t_{1/2}$ ), i.e. the time that it takes for the initial foam volume to be reduced by 50%, obtained in the three bulk foam experiments are shown in **Table 5.7**. The data show that Surfactant X was able to produce a much more stable drive foam in bulk ( $t_{1/2} = 738$  min) compared to IOS2024 ( $t_{1/2} = 69$  min), in the absence of crude oil. This resulted in Surfactant X to be selected for the drive foam formulation in succeeding *FACF* core-floods. To assess the impact of crude oil on bulk foam stabilized by Surfactant X, one additional test was conducted in the presence of 5 vol. % crude oil. The presence of 5 vol. % crude oil was able to reduce the  $t_{1/2}$  of Surfactant X drive foam from 738 to 62 min, a factor 12 reduction.

### 5.3.2 Foam quality scan

In Exp. 1, a Surfactant X drive (see formulation in **Table 5.2**) was co-injected with  $\text{N}_2$  at varying foam qualities (i.e. gas fractional flows) into a Bentheimer sandstone core (**Table 5.4**). The total, that is, gas + liquid, injection rate was kept constant at  $2.1 \pm 0.1$  ft/day. Measured steady-state pressure drops over the entire core length, for each single foam quality ( $f_g$ ) studied, were used to estimate

**Table 5.7:** Foam half-decay times ( $t_{1/2}$ ) obtained during the bulk foam experiments. All tests were conducted at  $20 \pm 1$  °C and atmospheric pressure.

Drive Type	Crude oil added (vol.%)	$t_{1/2}$ (min)
3.44 wt% NaCl 0.37 wt% Na <sub>2</sub> SO <sub>4</sub> 0.06 wt% KCl 0.03 wt% NaHCO <sub>3</sub> 0.50 wt% AM IOS2024	0.0	69
3.44 wt% NaCl 0.37 wt% Na <sub>2</sub> SO <sub>4</sub> 0.06 wt% KCl 0.03 wt% NaHCO <sub>3</sub> 0.50 wt% AM Surfactant X	0.0	738
3.44 wt% NaCl 0.37 wt% Na <sub>2</sub> SO <sub>4</sub> 0.06 wt% KCl 0.03 wt% NaHCO <sub>3</sub> 0.50 wt% AM Surfactant X	5.0	62

corresponding apparent foam viscosities ( $\mu_{app}$  in Pa·s) by:

$$\mu_{app} = \frac{k\nabla P}{(u_l + u_g)} \quad (5.1)$$

where  $k$ ,  $u_l$ ,  $u_g$ , and  $\nabla P$  represent the absolute permeability (m<sup>2</sup>), liquid and gas superficial velocities (m/s), and the pressure gradient across the entire core (Pa/m), respectively. Corresponding foam apparent viscosities as function of foam quality are shown in **Figure 5.3**. Foam apparent viscosity increases with increasing foam quality from  $0.63 \pm 0.11$  Pa·s at  $f_g = 20.0\%$  to a maximum of  $1.45 \pm 0.11$  Pa·s obtained at a critical foam quality ( $f_g^*$ ) of 75.0%. For  $f_g > f_g^*$ , apparent viscosities slightly decrease to roughly  $0.84 \pm 0.08$  Pa·s at  $f_g = 98.0\%$ . The observed trend is consistent with data reported by others for similar foam systems (Osterloh and Jante, 1992; Alvarez *et al.*, 2001; Jones *et al.*, 2016). Foam flow in the low-quality regime ( $f_g < f_g^*$ ) is mainly affected by bubble trapping and the foam apparent viscosity is essentially controlled by the gas flow rate; increasing  $\mu_{app}$  with increasing  $f_g$ . However, in the high-quality regime ( $f_g > f_g^*$ ), foam behaviour is influenced by bubble coalescence and here the foam apparent viscosity is mostly dependent on the liquid superficial velocity; decreasing  $\mu_{app}$  with increasing  $f_g$ . For more information regarding the foam flow regimes, see **Section 1.3.3**. The Surfactant X drive formulation (**Table 5.2**) proved to be able to generate strong, stable drive foams for the entire range of foam qualities studied in the absence of crude oil. Because previous studies have shown that high-quality foams are more vulnerable to the presence of oil than low-quality foams, the drive foam quality to be used in the following *FACF* core-floods (Exp. 2, 3, 4, and 5) needs to be sufficiently lower than  $f_g^*$  (Aarra and Skauge, 1994; Tang *et al.*, 2017). It is for this reason that a fixed drive foam quality of 57.5% was used in all succeeding *FACF* core-flood experiments. The apparent foam viscosity of  $f_g = 57.5\%$  equalled  $1.32 \pm 0.05$  Pa·s.

Exp. 1 revealed that the Surfactant X drive solution is capable of generating strong foams, over a wide range of foam qualities, in the absence of crude oil. In order to assess the effect of the crude oil on foam strength and stability in Bentheimer sandstone cores, N<sub>2</sub> and the same Surfactant X drive solution were co-injected ( $f_g = 57.5\%$ ) at  $S_{or\_WF} = 0.34 \pm 0.02$  to generate foam. Results indicated a reduction in  $\mu_{app}$  with roughly a factor of 170 compared to steady-state foam flow in the absence of crude oil:  $0.007 \pm 0.002$  Pa·s. These observations, together with the bulk foam results discussed in **Section 5.3.1**, suggest that the crude oil is detrimental to foam strength and stability in both bulk and

porous media. The composition of the crude oil (roughly 75 wt % consist of carbon chains from C1 to C12) might explain the detrimental impact as previous studies showed an increasing detrimental effect to foam stability (i.e. increase of gas bubble coalescence) with reducing carbon chain lengths (Simjoo *et al.*, 2013; Osei-Bonsu *et al.*, 2015). Whether the same observations are expected when applying Surfactant X drive foam in a *FACF* process is debatable as part of  $S_{or\_WF}$  will be mobilized by injecting an IOS2024 surfactant slug prior to drive foam injection, lowering  $S_{or}$ , which might promote foaming.

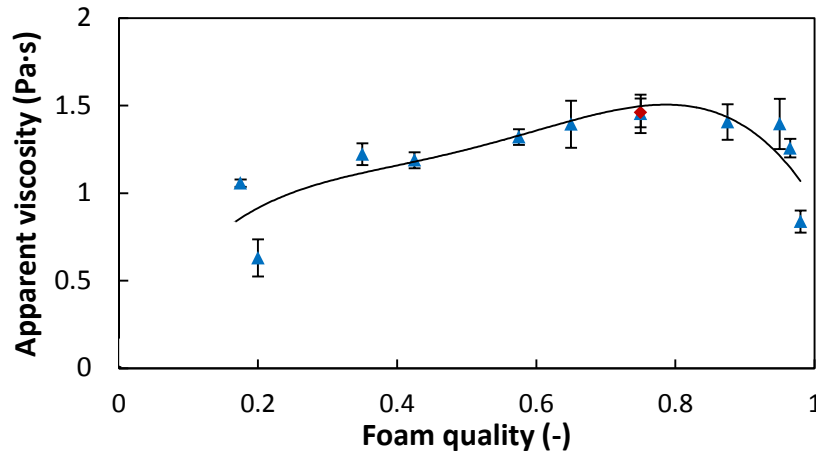


**Figure 5.3:** Apparent foam viscosity as function of foam quality at  $90 \pm 1^\circ\text{C}$  and 20 bar backpressure for the drive solution shown in **Table 5.2**. For each foam quality investigated, co-injection continued until a steady-state pressure drop was observed. Foam flooding at  $f_g = 0.75$  was repeated at the end of the experiment in order to verify its reproducibility (red diamond). A polynomial of the 4th order has been fitted to the data.

### 5.3.3 *FACF*

**Table 5.8** presents a summary of the performed *FACF* core-flood experiments (Exp. 2, 3, 4, and 5). This section discusses the chemical *EOR* injection stages for all four experiments, i.e. surfactant slug and surfactant drive foam injection. Results will be interpreted and discussed in terms of total pressure drops, oil saturation profiles, and ultimate oil recoveries. The preparatory injection stages, primary drainage (oil injection) and forced imbibition (water flooding), are not discussed in detail here as they yield major similarities with our work at model-like conditions (**Section 3.3.2.1**). The variation in  $M^0$ , representative for oil displacement during water flooding, is mainly because of differences in  $k_{ro}^0$  and  $k_{rw}^0$  (**Table 5.8**). The more water-wet the system is, the larger is the difference between  $k_{ro}^0$  and  $k_{rw}^0$ , the lower  $M^0$ .

#### 5.3.3.1 Mobilization of residual oil

After reaching  $S_{or\_WF}$  in Exp. 2 to 5 (**Table 5.8**), an IOS2024-based surfactant slug (**Table 5.2**) was injected, either at under-optimum (Exp. 2 and 3) or at optimum (Exp. 4 and 5) salinity conditions, for promoting oil mobilization by reducing the capillary forces that kept  $S_{or\_WF}$  in place. The analysis in this section will be limited to Exp. 3 and 4 only because both were performed with the assistance of a medical CT scanner, and the other *FACF* core-floods showed similar results in terms of observed pressure drops.

Total pressure drops, CT scan images, and related  $S_o$  profiles during surfactant slug injection in Exp. 3 and 4 are presented in **Figure 5.4**. At first, CT images and associated  $S_o$  profiles will be discussed as they give insight in saturation distributions which affect measured total pressure drops. The images

for Exp. 3 (**Figure 5.4A**) indicate that injection of the under-optimum surfactant slug mobilized part of  $S_{or\_WF}$  rather efficiently, leading to the formation of an oil bank. The tilted oil bank shape is a consequence of the difference in propagation velocity between its leading edge ( $53 \pm 2$  cm/PV) (i.e. downstream side) and its trailing edge ( $29 \pm 1$  cm/PV) (i.e. upstream side). The driving force for the latter is the effective density difference between the injected surfactant slug and the oil and water in place ( $\Delta\rho = 0.047 \pm 0.003$  g/cm<sup>3</sup>), which resulted in a gravity underriding tongue of the injected slug. It is expected that at the pore-scale the gravity effect is substantially reduced because of a significant reduction in length scale. The under-optimum slug proved to be able to reduce  $S_{or\_WF}$  by roughly 30% upstream of the oil bank after 0.46 PV injection, yielding an average  $S_o$  of  $0.23 \pm 0.05$  in that section. The averaged peak  $S_o$  in the oil bank remained fairly constant over time and equalled  $0.41 \pm 0.01$  at the end of slug injection.

**Table 5.8:** Summary of FACF core-flood experiments performed.  $k_{ro}^0$ ,  $k_{rw}^0$ ,  $M^0$ ,  $S_{wc}$ ,  $S_{oi}$ ,  $S_{or\_WF}$ ,  $S_{or\_CEOR}$ ,  $R_{FWF}$ ,  $R_{FCEOR}$ ,  $OIP$ , and  $OIIP$  represent the oil end-point relative permeability, water end-point relative permeability, end-point mobility ratio, connate water saturation, initial oil saturation, residual oil saturation to waterflood, residual oil saturation to FACF, recovery factor corresponding to water flooding, recovery factor corresponding to FACF, oil in place, and the oil initially in place, respectively. The end-point mobility ratios ( $M^0$ ) were calculated using the following formula:  $(k_{rw}^0/\mu_w)/(k_{ro}^0/\mu_o)$  where  $\mu_w$  and  $\mu_o$  represent the water and oil viscosity at 90°C, respectively.  $R_{FCEOR}$  as a function of  $OIP$  after  $WF$  is calculated in Exp. 3 and 4 based on CT processing as follows:  $((S_{or\_WF} - S_{or\_CEOR})/S_{or\_WF}) \times 100$ . Corresponding relatively large error is mainly due to the non-uniform distribution of  $S_{or\_CEOR}$ , which is of a higher magnitude in Exp. 4 compared to Exp. 3. The fairly large error in  $S_{wc}$  and  $S_{oi}$ , obtained from CT processing in Exp. 3 and 4, is due to the presence of the capillary end effect.

Exp.	$k_{ro}^0$	$k_{rw}^0$	$M^0$	$S_{wc}$	$S_{oi}$	$S_{or\_WF}$	$S_{or\_CEOR}$	$R_{FWF}$ (% of $OIIP$ )	$R_{FCEOR}$ (% of $OIIP$ )	$R_{FCEOR}$ (% of $OIP$ after $WF$ )
2	$0.54 \pm 0.09$	$0.15 \pm 0.02$	$0.75 \pm 0.46$	$0.21 \pm 0.02^a$	$0.79 \pm 0.02^a$	$0.36 \pm 0.01^a$	$0.23 \pm 0.01^a$	$54 \pm 3^a$	$71 \pm 2^a$	$36 \pm 5^a$
3	$0.48 \pm 0.03$	$0.20 \pm 0.01$	$1.12 \pm 0.37$	$0.25 \pm 0.02^a$ $0.16 \pm 0.08^b$	$0.75 \pm 0.02^a$ $0.84 \pm 0.08^b$	$0.31 \pm 0.02^a$ $0.33 \pm 0.02^b$	$0.20 \pm 0.01^a$ $0.21 \pm 0.03^b$	$59 \pm 4^a$ $61 \pm 5^b$	$73 \pm 2^a$ $75 \pm 5^b$	$35 \pm 7^a$ $36 \pm 13^b$
4	$0.46 \pm 0.03$	$0.22 \pm 0.01$	$1.32 \pm 0.38$	$0.23 \pm 0.02^a$ $0.20 \pm 0.09^b$	$0.77 \pm 0.02^a$ $0.80 \pm 0.09^b$	$0.30 \pm 0.01^a$ $0.31 \pm 0.05^b$	$0.18 \pm 0.01^a$ $0.16 \pm 0.06^b$	$61 \pm 3^a$ $61 \pm 10^b$	$77 \pm 2^a$ $80 \pm 9^b$	$40 \pm 5^a$ $48 \pm 24^b$
5	$0.50 \pm 0.03$	$0.15 \pm 0.01$	$0.83 \pm 0.26$	$0.20 \pm 0.02^a$	$0.80 \pm 0.02^a$	$0.34 \pm 0.02^a$	$0.16 \pm 0.01^a$	$58 \pm 3^a$	$80 \pm 2^a$	$53 \pm 5^a$

<sup>a</sup>Based on material balance calculations.

<sup>b</sup>Based on CT processing.

The CT images for surfactant slug injection at optimum salinity (Exp. 4) show, similar to under-optimum salinity injection, the formation of an unstable, diffuse, oil bank (**Figure 5.4C**). However, some distinctive features can be observed. One of them is the magnitude of oil mobilization by the injected slug. At optimum salinity, the slug was significantly more effective at mobilizing  $S_{or\_WF}$ , yielding an average  $S_o$  of  $0.06 \pm 0.06$  (81% reduction of  $S_{or\_WF}$ ) at the end of slug injection upstream of the oil bank's trailing edge. It can be attributed to the increase in capillary number (**Equation 3.1**) from  $10^{-5}$  (under-optimum salinity) to  $10^{-4}$  (optimum salinity) due to the change in  $o/w$  IFT from  $10^{-2}$  to  $10^{-3}$  mN/m upon switching from under-optimum to optimum salinity conditions. Furthermore, peak  $S_o$  tends to increase as function of injection time, yielding a somewhat higher peak  $S_o$  ( $0.45 \pm 0.01$ ) in the oil bank at the end of slug injection compared to Exp. 3. At 0.23 PV of injection, the shape of the formed oil bank exhibits heterogeneous characteristics where accumulation of mobilized oil happened at distinctive parts within the core (**Figure 5.4C**). The latter is the reason why two separate

cross-sections, that deviate from the centre of the core, are shown at 0.23 PV injected. The surfactant slug clearly had a preferred area within the pore network where it mobilized  $S_{or\_WF}$  (see cross-section at 5.85 cm distance from inlet in **Figure 5.4**). Most likely this is because of the core heterogeneity itself. After being mobilized at 0.23 PV, the oil tends to propagate and accumulate towards the top of the core because of a combination of core heterogeneity and gravitational forces ( $\Delta\rho_{wo} = 0.150 \pm 0.002 \text{ g/cm}^3$ ). The latter resulted in the formation of a leading edge that could spread across the entire core cross-sectional area, only at injection times later than 0.23 PV. Consistent with our observations made earlier (**Figure 4.4**), the final stationary location of the oil bank is closer to the inlet when flooding at optimum salinity compared to under-optimum salinity. This might be controlled by the accessible PV for the injected slug and moveable oil and water in place, which is higher at optimum salinity conditions because of increased displacement efficiency.

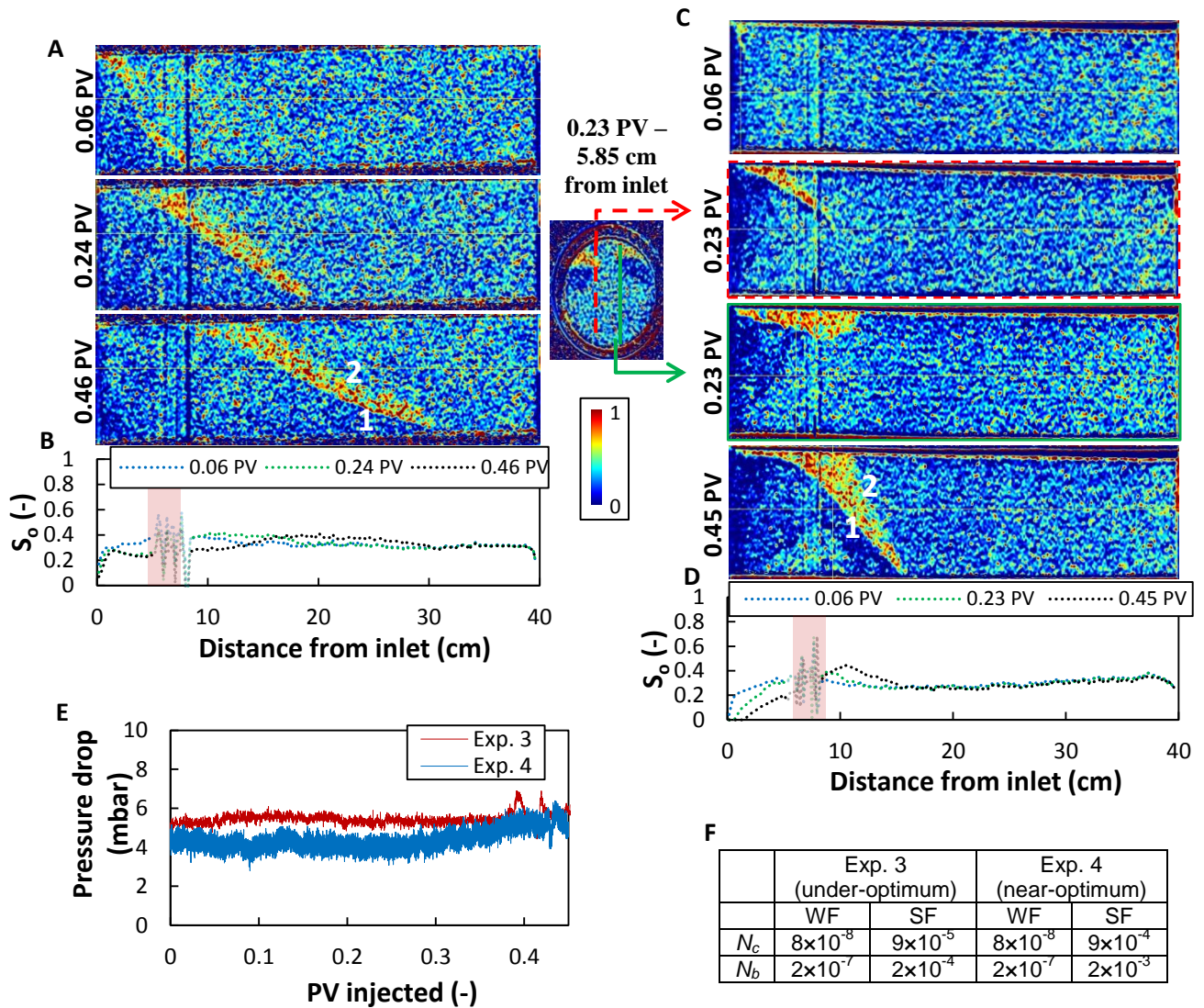


**Figure 5.4:** Two-dimensional CT images taken during surfactant slug injection at under-optimum salinity, Exp. 3 (A), and during slug injection at optimum salinity, Exp. 4 (C), and related  $S_o$  profiles (B and D). CT images shown were taken at the centre of the core by default. At 0.23 PV injection at optimum salinity two cross-sections are shown, both deviating from the centre of the core, due to heterogeneous characteristics of the oil bank's shape at that injection time. Numbers 1 and 2 refer to the two displacement interfaces present at the upstream and downstream side of the oil bank, respectively. The edges of the two heating sleeves used (**Figure 5.1B**) resulted in CT artefacts of a significant magnitude in between 5.6 and 8.6 cm distance from the inlet (red band in graphs B and D). Note that for further CT analysis these areas were ignored. The bottom left graph (E) presents the total pressure drop values obtained during surfactant slug injection for both Exp. 3 and 4. Table F shows the related capillary numbers ( $N_c$ ) and Bond numbers ( $N_b$ ) during water flooding (WF) and surfactant slug injection (SF) for both experiments. Capillary numbers were calculated using  $N_c = (\mu * u) / \sigma$  where  $\mu$ ,  $u$ , and  $\sigma$  represent the fluid viscosity, injection velocity, and the  $o/w$  IFT, respectively. Bond numbers were estimated using  $N_b = (\bar{\rho} * g * K) / \sigma$  where  $\bar{\rho}$ ,  $g$ , and  $K$  represent the density difference, gravitational constant, and absolute permeability, respectively.

The stabilities of both the displacement front at the trailing edge and leading edge (respectively interfaces 1 and 2 in **Figure 5.4A** and **C**) are a combined function of capillary, viscous, and gravitational forces (Lovoll *et al.*, 2005). They can be analysed in terms of capillary number (i.e. ratio of viscous forces to  $IFT$ ), and bond number (i.e. ratio of gravitational forces to  $IFT$ ). Relatively, capillary forces are expected to have a minimal effect on the interface stability as the surfactant slug yielded an increase in capillary and bond number of a factor 1,000 (under-optimum) and 10,000 (optimum) compared to water flooding (**Figure 5.4F**). As aforementioned, the relative dominance of gravitational forces increased during oil mobilization at low  $o/w$   $IFT$  conditions, compared to water flooding, which is in good agreement with earlier work (Oughanem *et al.*, 2013). However, the either stabilizing or destabilizing effect of viscous forces on both displacement fronts can be observed. Let us define the viscosity ratio as the total viscosity upstream over the total viscosity downstream of a particular interface, such that if  $>1$  viscous forces tend to stabilize the interface. Averaged viscosity ratios of 0.83 and 1.14 were calculated, for interfaces 1 and 2, respectively, for Exp. 3. In Exp. 4, these ratios equalled 0.65 (interface 1) and 1.25 (interface 2). At both salinities studied, interface 2 reveals a more stable front compared to interface 1. Note that this effect is of a higher magnitude in Exp. 4 compared to Exp. 3 because of sharper contrasts in viscosity ratios as a result of a more favourable displacement efficiency, i.e. lower  $o/w$   $IFT$ .

The total pressure drop profiles obtained during surfactant slug injection in Exp. 3 and 4 are shown in **Figure 5.4E**. For Exp. 3, a roughly constant total pressure drop can be observed. This is most likely a result of the fairly constant peak  $S_o$  within the oil bank which yielded constant averaged phase saturations and, thus, relative permeabilities. The pressure drop profile related to Exp. 4 remained constant until it started to gradually increase after  $0.30 \pm 0.02$  PV injection because of the formation of the oil bank (Guo *et al.*, 2012). The latter might be explained by an increase in the oil bank's peak  $S_o$  as injection continued. As peak  $S_o$  increased, local water mobility decreased which could lead to an increase in total pressure drop that was not compensated by the local increase in oil mobility (**Appendix B** and **Section 4.3.3.1.2**).

### 5.3.3.2 Displacement of mobilized oil by foam

After surfactant slug injection for oil mobilization, drive foam was either generated in-situ by co-injection of surfactant drive solution with  $N_2$  (Exp. 2, 3, and 4) or pre-generated ex-situ and then injected in the core (Exp. 5). This section presents the obtained total pressure drops and, when available, acquired CT scan images and associated  $S_o$  profiles during drive foam injection for Exp. 2, 3, 4, and 5.

Again, at first CT images and related  $S_o$  profiles for Exp. 3 and 4 will be discussed as they give insight in saturation distributions which affect the measured total pressure drops. They are shown in **Figure 5.5**. Note that hereafter, PV refers to the sum of gas and liquid PV injected in slug and drive (i.e. total PV). Let us first consider the presented data related to Exp. 3 (**Figure 5.5A** and **B**). Initiating co-injection into the system led to spreading of the oil bank, that is, increasing the difference in propagation velocity between its leading and trailing edge. It caused a reduction of the oil bank's peak  $S_o$ , now only slightly higher than  $S_{or\_WF}$ . Breakthrough of the oil bank happened at  $0.63 \pm 0.02$  PV injected. Lastly, after complete production of the oil bank, a fairly homogeneous residual oil saturation to  $FACF$  was achieved:  $S_{or\_CEOR}$  of  $0.21 \pm 0.03$  (**Figure 5.5B** and **Table 5.8**).

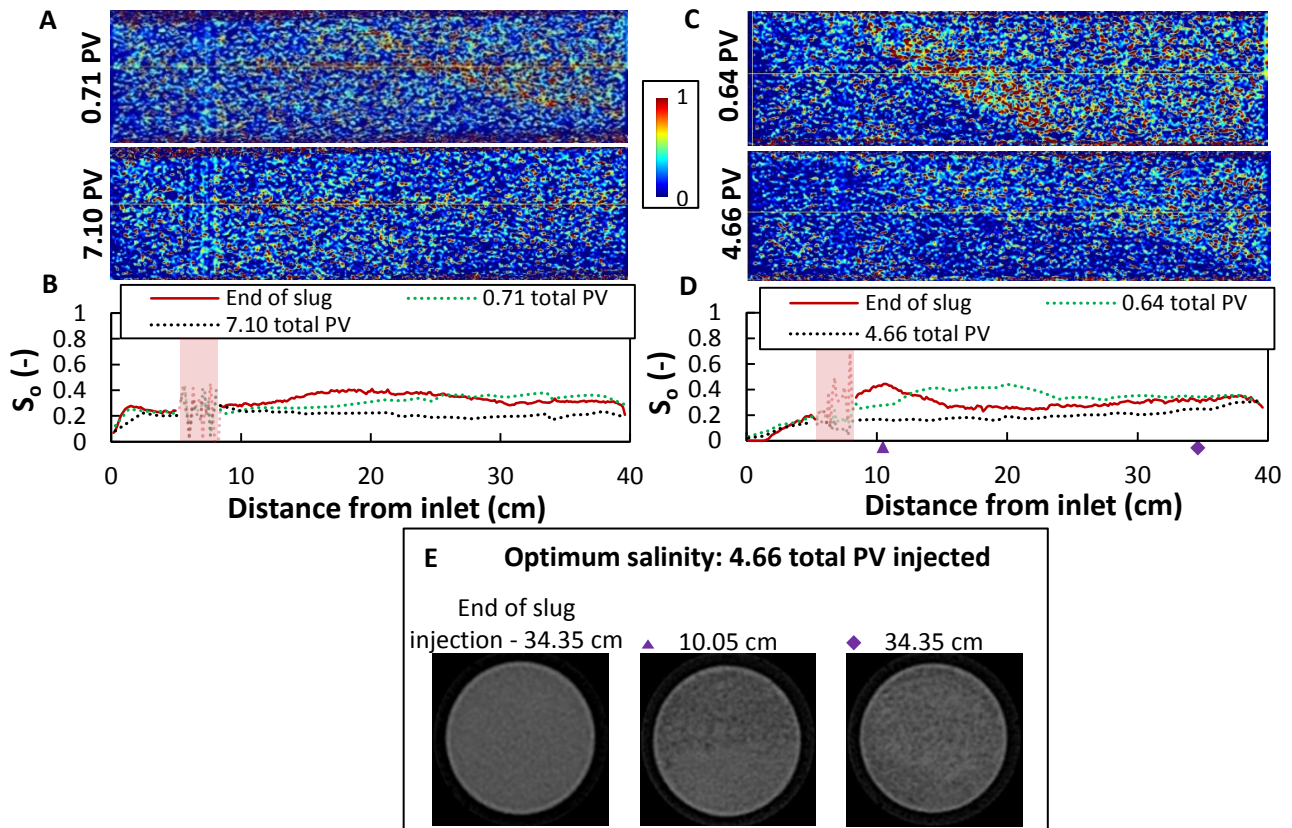


**Figure 5.5:** CT images taken during drive co-injection at under-optimum salinity, Exp. 3 (A), and at optimum salinity, Exp. 4 (C) and related oil saturation profiles (B and D). CT images shown were taken at the centre of the core. Total PV = 0 refers to the start of surfactant slug injection. The edges of the two heating sleeves used (Figure 5.1B) resulted in CT artefacts of a significant magnitude in between 5.6 and 8.6 cm distance from the inlet (red band in graphs B and D). Note that for further CT analysis these areas were ignored. Oil saturation profiles were constructed by applying a moving average (interval of 8) to the original dataset. In the bottom two cross-sectional areas are shown for 4.66 total PV injected in Exp. 4 and one for the condition after slug injection in Exp. 4 (E). Cross-sectional areas shown represent original CT data in Hounsfield units where the gas phase is shown in black.

The CT images for Exp. 4 show the same alteration in oil bank shape because of initiation of drive co-injection: a more unstable, spread out behaviour of the banked oil. Although peak  $S_o$  reduced during co-injection, it is still significantly higher than  $S_{or\_WF}$ . A  $S_{or\_CEOR}$  of  $0.16 \pm 0.06$  was reached at the end of the experiment (Table 5.8). Breakthrough of the oil bank occurred at  $0.67 \pm 0.02$  PV injected. The non-uniform behaviour of  $S_{or\_CEOR}$  (4.66 total PV in Figure 5.5C and D) is a result of dominant gravitational forces. They resulted in mainly the lower part of the core being properly swept because of the overriding tendency of the surfactant slug (Section 5.3.3.1). This effect is less observable in Exp. 3 (Figure 5.5A) because of a worse displacement efficiency (i.e. higher  $o/w$  IFT) compared with Exp. 4. Figure 5.5E shows several cross-sectional areas for the scan taken at 4.66 total PV (slug + drive) injected in Exp. 4. A more equally divided gas phase across the entire cross-sectional area was observed downstream in the core, which is consistent with our earlier observations at model-like conditions (Sections 3.3.2.3.3. and 4.3.2.2.3.). It might be a qualitative indicator of foam generation or an increasing foam strength. At locations closer to the inlet, the injected  $N_2$  tends to partly override. Note that this feature was not observed in Exp. 3.

The total pressure drops obtained during surfactant slug and drive foam injection in Exp. 2, 3, 4, and 5 are presented in Figure 5.6. Let us first focus on the under-optimum salinity *FACF* core-floods: Exp. 2 and 3 (Figure 5.6A and B). When co-injection started, and co-injected gas and liquid entered the

core, a step-wise increase in pressure drop towards  $46 \pm 2$  mbar (Exp. 2) and  $28 \pm 2$  mbar (Exp. 3) was observed. This is because of the fact that the injection of the liquid drive solution started slightly earlier than  $N_2$  injection, both at higher flow rates compared to slug injection (**Table 5.6**). This was done in order to make sure both phases entered the core simultaneously (**Figure 5.1**). Exp. 2 yielded higher pressure drops because of the lower absolute permeability of the sandstone used (**Table 5.4**). After the initial jump in pressure drop, both Exp. 2 and 3 reveal a slight reduction. We propose that the moderate reduction in total pressure drop in both Exp. 2 and 3 is the combined result of the reduction in the peak  $S_o$  of the oil bank (increasing water mobility), and the absence of stable foam generation. Gas breakthrough occurred after  $0.95 \pm 0.02$  and  $1.11 \pm 0.02$  PV in Exp. 2 and 3, respectively, resulting in pressure drop fluctuations as gas is leaving the backpressure. Co-injection stopped after  $2.15 \pm 0.02$  PV injection in Exp. 2 as no more oil was produced. *MRF*, which is defined as the steady-state pressure drop of drive foam injection over single-phase brine flooding at the same superficial velocity, equalled  $4 \pm 2$  in both experiments.

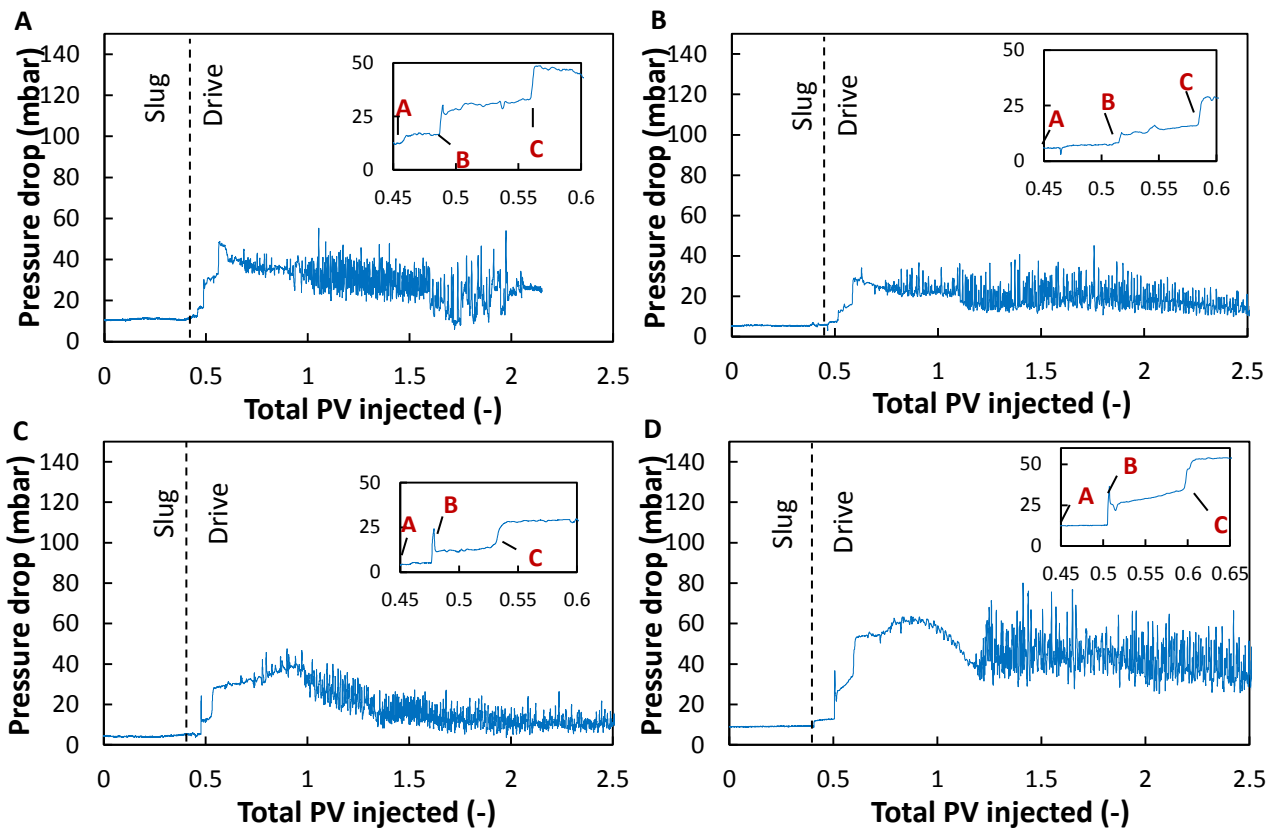


**Figure 5.6:** Total pressure drop profiles during surfactant slug and drive foam injection for Exp. 2 (A), Exp. 3 (B), Exp. 4 (C), and Exp. 5 (D). The total superficial velocity during drive foam injection equalled  $2.1 \pm 0.1$  ft/day in all *FACF* core-floods. In each pressure drop plot a second graph is presented in the top right corner that zooms in on early drive foam injection times where A, B, and C refer to the times drive liquid injection started, drive  $N_2$  injection was initiated, and when both injectants entered the core, respectively. The high fluctuations in pressure drop are due to gas/foam leaving the backpressure. Presented pressure drop profiles were constructed by applying a moving average (interval of 6) to the original data. Note that PV refers to total PV, i.e. slug + drive.

The pressure drop profile for Exp. 4 (**Figure 5.6C**) shows the same step-wise increase towards  $28 \pm 2$  mbar as soon as the co-injected gas and drive fluid entered the core. Afterwards, instead of a slight reduction (Exp. 2 and 3), the total pressure drop started to increase gradually. The gradually increasing total pressure drop observed in Exp. 4 seemed to occur as soon as the co-injectants

reached the oil bank. The latter is in agreement with our earlier work at model conditions (**Figure 4.5**). This may be explained as follows. A rather weak drive foam was generated and propagated upstream of the oil bank. However, foam generation seems to increase upon touching the oil bank, yielding the more equally divided gas phase (**Figure 5.5E**), thus displacing the banked oil toward the outlet. The proposed mechanism for the latter is described in more detail in **Section 3.4.3**. After foam breakthrough (at  $0.99 \pm 0.02$  PV), total pressure drop decreased toward a steady-state value corresponding to a *MRF* of  $4 \pm 2$ . Comparison with Exp. 3 (under-optimum salinity) indicates that a somewhat more favourable, i.e. lower, drive mobility was achieved in Exp. 4 (optimum salinity) during oil bank displacement.

For assessing the impact of pre-generated foam on the measured total pressure drops during drive foam injection, Exp. 4 is compared with Exp. 5 (**Figure 5.6C and D**). Directly, after the pre-generated foam entered the sandstone core, an instantaneous jump in pressure drop to  $53 \pm 1$  mbar was seen. Subsequently, a small increase followed by a gradually decreasing trend in pressure difference was measured. This behaviour is most probably related to a combination of the oil bank being produced and further development of the drive foam. Eventually, after breakthrough of the drive foam at  $1.24 \pm 0.02$  PV, pressure drops reached steady values in agreement with an averaged *MRF* of  $9 \pm 3$ . Results showed that injecting a pre-generated foam drive (Exp. 5) yields a more favourable drive mobility, delayed foam breakthrough, and thus a more efficient displacement of the banked oil compared to in-situ drive foam generation (Exp. 4).

### 5.3.3.3 Oil recovery

**Figure 5.7** presents the cumulative oil recovery profiles during water flooding (Exp. 5) and surfactant slug and drive co-injection (Exp. 3, 4, and 5). The recovery profiles for Exp. 2 could not be generated because of electrical failures. Because all *FACF* core-floods performed showed very similar oil recovery profiles during water flooding, only Exp. 5 is highlighted here. Prior to water breakthrough, an oil recovery of  $48 \pm 3\%$  of the *OIIP* was reached. This could be increased further to  $58 \pm 3\%$  of the *OIIP* at the end of water flooding (**Table 5.8**). Next, the effects of slug salinity and drive foam strength, that is, co-injection versus pre-generated, on the oil recovery during the performed *FACF* core-floods will be discussed.

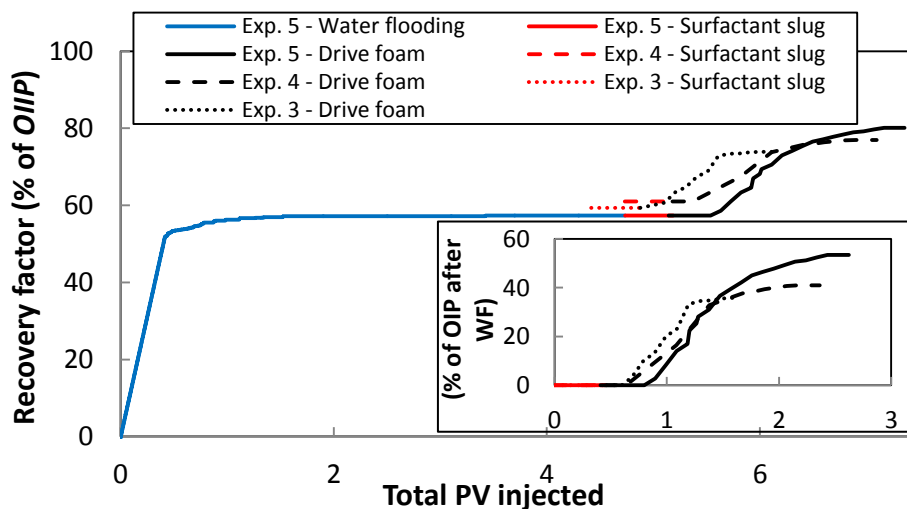


**Figure 5.7:** Oil recovery profiles during water flooding (Exp. 5), surfactant slug and drive foam injection (Exp. 3, 4, and 5). The recovery shown is expressed as a percentage of the oil initially in place (*OIIP*). The lower right graph states the oil recovery, during surfactant slug and drive injection in Exp. 3, 4, and 5, as percentage of the oil in place (*OIP*) after water flooding. All recovery profiles were constructed using material balance calculations. Drive injection continued in each experiment until no more oil was produced.

For assessing the impact of surfactant slug salinity, Exp. 3 (under-optimum salinity) is compared with Exp. 4 (optimum salinity). When shifting from under-optimum salinity conditions in Exp. 3 toward the optimum salinity applied in Exp. 4, the recovery factor could be increased with 5% of the *OIP* after water flooding. This can be attributed to a better displacement efficiency, i.e. lower *o/w IFT*, in Exp. 4. Moreover, the pressure drop profile related to Exp. 4 (**Figure 5.6C**) also suggests a more favourable, lower, drive mobility during oil bank displacement (compared with Exp. 3) which may promote oil recovery in Exp. 4. Oil bank breakthrough happened slightly earlier in Exp. 3 compared to Exp. 4 because of the oil bank shape and position, formed during slug injection (**Figure 5.4A and C**). After complete production of the banked oil in Exp. 3 and 4, part of the oil was produced as solubilized oil, resulting in the tail-shaped production profile after approximately  $1.30 \pm 0.20$  total PV slug and drive injected (**Figure 5.7**).

For studying the impact of drive foam strength (pre-generated vs. in-situ generated) on the oil being recovered in a *FACF* process conducted at optimum salinity, Exp. 4 is compared with Exp. 5. The experimental results presented in this study showed that the ultimate oil recovery could be increased with 13% of the *OIP* after water flooding when injecting pre-generated drive foam as an alternative to conducting co-injection. The increment in oil recovery can be fully assigned to the more favourable drive mobility, i.e. higher apparent drive foam viscosity, in Exp. 5 as the *o/w IFT* and total injection rates were kept constant. The more promising drive mobility in Exp. 5 most probably also resulted in a somewhat more efficient oil bank displacement which in turn might explain the delayed oil bank breakthrough time compared to Exp. 4. In Exp. 4, the gravity underriding tendency of the liquid slug and drive (**Figures 5.4C and 5.5C**) might yield a relatively early breakthrough of the oil bank's leading edge. After approximately  $2.05 \pm 0.02$  PV slug and drive injected, a type III *ME* broke through in Exp. 5.

## 5.4 General discussion

In this section, the results presented and observations made in this study will be discussed in terms of applicability to real-field conditions. Our experimental setting yielded a capillary number (**Equation 3.1**) of  $10^{-5}$  and  $10^{-4}$  for under-optimum and optimum salinity conditions, respectively. It resulted in the mobilization of  $S_{or\_WF}$  as depicted in **Figure 5.4**. One may argue whether it is realistic to expect the same relative amount of oil being mobilized at the conditions of the case study reservoir, at constant capillary number. This is most likely not the case. Although reservoir rocks exhibit similar porosities compared to the Bentheimer sandstone cores used in this work (**Section 5.2.2**), their absolute permeability is considerably lower (0.64 vs.  $3.39 \pm 0.47$  Darcy). At fixed capillary number, i.e. constant injection velocity, *o/w IFT*, and fluid viscosity, a lower absolute permeability will result in a higher pressure drop. The latter implying an increased capacity to mobilize and displace residual oil, during surfactant slug injection, at the conditions of the case study reservoir compared to the experimental setting in this work (Yeganeh *et al.*, 2016). Note that the latter is only valid when we assume a similar, unaltered, rock wettability for the reservoir rock compared to the cores used in this work. However, because reservoir pressures are in the order of 200 bar, which is far higher than the experimental pressure of 20 bar, this assumption might be too simplistic. As elevated pressures may cause the reservoir rock to change its wettability towards more oil-wet conditions (Pan *et al.*, 2018), oil may be absorbed onto the rock which subsequently can lead to a higher capillary resistance that enhances the pressure drop. In this case, higher pressure drop does not necessarily imply larger mobilization capacity of residual oil.

As discussed in **Sections 5.3.3.1** and **5.3.3.2**, the relatively dominant gravitational forces led to an unstable oil bank formation at both slug salinities studied (**Figure 5.4**). It is essential to note that these observations are related to a sandstone core with a diameter of  $3.80 \pm 0.10$  cm only. The case study reservoir has an averaged net thickness of approximately 18 m. It is expected that for real-field conditions, the gravity underriding effect of the liquid surfactant slug is of a considerably higher magnitude compared to the experimental findings in this work. As a consequence, most probably only the lower part of the reservoir will be properly swept (**Figure 5.5C**). One might compensate for this effect by adding a polymer to or foam the surfactant slug in order to favour the mobility ratio (Turta, 2013).

The core-flood experiments conducted in this study showed that injection of pre-generated Surfactant X drive foam yielded an increase of 13 % of the *OIP* after water flooding compared to in-situ drive foam generation at optimum salinity (Exp. 4 vs. 5) because of the more favourable drive mobility. In terms of real-field conditions, Exp. 5 might be quite representative. Assuming near-zero oil saturations in the near-wellbore region, as a consequence of the relatively high pressure drop in that area, it might function as a foam generator [equivalent to the mixing tee installed for Exp. 5 (**Figure 5.1**)].

## 5.5 Conclusions

A laboratory study on the feasibility of *FACF* for *EOR* was conducted at reservoir temperature of  $90 \pm 1$  °C in Bentheimer sandstones utilizing crude oil. Dedicated phase behaviour and bulk foam experiments yielded the design of a surfactant slug and drive solution that was used in core-flood experiments. Controlled (CT-assisted) *FACF* core-flood experiments were performed where an IOS2024 surfactant slug mobilized residual oil to waterflood and, afterwards, Surfactant X drive foam displaced the mobilized oil bank. Drive foam strength, i.e. in-situ drive foam generation by co-injection versus injecting a pre-generated drive foam, and surfactant slug salinity were varied.

Phase behaviour studies performed at reservoir temperature showed that Surfactant X does not lower the oil-water interfacial tension to ultralow values, whereas IOS2024 does. The designed IOS2024 surfactant slug revealed a Winsor Type III system (optimum salinity conditions) at salinities of 1.50–1.75 wt % NaCl + KCl. The addition of 1-iododecane to the oleic phase did not alter the crude oil-IOS2024 phase behaviour.

Bulk foam experiments in the absence of oil showed a roughly 11 times greater foam half-decay time for the Surfactant X drive solution compared to the IOS2024 drive formulation. The addition of 5 volume percent crude oil to the drive solution reduced the foam half-decay time of the Surfactant X drive foam with approximately a factor 12 in bulk.

The foam quality scan showed that the Surfactant X drive formulation was able to generate strong, stable foams in a Bentheimer sandstone for all gas fractional flows assessed in the absence of crude oil. The largest apparent foam viscosity of  $1.45 \pm 0.11$  Pa·s was reached at a foam quality of 75.0%. Foam qualities below are in the low foam-quality regime, whereas higher foam qualities describe the high-quality regime. A 57.5% foam quality resulted in an apparent foam viscosity of  $1.32 \pm 0.05$  Pa·s.

An unstable oil bank was formed during both under-optimum and optimum salinity *FACF* because of relatively dominant gravitational forces. The IOS2024 surfactant slug at optimum salinity was

significantly more effective at reducing residual oil to waterflood (81% reduction) compared to the under-optimum salinity slug (30% reduction).

Optimum salinity *FACF* was able to increase its ultimate oil recovery to  $40 \pm 5\%$  of the *OIP* after water flooding while under-optimum salinity *FACF* yielded an oil recovery of  $35 \pm 7\%$ . The injection of pre-generated Surfactant X drive foam yielded an increase of 13% of the *OIP* after water flooding compared to in-situ drive foam generation by co-injection, both performed at optimum salinity.

## 6. Mechanistic modelling of water-alternating-gas injection and foam-assisted chemical flooding

---

### Abstract

*History-matching of core-flood experimental data through numerical modelling is a powerful tool to get insight into the relevant physical parameters and mechanisms that control fluid flow in enhanced oil recovery processes. We conducted a mechanistic numerical simulation study aiming at modelling previously performed water-alternating-gas and foam-assisted chemical flooding core-flood experiments. For each experiment, a one-dimensional model was built. Obtained CT scan data was used in order to assign varying porosity, and permeability, values to each grid block. The main goal of this study was to history-match measured phase saturation profiles along the core length, pressure drops, produced phase cuts, and oil recovery profiles for each of the experiments simulated. Results show that, in order to obtain a good match for the water-alternating-gas experiment, gas relative permeability needed to be reduced as function of injection time due to gas trapping. The surfactant phase behaviour was successfully simulated and its robustness was verified by effectively applying the same phase behaviour model to the two different salinity conditions studied. It resulted in the oil mobilization, through the injection of a surfactant slug, being properly modelled. The mechanistic simulation of foam using the steady-state foam model built in UTCHEM proved inadequate for the mechanistic modelling of a foam drive in presence of oil. An alternative heuristic approach was adopted to overcome this limitation.*

---

The content of this chapter is based on the following publication:

Janssen, M.T.G., Torres Mendez, F.A., and Zitha, P.L.J. Mechanistic Modelling of Water-Alternating-Gas Injection and Foam-Assisted Chemical Flooding for Enhanced Oil Recovery. *Submitted to Industrial and Engineering Chemistry Research.*

## 6.1 Introduction

The experimental work presented in all previous chapters gives us a comprehensive picture of the *FACF* process, and related physical mechanisms, both in a model-like setting and at reservoir conditions. Corresponding results allowed us to come up with proposed mechanisms that are likely to take place during *FACF*. This chapter presents the final study of this thesis where multiple mechanistic models are developed in order to history-match *WAG* and *FACF* experiments at the model-like conditions imposed. This section continues with a short overview of the laboratory results of the *WAG* and *FACF* experiments performed.

In **Chapter 2** we presented an experimental study on continuous gas and *WAG* injection in Bentheimer sandstone cores. Experimental results suggest that, when applying *WAG* instead of immiscible gas injection, one can increase the ultimate oil recovery due to an increased  $E_V$  as a result of the establishment of  $S_{gt}$  (**Section 2.5**).

In **Section 1.3** we introduced an alternative to applying *WAG* for controlling gas mobility: foaming of the gas. The process that combines gas foaming, for ensuring a favourable  $E_V$ , with the use of a surfactant slug for achieving good  $E_D$ , is known as *FACF* (**Section 1.5**). The study presented in **Chapter 3** addressed the effect of the drive foam quality on oil bank propagation in a *FACF* process. It showed that the oil bank displacement, during a *FACF* process at model-like conditions, was most stable at the lowest foam quality investigated (**Section 3.5**). In **Chapter 4** we discussed the effect of surfactant slug salinity on the efficiency of *FACF* in a model-like setting. The increase in  $E_D$ , when performing *FACF* at (near-)optimum salinity conditions compared to under-optimum salinity, led to the formation of a more uniform and elongated oil bank. Eventually, the ultimate oil recovery could be increased with  $15 \pm 5\%$  of the *OIIP* when conducting *FACF* at (near-)optimum salinity conditions instead of under-optimum salinity (**Section 4.5**).

The goal of this study was the mechanistic modelling of *WAG* and *FACF* core-flood experiments presented in **Chapters 2, 3, and 4**. More specifically, we aimed to capture the underlying mechanisms that drives each of the aforementioned *EOR* processes. Simulation results were compared with experimental results to see whether we can validate the conclusions, and suggestions, made based on the experimental studies. For this purpose a three-dimensional chemical flooding simulator for multiphase and multicomponent systems was used: the UTCHEM simulator. The *FACF* core-floods presented in **Chapters 3 and 4** were modelled by including the surfactant phase behaviour as a function of salinity, fluid rheology, capillary desaturation of oil, gas mobility reduction due to foam generation, and potential essential geochemical reactions that occurred in the sandstone core. All simulations were performed under an one-dimensional configuration.

## 6.2 Materials and methods

### 6.2.1 *WAG* injection

The first experiment that was simulated using the UTCHEM simulator is the *WAG* experiment (Exp. 3 in **Table 2.4**). Related chemicals, utilized for performing the *WAG* experiment, are shown in **Tables 2.1 and 2.2**. Physical properties of the sandstone core used are presented in **Table 2.3**. The experimental set-up and procedure are shown in **Figure 2.1** and **Table 2.5**, respectively.

### 6.2.2 Foam-assisted chemical flooding

The second simulated experiment is the extended surfactant slug injection experiment (Exp. 1 in **Table 3.2**). Simulations 3 to 5 represent Exp. 2 to 4 in **Table 3.2**, respectively. The chemicals and sandstone samples used in these experiments are discussed in **Sections 3.2.1** and **3.2.2**. The experimental set-up and procedure utilized for these four core-flood experiments is shown in **Figure 3.1** and **Table 3.3**, respectively.

The final experiment that was modelled in this study is *FACF* at (near-)optimum salinity conditions (i.e. Exp. 2 in **Table 4.3**). Related chemical and core samples, that were used for successfully conducting the experiment, are presented in **Sections 4.2.1** and **4.2.2**. Information regarding the experimental set-up and procedure used for performing the (near-)optimum *FACF* can be found in **Sections 4.2.3** and **4.2.5.3**, respectively. **Table 6.1** presents an overview of all the simulations conducted in this study.

**Table 6.1:** Overview of core-flood experiments simulated in this study.

Simulation	Procedure	Information on chemicals and core samples	Information on experimental set-up and procedure
1	WAG	Sections 2.2.1 and 2.2.2	Sections 2.2.3 and 2.2.5
2	AS	Sections 3.2.1 and 3.2.2	Sections 3.2.3 and 3.2.5
3	FACF	Sections 3.2.1 and 3.2.2	Sections 3.2.3 and 3.2.5
4	FACF	Sections 3.2.1 and 3.2.2	Sections 3.2.3 and 3.2.5
5	FACF	Sections 3.2.1 and 3.2.2	Sections 3.2.3 and 3.2.5
6 <sup>a</sup>	FACF	Sections 4.2.1 and 4.2.2	Sections 4.2.3 and 4.2.5

<sup>a</sup>In Simulation 6 the drive foam part was not modelled since we aimed to compare oil mobilization by slug injection at under-optimum salinity (Simulation 3) to injection at (near-)optimum salinity (Simulation 6).

### 6.2.3 UTCHEM simulator

Recently, only a few three-phase chemical flooding simulators have been developed that are able to model the oil-water-*ME* equilibrium state (Goudarzi *et al.*, 2013; Lashgari *et al.*, 2015a; Lashgari *et al.*, 2015b; Fortenberry *et al.*, 2015). These simulators are suitable for modelling *EOR* applications such as surfactant flooding and *ASP* injection. Well-known commercial reservoir simulators like ECLIPSE, STARS, INTERSECT, and VIP are only capable of modelling three-phase oil-water-gas conditions, appropriate for simulating gas flooding and *WAG* (Lashgari *et al.*, 2015c). However, in order to capture all physical mechanisms related to *FACF*, a four-phase oil-water-gas-*ME* equilibrium model is required: UTCHEM. The results presented throughout this study were acquired using UTCHEM-2017.3. It is a finite difference implicit pressure explicit concentration, i.e. IMPES type, formulation that was developed at the Center for Petroleum and Geosystems Engineering at The University of Texas in Austin (Delshad *et al.*, 2006).

In order to simulate chemical *EOR* with gas, UTCHEM couples a black-oil model (for oil-water-gas systems) with Hand's rule for *ME* phase behaviour (oil-water-*ME* systems). Hand's rule (Hand, 1939) is used to calculate the oil-water-surfactant phase behaviour as function of salinity and concentrations. **Figure 6.1** presents a schematic that illustrates how the equilibrium between the several phases is calculated for an oil-water-gas-*ME* system.

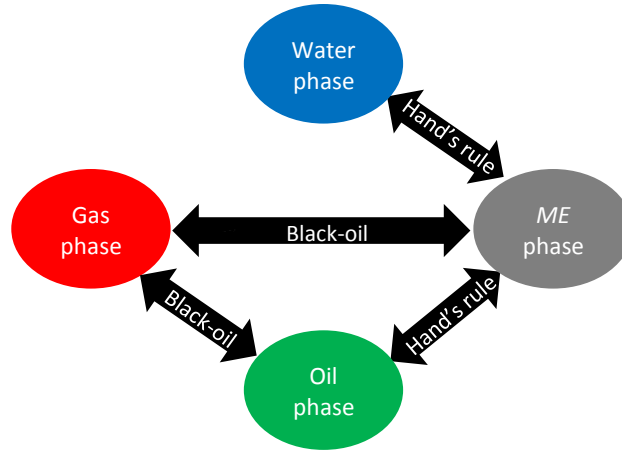


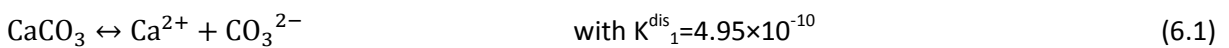
Figure 6.1: Four-phase coupling scheme in UTCHEM for an oil-water-gas-ME system.

## 6.3 Results and discussion

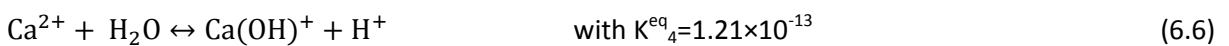
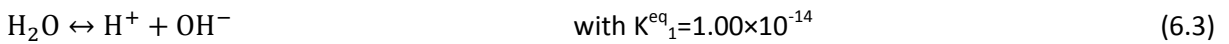
### 6.3.1 Geochemical reactions

EQBATCH, the geochemical module of UTCHEM, was used to obtain initial equilibrium concentrations of various components within the aqueous phase. It describes geochemical reactions that occurred in the sandstone core during the flooding processes. These initial conditions, of the components within the aqueous phase, serve as an input for the final UTCHEM model. In order to set up the geochemical model, the rock's mineralogical composition, together with the formation water composition, should be considered. Ion exchange reactions with rock minerals, soap generation, dissolution/precipitation reactions, and aqueous phase reactions are crucial features for the numerical simulation of surfactant-based flooding. In this section we discuss the geochemical model related to Simulation 2 (Table 6.1).

The formation water considered contains the following components: 2.0 wt% NaCl and small amounts of calcium and carbonate ions ( $\text{Ca}^{2+}$  and  $\text{CO}_3^{2-}$ , respectively) that came from the calcite mineral (carbonate minerals in Table 6.2) as a result of the following dissolution reactions:



Moreover, we considered the following aqueous reactions:



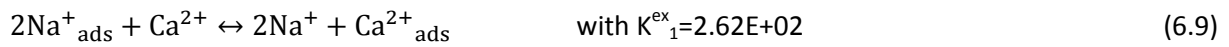
## Chapter 6 – Mechanistic modelling of water-alternating-gas injection and foam-assisted chemical flooding

The abovementioned equilibrium constants (K) were obtained from the MINTEQA thermodynamic database (Plummer and Busenberg, 1982; Nordstrom *et al.*, 1990).

**Table 6.2:** Mineralogical composition of a Bentheimer sandstone core (Peksa *et al.*, 2015). The numbers represent weight percentages (wt%).

Quartz	Feldspar	Clay minerals	Carbonate minerals	Other
91.70	4.86	2.68	0.41	0.35

From **Table 6.2** it can be concluded that the rock type used consists mainly of quartz minerals. However, a small amount of clay minerals are present; e.g. Kaolinite. The presence of Kaolinite, which is a weathering product of Feldspars, implies the manifestation of the interchange between a cation in solution and another cation on the clay's surface (i.e. cation exchange reactions). As  $\text{Ca}^{2+}$ ,  $\text{CO}_3^{2-}$ , sodium ions ( $\text{Na}^+$ ), and hydrogen ions ( $\text{H}^+$ ) are all present in the formation water, the following cation exchange reactions are considered:



The exchange constants were taken from Sheng (2015). The exchange capacity of the rock was assumed to be 0.047 mEq/ml (Hosseini-Nasab *et al.*, 2016). It determines the amount of cations that can be adsorbed onto the rock. In the aforementioned geochemical model the following assumptions were made: a) dissolution of quartz was assumed to be negligible as the experiment was performed at room temperature (Fournier and Rowe, 1977), b) in-situ generation of soap was ignored as the model oil used did not contain any naphthenic acids, and c) the major cause of alkali loss was assumed to be due to the cation exchange between  $\text{Na}^+$  and  $\text{H}^+$ . The EQBATCH output file defines new initial component concentrations of the formation water; initial conditions of chemical *EOR*.

### 6.3.2 Model set-up: grid size, porosity, permeability, and initial water saturation

For setting up the mechanistic model, for the aid of history-matching previously performed experiments, we assume one-dimensional displacement with the amount of grid blocks in the x-direction equal to one-fourth of the amount of CT slices taken (Simulations 2 to 6). For Simulation 1, we set the amount of grid blocks in the z-direction equal to 100, as corresponding experiment was conducted vertically. The porosity and permeability values assigned to each grid block in Simulation 1 was constant for each block and correspond to the porosity and permeability values for Exp. 3 presented in **Table 2.3**. For Simulations 2 to 6, porosity values were calculated per CT slice (**Appendix A**), averaged over 4 consecutive CT slices, and finally assigned to a grid block. In order to allocate an absolute permeability value to each grid block, in Simulations 2 to 6, the Carman-Kozeny equation, which relates porosity to absolute permeability, was used (Kozeny, 1927; Carman, 1937):

$$K = \frac{D_p^2 \varphi^3}{a(1-\varphi)^2} \quad (6.11)$$

where  $D_p$ ,  $\varphi$ , and  $a$  represent the average grain diameter in m, the porosity, and a constant factor to account for tortuosity, respectively. An averaged grain size diameter of 0.27 mm was used (Peksa *et al.*, 2015). The tortuosity factor was estimated by solving **Equation 6.11** for the core-sections over which we measured the sectional pressure drop (**Figure 3.1**), using the averaged porosity, based on CT processing, and absolute permeability to brine for that specific section. Finally, **Equation 6.11** was used for estimating absolute permeability values for each grid block separately.

The initial saturation conditions per grid cell at each injection phase were obtained by a standard restart procedure. At the start of the experiments, i.e. prior to oil injection (primary drainage), all grid blocks were at  $S_w = 100\%$ . For the following injection stages, the output of the previous injection phase was used as an input for the current injection stage for all dependent variables. During the mechanistic modelling of the various *EOR* injection strategies assessed, the following assumptions were made: a) rock compressibility is negligible, b) there is no wettability alteration, c) fluids are incompressible, and c) rock is strongly water-wet. **Appendix C** presents an overview of the basic simulation parameters used per injection stage per simulation.

### 6.3.3 Primary drainage and forced imbibition

In order to history-match pressure drops and saturation distributions during primary drainage and water flooding, it is crucial to select correct  $k_r$  functions for both the aqueous and oleic phases. **Appendix D** presents an overview of  $k_r$  curves, and parameters, used for simulating primary drainage and forced imbibition in all simulations performed. In this section, we only highlight Simulation 3 as it is prototypical of all mechanistic models constructed. **Figure 6.2** presents the relative permeability curves and parameters, respectively, used for simulating primary drainage and forced imbibition in Simulation 3.

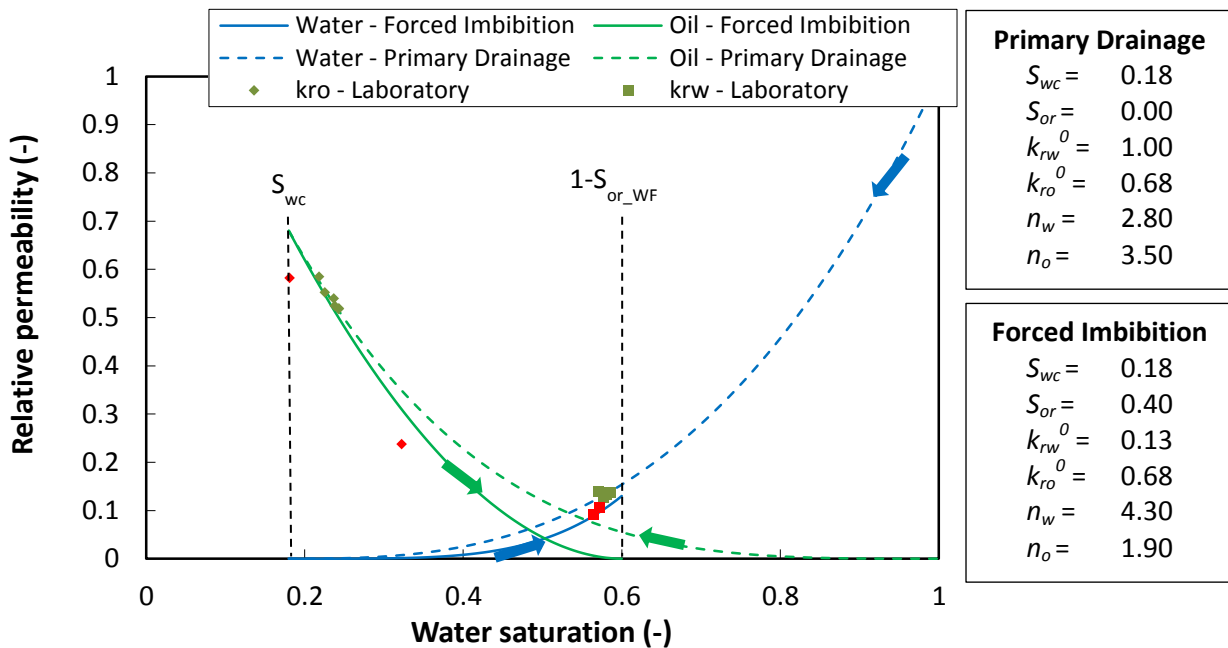


**Figure 6.2:** Relative permeability curves for the aqueous (blue) and oleic (green) phases during primary drainage (dashed lines) and water flooding (continuous lines) used for Simulation 3. More information on how we used the experimental data to obtain a  $k_{ro}^0$  and  $k_{rw}^0$  for simulation purposes is given in **Appendix D.7**. The red diamonds and squares are considered to be outliers (**Appendix D.7**). The two tables on the right-hand side present the  $k_r$  parameters for both injection stages using the Corey-type functions within UTCHEM (UTCHEM Technical Documentation, 2017).

During primary drainage, i.e. oil injection, the wetting phase saturation decreased from 1.00 to a  $S_{wc}$  of 0.18. The displacement of brine by oil followed the blue dashed line downward and the green dashed line upward until it reached  $S_{wc}$  (**Figure 6.2**). This is the starting point of water flooding, i.e. forced imbibition. During water flooding, water is displacing oil, reducing the non-wetting phase saturation according to the continuous green line downward and the continuous blue line upward until  $S_{or\_WF}$  was reached (**Figure 6.2**).

Simulated pressure drops, phase cuts, and saturation profiles were compared with results obtained from the laboratory. **Figure 6.3** shows a good match between measured pressure drops in the laboratory and corresponding simulated pressure drops, for both primary drainage and water flooding. As soon as drainage was initiated, pressure drops gradually increased until oil breakthrough occurred. Afterwards, a plateau value was reached. The exact same behaviour in pressure drop was seen during water flooding. Note that flowrates were varied at the end of each injection stage in order to estimate  $k_{ro}^0$  and  $k_{rw}^0$  (**Section 3.2.5.2**).

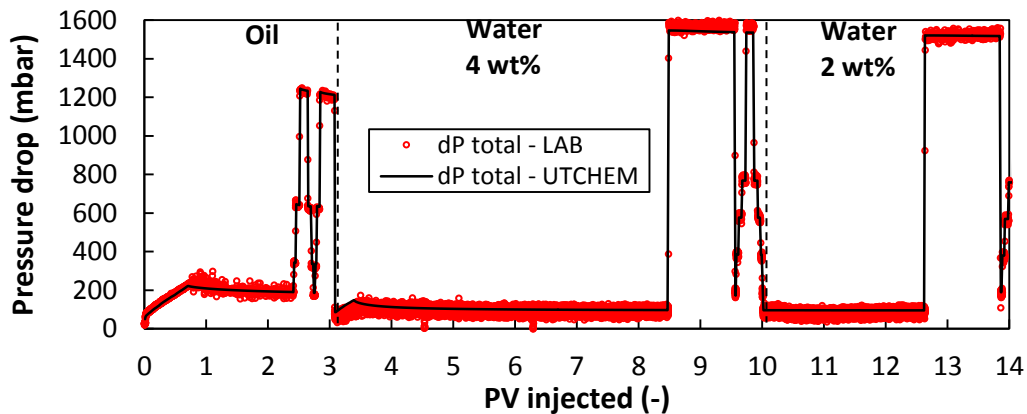


**Figure 6.3:** Simulated and measured total pressure drop profiles for primary drainage (oil) and water flooding (water) for Simulation 3. Approximately 3.0 PV of oil was injected prior to water flooding.

**Figure 6.4** presents the simulated and processed  $S_o$  profiles as function of distance from inlet for both primary drainage and water flooding in Simulation 3. The profiles for oil injection show typical Buckley-Leverett displacement behaviour, including a shock front region with a rarefaction wave upstream of it (Buckley and Leverett, 1942). Eventually, an  $S_{oi}$  of  $0.76 \pm 0.03$  was reached in the simulation, which is very similar to the measured  $S_{oi}$  of  $0.78 \pm 0.04$  (Exp. 2 in **Table 3.4**). Note that the simulated positions of the displacement fronts (0.30 and 0.52 PV) are located somewhat more downstream compared to our observations. The latter yielded an oil breakthrough time of 0.71 PV;  $0.04 \pm 0.02$  PV earlier compared to experimental data. Note the magnified capillary end effect simulated. The simulated saturation profiles for water flooding (**Figure 6.4B**) show similar behaviour to that for primary drainage (**Figure 6.4A**). Although we could capture the location of the displacement front at 0.19 PV injected very well, water breakthrough happened  $0.04 \pm 0.02$  PV earlier in the simulation compared to our observations. A  $S_{or\_WF}$  of  $0.40 \pm 0.01$  was reached in the simulation which corresponds well with the measured one of  $0.41 \pm 0.02$  (Exp. 2 in **Table 3.4**). **Figure 6.5** presents measured and simulated phase cuts during both injection stages. **Appendix E** presents observed and simulated pressure drops,  $S_o$  profiles (if available), and phase cuts (if available) for Simulations 1 – 2 and 4 – 6 during primary drainage and forced imbibition.

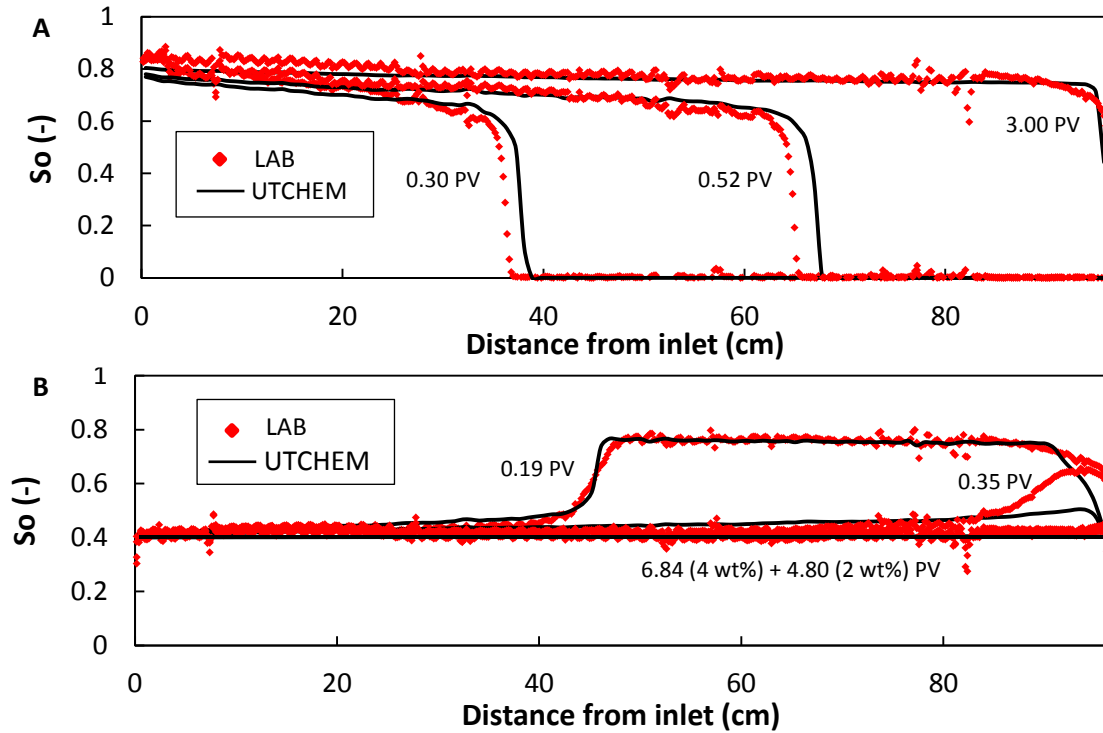


Figure 6.4: Oil saturation profiles obtained from experimental data and simulation for primary drainage (A) and water flooding (B) in Simulation 3.

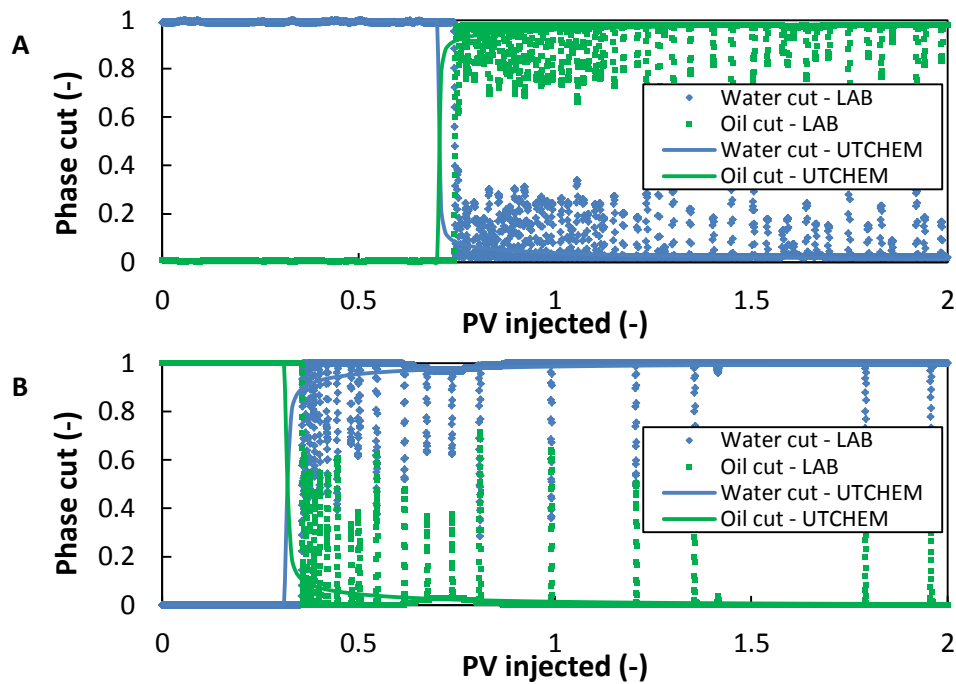


Figure 6.5: Comparison between measured and simulated phase cuts during primary drainage (A) and water flooding (B) in Simulation 3.

### 6.3.4 WAG injection

After the mechanistic modelling of primary drainage, WAG flooding was simulated for Simulation 1 (Table 6.1). In order to do so, it is essential to select appropriate  $k_r$  functions for the three-phase system present in the simulation. Appendix F presents an overview of the  $k_r$  curves used as an input for the mechanistic modelling of WAG injection at  $S_{oi}$ . Figure 6.6 presents the  $k_{rg}$  curves used for simulating WAG injection. It clearly indicates that, in order to properly match our experimental observations,  $k_{rg}$  needed to be reduced as function of increasing WAG cycles. The latter seems to support the statement made in Section 2.5: the establishment of  $S_{gt}$  reduced gas mobility in subsequent WAG cycles.

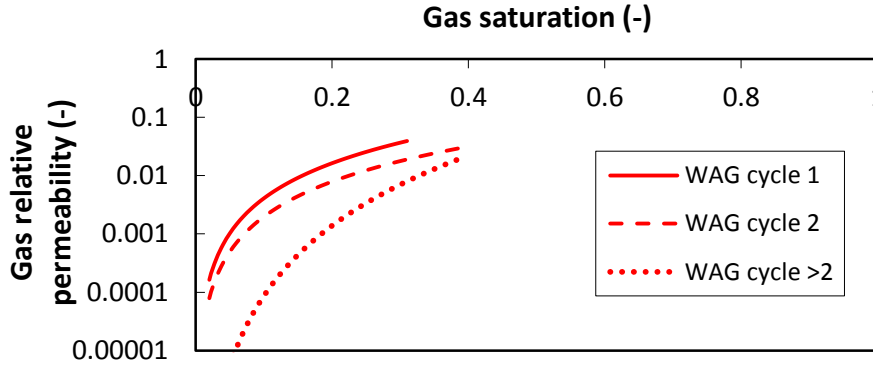


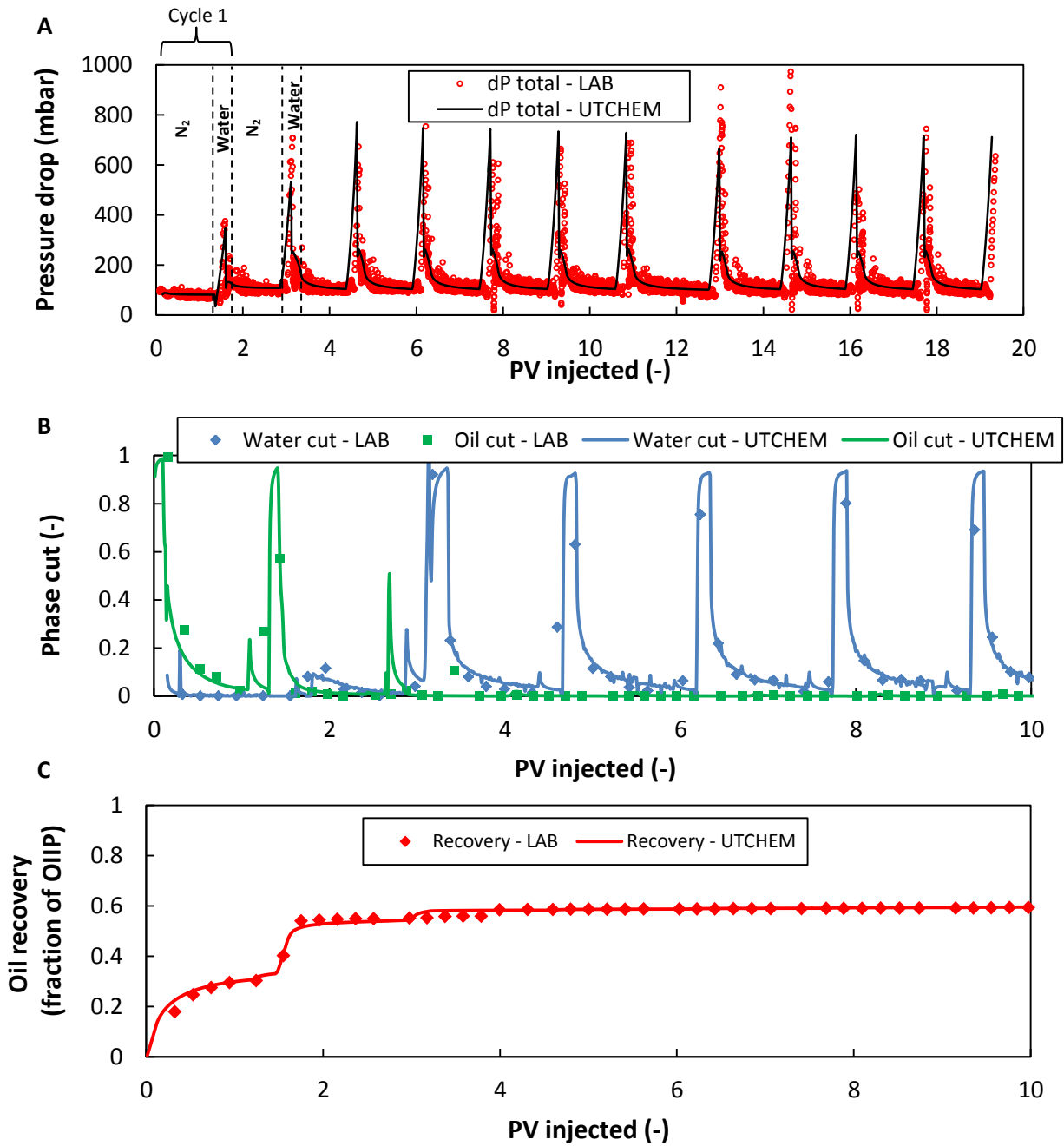
Figure 6.6:  $k_{rg}$  curves used as an input for simulating WAG injection in Simulation 1.

Figure 6.7 presents observed and simulated pressure drops, phase cuts, and oil recovery profiles for Simulation 1. An excellent match was obtained between the simulated and measured pressure drops. The sharp increase in pressure drop due to the shift from gas to water injection obtained from the experiments (see Section 2.3.4.1) was correctly reproduced by the simulations. The latter is a combined result of an increasing injection rate as soon as the water slug was injected, and the reduced  $k_{rg}$  as function of increasing WAG cycles (Figure 6.6). The higher steady-state pressure drop simulated for gas injection during the second WAG cycle, compared to the first WAG cycle, is due to the reduced  $k_{rg}$  (i.e. presence of  $S_{gt}$ ) in combination with the introduced water phase in the previous cycle. In general, a good match between the measured and simulated phase cuts (Figure 6.7B) was achieved. However, simulation results show a peak in oil cut at approximately 2.7 PV injected, whereas experimental observations suggest the presence of this peak at a later stage (roughly at 3.5 PV injected). The oil recovery plot (Figure 6.7C) clearly shows a reasonably good match between experimental observations and simulation results. The data noticeably shows that bulk of the oil was produced throughout the first two WAG cycles, as discussed in Section 2.3.5.

### 6.3.5 Surfactant phase behaviour simulation

A detailed phase behaviour model is one of the key aspects of simulating surfactant flooding in UTCHEM. The relevant phase behaviour model parameters for the different phases, i.e. aqueous, oleic, and ME phases, can be obtained by fitting the available models to the oil and water solubilisation ratios obtained from the laboratory. The solubilisation ratio of phase  $l$  is given by the ratio of the concentration of phase  $l$  solubilized in the ME to the concentration of the surfactant present in the ME:

$$R_{l3} = \frac{C_{l3}}{C_{33}} \text{ for } l = 1 (\text{water}), 2 (\text{oil}) \quad (6.12)$$



**Figure 6.7:** Simulated and measured total pressure drop profiles (A), oil and water cut (B), and oil recovery (C) during WAG injection at  $S_{oi}$  (Simulation 1). Oil recoveries are expressed as a fraction of the oil initially in place.

where  $R_{l3}$ ,  $C_{l3}$ , and  $C_{33}$  are respectively the solubilisation ratio, the concentration of phase  $l$  solubilized in the  $ME$ , and the surfactant concentration solubilized in the  $ME$ . A salinity scan was conducted in order to assess the ability of the surfactant concentration used to lower the  $o/w$  IFT at various salinities of the aqueous phase. Its result, together with the simulated solubilisation ratios, is shown in **Figure 6.8**. Several simulations were performed under batch mode using model reservoir parameters to model the phase behaviour of our oil-water-surfactant system (**Table 6.3**). UTCHEM uses Hand's model (Hand, 1939) to represent the phase behaviour. The height of binodal curve (HBNC), and the lower (CSEL) and upper (CSEU) effective salinities are used to solve the model. These parameters can be found by matching the experimental phase behaviour data. As the salinity scan performed used an  $o/w$  ratio of 1:2, phase behaviour simulations were carried out using 33/67 vol.% oil and water concentrations, respectively. Water and oil viscosities were set at 1.0 cP. Water, oil,

surfactant, and co-solvent were co-injected for several PV in order to reach steady state flow which represents equilibrium conditions in the salinity scan conducted in the laboratory. The used reservoir properties and phase behaviour parameters (HBNCs, CSEL, and CSEU) are shown in **Table 6.3**. **Figure 6.8** presents the final simulated solubilisation ratio's with the ones estimated in the laboratory.

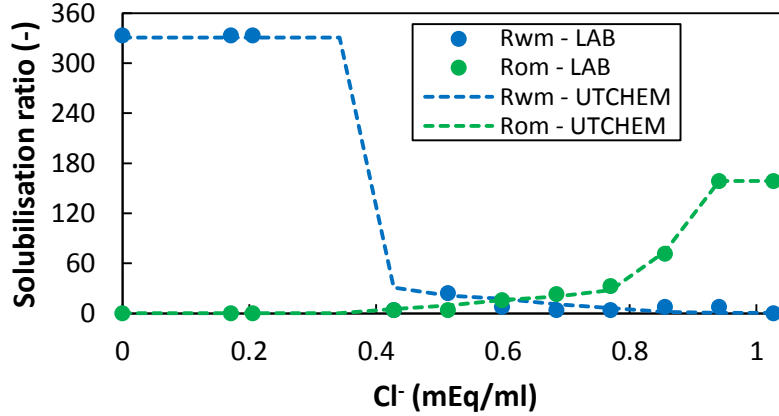


**Figure 6.8:** Simulated water ( $R_{wm}$ ) and oil ( $R_{om}$ ) solubilisation ratios compared with the measured ones in the laboratory as function of milliequivalent  $Cl^-$  per millilitre water. Simulated solubilisation ratios were used as an input for modelling (foam-assisted) chemical flooding in Simulations 2 to 6.

The match between simulated and estimated solubilisation ratios is fairly good. The computed optimum salinity range occurs between 0.43 – 0.77 mEq  $Cl^-$ /ml water for the oil-water-surfactant system assessed (**Section 6.2.3**), which is in good agreement with experimental data.

**Table 6.3:** Reservoir properties and phase behaviour model parameters used.

Parameter	Value
Simulation time (days)	350
Permeability (Darcy)	1000
Porosity (%)	100
Height of binodal curve at zero salinity (HBNC70)	0.061
Height of binodal curve at optimal salinity (HBNC71)	0.030
Height of binodal curve at twice optimal salinity (HBNC72)	0.061
Lower effective salinity (meq/mL) (CSEL7)	0.540
Upper effective salinity (meq/mL) (CSEU7)	1.070

### 6.3.6 Surfactant adsorption, ME viscosity, and IFT parameters

Surfactant adsorption was modelled in UTCHEM using a Langmuir-type isotherm which is a function of surfactant concentration, salinity, and rock permeability (Hirasaki and Pope, 1974). It is given by:

$$\hat{C}_3 = \min\left(\hat{C}_3, \frac{a_3(\hat{C}_3 - \hat{C}_3)}{1 + b_3(\hat{C}_3 - \hat{C}_3)}\right), \quad a_3 = (a_{31} + a_{32}C_{SE})\left(\frac{k_{ref}}{k}\right)^{0.5} \quad (6.13)$$

where  $\hat{C}_3$  is the adsorbed concentration of surfactant and  $\hat{C}_3$  represents the total surfactant concentration. Adsorption parameters  $a_3$  and  $b_3$  can be found by matching laboratory data, if available. The minimum is taken to ensure that the adsorbed concentration does not exceed the total surfactant concentration. Surfactant adsorption increases linearly with effective salinity ( $C_{SE}$ ), and decreases with increasing permeability ( $k$ ). All input parameters ( $a_{31}$ ,  $a_{32}$ , and  $b_3$ ) need to be specified at a reference permeability ( $k_{ref}$ ). Since we did not measure the amount of surfactant that retained in the core during surfactant flooding in the performed *FACF* core-floods, we used the average surfactant adsorption in Bentheimer sandstones measured by Battistutta et al. (2015) for the same type of surfactant slug:  $0.25 \pm 0.12$  mg/g rock. Note that this value for surfactant retention lies

within the ranges measured by Solairaj et al. (2012) who performed surfactant retention measurements for a large number of cores. Initially, model parameters were chosen that match the average surfactant adsorption of 0.25 mg/g rock. At a later stage, parameters were tuned in order to obtain a better match for the pressure drop and saturation profiles, whilst ensuring that the surfactant adsorption remained within its boundaries ( $0.25 \pm 0.12$  mg/g rock). **Figure 6.9** presents the final Langmuir-type adsorption isotherm that was used in Simulation 2.

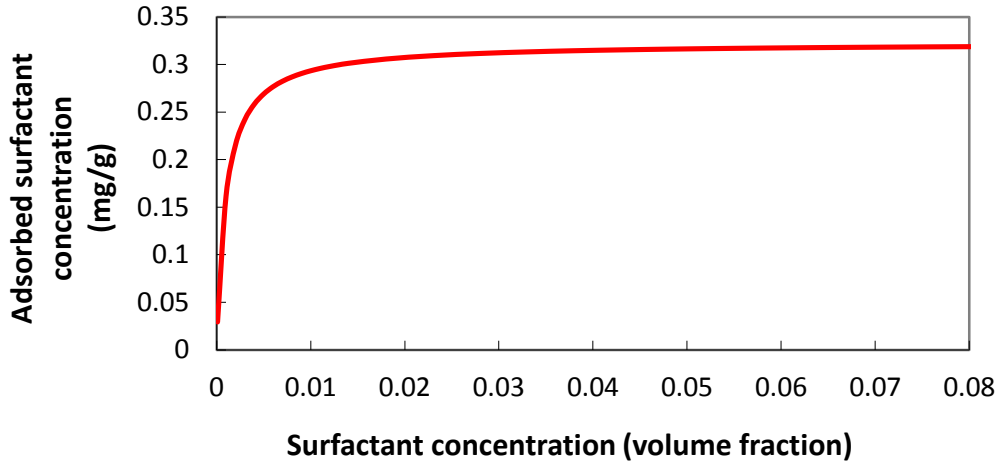


**Figure 6.9:** Langmuir-type isotherm used for modelling surfactant adsorption in Simulation 2. The best model fit was obtained when using a surfactant adsorption of 0.24 mg/g rock for the surfactant concentration used of 0.003 (volume fraction). This was achieved by using adsorption model parameters of 2.6, 0.5, and 1000 for respectively  $a_{31}$ ,  $a_{32}$ , and  $b_3$ .

The viscosity of the *ME* generated during the core-floods could not be measured. Therefore, the *ME* viscosity as function of aqueous phase salinity was initially determined using default parameters. *ME* viscosity parameters were adjusted, if needed, until a good match between measured and simulated pressure drops, and  $S_o$  profiles, was obtained. The resulting *ME* viscosity that was used in the mechanistic model equalled 1.41 cP (Simulation 2 to 5) or 1.67 cP (Simulation 6).

In order to estimate *ME*/oil and *ME*/water *IFTs*, a modified version of Huh's (1979) relationship was used:

$$\sigma_{l3} = \sigma_{ow} e^{-aR_{l3}} + \frac{cF_l}{R_{l3}^2} (1 - e^{-aR_{l3}^3}) \text{ for } l = 1 (\text{water}), 2 (\text{oil}) \quad (6.14)$$

where  $\sigma_{l3}$ ,  $\sigma_{ow}$ ,  $R_{l3}$  represent the phase *l*/*ME* *IFT* in mN/m, the *o/w* *IFT* in the absence of surfactant (roughly 24 mN/m), and the solubilisation ratio of phase *l* in phase 3 (**Equation 6.12**). **Equation 6.14** uses Hirasaki's correction factor,  $F_l$ , in order to ensure that the *IFT* equals zero at the plait-point (Hirasaki, 1981). The abovementioned equation contains two matching parameters, *c* and *a*, which were set to 0.1 (*c*) and 20 (*a*) for all simulations.

### 6.3.7 Relative permeabilities surfactant flooding

For history-matching measured pressure drops, phase cuts, and  $S_o$  profiles, the  $k_r$  curves for both oil and water, at the respective salinity conditions during surfactant slug injection, are crucial. In order to construct such  $k_r$  curves, the Corey-type functions (Brooks and Corey, 1966) are used; similar to simulation of primary drainage and forced imbibition (**Section 6.3.3**). For modelling  $k_r$  for surfactant flooding, UTCHEM assumes that at optimum salinity conditions ultra-low *o/w* *IFT* is achieved, yielding miscible conditions. This assumption implies that at optimum salinity,  $k_{ro}^0$  and  $k_{rw}^0$  are unity as well as

the Corey exponents, and corresponding residual oil and water saturations equal zero. The  $k_{ro}$  and  $k_{rw}$  curves at under-optimum salinity surfactant injection are constructed by interpolating the  $k_r$  curves between forced imbibition (**Appendix D**) and the aforementioned optimum salinity conditions. **Figure 6.10** presents the representative  $k_{ro}$  and  $k_{rw}$  curves for forced imbibition (i.e. low trapping number), for optimum salinity (i.e. high trapping number), and for the under-optimum salinity conditions imposed in Simulation 2 (used for simulating surfactant slug injection). **Appendix G** presents the  $k_{ro}$  and  $k_{rw}$  curves used for the mechanistic modelling of surfactant slug injection in Simulations 3 to 6.

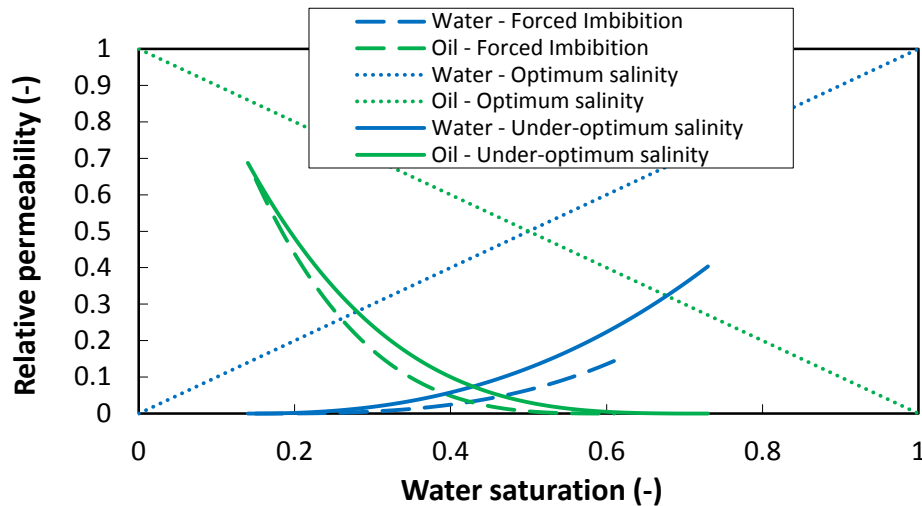


**Figure 6.10:** Oil and water relative permeability curves for forced imbibition, under-optimum, and optimum salinity flooding in Simulation 2. The curves for under-optimum salinity are used as input in the simulation.

### 6.3.8 Oil mobilization by surfactant slug injection

Once all aforementioned parameters were implemented in the UTCHEM model, simulated pressure drops and  $S_o$  profiles, for surfactant slug injection, were compared with the experimental results acquired in the laboratory. In this section we focus on Simulations 3 and 6 in order to shed light on the effect of salinity on oil mobilization during surfactant slug injection. **Figure 6.11** presents an overview of measured and simulated pressure drops and  $S_o$  profiles for surfactant slug injection in Simulations 3 (under-optimum salinity) and 6 (near-optimum salinity). Phase cuts and oil recovery profiles are not shown since no oil was recovered during the slug injection of approximately 0.46 PV. **Appendix H** presents the simulation results, during surfactant slug injection, for all other simulations. Note that the latter includes the mechanistic simulation of the baseline core-flood discussed in **Chapter 3**, i.e. extended surfactant flooding (Simulation 2 in **Table 6.1**).

To confirm the robustness of the phase behaviour model presented in **Section 6.3.5**, we applied it to the two different salinity conditions used in Simulations 3 and 6 (Exp. 1 and 2 in **Chapter 4**). **Figure 6.11A** shows a fairly good match between simulated and observed pressure drops for both cases. We were able to capture the gradually increasing trend in pressure drop, as function of PV injected, in Simulation 3, whereas Simulation 6 shows a fairly constant pressure drop as function of injection time; similar to related experimental observations (**Section 4.3.3.1.1**). The  $S_o$  profiles corresponding to Simulation 3 (**Figure 6.11B**) show in general a satisfactory match with related experimental observations. Peak  $S_o$  values within the generated oil bank were successfully matched, especially for later injection times (i.e. 0.38 and 0.46 PV). Although experimental results indicate that, as injection

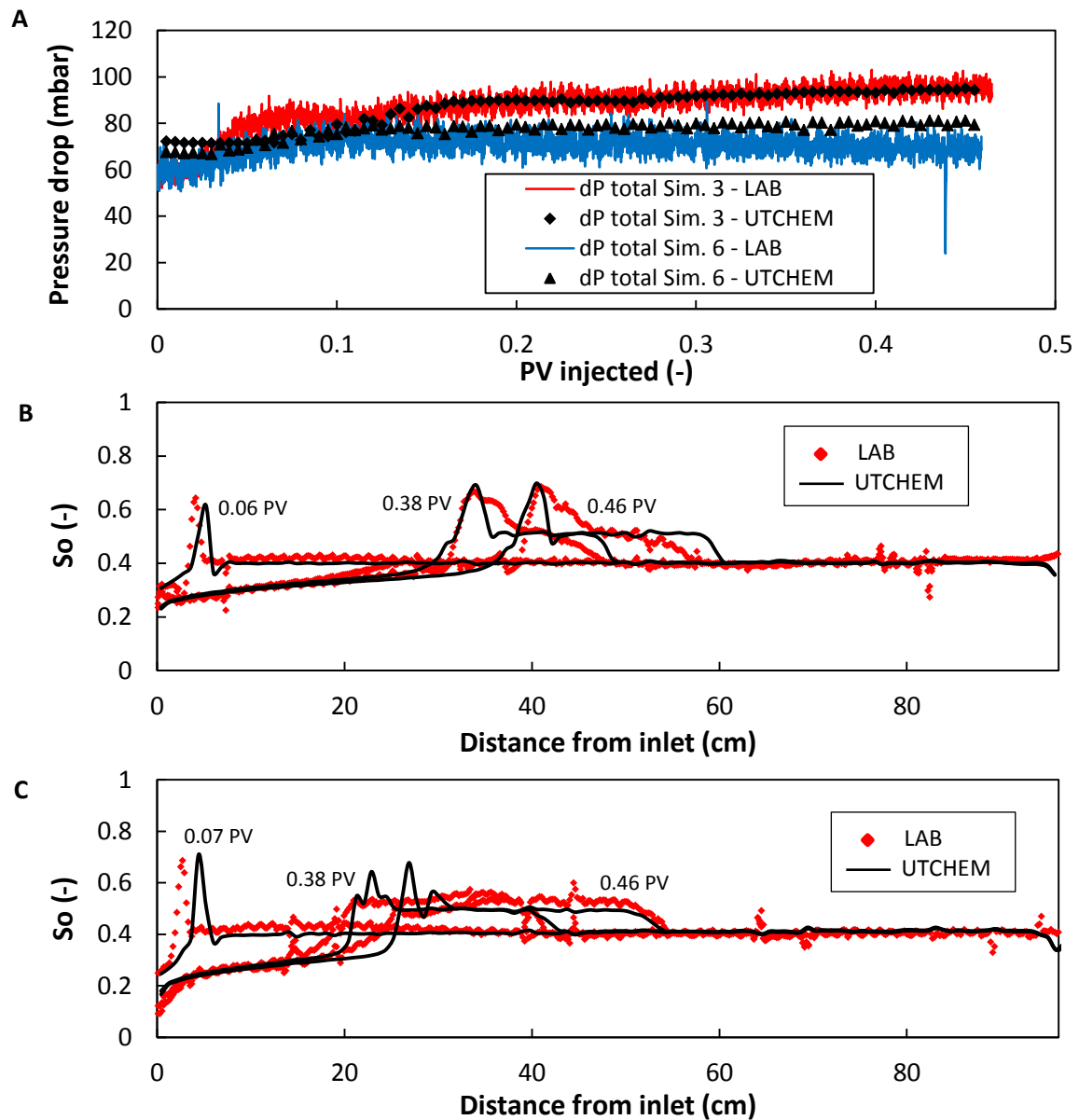


**Figure 6.11:** Simulated and measured total pressure drop profiles for the surfactant slug injection stage in Simulations 3 and 6 (A), oil saturation profiles obtained from experimental data and simulation for slug injection in Simulation 3 (B), and oil saturation profiles obtained from experimental data and simulation for slug injection in Simulation 6 (C).

continued, the oil bank became more dispersed [shown by the gradual reduction of  $S_o$  on the leading edge (i.e. downstream side)], this phenomena was hard to capture in the model. The  $S_o$  profiles constructed with the UTCHEM model exhibit a more uniform structure of the banked oil at its leading edge compared to the experimental observations. Note that this was not the case for Simulations 4 and 5 (**Appendix H**). The constructed  $S_o$  profiles related to Simulation 6 (**Figure 6.11C**) show a reasonable match with corresponding laboratory results. The propagation of the oil bank's leading edge was perfectly matched at injection times of 0.38 and 0.46 PV. At early injection times, i.e. at 0.07 PV, there is a small gap in the location of the oil bank between observed and simulated data. Although here we observed an uniform shape of the oil bank in the laboratory, at later injection times, corresponding simulation results indicate a more dispersed character of the oil accumulation at its trailing edge (i.e. upstream side). Note that the match in Simulation 6 required a slight increase

in surfactant adsorption due to an increased aqueous phase salinity, which is in agreement with Song and Islam (1994).

### 6.3.9 Displacement of mobilized oil by foam

The local equilibrium foam model in UTCHEM is based on the work of Cheng et al. (2000). It uses the following parameters to control foam generation: a) the surfactant concentration ( $C_s$ ) needs to exceed a threshold surfactant concentration ( $C_s^*$ ), b)  $S_w$  needs to exceed a threshold saturation ( $S_w^*$ ), and c)  $S_o$  should not be higher than a critical oil saturation ( $S_o^*$ ). The foam model used here assigns the reduction in gas mobility, due to foam generation, fully to the reduction in  $k_{rg}$  (Lotfollahi, 2015; UTCHEM Technical Documentation, 2017). The first two threshold parameters ( $C_s^*$  and  $S_w^*$ ) affect  $k_{rg}$  as follows:

$$k_{rg}^f = \begin{cases} k_{rg}, & S_w < S_w^* - \varepsilon \text{ or } C_s < C_s^* \\ \frac{k_{rg}}{1 + \frac{(R-1)(S_w - S_w^* + \varepsilon)}{2\varepsilon}}, & S_w^* - \varepsilon \leq S_w \leq S_w^* + \varepsilon \text{ and } C_s \geq C_s^* \\ \frac{k_{rg}}{R}, & S_w > S_w^* + \varepsilon \text{ and } C_s \geq C_s^* \end{cases} \quad (6.15)$$

where  $k_{rg}^f$ ,  $\varepsilon$ , and  $R$  represent the effective gas relative permeability modified for the presence of foam, a tolerance parameter for  $S_w$ , and the gas mobility reduction factor, respectively. The latter is given by:

$$R = R_{ref} \left( \frac{u_g}{u_{g,ref}} \right)^{\sigma-1} \quad (6.16)$$

where  $R_{ref}$ ,  $u_{g,ref}$ , and  $\sigma$  stand for the reference gas mobility reduction factor, the reference gas velocity at which  $R_{ref}$  is calculated, and a power-law exponent, respectively. **Equation 6.16** indicates that  $R$  is modified according to the gas flowrate to allow for shear thinning behaviour of foam in the low-quality regime (**Section 1.3.3**). The model implies that foam cannot be formed at  $S_o > S_o^*$ .

In order to assess whether the local equilibrium foam model in UTCHEM can potentially be used for reproducing our experimental observations discussed in **Section 3.3.2.3**, first we need to recapitulate the interpretation of the experimental results. As discussed in **Section 3.4.3**, in the case of a 57% and 77% drive foam quality (Simulations 3 and 4), obtained pressure drop data and  $S_g$  profiles indicate foaming characteristics to occur at an area with relatively high  $S_o$ , which are remnants of the oil bank. The suggested mechanism includes reduction in effective porosity, increased gas and liquid interstitial velocities, and, consequently, an increased local pressure drop which might be the trigger for foam generation. The aforementioned foam model in UTCHEM is not in line with our experimental observations, and suggested mechanism, since it entails complete collapse of foam at  $S_o > S_o^*$ . It involves foam destruction as function of increasing  $S_o$ , whereas laboratory investigation suggested foam generation being promoted at an area with relatively high  $S_o$ . The latter indicates that the local equilibrium foam model within UTCHEM is not suitable for simulating the foam generation mechanism observed in our experiments.

For testing purposes, we tried to use the model in an inconvenient, non-physical, way for reproducing our experimental results in Simulation 3. For this purpose we propose to use variable  $S_w^*$ , i.e. the value of  $S_w$  at which foam will collapse, as our controlling parameter. Parameter  $S_w^*$  was predefined at each local grid cell, based on measured  $S_g$  profiles that indicate foam generation, in

order to control the location at which foam starts to generate. By doing so, it was possible to selectively control the behaviour of  $k_{rg}^f$ . Note that variable  $S_w^*$  was, in fact, the only parameter in the foam model that could be selectively controlled. The other two threshold parameters,  $C_s^*$  and  $S_o^*$ , are chosen such that they allow foam generation to occur at all locations in space. **Figure 6.12** presents the  $S_w^*$  distribution for Simulation 3. It was generated as follows: a) find a function ( $f$ ) that effectively reproduces the  $S_g$  profile, which is the qualitative indicator of foam generation, observed at 1.08 PV injected (**Figure 3.10**), b) take  $1-f$  to obtain the correct shape of the  $S_w^*$  curve, and c) use **Equation 6.17** in an iterative way to obtain the final  $S_w^*$  curve:

$$S_{w_i}^* = S_l + \frac{(S_h - S_l)}{1 + a(10^{(x_{Di} - 1)b})} \quad (6.17)$$

where  $a$  and  $b$  function as fitting parameters,  $S_l$  and  $S_h$  represent the lower and higher limit values for  $S_w^*$ , respectively, and  $x_{Di}$  is the dimensionless distance in the x-direction of cell  $i$ .

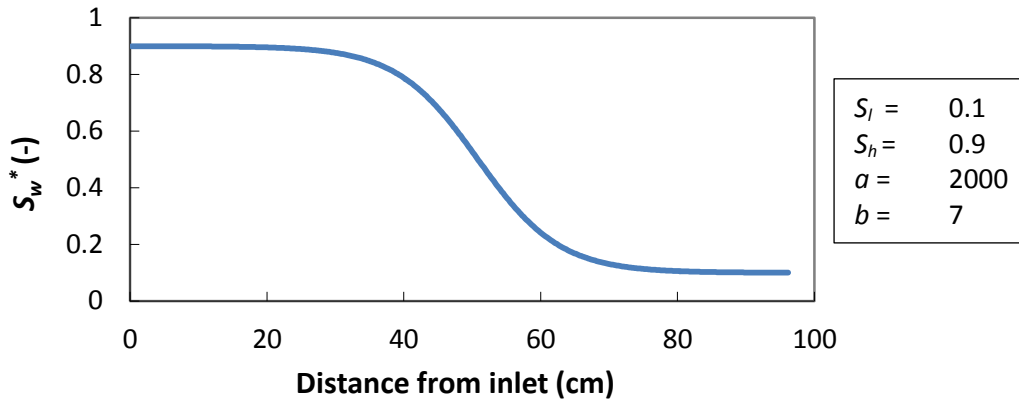


**Figure 6.12:**  $S_w^*$  distribution applied in Simulation 3 for the simulation of drive foam injection.

**Figure 6.13** presents an overview of measured and simulated pressure drops, oil recovery, and  $S_o$  profiles for drive foam injection in Simulation 3. Overall, a good representation of the pressure drop was obtained. The simulated oil recovery profile corresponds perfectly well with laboratory observations. The latter implies representative modelling of the oil bank propagation, which is verified by the  $S_o$  profiles shown in **Figure 6.13C**. Similar to our experimental observations, the oil bank's peak  $S_o$  is reduced as soon as co-injection of gas and surfactant solution was initiated.

## 6.4 Conclusions

A mechanistic modelling study on WAG and FACF, based on the core-flood experiments presented in **Chapters 2, 3, and 4**, was conducted. An in-house three-dimensional chemical flooding research simulator (UTCHEM) for multiphase and multicomponent systems was used. The FACF core-floods presented in **Chapters 3 and 4** were modelled by including the surfactant phase behaviour as a function of salinity, fluid rheology, capillary desaturation of oil, gas mobility reduction due to foam generation, and potential essential geochemical reactions that occurred in the sandstone core. All simulations were performed under an one-dimensional configuration.

Primary drainage and forced imbibition were successfully modelled. Relative permeability curves for primary drainage and forced imbibition were estimated using CT scan-based saturation distributions, and effective permeability measurements based on sectional pressure drops in the core.

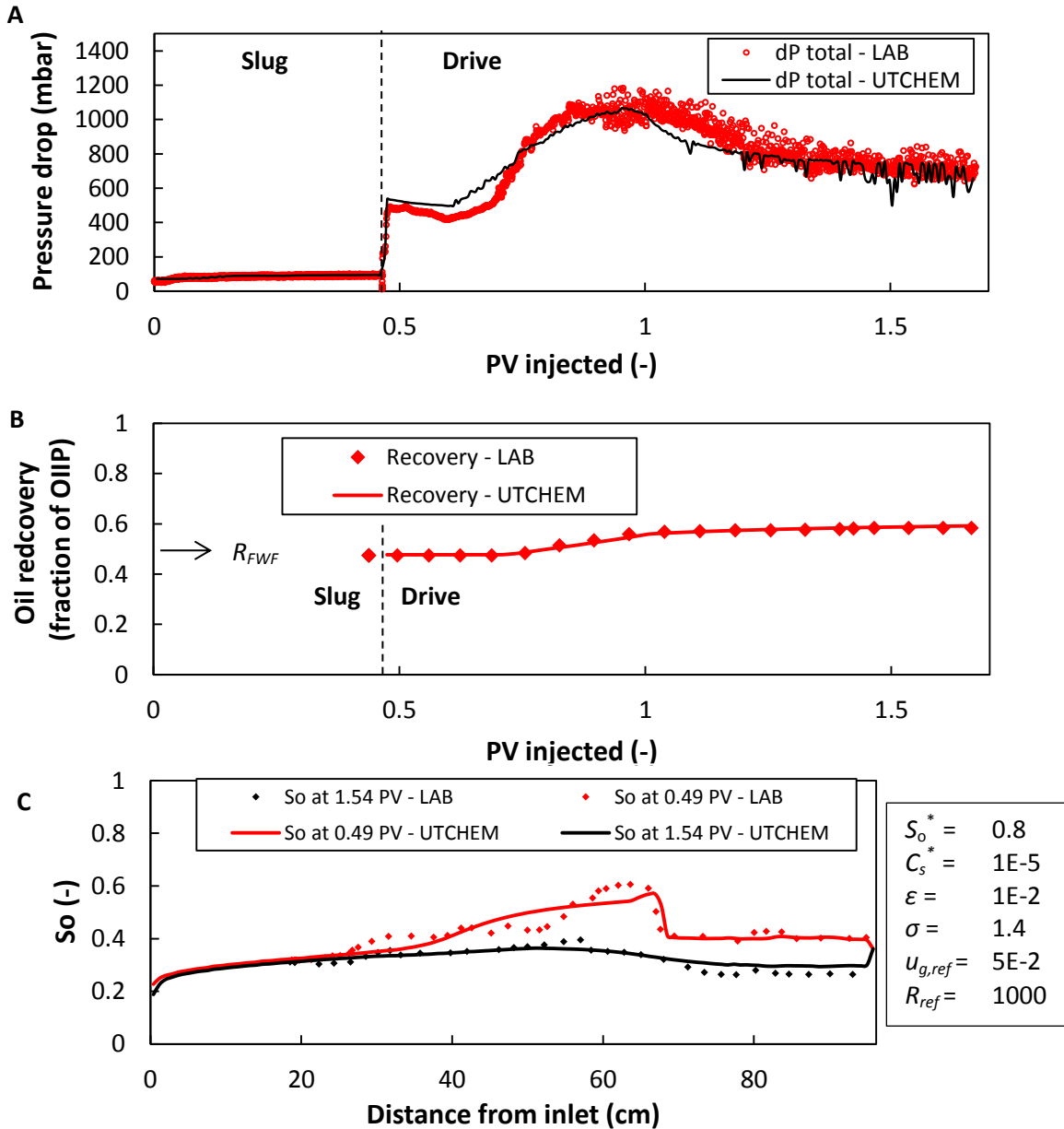


**Figure 6.13:** Simulated and measured total pressure drop profiles for slug and drive foam injection in Simulation 3 (A), oil recovery profiles as function of  $OIIP$  (B), and oil saturation profiles obtained from experimental data and simulation for drive foam injection in Simulation 3 (C).  $PV = 0$  equals to the start of surfactant slug injection. The table on the bottom right-hand side presents an overview of the model parameters used (except for  $S_w^*$ ). Note that extreme values for  $S_o^*$  and  $C_s^*$  were assumed which allowed us to use  $S_w^*$  as a controlling parameter (Figure 6.12).

History-matching WAG injection revealed that a reduction in  $k_{rg}$  was required as a function of increasing WAG cycles. This, most likely, verifies the effect of the establishment of  $S_{gt}$ . Similar to our experimental results, bulk of the oil was produced during the injection of the first two WAG cycles.

The surfactant phase behaviour for our experimental conditions was successfully modelled. Robustness of the model was verified by effectively applying the same phase behaviour model to the two different salinity conditions studied. Moreover, we were able to identify the correct trapping number parameters in order to acquire representative water and oil relative permeability curves for low  $o/w$  IFT flooding. This laid a solid foundation for proper modelling of oil mobilization due to surfactant slug injection.

## Chapter 6 – Mechanistic modelling of water-alternating-gas injection and foam-assisted chemical flooding

Although UTCHEM demonstrated to be a useful simulation tool, able to represent complex phenomena involved in a four-phase system, its local equilibrium foam model was not able to cover a wide range of possible foam generation mechanisms. To overcome this drawback, we introduced a selectively controlled  $S_w^*$ .

# 7. Conclusions and recommendations

---

The experimental and numerical simulation study reported in this thesis provides new insights on the oil mobilization and displacement mechanisms in a foam-assisted chemical flooding process. Firstly, several immiscible gas injection schemes were investigated. They provide a baseline against which the results of foam-assisted chemical flooding will be compared to in order to identify its advantages. Subsequently, foam-assisted chemical flooding was investigated at model-like conditions before assessing the novel enhanced oil recovery technique in a reservoir setting. Finally, we conducted a modelling and numerical simulation study and matched its outcome with the experiments to validate the proposed mechanisms for oil mobilization and displacement. This chapter presents the general conclusions of this thesis followed by a few recommendations for future research.

## 7.1 Conclusions

In **Chapter 2** we investigated oil displacement mechanisms for oil recovery during immiscible continuous gas and water-alternating-gas (*WAG*) injection, using Bentheimer sandstone cores and a light model oil. Several gas injection schemes were investigated in controlled core-flood experiments including: 1) continuous  $N_2$  injection at connate water saturation, 2) continuous  $N_2$  injection at residual oil to waterflood, and 3) *WAG* injection at connate water saturation. This work formed the basis for understanding the relevance of foam-assisted chemical flooding (*FACF*). Results were displayed as saturation paths in a ternary diagram. The constructed ternary saturation diagram revealed that the injection of  $N_2$  at connate water saturation followed a two-phase gas-oil displacement path at constant water saturation. The injection of  $N_2$  at residual oil to waterflood showed a saturation path where at first oil was displaced by  $N_2$  at a fairly constant oil saturation, and eventually, similar to  $N_2$  flooding at connate water saturation, the injected gas displaced the oil at a roughly constant water saturation. Furthermore, experimental data showed that *WAG* provided the largest ultimate oil recovery factor. The formation of trapped gas, reducing gas mobility thus increasing its sweep efficiency, is most likely a key factor for the incremental oil recovered. Moreover, obtained results are consistent with the hypothesis that an increment in oil recovery arises mostly from the fact that the residual oil to gas flooding is lower under three-phase flow conditions compared to two-phase flow.

**Chapter 3** presented an experimental study on *FACF* at model-like conditions, focussing on the impact of drive foam quality on oil bank displacement during under-optimum salinity *FACF*. To start with, the surfactant slug phase behaviour was studied in bulk, which led to the surfactant slug formulation to be used in following core-floods. Once the surfactant slug and drive formulations were selected, well-controlled CT-assisted core-flood experiments were performed in a 1 meter Bentheimer sandstone core, varying the foam quality of the drive foam. True dual-energy CT data were used to construct three-phase saturation profiles over the course of the core-flood experiments. Experimental results indicate that the formulated surfactant slug operated at under-optimum salinity conditions. It was able to lower the oil-water interfacial tension by a factor 130. Oil coalescence took place at the leading edge of the oil bank, yielding expansion of the banked oil. Dispersion at its leading edge was a strong function of injection time as verified by the baseline core-flood. The performed core-floods showed that co-injection at constant drive foam qualities of 57 and 77% yielded weak foam generation in the presence of residual oil. Foam strength increased upon touching the oil bank, leading to an effective oil bank displacement. The suggested mechanism

responsible implies foaming behaviour being controlled by the presence of a zone with potentially micro-emulsion and oil bearing pores. Oil bank displacement by foam was most stable, i.e. better mobility control, at the lowest gas fractional flow investigated (57%) and least stable at the highest foam quality considered (97%). Cumulative clean oil recovery was not affected by the constant drive foam qualities assessed.

**Chapter 4** reported on an elaborated study on the effect of surfactant slug salinity on oil mobilization and displacement processes in *FACF* at conditions similar to **Chapter 3**. While the main goal was to further elucidate the oil bank formation and displacement mechanisms, special attention was paid the effect of slug salinity on the produced clean oil-solubilized oil ratio. CT-assisted *FACF* core-flood experiments, both at (near-)optimum and under-optimum salinity, were performed and led to the construction of three-phase saturation paths presented in ternary diagrams. The designed surfactant slug formulation lowered the oil-water interfacial tension by a factor of 130 (as in **Chapter 3**) and 540 for under-optimum and (near-)optimum salinity conditions, respectively. At (near-)optimum salinity, the oil bank formed was more uniform and elongated compared to the oil bank developed at under-optimum salinity conditions. Furthermore, the surfactant drive formulation showed good foaming characteristics in bulk. Co-injection of drive solution and  $N_2$ , in presence of *n*-hexadecane, generated weak foams. Foam strength surged upon hitting the oil bank, leading to effective displacement of the banked oil at both salinity conditions. The higher ultimate oil recovery for *FACF* at (near-)optimum salinity, compared to under-optimum salinity, proved the increase in effectiveness of oil mobilization and displacement in a *FACF* process. Performing *FACF* at (near-)optimum salinity increased the produced clean oil-solubilized oil ratio over under-optimum flooding with roughly a factor 10.

**Chapter 5** examined the feasibility of *FACF* to reservoir conditions as an extension of **Chapters 3** and **4**. It included surfactant stability, crude oil-surfactant phase behaviour, and bulk foam stability tests that yielded various surfactant formulations to be used in the core-floods. Core-flood experiments included a foam quality scan, where one surfactant drive formulation was used to generate foam at varying gas fractional flows in the absence of oil, and a series of CT-scanned *FACF* core-floods. Novel qualitative and quantitative analyses of the oil bank formation and its displacement during *FACF* at reservoir conditions were presented. Special attention was paid to the effects of surfactant slug salinity and drive foam strength. The phase behaviour study showed that the designed IOS2024 surfactant slug revealed a Winsor Type III system (i.e. optimum salinity conditions) at salinities of 1.50 – 1.75 wt % NaCl + KCl. The addition of 1-iododecane to the oleic phase did not alter the crude oil-IOS2024 phase behaviour. Bulk foam experiments in the absence of oil indicated a roughly 11 times greater foam half-decay time for the Surfactant X drive solution compared to the IOS2024 drive formulation. The addition of 5 volume percent crude oil to the drive solution reduced the foam half-decay time of the Surfactant X drive foam with approximately a factor 12 in bulk. The foam quality scan proved that, in absence of crude oil, the Surfactant X drive formulation generates strong and stable foams in Bentheimer sandstone cores for all gas fractional flows investigated. The largest apparent foam viscosity of  $1.45 \pm 0.11$  Pa·s was reached at a foam quality of 75.0%. Foam qualities below are in the low foam-quality regime, whereas higher foam qualities describe the high-quality regime. A 57.5% foam quality resulted in an apparent foam viscosity of  $1.32 \pm 0.05$  Pa·s. Surfactant slug injection in *FACF* core-floods showed that unstable oil banks were formed during both under-optimum and optimum salinity *FACF* as a result of relatively dominant gravitational forces. The IOS2024 surfactant slug at optimum salinity was significantly more effective at reducing residual oil to waterflood (81% reduction) compared to the under-optimum salinity slug (30% reduction). The

injection of pre-generated Surfactant X drive foam instead of performing co-injection, at optimum salinity conditions, resulted in a higher incremental oil recovery compared to operating at optimum salinity versus under-optimum salinity conditions (in combination with in-situ drive foam generation).

**Chapter 6** reports on the mechanistic modelling and numerical simulation of *WAG* and *FACF* experiments at model-like conditions presented in **Chapters 2, 3, and 4**. For this purpose we used UTCHEM, an in-house three-dimensional research simulator. History-matching of the reported core-flood experiments was carried out to explore the main mechanisms, and determine the relevant parameters, controlling incremental oil recovery in *WAG* and *FACF*. CT scan-based saturation distributions, and effective permeability measurements based on sectional pressure drops in the core, allowed for a proper estimation of relative permeability curves for primary drainage and forced imbibition. For accurate simulation of *WAG* injection, a reduction in gas relative permeability was required as a function of increasing *WAG* cycles. It verified the formation of a trapped gas saturation. Analogous to experimental observations, the majority of the oil was produced during the injection of the first two *WAG* cycles. A successful model was built that represent the surfactant phase behaviour during *FACF* at both salinity conditions studied in **Chapter 4**. It provided a strong foundation for modelling of oil mobilization by the injected surfactant slug. For modelling drive foam injection, the built-in local equilibrium foam model was used. It proved to be inadequate for modelling drive foam injection in the presence of oil during a *FACF* process. To overcome this constraint, an alternative approach was adopted where we selectively controlled one of the threshold parameters involved.

## 7.2 Recommendations

This dissertation provides answers to many of the questions posed at the outset of this research, thus contributing to a better understanding of the mechanisms underlying oil mobilization and displacement in a foam-assisted chemical flooding process. However, several aspects still need further attention in order to fill in the knowledge gaps. Based on the insights provided in this thesis, it is recommended to consider the following points in future research efforts.

A further validation of the proposed mechanisms responsible for oil mobilization and in-situ drive foam generation (**Chapter 3**) would benefit from direct observation of those processes at the pore-scale. This could be done using either dynamic micro-CT scanning or more easily accessible micro-fluidic devices. The visualization of oil mobilization was studied using a quasi-two-dimensional microfluidic set-up and by using confocal microscopy to directly visualize oil mobilization within a model three-dimensional porous medium. Mainly due to time limitations it was not possible to fully explore and optimize these pore-level studies. Therefore they could be the focus of future research which, in addition, should include in-situ drive foam generation during *FACF*.

The application of *FACF* at more realistic reservoir conditions, examined in **Chapter 5**, clearly revealed the gravity underriding effect of the liquid surfactant slug utilized. For real-field dimensions, it is expected that this underriding effect is of a substantially higher magnitude compared to the experimental observations in **Chapter 5**. As a consequence, most probably only the lower part of the reservoir will be properly swept. Therefore, we recommend to investigate possibilities to favour the mobility ratio between the injected slug and the fluids in place.

UTCHEM proved to be a useful tool, able to represent complex phenomena involved in a four-phase system. However, its local equilibrium foam model could not capture several important features of

## Chapter 7 – Conclusions and recommendations

the foaming process as discussed in **Chapter 6**. UTCHEM should take stock of the development in the last two decades and include more robust foam models.

# Appendix A. CT imaging of two- and three-phase saturations using single- and dual-energy CT data

In our study, CT scans were taken over the course of several core-flood experiments to visualize and gain insight into the distribution of phase saturations. This appendix presents the formulas used to calculate the porosity, two-phase oil and water saturations, and three-phase oil, water, and gas saturations, respectively (Sharma *et al.*, 1997). Subscripts 1 and 2 represent 140 kV (250 mA) and 80 kV (550 mA) data, respectively. The acquired CT attenuation data were expressed in Hounsfield units (HU).

## A.1 Porosity

Porosities were calculated throughout the entire thesis using single-energy 140 kV data as follows:

$$\varphi_1 = \frac{CT_{wet_1} - CT_{dry_1}}{CT_{brine_1} - CT_{air_1}} \quad (A.1)$$

where  $\varphi$ ,  $CT_{dry}$ ,  $CT_{wet}$ ,  $CT_{air}$ , and  $CT_{brine}$  represent the porosity and the CT response in HU of the dry core, brine saturated core, air phase in bulk, and water phase in bulk, respectively. Subscript 1 denotes the use of single-energy 140 kV CT data.

## A.2 Two-phase oil and water saturations

Two-phase oil and water saturations were calculated throughout the entire study as follows:

$$S_o = \frac{1}{\varphi_1} \left( \frac{CT_1 - CT_{wet_1}}{CT_{oil_1} - CT_{brine_1}} \right) \quad (A.2)$$

$$S_w = 1 - S_o \quad (A.3)$$

where  $S_o$ ,  $S_w$ ,  $CT$ , and  $CT_{oil}$  stand for the oil saturation, water saturation, CT response of the scanned core of interest, and the CT response of the oleic phase in bulk, respectively. **Equation A.2** follows from:

$$CT_1 = S_w CT_{wet_1} + S_o CT_{o_1} \quad (A.4)$$

where  $CT_o$  represents the CT response in HU of a 100% oil saturated core. After substituting **Equation A.3** into **Equation A.4**, we get:

$$S_o = \frac{CT_1 - CT_{wet_1}}{CT_{o_1} - CT_{wet_1}} \quad (A.5)$$

During the course of the core-floods experiments conducted in this work we never reach a condition where the core is 100% saturated with the oleic phase. Hence,  $CT_o$  remains unknown. In order to avoid using  $CT_o$ , the following approximation is used:

$$CT_{o_1} - CT_{wet_1} = \varphi_1 (CT_{oil_1} - CT_{brine_1}) \quad (A.6)$$

which eventually leads to the formula used (**Equation A.2**).

### A.3 Three-phase oil, water, and gas saturations

For calculating three-phase saturation distributions, true dual-energy CT data is required. For this purpose 140 kV (subscript 1) and 80 kV (subscript 2) CT data is used as follows:

$$S_o = \frac{(CT_1 - CT_{wet_1})(CT_{dry_2} - CT_{wet_2}) - (CT_2 - CT_{wet_2})(CT_{dry_1} - CT_{wet_1})}{\varphi_1(CT_{oil_1} - CT_{brine_1})(CT_{dry_2} - CT_{wet_2}) - \varphi_2(CT_{oil_2} - CT_{brine_2})(CT_{dry_1} - CT_{wet_1})} \quad (\text{A.7})$$

$$S_g = \frac{(CT_1 - CT_{wet_1})\varphi_2(CT_{oil_2} - CT_{brine_2}) - (CT_2 - CT_{wet_2})\varphi_1(CT_{oil_1} - CT_{brine_1})}{\varphi_2(CT_{oil_2} - CT_{brine_2})(CT_{dry_1} - CT_{wet_1}) - \varphi_1(CT_{oil_1} - CT_{brine_1})(CT_{dry_2} - CT_{wet_2})} \quad (\text{A.8})$$

$$S_w = 1 - S_o - S_g \quad (\text{A.9})$$

where  $S_g$  represents the gas saturation. Similar to two-phase flow conditions, **Equations A.7** and **A.8** originate from:

$$CT_1 = S_w CT_{wet_1} + S_o CT_{o_1} + S_g CT_{dry_1} \quad (\text{A.10})$$

$$CT_2 = S_w CT_{wet_2} + S_o CT_{o_2} + S_g CT_{dry_2} \quad (\text{A.11})$$

After substituting **Equation A.9** into **Equation A.10**, one obtains an expression for  $S_g$  only depending on  $S_o$ . Finally, when substituting that expression, together with **Equation A.9**, into **Equation A.11**, we obtain an equation for  $S_o$  solely dependent on CT data. The same procedure is used to acquire an expression for  $S_g$  exclusively dependent on CT data. The final step to realize **Equations A.7** and **A.8** is to use **Equation A.6** in order to express  $CT_o$  as a function of  $CT_{brine}$ ,  $CT_{oil}$ , and  $\varphi$ .

# Appendix B. Pressure drop vs. oil bank shape during surfactant slug injection

In order to study the relationship between the observed pressure drops (**Figure 4.3**) and corresponding shapes of the oil bank (**Figure 4.4**), Darcy's law, in combination with Brooks and Corey model for relative permeabilities (Brooks and Corey, 1966), was applied to simple test cases presented in **Table B.1** and **Figure B.1**. The formulas used are shown below. A simplified one dimensional Darcy's law was assumed:

$$\Delta P = u_{tot} \left( \frac{f_o \mu_o}{k_{ro} k} + \frac{f_w \mu_w}{k_{rw} k} \right) L \quad (\text{B.1})$$

where  $\Delta P$ ,  $u_{tot}$ ,  $\mu_a$ ,  $k_{ra}$ ,  $k$ ,  $f_a$ , and  $L$  represent the pressure drop, total superficial velocity, viscosity of phase a, relative permeability of phase a, absolute permeability to brine, fractional flow of phase a, and the core length, respectively. Subscripts o and w refer to the oil and water phases, respectively. The relative permeabilities are derived using Brooks and Corey model:

$$k_{ro} = k_{ro}^0 \left( \frac{S_o - S_{or}}{1 - S_{or} - S_{wc}} \right)^{n_o} \quad (\text{B.2})$$

$$k_{rw} = k_{rw}^0 \left( \frac{S_w - S_{wc}}{1 - S_{or} - S_{wc}} \right)^{n_w} \quad (\text{B.3})$$

Where  $k_{ra}^0$  and  $n_a$  represent the end-point relative permeability and the Brooks-Corey exponent for phase a, respectively. Pressure drops are derived using a space interval of 1.0 cm (i.e. for every cm pressure drops are calculated using the saturation distributions presented in **Figure B.1**). Note that we only address the variations in phase saturations, i.e. relative permeabilities, and its impact on the total pressure drop.

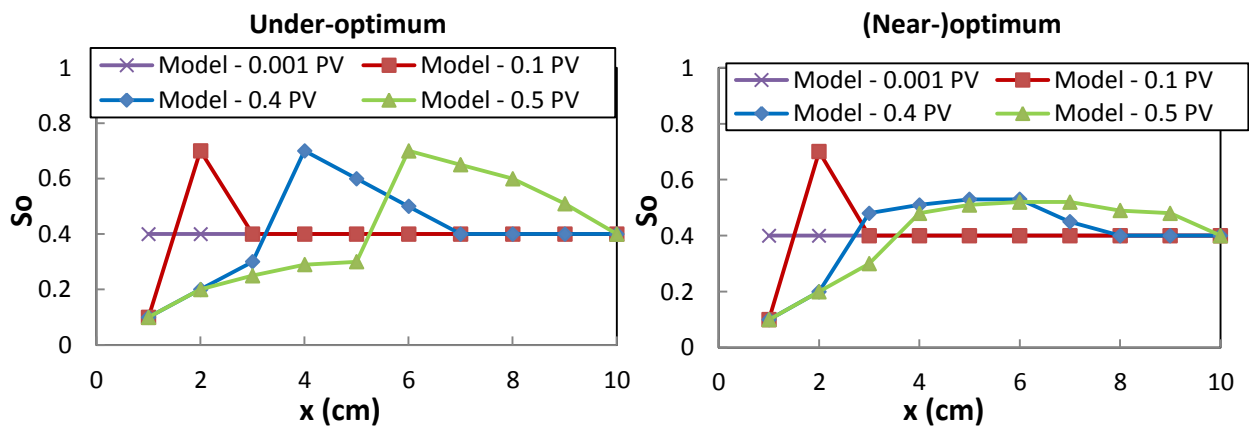


**Figure B.1:** The simplified test cases that represent the development of the oil bank during AS slug injection at, respectively, under-optimum (left) and (near-)optimum (right) salinity conditions (Exp. 1 and 2 in **Chapter 4**). Note that the development of the oil bank in the model has similar characteristics as the observations made during the performed experiments (**Figure 4.4**). Water saturations were calculated using  $1 - S_o$ . The total amount of oil present at each time was held constant; assuming no oil being produced.

**Table B.1:** The parameters used to derive the pressure drop analytically for the two model cases shown in **Figure B.1**.

$L$ (m)	$U_{tot}$ (m/s)	$\mu_o$ (Pa*s)	$\mu_w$ (Pa*s)	$k$ (m <sup>2</sup> )	$k_{ro}^0$	$k_{rw}^0$	$S_{or}$	$S_{wc}$	$n_o$	$n_w$
0.01	2.09E-06	3.38E-3	1.07E-3	3.2E-12	0.51	0.13	0.09	0.22	1	2

The derived total pressure drop profiles, i.e. the sum of pressure drops calculated over 1.0 cm sections, are shown in **Figure B.2**. Qualitatively they are similar to the observed pressure drops during AS slug injection in the experiments conducted (**Figure 4.3**): a sharp increase followed by a more gradual increase (under-optimum), and a sharp increase followed by a gradual decrease [(near-)optimum]. The higher pressure drops during under-optimum compared to (near-)optimum injection is due to the relatively high peak  $S_o$  (close to  $1-S_{wc}$ ) within the oil bank. The reduction in water mobility,  $\frac{k_{rw}k}{\mu_w}$ , has the greatest impact on the increase in pressure drop. Furthermore, as injection continued at under-optimum salinity conditions, the oil bank grew continuously while maintaining its peak  $S_o$ , thus enlarging the total pressure drop.

At (near-)optimum salinity injection, first a sharp increase in pressure drop is seen due to the formation of the sharp oil bank at early injection times (similar to under-optimum salinity injection). Afterwards, peak  $S_o$  reduced and the oil bank became more uniform. The constant, relatively low,  $S_o$  of around 0.5 revealed a slight reduction in total pressure drop as the peak  $S_o$  within the oil bank was reduced significantly. This effect could not be compensated by the growth of the oil bank. Further development of the oil bank hardly effects the pressure drop as the expansion at the leading edge is neutralized by a slight reduction in peak  $S_o$ .

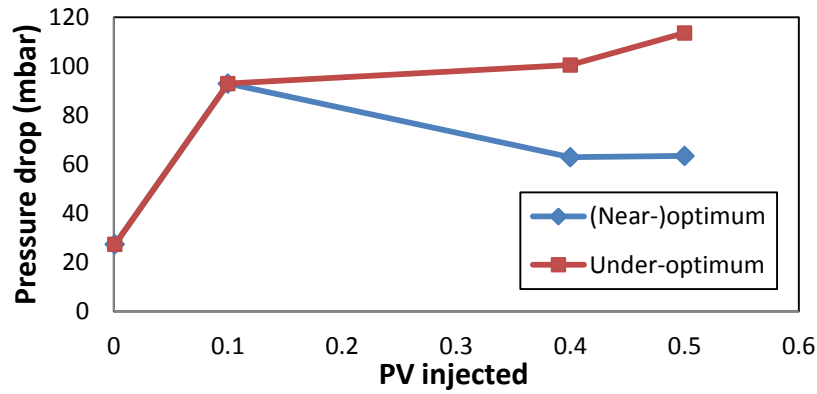


**Figure B.2:** Total pressure drop profiles constructed for the two simplified models shown in **Figure B.1**. Note that, qualitatively, it represents the observations made during AS slug injection in Exp. 1 and 2 in **Chapter 4**.

# Appendix C. Simulation parameters used per injection stage per experiment.

Here we present an overview of the basic simulation parameters used per injection stage for each of the Simulations presented in **Chapter 6**.

## C.1 Simulation 1: WAG

**Table C1** gives an overview of the basic simulation parameters used in Simulation 1.

**Table C1:** Simulation parameters for the various injection phases used in Simulation 1.

Parameter	Primary drainage	WAG cycle 1	WAG cycle 2	WAG cycle $\geq 3$
Number of grid blocks (x, y, z)	1x1x100	1x1x100	1x1x100	1x1x100
Grid block size (mxmxm)	0.0345x0.0345x0.0017	0.0345x0.0345x0.0017	0.0345x0.0345x0.0017	0.0345x0.0345x0.0017
Simulation time (PV)	5.92	1.30	2.65	17.00
Initial water saturation (-)	1.00 for all grid blocks	Saturation distribution output of primary drainage stage	Saturation distribution output of WAG cycle 1	Saturation distribution output of WAG cycle 2
Initial brine salinity (wt% NaCl)	3.0	3.0	3.0	3.0
Bottom hole pressure production well (bar)	5.0	5.0	5.0	5.0
Porosity (%)	23.59	23.59	23.59	23.59
Absolute permeability to brine (Darcy)	2.23	2.23	2.23	2.23
Reservoir temperature ( $^{\circ}$ C)	18	18	18	18

## C.2 Simulation 2: Extended surfactant slug injection

**Table C2** gives an overview of the basic simulation parameters used in Simulation 2.

**Table C2:** Simulation parameters for the various injection phases used in Simulation 2.

Parameter	Primary drainage	Water flooding	Surfactant flooding
Number of grid blocks (x, y, z)	120x1x1	120x1x1	120x1x1
Grid block size (mxmxm)	0.0081x0.0337x0.0337	0.0081x0.0337x0.0337	0.0081x0.0337x0.0337
Simulation time (PV)	2.92	6.55	2.40
Initial water saturation (-)	1.00 for all grid blocks	Saturation distribution output of primary drainage stage	Saturation distribution output of water flooding stage
Initial brine salinity (wt% NaCl)	2.0	2.0	2.0
Bottom hole pressure production well (bar)	20.0	20.0	20.0
Porosity (%)	23.60 $\pm$ 0.34 varies per grid block	23.60 $\pm$ 0.34 varies per grid block	23.60 $\pm$ 0.34 varies per grid block
Absolute permeability to brine (Darcy)	3.17 $\pm$ 0.16 varies per grid block	3.17 $\pm$ 0.16 varies per grid block	3.17 $\pm$ 0.16 varies per grid block
Reservoir temperature ( $^{\circ}$ C)	21	21	21

### C.3 Simulation 3: Under-optimum FACF – 57% foam quality

Table C3 gives an overview of the basic simulation parameters used in Simulation 3.

Table C3: Simulation parameters for the various injection phases used in Simulation 3.

Parameter	Primary drainage	Water flooding	Surfactant slug injection	Drive foam injection
Number of grid blocks (x, y, z)	120×1×1	120×1×1	120×1×1	120×1×1
Grid block size (m×m×m)	0.0080×0.0337×0.0337	0.0080×0.0337×0.0337	0.0080×0.0337×0.0337	0.0080×0.0337×0.0337
Simulation time (PV)	3.08	6.93 4.83	0.47	1.67
Initial water saturation (-)	1.00 for all grid blocks	Saturation distribution output of primary drainage stage	Saturation distribution output of water flooding stage	Saturation distribution output of surfactant injection stage
Initial brine salinity (wt% NaCl)	4.0	4.0 2.0	2.0	2.0
Bottom hole pressure production well (bar)	20.0	20.0	20.0	20.0
Porosity (%)	23.67 ± 0.36 varies per grid block	23.67 ± 0.36 varies per grid block	23.67 ± 0.36 varies per grid block	23.67 ± 0.36 varies per grid block
Absolute permeability to brine (Darcy)	3.05 ± 0.13 varies per grid block	3.05 ± 0.13 varies per grid block	3.05 ± 0.13 varies per grid block	3.05 ± 0.13 varies per grid block
Reservoir temperature (°C)	21	21	21	21

### C.4 Simulation 4: Under-optimum FACF – 77% foam quality

Table C4 gives an overview of the basic simulation parameters used in Simulation 4.

Table C4: Simulation parameters for the various injection phases used in Simulation 4.

Parameter	Primary drainage	Water flooding	Surfactant slug injection	Drive foam injection
Number of grid blocks (x, y, z)	121×1×1	121×1×1	121×1×1	121×1×1
Grid block size (m×m×m)	0.0060/0.0080×0.0337×0.0337	0.0060/0.0080×0.0337×0.0337	0.0060/0.0080×0.0337×0.0337	0.0060/0.0080×0.0337×0.0337
Simulation time (PV)	3.87	5.75	0.49	6.48
Initial water saturation (-)	1.00 for all grid blocks	Saturation distribution output of primary drainage stage	Saturation distribution output of water flooding stage	Saturation distribution output of surfactant injection stage
Initial brine salinity (wt% NaCl)	2.0	2.0	2.0	2.0
Bottom hole pressure production well (bar)	20.0	20.0	20.0	20.0
Porosity (%)	23.53 ± 0.50 varies per grid block	23.53 ± 0.50 varies per grid block	23.53 ± 0.50 varies per grid block	23.53 ± 0.50 varies per grid block
Absolute permeability to brine (Darcy)	3.09 ± 0.19 varies per grid block	3.09 ± 0.19 varies per grid block	3.09 ± 0.19 varies per grid block	3.09 ± 0.19 varies per grid block
Reservoir temperature (°C)	21	21	21	21

## C.5 Simulation 5: Under-optimum FACH – 97% foam quality

Table C5 gives an overview of the basic simulation parameters used in Simulation 5.

Table C5: Simulation parameters for the various injection phases used in Simulation 5.

Parameter	Primary drainage	Water flooding	Surfactant slug injection	Drive foam injection
Number of grid blocks (x, y, z)	121x1x1	121x1x1	121x1x1	121x1x1
Grid block size (m×m×m)	0.0060/0.0080 ×0.0337×0.0337	0.0060/0.0080 ×0.0337×0.0337	0.0060/0.0080 ×0.0337×0.0337	0.0060/0.0080 ×0.0337×0.0337
Simulation time (PV)	3.62	6.12	0.47	6.84
Initial water saturation (-)	1.00 for all grid blocks	Saturation distribution output of primary drainage stage	Saturation distribution output of water flooding stage	Saturation distribution output of surfactant injection stage
Initial brine salinity (wt% NaCl)	2.0	2.0	2.0	2.0
Bottom hole pressure production well (bar)	20.0	20.0	20.0	20.0
Porosity (%)	23.27 ± 0.43 varies per grid block	23.27 ± 0.43 varies per grid block	23.27 ± 0.43 varies per grid block	23.27 ± 0.43 varies per grid block
Absolute permeability to brine (Darcy)	3.30 ± 0.20 varies per grid block	3.30 ± 0.20 varies per grid block	3.30 ± 0.20 varies per grid block	3.30 ± 0.20 varies per grid block
Reservoir temperature (°C)	21	21	21	21

## C.6 Simulation 6: (Near-)optimum FACH –57% foam quality

Table C6 gives an overview of the basic simulation parameters used in Simulation 6.

Table C6: Simulation parameters for the various injection phases used in Simulation 6.

Parameter	Primary drainage	Water flooding	Surfactant slug injection
Number of grid blocks (x, y, z)	121x1x1	121x1x1	121x1x1
Grid block size (m×m×m)	0.0080×0.0337×0.0337	0.0080×0.0337×0.0337	0.0080×0.0337×0.0337
Simulation time (PV)	3.16	10.16	0.46
Initial water saturation (-)	1.00 for all grid blocks	Saturation distribution output of primary drainage stage	Saturation distribution output of water flooding stage
Initial brine salinity (wt% NaCl)	3.6	3.6	3.6
Bottom hole pressure production well (bar)	20.0	20.0	20.0
Porosity (%)	23.70 ± 0.31 varies per grid block	23.70 ± 0.31 varies per grid block	23.70 ± 0.31 varies per grid block
Absolute permeability to brine (Darcy)	3.44 ± 0.19 varies per grid block	3.44 ± 0.19 varies per grid block	3.44 ± 0.19 varies per grid block
Reservoir temperature (°C)	21	21	21



# Appendix D. Relative permeability curves: primary drainage and forced imbibition.

For the aid of history-matching performed laboratory core-flood experiments, it is essential to select the correct  $k_r$  functions of all phases present. Here we present an overview of  $k_r$  curves, and parameters, used for simulating primary drainage and forced imbibition in all simulations performed. The relative permeabilities are modelled using the Corey-type functions (Equations B.2 and B.3).

## D.1 Simulation 1: WAG

Figure D.1 presents the  $k_r$  curves for the oleic and aqueous phases used for simulating primary drainage in Simulation 1.

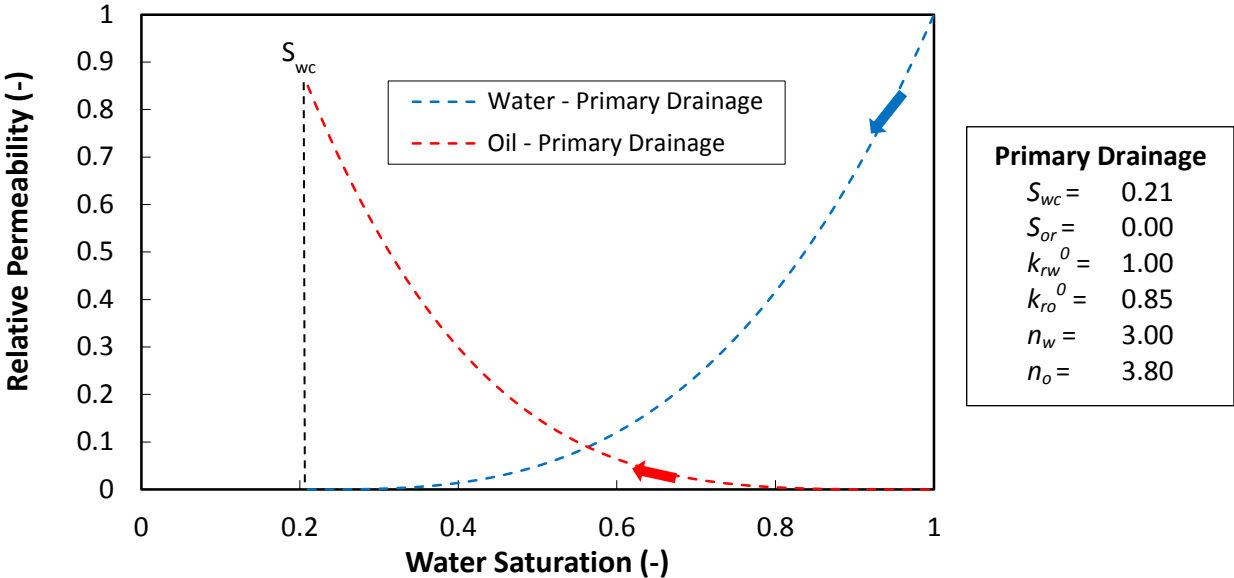


Figure D.1: Relative permeability curves for the aqueous (blue) and oleic (red) phases during primary drainage used for Simulation 1.

## D.2 Simulation 2: Extended surfactant slug injection

Figure D.2 presents the  $k_r$  curves for the oleic and aqueous phases used for simulating primary drainage and forced imbibition in Simulation 2.

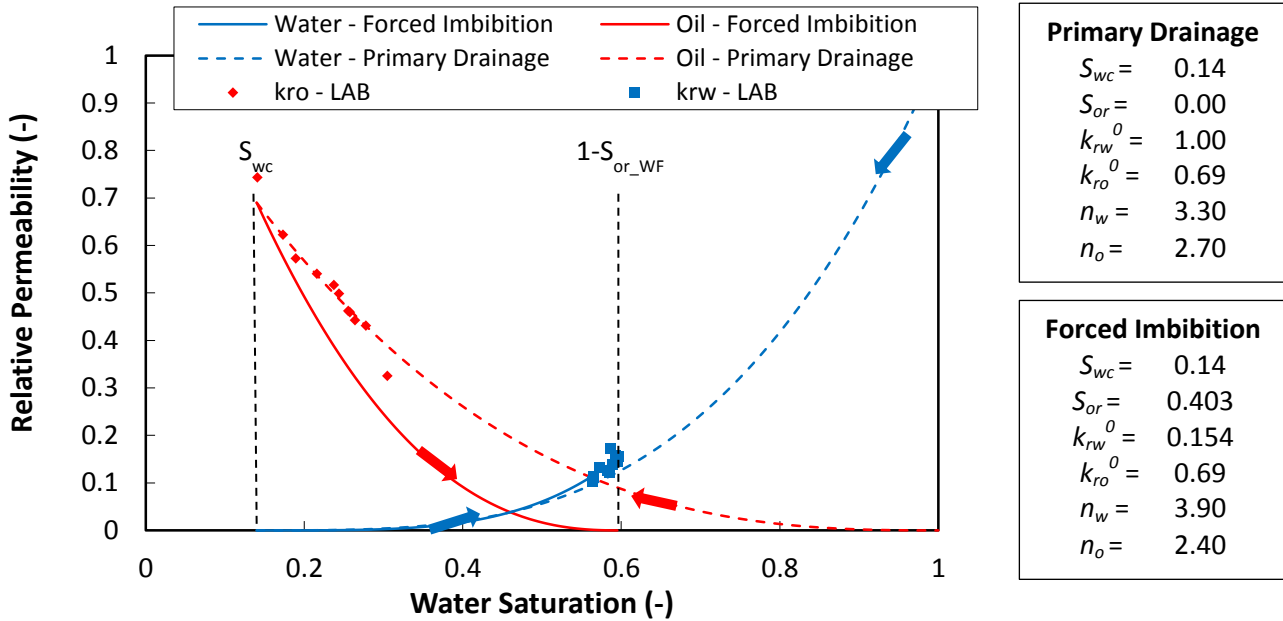


Figure D.2: Relative permeability curves for the aqueous (blue) and oleic (red) phases during primary drainage (dashed lines) and water flooding (continuous lines) used for Simulation 2. More information on how we used the experimental data to obtain a  $k_{ro}^0$  and  $k_{rw}^0$  for simulation purposes is given in Appendix D.7.

## D.3 Simulation 3: Under-optimum FACF – 57% foam quality

Figure D.3 presents the  $k_r$  curves for the oleic and aqueous phases used for simulating primary drainage and forced imbibition in Simulation 3. Please note that the same set of parameters was used for simulating 4 wt% NaCl and 2 wt% NaCl water flooding.

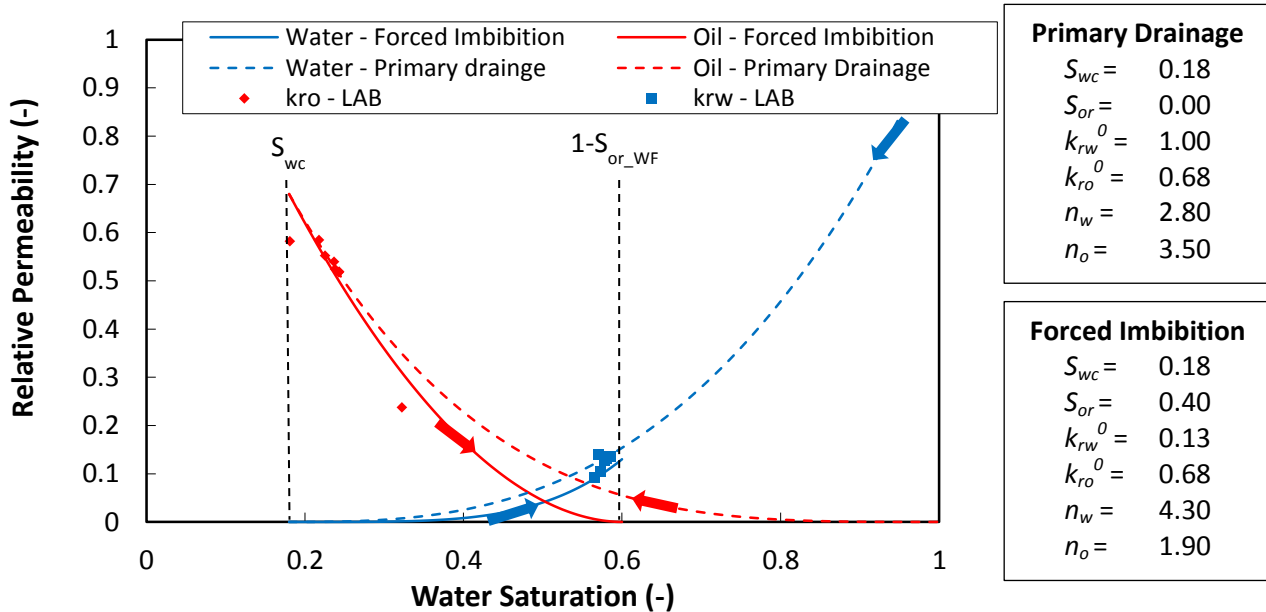


Figure D.3: Relative permeability curves for the aqueous (blue) and oleic (red) phases during primary drainage (dashed lines) and water flooding (continuous lines) used for Simulation 3. More information on how we used the experimental data to obtain a  $k_{ro}^0$  and  $k_{rw}^0$  for simulation purposes is given in Appendix D.7.

### D.4 Simulation 4: Under-optimum FACF – 77% foam quality

Figure D.4 presents the  $k_r$  curves for the oleic and aqueous phases used for simulating primary drainage and forced imbibition in Simulation 4.

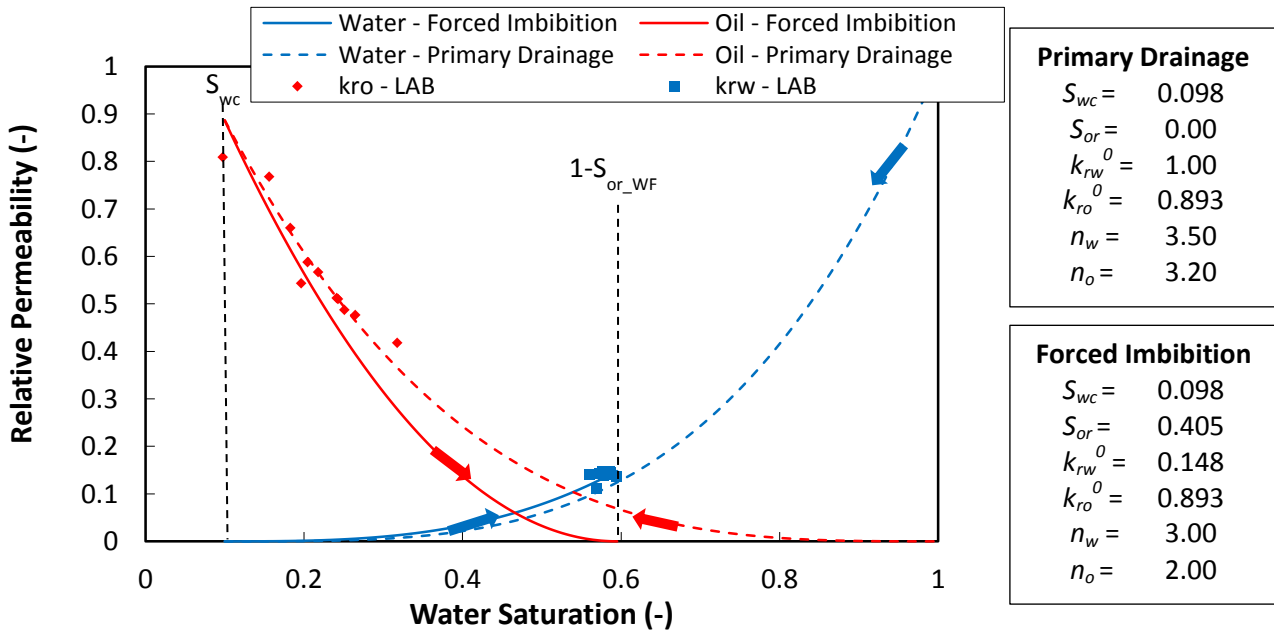


Figure D.4: Relative permeability curves for the aqueous (blue) and oleic (red) phases during primary drainage (dashed lines) and water flooding (continuous lines) used for Simulation 4. More information on how we used the experimental data to obtain a  $k_{ro}^0$  and  $k_{rw}^0$  for simulation purposes is given in Appendix D.7.

### D.5 Simulation 5: Under-optimum FACF – 97% foam quality

Figure D.5 presents the  $k_r$  curves for the oleic and aqueous phases used for simulating primary drainage and forced imbibition in Simulation 5.

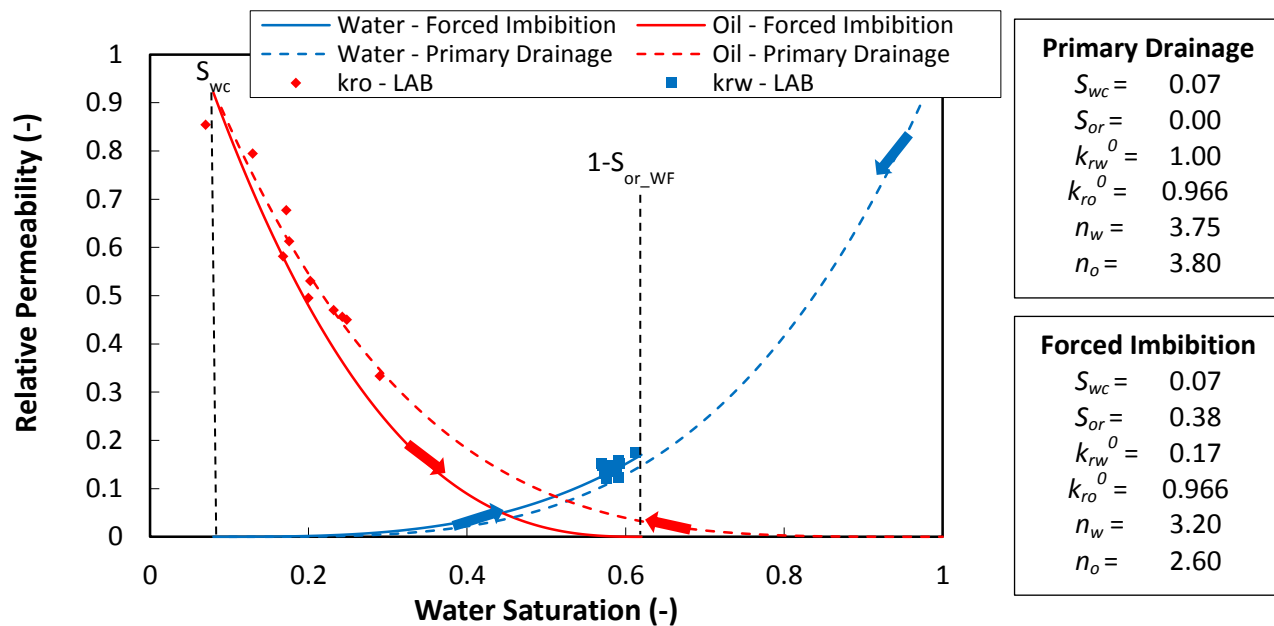


Figure D.5: Relative permeability curves for the aqueous (blue) and oleic (red) phases during primary drainage (dashed lines) and water flooding (continuous lines) used for Simulation 5. More information on how we used the experimental data to obtain a  $k_{ro}^0$  and  $k_{rw}^0$  for simulation purposes is given in Appendix D.7.

## D.6 Simulation 6: (Near-)optimum FACF -57% foam quality

Figure D.6 presents the  $k_r$  curves for the oleic and aqueous phases used for simulating primary drainage and forced imbibition in Simulation 6.

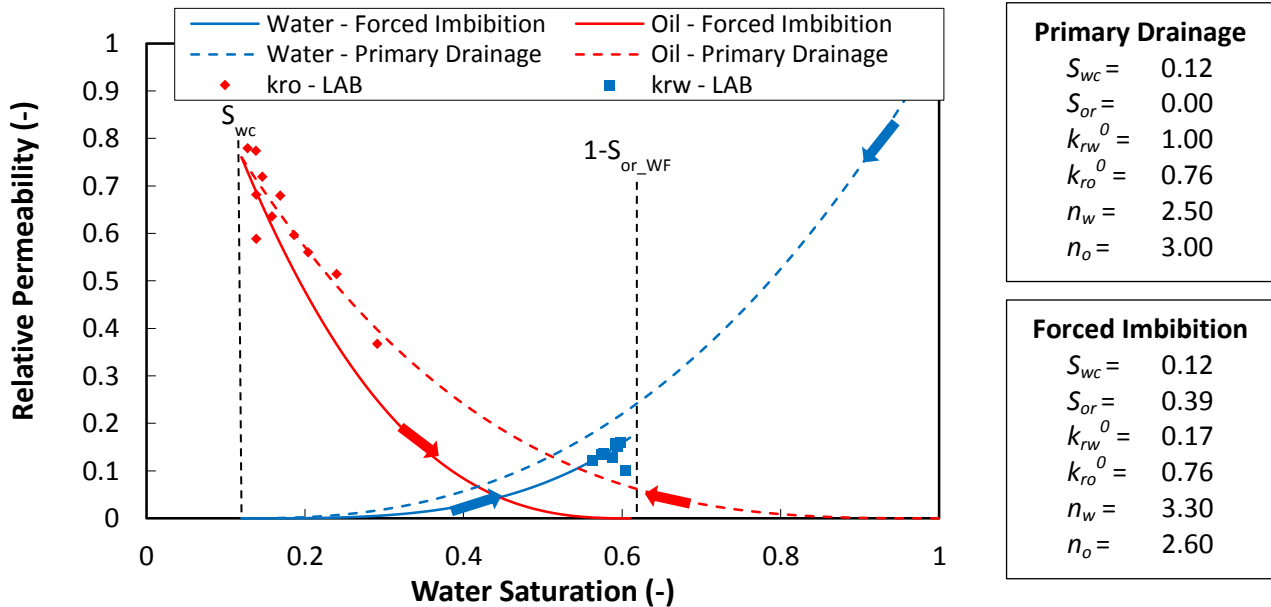


Figure D.6: Relative permeability curves for the aqueous (blue) and oleic (red) phases during primary drainage (dashed lines) and water flooding (continuous lines) used for Simulation 6. More information on how we used the experimental data to obtain a  $k_{ro}^0$  and  $k_{rw}^0$  for simulation purposes is given in **Appendix D.7**.

## D.7 Relative permeability parameters: experiment vs. simulation

The aforementioned relative permeability parameters used for simulating primary drainage and water flooding may differ from the experimental parameters ( $k_{rw}^0$ ,  $k_{ro}^0$ , and  $S_{wc}$ ) presented in **Tables 2.6, 3.4, and 4.5**. Reason for this is that the experimental parameters shown in the tables mentioned are averaged over the entire core length. The latter implies that, for instance, the  $S_{wc}$  value mentioned for Exp. 2 in **Table 3.4** might actually be lower (see inlet area in **Figure 3.4**). The same holds for the obtained  $k_{rw}^0$  and  $k_{ro}^0$  during the core-flood experiments. These were acquired by considering the total pressure drop, and not the sectional pressure drops individually. Once we estimate  $k_{rw}^0$  and  $k_{ro}^0$  per section (**Figure 3.1**), and relate it to the  $S_w$  in that section based on CT processing (**Appendix A**), we can plot multiple  $k_{rw}^0$  and  $k_{ro}^0$  values in a relative permeability plot. This has been done for Simulation 5 in **Figure D.7**.

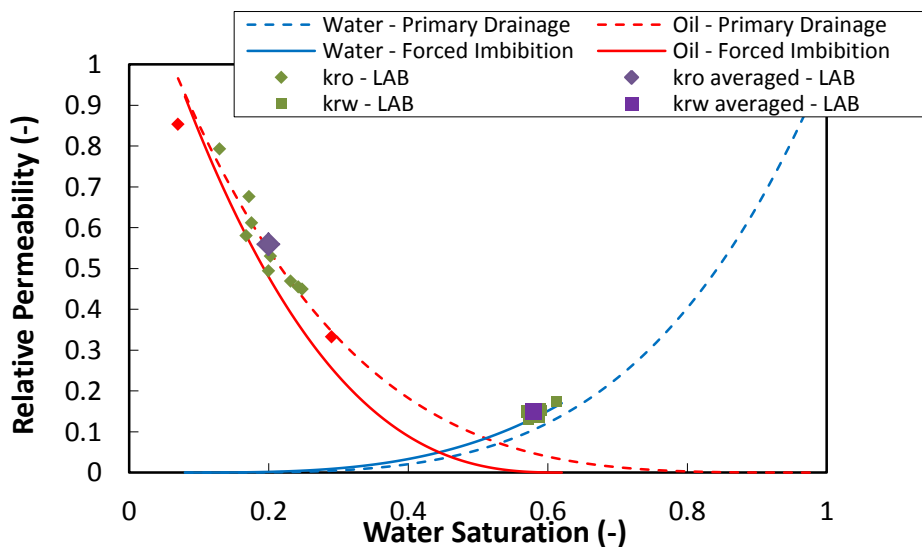
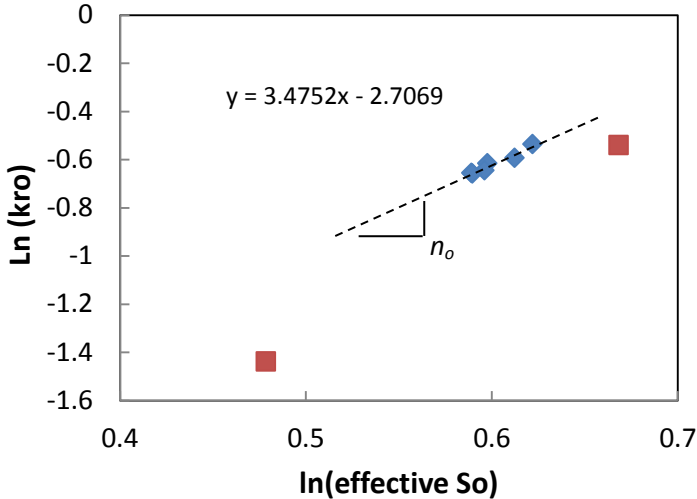


Figure D.7: Relative permeability curves for the aqueous (blue) and oleic (red) phases during forced imbibition used for Simulation 5. Note that the true  $k_{ro}^0$  is significantly larger than the averaged  $k_{ro}^0$ .

The two red diamonds in **Figure D.7** are the  $k_{ro}^0$  values estimated for the inlet and outlet section (**Figure 3.1**). These two points are not considered as accurate values because of the inlet/outlet tubing effect on the observed pressure drop; which is the input for  $k_{ro}^0$  calculation. In order to achieve the  $k_{ro}^0$  used in the simulation (0.9657), we used the observed trend of the green diamond dataset in **Figure D.7** and applied extrapolation towards the lowest  $S_{wc}$  that was found near the core inlet section. The same procedure is applied to obtain  $k_{rw}^0$  that was used in each simulation.

**D.8 Estimating Corey’s exponents ( $n_w$  and  $n_o$ )**

The sectional  $k_{rw}^0$  and  $k_{ro}^0$  calculated, at the end of water flooding and primary drainage, respectively, were used to obtain first guesses of the Corey exponents by linearizing the Brooks-Corey equation. These values for  $n_w$  and  $n_o$  were taken as initial parameters in the model, and can be fine-tuned during the process of history-matching. **Figure D.8** presents an example where we obtained the first guess for  $n_o$  during primary drainage in Simulation 3.



**Figure D.8:** Estimation of Corey exponent  $n_o$  that is used as an initial starting point for obtaining the oil relative permeability curve presented in **Figure D.3**.



# Appendix E. Pressure drops, oil saturation profiles and phase cuts: primary drainage and forced imbibition.

This appendix presents comparisons between observed and simulated pressure drops,  $S_o$  profiles (if available), and phase cuts (if available) for Simulations 1 – 2 and 4 – 6 during primary drainage and forced imbibition.

## E.1 Simulation 1: WAG

Figure E.1 presents the comparison between observed and simulated pressure drops for Simulation 1 during primary drainage. Unfortunately, phase cut data and saturation profiles were not available during this injection stage for this particular experiment.

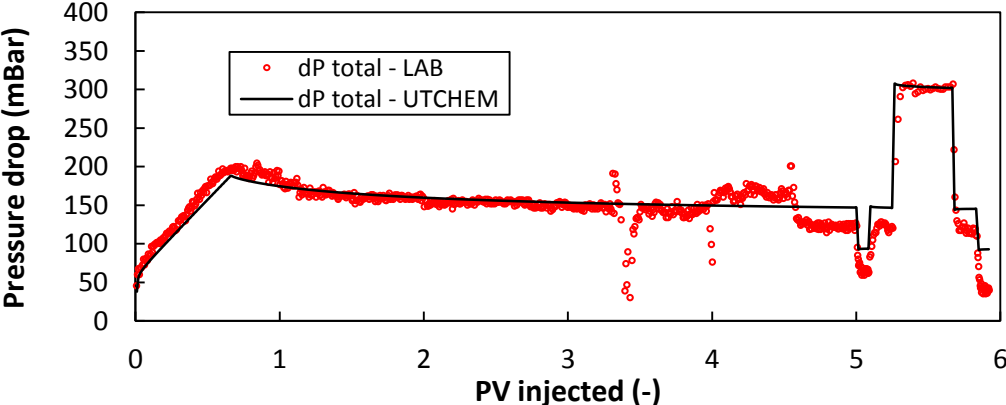


Figure E.1: Simulated and measured total pressure drop profile for primary drainage for Simulation 1.

## E.2 Simulation 2: Extended surfactant slug injection

Figure E.2 presents the comparison between observed and simulated pressure drops (E.2A), phase cuts (E.2B and D), and  $S_o$  profiles (E.2C) for Simulation 2 during primary drainage and forced imbibition.

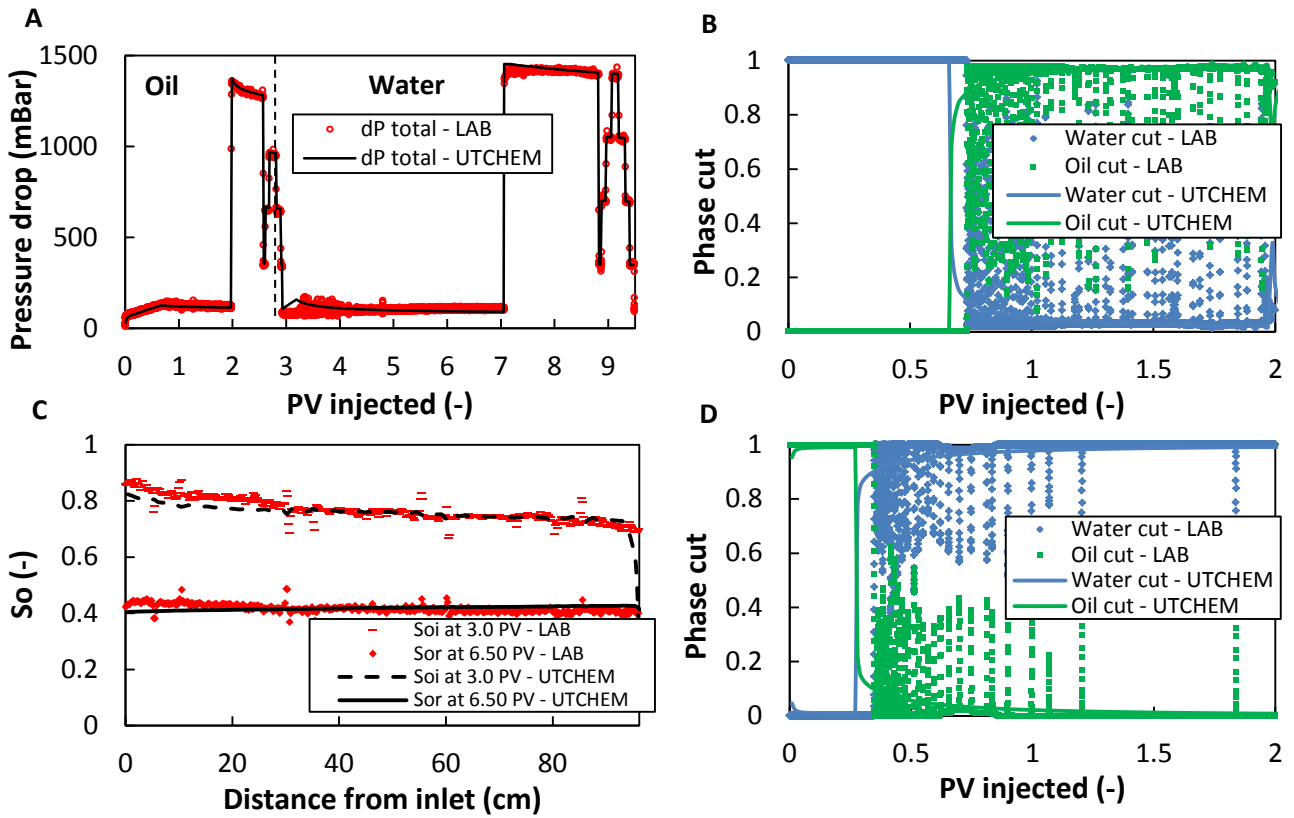


Figure E.2: A: Simulated and measured total pressure drop profiles for primary drainage (oil) and water flooding (water). B: Simulated and measured phase cuts during primary drainage. C: Simulated and measured saturation profiles at the end of primary drainage ( $S_{oi}$ ) and water flooding ( $S_{or}$ ). D: Simulated and measured phase cuts during water flooding.

### E.3 Simulation 4: Under-optimum FACH – 77% foam quality

Figure E.3 presents the comparison between observed and simulated pressure drops (E.3A), phase cuts during water flooding (E.3B), and  $S_o$  profiles (E.3C) for Simulation 4 during primary drainage and forced imbibition.

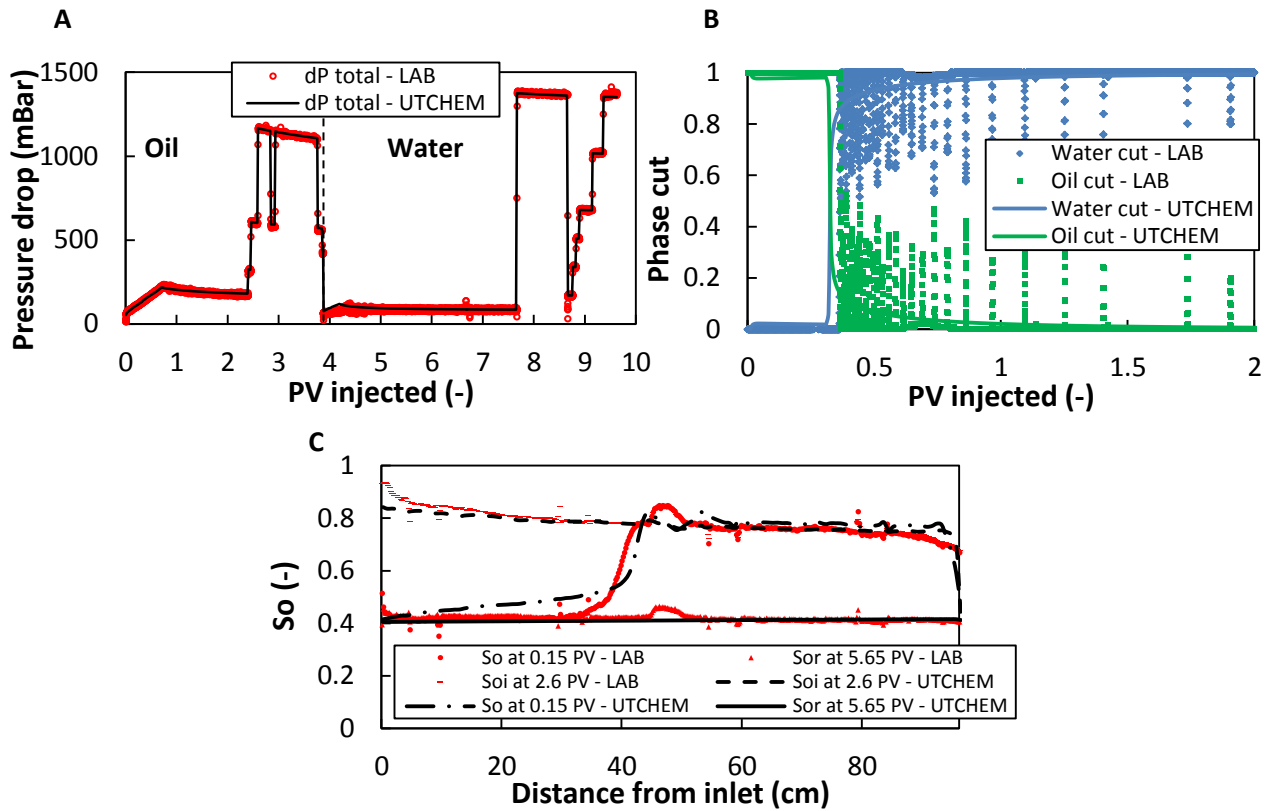


Figure E.3: A: Simulated and measured total pressure drop profiles for primary drainage (oil) and water flooding (water). B: Simulated and measured phase cuts during water flooding. C: Simulated and measured saturation profiles at the end of primary drainage ( $S_{oi}$ ), during water flooding ( $S_o$  at 0.15 PV), and at the end of water flooding ( $S_{or}$ ).

### E.4 Simulation 5: Under-optimum FACH – 97% foam quality

Figure E.4 presents the comparison between observed and simulated pressure drops (E.4A) and  $S_o$  profiles (E.4C) for Simulation 5 during primary drainage and forced imbibition.

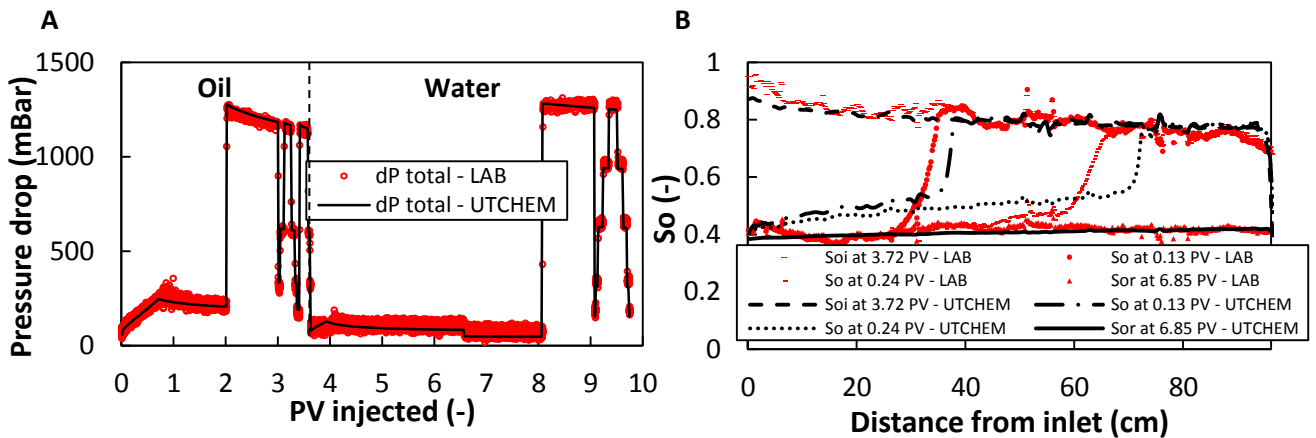


Figure E.4: A: Simulated and measured total pressure drop profiles for primary drainage (oil) and water flooding (water). B: Simulated and measured saturation profiles at the end of primary drainage ( $S_{oi}$ ), during water flooding ( $S_o$  at 0.13 and 0.24 PV), and at the end of water flooding ( $S_{or}$ ).

### E.5 Simulation 6: (Near-)optimum FACF -57% foam quality

Figure E.5 presents the comparison between observed and simulated pressure drops (E.5A) and  $S_o$  profiles (E.5C) for Simulation 6 during primary drainage and forced imbibition.

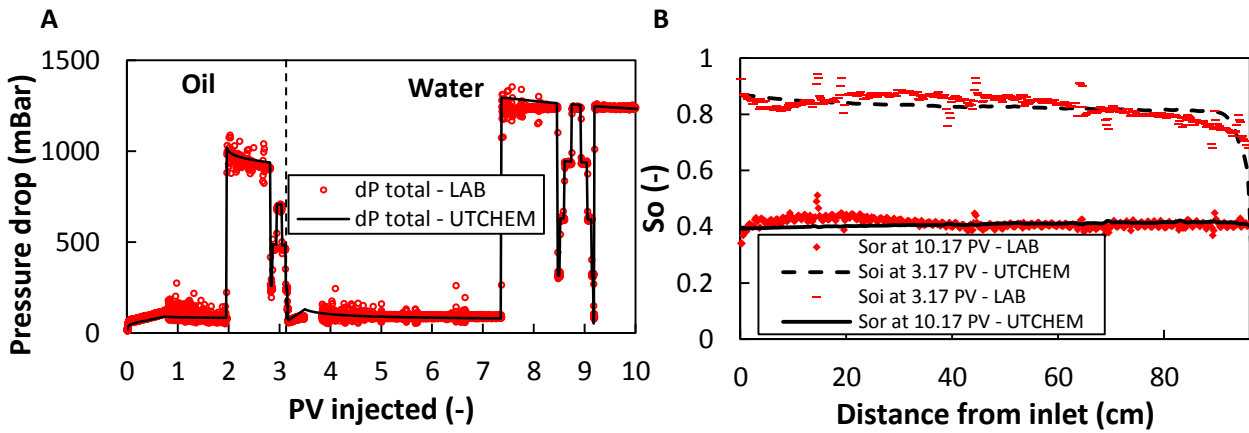


Figure E5: A: Simulated and measured total pressure drop profiles for primary drainage (oil) and water flooding (water). B: Simulated and measured saturation profiles at the end of primary drainage ( $S_{oi}$ ) and at the end of water flooding ( $S_{or}$ ).

### E.6 Comparison of $S_{oi}$ , $S_{or\_WF}$ and $R_{FWF}$

Table E.1 presents an overview of the simulated and measured  $S_{oi}$ ,  $S_{or\_WF}$  and  $R_{FWF}$  values for Simulations 1 to 6.

Table E.1: Overview of the simulated and measured  $S_{oi}$ ,  $S_{or\_WF}$  and  $R_{FWF}$  values for Simulations 1 to 6.

Simulation	$S_{oi}$		$S_{or\_WF}$		$R_{FWF}$ (% of OIIP)	
	simulated	observed	simulated	observed	simulated	observed
1	$0.73 \pm 0.07$	$0.74 \pm 0.02$	-	-	-	-
2	$0.72 \pm 0.06$	$0.77 \pm 0.04$	$0.42 \pm 0.01$	$0.42 \pm 0.01$	$42 \pm 5$	$45 \pm 5$
3	$0.76 \pm 0.03$	$0.78 \pm 0.04$	$0.40 \pm 0.01$	$0.41 \pm 0.02$	$47 \pm 4$	$47 \pm 6$
4	$0.78 \pm 0.03$	$0.78 \pm 0.05$	$0.41 \pm 0.01$	$0.42 \pm 0.01$	$47 \pm 4$	$46 \pm 6$
5	$0.79 \pm 0.05$	$0.80 \pm 0.05$	$0.41 \pm 0.01$	$0.42 \pm 0.02$	$48 \pm 4$	$48 \pm 7$
6	$0.82 \pm 0.06$	$0.83 \pm 0.05$	$0.41 \pm 0.01$	$0.41 \pm 0.02$	$50 \pm 5$	$51 \pm 7$

# Appendix F. Relative permeability curves: WAG injection.

This appendix presents an overview of the  $k_r$  curves used as an input for the mechanistic modelling of WAG injection at  $S_{oi}$  (Simulation 1).

## F.1 WAG cycle 1

Figure F.1 presents an overview of the  $k_r$  curves used as an input for the mechanistic modelling of the first WAG cycle.

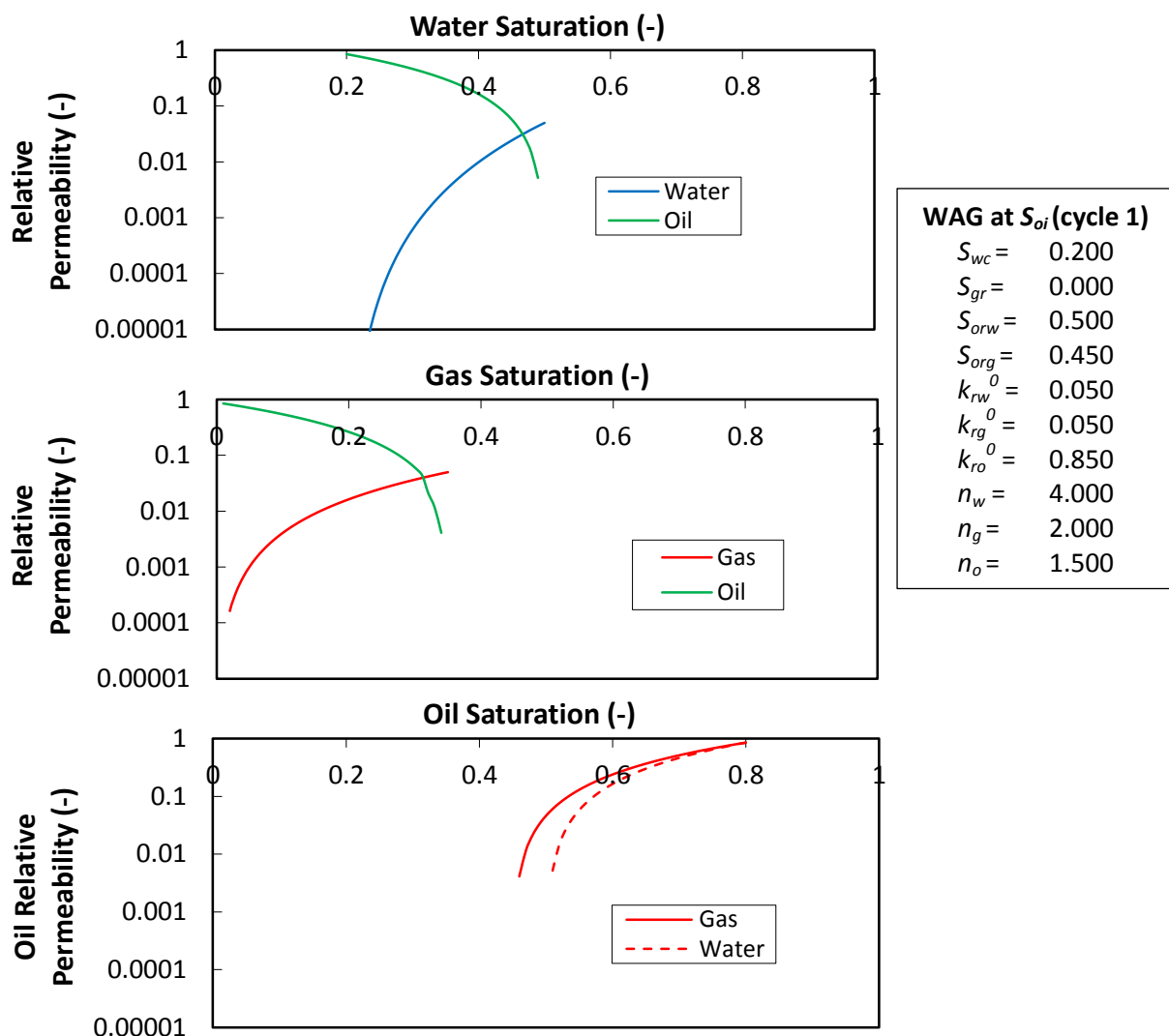


Figure F.1: Relative permeability curves for the aqueous (blue), gaseous (red), and oleic (green) phases during the injection of the first WAG cycle in Simulation 1. The table on the right-hand side present the  $k_r$  parameters using the Corey-type functions within UTCHEM (UTCHEM Technical Documentation, 2017).

## F.2 WAG cycle 2

Figure F.2 presents an overview of the  $k_r$  curves used as an input for the mechanistic modelling of the second WAG cycle.

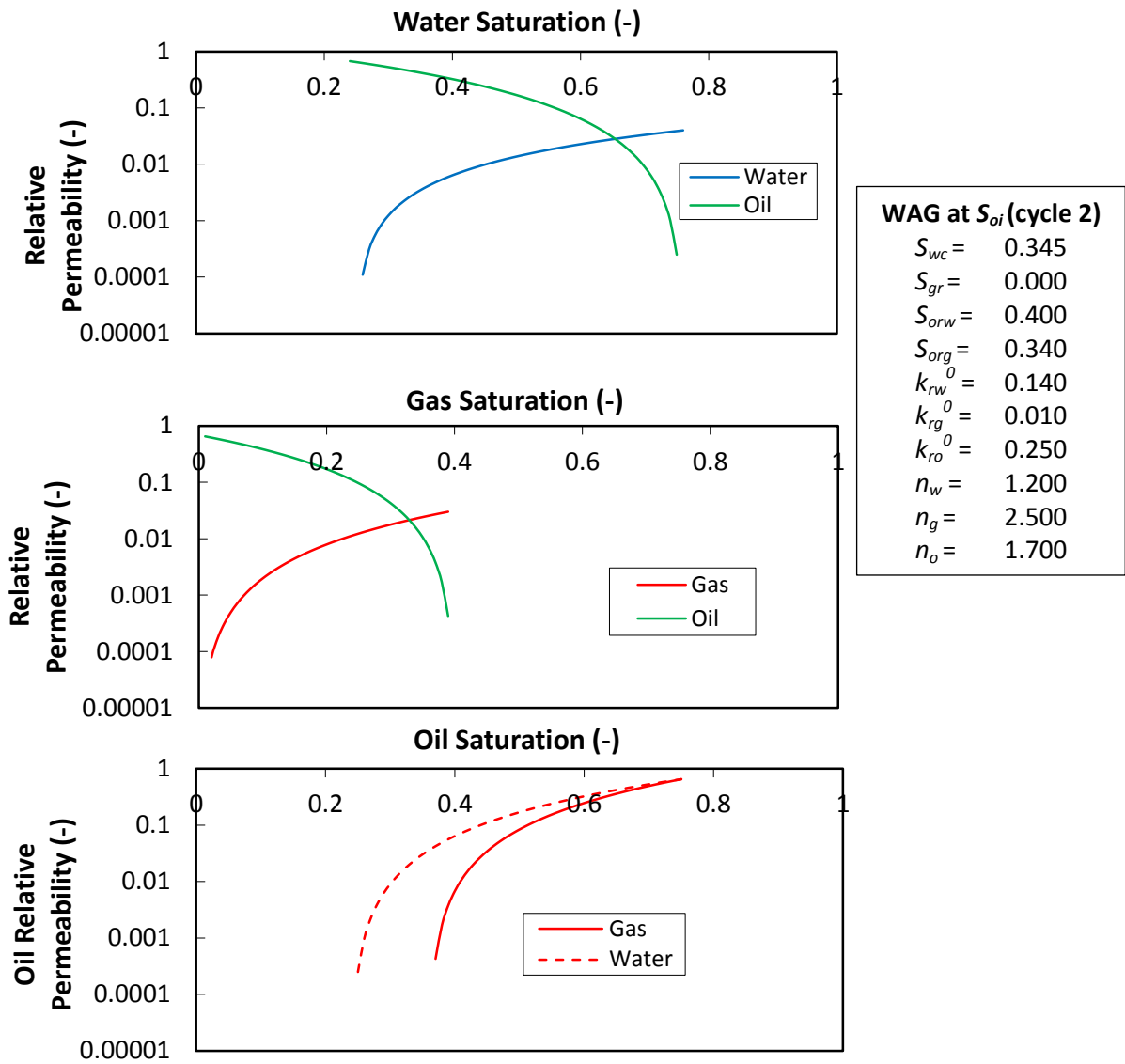


Figure F.2: Relative permeability curves for the aqueous (blue), gaseous (red), and oleic (green) phases during the injection of the second WAG cycle in Simulation 1. The table on the right-hand side present the  $k_r$  parameters using the Corey-type functions within UTCHEM (UTCHEM Technical Documentation, 2017).

### F.3 WAG cycles >2

Figure F.3 presents an overview of the  $k_r$  curves used as an input for the mechanistic modelling of the WAG cycles subsequent to the second cycle.

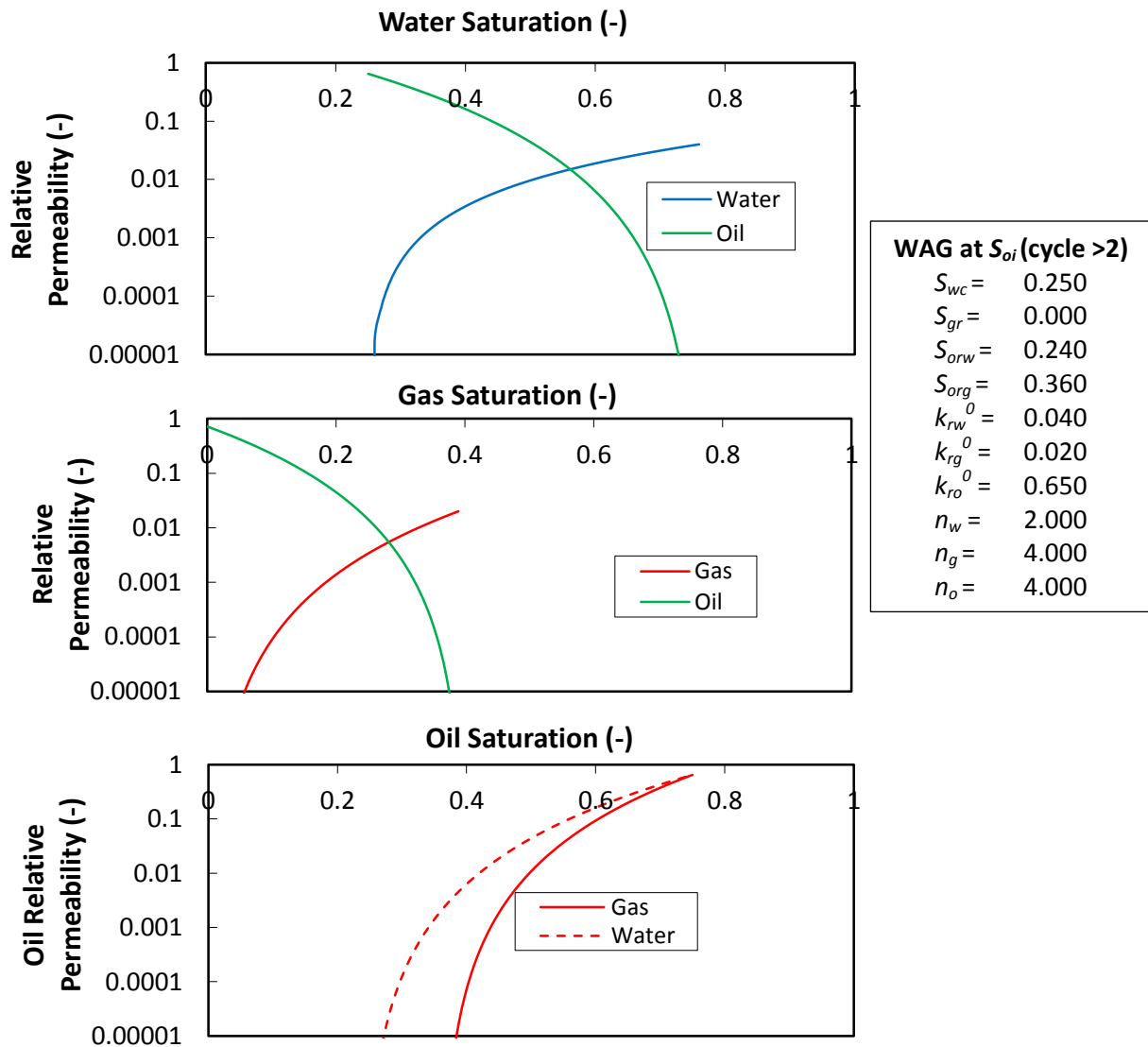


Figure F.3: Relative permeability curves for the aqueous (blue), gaseous (red), and oleic (green) phases during the injection of WAG cycles >2 in Simulation 1. The table on the right-hand side present the  $k_r$  parameters using the Corey-type functions within UTCHEM (UTCHEM Technical Documentation, 2017).



# Appendix G. Relative permeability curves: surfactant slug injection.

This appendix presents an overview of the  $k_r$  curves used as an input for the mechanistic modelling of surfactant slug injection in Simulations 3 to 6.

## G.1 Simulation 3: Under-optimum FACH – 57% foam quality

Figure G.1 presents the  $k_r$  curves for the oleic and aqueous phases used for simulating surfactant slug injection in Simulation 3.

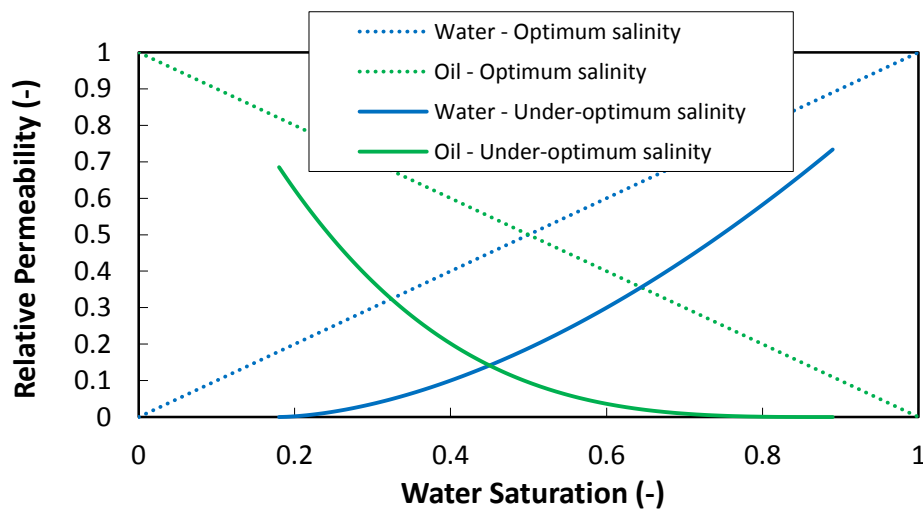


Figure G.1: Oil and water relative permeability curves for under-optimum and optimum salinity flooding in Simulation 3. The curves for under-optimum salinity are used as input in the simulation.

## G.2 Simulation 4: Under-optimum FACH – 77% foam quality

Figure G.2 presents the  $k_r$  curves for the oleic and aqueous phases used for simulating surfactant slug injection in Simulation 4.

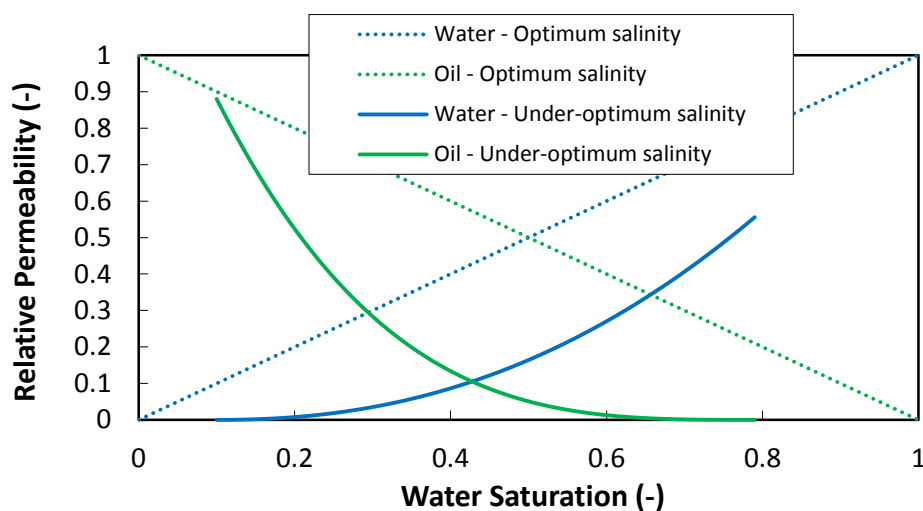


Figure G.2: Oil and water relative permeability curves for under-optimum and optimum salinity flooding in Simulation 4. The curves for under-optimum salinity are used as input in the simulation.

### G.3 Simulation 5: Under-optimum FACH – 97% foam quality

Figure G.3 presents the  $k_r$  curves for the oleic and aqueous phases used for simulating surfactant slug injection in Simulation 5.

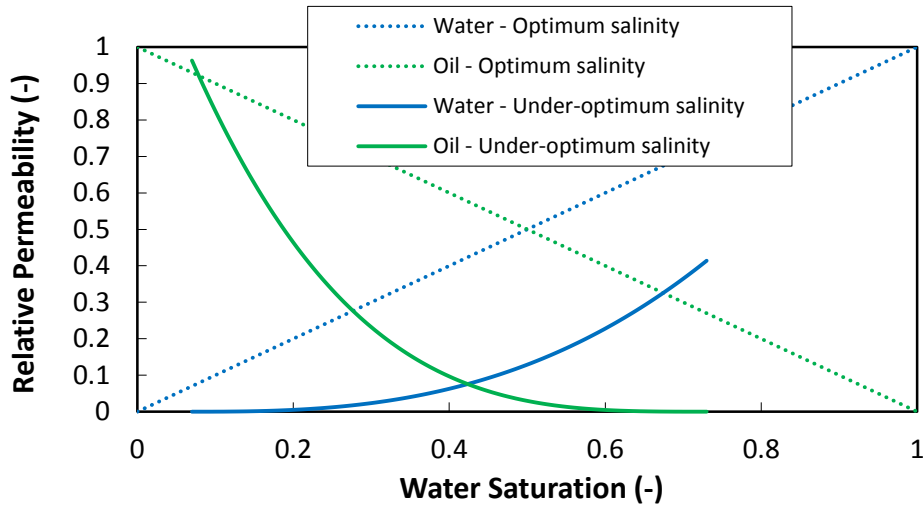


Figure G.3: Oil and water relative permeability curves for under-optimum and optimum salinity flooding in Simulation 5. The curves for under-optimum salinity are used as input in the simulation.

### G.4 Simulation 6: (Near-)optimum FACH – 57% foam quality

Figure G.4 presents the  $k_r$  curves for the oleic and aqueous phases used for simulating surfactant slug injection in Simulation 6.

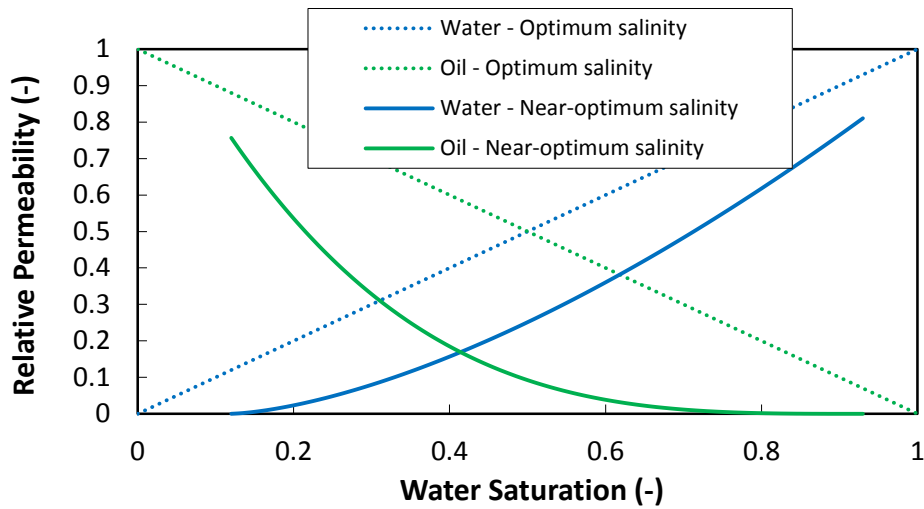


Figure G.4: Oil and water relative permeability curves for near-optimum and optimum salinity flooding in Simulation 6. The curves for near-optimum salinity are used as input in the simulation.

# Appendix H. Pressure drops and oil saturation profiles: surfactant slug injection.

This appendix presents comparisons between observed and simulated pressure drops and  $S_o$  profiles for Simulations 4 and 5 during surfactant slug injection. For Simulation 2 (i.e. the extended surfactant slug injection experiment), simulated pressure drops,  $S_o$  profiles, phase cuts, and oil recovery profiles are compared with experimental observations.

## H.1 Simulation 2: Extended surfactant slug injection

Figure H.1 presents the comparison between observed and simulated pressure drops (H.1A), oil cut and ultimate oil recovery (H.1B), and  $S_o$  profiles (H.1C) for Simulation 2 during the extended surfactant slug injection at  $S_{or\_WF}$ .

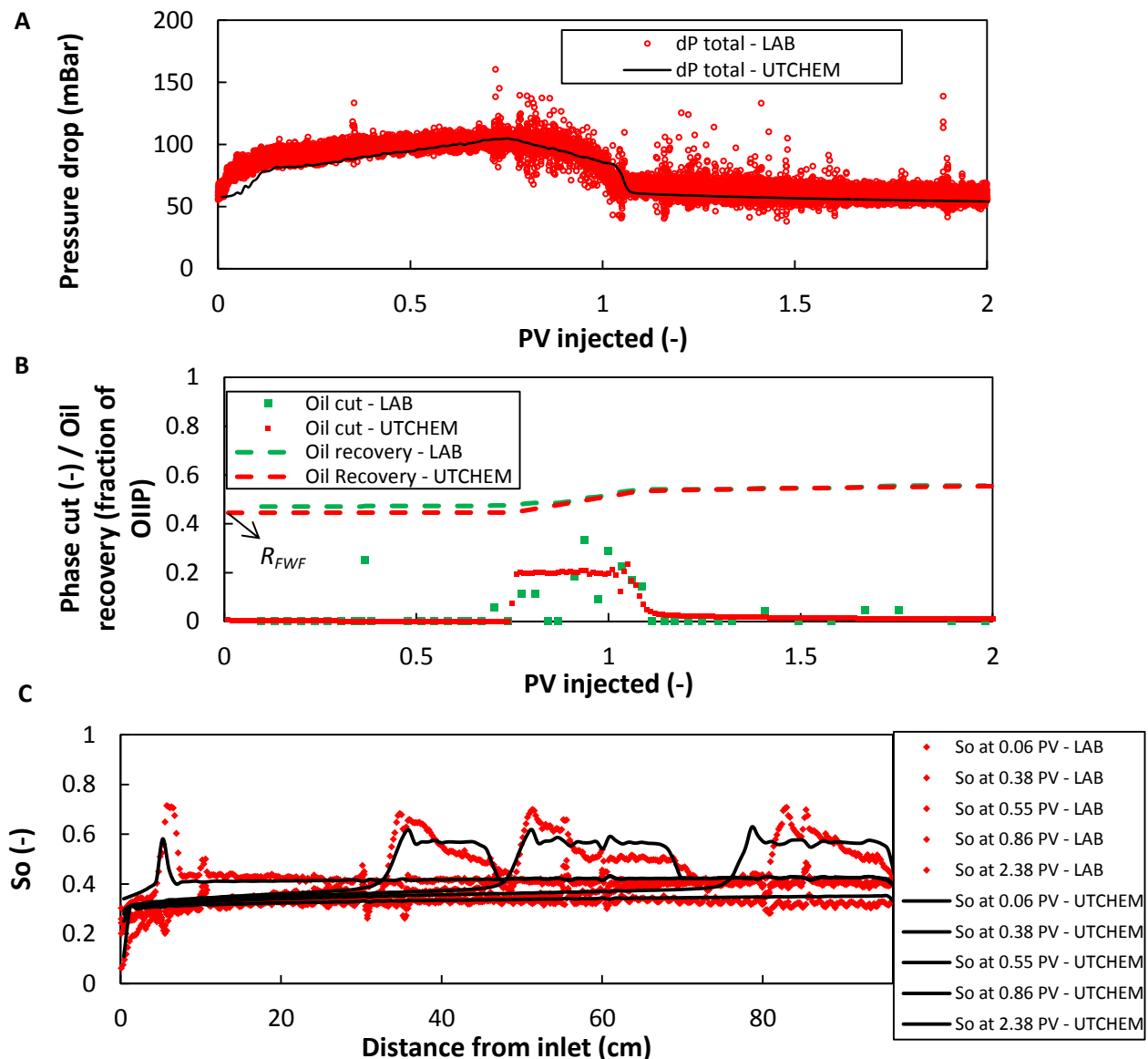
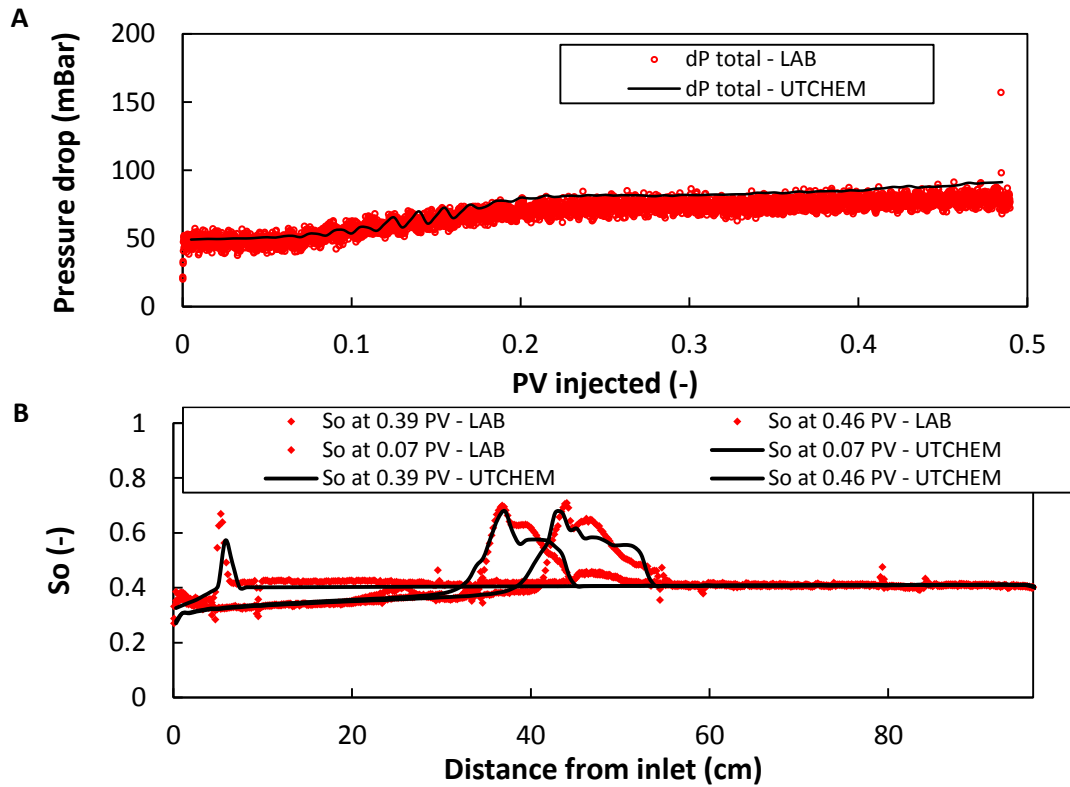


Figure H.1: Simulated and measured total pressure drop profiles for the extended surfactant slug injection in Simulation 2 (A), simulated and observed oil phase cut and ultimate oil recovery profile (B), and oil saturation profiles obtained from experimental data and simulation for surfactant injection in Simulation 2 (C).

## H.2 Simulation 4: Under-optimum FACH – 77% foam quality

Figure H.2 presents the comparison between observed and simulated pressure drops (H.2A) and  $S_o$  profiles (H.2B) for Simulation 4 during surfactant slug injection.



**Figure H.2:** Simulated and measured total pressure drop profiles for the surfactant slug injection in Simulation 4 (A), and oil saturation profiles obtained from experimental data and simulation for surfactant slug injection in Simulation 4 (B).

### H.3 Simulation 5: Under-optimum FACH – 97% foam quality

Figure H.3 presents the comparison between observed and simulated pressure drops (H.3A) and  $S_o$  profiles (H.3B) for Simulation 5 during surfactant slug injection.

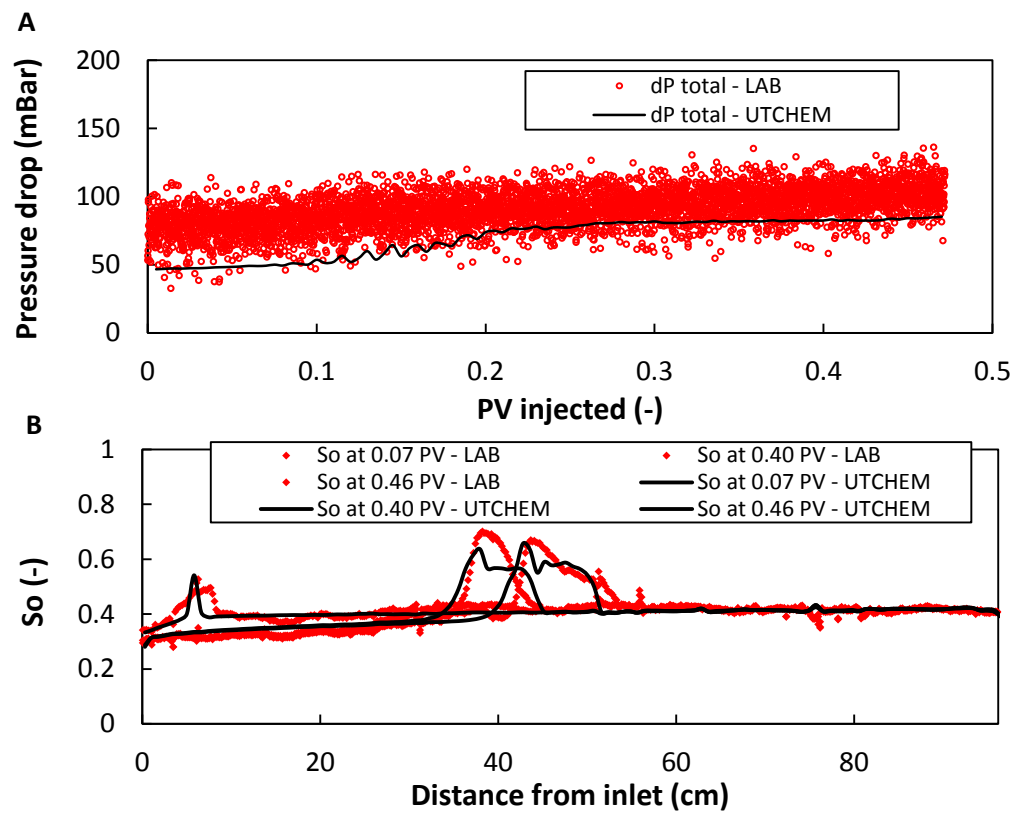


Figure H.3: Simulated and measured total pressure drop profiles for the surfactant slug injection in Simulation 5 (A), and oil saturation profiles obtained from experimental data and simulation for surfactant slug injection in Simulation 5 (B).



# Bibliography

---

- Aarra, M.G., and Skauge, A.A. 1994. Foam Pilot in a North Sea Oil Reservoir: Preparation for a Production Well Treatment. Presented at the SPE Annual Technical Conference and Exhibition, New Orleans, Louisiana, USA, 25 – 28 September. SPE-28599-MS. <https://doi.org/10.2118/28599-MS>.
- Aderangi, N., and Wasam, D.T. 1995. Coalescence of single drops at a liquid-liquid interface in the presence of surfactants/polymers. *Chem. Eng. Commun.*, 132(1), 207–222.
- Alvarez, J.M., Rivas, H.J., and Rossen, W.R. 2001. Unified Model for Steady-State Foam Behavior at High and Low Foam Qualities. *SPE J.*, 6(3), 325–333.
- Andrianov, A.I., Liu, M.K., and Rossen, W.R. 2011. Sweep Efficiency in CO<sub>2</sub> Foam Simulations With Oil. Presented at the SPE EUROPEC/EAGE Annual Conference and Exhibition, Vienna, Austria, 23 – 26 May. SPE-142999-MS. <https://doi.org/10.2118/142999-MS>.
- Aronson, A.S., Bergeron, V., Fagan, M.E., and Radke, C.J. 1994. The influence of disjoining pressure on foam stability and flow in porous media. *Colloid. Surface. Physicochem. Eng. Aspect.*, 83(2), 109–120.
- Barnes, J.R., Dirkwager, H., Smit, J., Smit, J., On, A., Navarette, R.C., Ellison, B., and Buijse, M.A. 2010. Application of Internal Olefin Sulfonates and Other Surfactants to EOR. Part 1: Structure—Performance Relationships for Selection at Different Reservoir Conditions. Presented at the SPE Improved Oil Recovery Symposium, Tulsa, Oklahoma, USA, 24 – 28 April. SPE-129766-MS. <https://doi.org/10.2118/129766-MS>.
- Battistutta, E., van Kuijk, S.R., Groen, K.V., and Zitha, P.L.J. 2015. Alkaline-Surfactant-Polymer (ASP) Flooding of Crude Oil at Under-Optimum Salinity Conditions. Presented at the SPE Asia Pacific Enhanced Oil Recovery Conference, Kuala Lumpur, Malaysia, 11 – 13 August. SPE-174666-MS. <https://doi.org/10.2118/174666-MS>.
- Bear, J., and Bachmat, Y. 1990. Introduction to Modeling of Transport Phenomena in Porous Media (Vol. 4). Springer Netherlands.
- Bernard, G.G., Holm, L.W., and Jacobs, W.L. 1965. Effect of Foam on Trapped Gas Saturation and on Permeability of Porous Media to Water. *SPE J.*, 5(4), 195–300.
- Blunt, M., Zhou, D., and Fenwick, D. 1995. Three-phase flow and gravity drainage in porous media. *Transp. Porous Media*, 20(1-2), 77 – 103.
- Boeije, C.S., and Rossen, W.R. 2018. SAG foam flooding in carbonate rocks. *J. Petrol. Sci. Eng.*, 171, 843 – 853.
- BP Energy Outlook. 2019. Retrieved from <https://www.bp.com/content/dam/bp/business-sites/en/global/corporate/pdfs/energy-economics/energy-outlook/bp-energy-outlook-2019.pdf>
- Brooks, R.H., and Corey, A.T. 1966. Properties of porous media affecting fluid flow. *J. Irrig. Drain. Div.*, 92(2), 61 – 90.
- Buckley, S.E., and Leverett, M. 1942. Mechanism of fluid displacement in sands. *Trans. AIME*, 146(1), 107 – 116.
- Carman, P.C. 1937. Fluid flow through granular beds. *Trans. Inst. Chem. Eng.*, 15, 150 – 166.
- Castanier, L.M. 1988. Introduction to computerized X-ray tomography for petroleum research. US Department of Energy. Technical Report DOE/BC/14126-7. Stanford Univ., CA (USA). Petroleum Research Inst.
- Chambers, K.T., and Radke, C.J. 1990. Capillary phenomena in foam flow through porous media. In

- Interfacial Phenomena in Oil Recovery*, Chap. 6, 191 – 256. New York City, Marcel Dekker Inc.
- Chatterjee, J., and Wasan, D.T. 1998. A Kinetic Model for Dynamic Interfacial Tension Variation in an Acidic Oil/Alkali/Surfactant System. *Chem. Eng. Sci.*, 53(15), 2711 – 2725.
- Cheng, L., Reme, A.B., Shan, D., Coombe, D.A., and Rossen, W.R. 2000. Simulating Foam Processes at High and Low Foam Qualities. Presented at the SPE Improved Oil Recovery Symposium, Tulsa, Oklahoma, USA, 3 – 5 April. SPE-59287-MS. <https://doi.org/10.2118/59287-MS>.
- Dake, L.P. 1983. *Fundamentals of reservoir engineering* (Vol. 8). Elsevier.
- Darcy, H. 1856. *Les fontaines publiques de la ville de Dijon: exposition et application*. Victor Dalmont.
- de Vries, A.S., and Wit, K. 1990. Rheology of gas/water foam in the quality range relevant to steam foam. *SPE Reserv. Eng.*, 5(2), 185 – 192.
- Delamaide, E., Tabary, R., and Rousseau, D. 2014. Chemical EOR in low permeability reservoirs. Presented at the SPE EOR Conference at Oil and Gas West Asia, Muscat, Oman, 31 March – 2 April. SPE-169673-MS. <https://doi.org/10.2118/169673-MS>.
- Delshad, M., Najafabadi, N.F., Anderson, G.A., Pope, G.A., and Sepehrnoori, K. 2006. Modeling Wettability Alteration in Naturally Fractured Reservoirs. Presented at the SPE Improved Oil Recovery Symposium, Tulsa, Oklahoma, USA, 22 – 26 April. SPE-100081-MS. <https://doi.org/10.2118/100081-MS>.
- Dicarlo, D.A., Sahni, A., and Blunt, M.J. 2000. Three-phase relative permeability of water-wet, oil-wet and mixed-wet sandpacks. *SPE J.*, 5(1), 82 – 91.
- Dietz, D.N. 1953. A Theoretical Approach to the Problem of Encroaching and by-passing Edge Water. In: *Akad. van Wetenschappen, Amsterdam. Proc. B vol. 56*, 83 – 92.
- Dong, M., Dullien, F.A.L., Chatzis, I. 1995. Imbibition of oil in film form over water present in edges of capillaries with an angular cross section. *J. Colloid Interface Sci.*, 172(1), 21 – 36.
- Dong, M., Forai, J., Huang, S., and Chatzis, I. 2002. Analysis of immiscible water-alternating-gas (WAG) injection using micromodel. Presented at the Canadian International Petroleum Conference, Calgary, Alberta, Canada, 11 – 13 June. PETSOC-2002-158. <https://doi.org/10.2118/2002-158>.
- Dong, M., Forai, J., Huang, S., Chatzis, I. 2005. Analysis of immiscible water-alternating-gas (WAG) injection using micromodel tests. *J. Can. Pet. Technol.*, 44(2), 17 – 25.
- Du, D., Zitha, P.L.J., and Uijttenhout, M.G. 2007. Carbon dioxide foam rheology in porous media: a CT scan study. *SPE J.*, 12(2), 245 – 252.
- Du Noüy, P.L. 1925. An Interfacial Tensiometer for Universal Use. *J. Gen. Physiol.*, 7(5), 625 – 631.
- Dyer, S.B., and Farouq Ali, S.M. 1994. Linear Model Studies of the Immiscible CO<sub>2</sub> WAG process for Heavy-Oil Recovery. *SPE Reserv. Eng.*, 9(2), 107 – 111.
- Ettinger, R.A., and Radke, C.J. 1992. Influence of Texture on Steady Foam Flow in Berea Sandstone. *SPE Reserv. Eng.*, 7(1), 83 – 90.
- Falls, A.H., Hirasaki, G.J., Patzek, T.W., Gauglitz, D.A., Miller, D.D., and Ratulowski, T. 1988. Development of a Mechanistic Foam Simulator: The Population Balance and Generation by Snap-Off. *SPE Reserv. Eng.*, 3(3), 884 – 892.
- Falode, O., and Manuel, E. 2014. Wettability effects on capillary pressure, relative permeability, and irreducible saturation using porous plate. *J. Pet. Eng.*, Vol. 2014, Article ID 465418, 12 pages.
- Farajzadeh, R., Andrianov, A., Bruining, J., and Zitha, P. 2009. Comparative Study of CO<sub>2</sub> and N<sub>2</sub> Foams in Porous Media at Low and High Pressure-Temperatures. *Ind. Eng. Chem. Res.*, 48(9), 4542 – 4552.
- Farajzadeh, R., Andrianov, A., and Zitha, P. 2010. Investigation of Immiscible and Miscible Foam for

- Enhancing Oil Recovery. *Ind. Eng. Chem. Res.*, 49(4), 1910 – 1919.
- Farajzadeh, R., Andrianov, A., Hirasaki, G.J., Krastev, R., and Rossen, W.R. 2012. Foam-oil interaction in porous media: implications for foam assisted enhanced oil recovery. Presented at the SPE EOR Conference at Oil and Gas West Asia, Muscat, Oman, 16 – 18 April. SPE-154197-MS. <https://doi.org/10.2118/154197-MS>.
- Farajzadeh, R., Lotfollahi, M., Eftekhari, A.A., Rossen, W.R., and Hirasaki, G.J.H. 2015. Effect of permeability on implicit-texture foam model parameters and the limiting capillary pressure. *Energ. Fuel.*, 29(5), 3011 – 3018.
- Farn, R.J. 2008. Chemistry and technology of surfactants. John Wiley & Sons.
- Fatemi, M.S., and Sohrabi, M. 2013. Experimental Investigation of Near-Miscible Water-Alternating-Gas Injection Performance in Water-Wet and Mixed-Wet Systems. *SPE J.*, 18(1), 114 – 123.
- Fayers, F.J. 1981. Enhanced Oil Recovery: Proceedings of the Third European Symposium on Enhanced Oil Recovery. Elsevier Scientific Publishing Company.
- Feng, Q., Di, L., Tang, G., Chen, Z., Wang, X., and Zou, J. 2004. A Visual Micro-Model Study: The Mechanism of Water Alternative Gas Displacement in Porous Media. Presented at the SPE Improved Oil Recovery Symposium, Tulsa, Oklahoma, USA, 17 – 21 April. SPE-89362-MS. <https://doi.org/10.2118/89362-MS>.
- Fortenberry, R. Suniga, P. Mothersele, S. Delshad, M. Lashgari, H. Pope, G.A. 2015. Selection of a Chemical EOR Strategy in a Heavy Oil Reservoir Using Laboratory Data and Reservoir Simulation. Presented at the SPE Canada Heavy Oil Technical Conference, Calgary, Alberta, Canada, 9 – 11 June. SPE-174520-MS. <https://doi.org/10.2118/174520-MS>.
- Fournier, R.O., and Rowe, J.J. 1977. The solubility of amorphous silica in water at high temperatures and high pressures. *Am. Mineral.*, 62(9-10), 1052 – 1056.
- Fuseni, A.B., AlSofi, A.M., AlJulaih, A.H., and AlAseeri, A A. 2018. Development and evaluation of foam-based conformance control for a high-salinity and high-temperature carbonate. *J. Pet. Exp. Prod. Technol.*, 8(4), 1341 – 1348.
- Gauglitz, P.A., Friedmann, F., Kam, S.I., and Rossen, W.R. 2002. Foam Generation in Porous Media. Presented at the SPE Improved Oil Recovery Symposium, Tulsa, Oklahoma, USA, 13 – 17 April. SPE-75177-MS. <https://doi.org/10.2118/75177-MS>.
- Goudarzi, A., Delshad, M., and Sepehrnoori, K. 2013. A Critical Assessment of Several Reservoir Simulators for Modeling Chemical Enhanced Oil Recovery Processes. Presented at the SPE Reservoir Simulation Symposium, The Woodlands, Texas, USA, 18 – 20 February. SPE-163578-MS. <https://doi.org/10.2118/163578-MS>.
- Grattoni, C.A., and Dawe, R.A. 2003. Gas and oil production from waterflood residual oil: effects of wettability and oil spreading characteristics. *J. Petrol. Sci. Eng.*, 39(3-4), 297 – 308.
- Guo, H., Zitha, P.L.J., Faber, R., and Buijse, M. 2012. A novel alkaline/surfactant/foam enhanced oil recovery process. *SPE J.*, 17(4), 1186 – 1195.
- Hagoort, J. 1980. Oil recovery by gravity drainage. *SPE J.*, 20(3), 139 – 150.
- Hallam, R.J., Ma, T.D., and Reinbold, E.W. 1995. Performance Evaluation and Optimization of the Kuparuk Hydrocarbon Miscible Water-Alternating-Gas Flood. *Geol. Soc, London Spec. Publ.*, 84(1), 153 – 164.
- Hand, D.B. 1939. Dineric Distribution: I. The Distribution of a Consolute Liquid Between Two Immiscible Liquids. *J. Physics and Chem.*, 34, 1961 – 2000.
- Hirasaki G.J. and Pope G.A. 1974. Analysis of factors Influencing mobility and adsorption in the Flow of polymer solution through porous media. *SPE J.*, 14(4), 337 – 346.

- Hirasaki, G.L. 1981. Application of the theory of multicomponent, multiphase displacement to three-component, two-phase surfactant flooding. *SPE J.*, 21(2), 191 – 204.
- Hirasaki, G.J., and Lawson, J.B. 1985. Mechanisms of Foam Flow in Porous Media: Apparent Viscosity in Smooth Capillaries. *SPE J.*, 25(2), 176 – 190.
- Hirasaki, G.J. 1993. Structural interactions in the wetting and spreading of van der Waals fluids, *J. Adhesion Sci. Technol.*, 7(3), 285 – 322.
- Hirasaki, G.J., and Zhang, D.L. 2004. Surface Chemistry of Oil Recovery From Fractured Oil-Wet Carbonate Formations. *SPE J.*, 9(2), 151 – 162.
- Hirasaki, G.J., Miller, C.A., and Puerto, M. 2011. Recent advances in surfactant EOR. *SPE J.*, 16(4), 889 – 907.
- Holm, L.W. 1968. The mechanism of gas and liquid flow through porous media in the presence of foam. *SPE J.*, 8(4), 359 – 369.
- Hook, M., Hirsch, R., and Aleklett, K. 2009. Giant oil field decline rates and their influence on world oil production, *Energ. Policy*, 37(6), 2262 – 2272.
- Hosseini-Nasab, S.M., and Zitha, P.L.J. 2015. Systematic phase behaviour study and foam stability analysis for optimal alkaline/surfactant/foam enhanced oil recovery. Presented at the 18<sup>th</sup> European Symposium on Improved Oil Recovery, Dresden, Germany, 14 – 16 April. EAGE.
- Hosseini-Nasab, S.M., Padalkar, C., Battistutta, E., and Zitha, P.L.J. 2016. Mechanistic modeling of the alkaline/surfactant/polymer flooding process under sub-optimum salinity conditions for enhanced oil recovery. *Ind. Eng. Chem. Res.*, 55(24), 6875 – 6888.
- Hou, B.F., Wang, Y.F., and Huang, Y. 2015. Mechanistic study of wettability alteration of oil-wet sandstone surface using different surfactants. *Appl. Surf. Sci.*, 330, 56 – 64.
- Howe, A.M., Clarke, A., Mitchell, J., Staniland, J., and Hawkes, L.A. 2015. Visualising Surfactant EOR in Core Plugs and Micromodels. Presented at the SPE Asia Pacific Enhanced Oil Recovery Conference, Kuala Lumpur, Malaysia, 11 – 13 August. SPE-174643-MS. <https://doi.org/10.2118/174643-MS>.
- Hu, Y., Devegowda, D., Striolo, A., Phan, A., Ho, T.A., Civan, F., and Sigal, R.F. 2014. Microscopic dynamics of water and hydrocarbon in shale-kerogen pores of potentially mixed wettability. *SPE J.*, 20(1), 112 – 124.
- Huang, D.D., and Honarpour, M.M. 1998. Capillary end effects in coreflood calculations. *J. Petrol. Sci. Eng.*, 19(1-2), 103 – 117.
- Huh, C. 1979. Interfacial tensions and solubilizing ability of a microemulsion phase that coexists with oil and brine. *J. Colloid Interface Sci.*, 71(2), 408 – 426.
- Janssen, M.T.G., Pilus, R.M., and Zitha, P.L.J. 2019a. A Comparative Study of Gas Flooding and Foam-Assisted Chemical Flooding in Bentheimer Sandstones. *Transp. Porous Media*, <https://doi.org/10.1007/s11242-018-01225-3>.
- Janssen, M.T.G., Mutawa, A.S., Pilus, R.M., and Zitha, P.L.J. 2019b. Foam-Assisted Chemical Flooding for Enhanced Oil Recovery: Effects of Slug Salinity and Drive Foam Strength. *Energ. Fuel.*, 33(6), 4951 – 4963.
- Janssen, M.T.G., Zitha, P.L.J., and Pilus, R.M. 2019c. Oil Recovery by Alkaline/Surfactant/Foam Flooding: Effect of Drive-Foam Quality on Oil-Bank Propagation. *SPE J.*, <https://doi.org/10.2118/190235-PA>.
- Johns, R.T., and Orr, F.M. 1996. Miscible gas displacement of multicomponent oils. *SPE J.*, 1(1), 39 – 50.
- Jones, S.A., Van Der Bent, V., Farajzadeh, R., Rossen, W.R., and Vincent-Bonnieu, S. 2016. Surfactant

- screening for foam EOR: Correlation between bulk and core-flood experiments. *Coll. Surf. A*, 500, 166 – 176.
- Jong, S., Nguyen, N.M., Eberle, C.M., Nghiem, L.X., and Nguyen, Q.P. 2016. Low tension gas flooding as a novel EOR method: an experimental and theoretical investigation. Presented at the SPE Improved Oil Recovery Conference, Tulsa, Oklahoma, USA, 11 – 13 April. SPE-179559-MS. <https://doi.org/10.2118/179559-MS>.
- Kalaydjian, F.J.M. 1992. Performance and analysis of three-phase capillary pressure curves for drainage and imbibition in porous media. Presented at the SPE Annual Technical Conference and Exhibition, Washington, D.C., USA, 4 – 7 October. SPE-24878-MS. <https://doi.org/10.2118/24878-MS>.
- Kapetas, L., Vincent-Bonnieu, S., Danelis, S., Rossen, W R., Farajzadeh, R., Eftekhari, A.A., Mohd Shafian, S.R., and Kamarul Bahrim, R.Z. 2015. Effect of Temperature on Foam Flow in Porous Media. Presented at the SPE Middle East Oil & Gas Show and Conference, Manama, Bahrain, 8 – 11 March. SPE-172781-MS. <https://doi.org/10.2118/172781-MS>.
- Keller, A.A., Blunt, M.J., and Roberts, P.V. 1997. Micromodel Observation of the Role of Oil Layers in Three-Phase Flow. *Transp. Porous Media*, 26(3), 277 – 297.
- Khatib, Z.I., Hirasaki, G.J., and Falls, A.H. 1988. Effects of capillary pressure on coalescence and phase mobilities in foams flowing through porous media. *SPE Reserv. Eng.*, 3(3), 919 – 926.
- Khorshidian, H., James, L.A., and Butt, D.S. 2016. The Role of Film Flow and Wettability in Immiscible Assisted Gravity Drainage. Presented at the International Symposium of the Society of Core Analyst, Snowmass, Colorado, USA, 21 – 26 August.
- Klitzing, R.V., Espert, A., Asnacios, A., Hellweg, T., Colin, A., and Langevin, D. 1999. Forces in Foam Films Containing Polyelectrolyte and Surfactant. *Coll. Surf. A*, 149(1), 131 – 140.
- Kovscek, A.R., and Radke, C.J. 1994. Fundamentals of foam transport in porous media. In: *Foams: Fundamentals and Applications in the Petroleum Industry*, Chap. 3, 115–163, Washington, D.C., American Chemical Society.
- Kozeny, J. 1927. Uber kapillare leitung der wasser in boden. *Royal Academy of Science, Vienna, Proc. Class I*, 136, 271 – 306.
- Kuhlman, M.I., Falls, A.M., Hara, S.K., Monger-McClure, T.G., and Borchardt, J.K. 1992. CO<sub>2</sub> Foam With Surfactants Used Below Their Critical Micelle Concentrations. *SPE Reserv. Eng.*, 7(4), 445 – 452.
- Lake, L.W. 1989. Enhanced oil recovery, Prentice-Hall, Englewood Cliffs, New Jersey.
- Lashgari, H.R., Sepehrnoori, K., Delshad, M., and DeRouffignac, E. 2015a. Development a Four-Phase Chemical-Gas Model in an IMPEC Reservoir Simulator. Presented at the SPE Reservoir Simulation Symposium, Houston, Texas, USA, 23 – 25 February. SPE-173250-MS. <https://doi.org/10.2118/173250-MS>.
- Lashgari, H.R., Delshad, M., Sepehrnoori, K., and DeRouffignac, E. 2015b. Development and Application of Electrical-Joule-Heating Simulator for Heavy-Oil Reservoirs. *SPE J.*, 21(1), 87 – 100.
- Lashgari, H.R., Sepehrnoori, K., and Delshad, M. 2015c. Modeling of Low-Tension Surfactant-Gas Flooding Process in a Four-Phase Flow Simulator. Presented at the SPE Annual Technical Conference and Exhibition, Houston, Texas, USA, 28 – 30 September. SPE-175134-MS. <https://doi.org/10.2118/175134-MS>.
- Lawson, J.B., and Reisberg, J. 1980. Alternate slugs of gas and dilute surfactant for mobility control during chemical flooding. Presented at the SPE Improved Oil Recovery Symposium, Tulsa,

- Oklahoma, USA, 20 – 23 April. SPE-8839-MS. <https://doi.org/10.2118/8839-MS>.
- Le, V.Q., Nguyen, Q.P., and Sanders, A. 2008. A Novel Foam Concept With CO<sub>2</sub> Dissolved Surfactants. Presented at the SPE Improved Oil Recovery Symposium, Tulsa, Oklahoma, USA, 20 – 23 April. SPE-113370-MS. <https://doi.org/10.2118/113370-MS>.
- Lee, H.O., and Heller, J.P. 1990. Laboratory Measurements of CO<sub>2</sub> Foam Mobility. *SPE Reserv. Eval. Eng.*, 5(2), 193 – 197.
- Liang, L., Luo, D., Liu, X., and Xiong, J. 2016. Experimental study on the wettability and adsorption characteristics of Longmaxi Formation shale in the Sichuan Basin, China. *J. Nat. Gas Sci. Eng.*, 33, 1107 – 1118.
- Lide, D.R. 2012. CRC Handbook of Chemistry and Physics. CRC Press, Boca Raton.
- Liu, S.H., Hirasaki, G.K., and Miller, C.A. 2008. Favorable attributes of alkaline-surfactant-polymer flooding. *SPE J.*, 12(1), 5 – 6.
- Lotfollahi, M. 2015. Development of a Four-Phase Flow Simulator to Model Hybrid Gas/Chemical EOR Processes. PhD dissertation. The University of Texas.
- Løvøll, G., Méheust, Y., Måløy, K. J., Aker, E., and Schmittbuhl, J. 2005. Competition of gravity, capillary and viscous forces during drainage in a two-dimensional porous medium, a pore scale study. *Energy*, 30(6), 861 – 872.
- Mannhardt, K., Novosad, J.J., and Schramm, L.L. 2000. Comparative Evaluation of Foam Stability to Oil. *SPE Reserv. Eval. Eng.*, 3(1), 23 – 34.
- Manrique, E.J., Thomas, C.P., Ravikiran, R., Izadi Kamouei, M., Lantz, M., Romero, J.L., and Alvarado, V. 2010. EOR: Current Status and Opportunities. Presented at the SPE Improved Oil Recovery Symposium, Tulsa, Oklahoma, USA, 24 – 28 April. SPE-130113-MS. <https://doi.org/10.2118/130113-MS>.
- Mast, R.F. 1972. Microscopic behavior of foam in porous media. Presented at the Fall Meeting of the Society of Petroleum Engineers of AIME, San Antonio, Texas, USA, 8 – 11 October. SPE-3997-MS. <https://doi.org/10.2118/3997-MS>.
- Mees, F., Swennen, R., Van Geet, M., and Jacobs, P. 2003. Applications of X-ray computed tomography in the geosciences. *Geol. Soc, London Spec. Publ.*, 215(1), 1 – 6.
- Melrose, J.C. 1974. Role of capillary forces in detennining microscopic displacement efficiency for oil recovery by waterflooding. *J. Can. Pet. Technol.*, 13(4).
- Myers, D. 2006. Surfactant science and technology. John Wiley & Sons.
- Naylor, P., and Frørup, M. 1989. Gravity-Stable Nitrogen Displacement of Oil. Presented at the SPE Annual Technical Conference and Exhibition, San Antonio, Texas, USA, 8 – 11 October. SPE-19641-MS. <https://doi.org/10.2118/19641-MS>.
- Nordstrom, D.K., Plummer, L.N., Langmuir, D., Busenberd, E., May, H.M., Jones, B.F., and Parkhurst, D.L. 1990. Revised chemical equilibrium data for major water-mineral reactions and their limitations. In: *Chemical modelling of aqueous systems II: American Chemical Society Symposium Series 416*, 398 – 413.
- Oren, P.E., Billiotte, J., and Pinczewski, W.V. 1992. Mobilization of Waterflood Residual Oil by Gas Injection for Water-Wet Conditions. *SPE J.*, 7(1), 70 – 78.
- Orr, F.M. 2007. Theory of gas injection processes (Vol. 5). Tie-line Publications, Copenhagen, Denmark.
- Osei-Bonsu, K., Shokri, N., and Grassia, P. 2015. Foam stability in the presence and absence of hydrocarbons: From bubble- to bulk-scale. *Coll. Surf. A*, 481, 514 – 526.
- Osterloh, W.T., and Jante, M.J. 1992. Effects of Gas and Liquid Velocity on Steady-State Foam Flow at

- High Temperature. Presented at the SPE Improved Oil Recovery Symposium, Tulsa, Oklahoma, USA, 22 – 24 April. SPE-24179-MS. <https://doi.org/10.2118/24179-MS>.
- Oughanem, R., Youssef, S., Bazin, B., Maire, E., and Vizika, O. 2013. Pore-scale to core-scale aspects of capillary desaturation curves using CT-scan imaging. Presented at the 17<sup>th</sup> European Symposium on Improved Oil Recovery, Saint Petersburg, Russia, 16 – 18 April. EAGE.
- Pan, B., Li, Y., Wang, H., Jones, F., and Iglauer, S. 2018. CO<sub>2</sub> and CH<sub>4</sub> Wettabilities of Organic-Rich Shale. *Energ. Fuel.*, 32(2), 1914 – 1922.
- Pan, B., Jones, F., Huang, Z., Yang, Y., Li, Y., Hejazi, S.H., and Iglauer, S. 2019. Methane (CH<sub>4</sub>) wettability of clay coated quartz at reservoir conditions. *Energ. Fuel.*, 33(2), 788 – 795.
- Parrish, D.R. 1966. Flooding process for recovery of oil. U.S. Patent No 3,244,228.
- Peksa, A.E., Wolf, K.H.A., and Zitha, P.L.J. 2015. Bentheimer sandstone revisited for experimental purposes. *Mar. Pet. Geol.*, 67, 701 – 719.
- Plummer, L.N., and Busenberg, E. 1982. The solubilities of calcite, aragonite and vaterite in CO<sub>2</sub> solutions between 0 and 90°C, and an evaluation of the aqueous model for the system CaCO<sub>3</sub>-CO<sub>2</sub>-H<sub>2</sub>O. *Geochim. Cosmochim. Acta*, 46(6), 1011 – 1040.
- Ransohoff, T.C., and Radke, C.J. 1988. Mechanisms of foam generation in glass-bead packs. *SPE Reserv. Eng.*, 3(2), 573 – 585.
- Rogers, J.D., and Grigg, R.B. 2001. A Literature Analysis of the WAG Injectivity Abnormalities in the CO<sub>2</sub> Process. *SPE Reserv. Eval. Eng.*, 4(5), 375 – 386.
- Romero-Zeron, L., and Kantzas, A. 2003. Pore Level Displacement Mechanisms During Foam Flooding. Presented at the Canadian International Petroleum Conference, Calgary, Alberta, Canada, 10 – 12 June. PETSOC-2003-128. <https://doi.org/10.2118/2003-128>.
- Rossen, W.R. and Gauglitz, P.A. 1990. Percolation theory of creation and mobilization of foams in porous media. *AIChE J.*, 36(8), 1176 – 1188.
- Rossen, W.R. 1996. Foams in Enhanced Oil Recovery. In: *Foams: Theory, Measurements and Applications*, Chap. 11, 413 – 464. New York City, Marcel Dekker Inc.
- Rossen, W.R., Van Duijn, C.J., Nguyen, Q.P., and Vikingstad, A.K. 2010. Injection Strategies to Overcome Gravity Segregation in Simultaneous Gas and Liquid Injection into Homogeneous Reservoirs. *SPE J.*, 15(1), 76 – 90.
- Rowlinson, J.S., and Widom, B. 1982. Molecular Theory of Capillarity. International Series of Monographs on Chemistry. Oxford, Clarendon Press.
- Sandrea I., and Sandrea R. 2007. Recovery factors leave vast target for EOR technologies. *Oil Gas J.*, 105(41), 44 – 47.
- Schramm, L.L., Turta, A.T., and Novosad, J.J. 1993. Microvisual and coreflood studies of foam interactions with a light crude oil. *SPE Reserv. Eng.*, 8(3), 201 – 206.
- Sebastian, H.M., and Lawrence, D.D. 1992. Nitrogen minimum miscibility pressures. Presented at the SPE Improved Oil Recovery Symposium, Tulsa, Oklahoma, USA, 22 – 24 April. SPE-24134-MS. <https://doi.org/10.2118/24134-MS>.
- Shabib-Asl, A., Ayoub, M.A., Alta'ee, A.F., Saaid, I.B.M., and Valentim, P.P.J. 2014. Comprehensive review of foam application during foam assisted water alternating gas (FAWAG) method. *Res. J. Appl. Sci. Eng. Technol.*, 8(17), 1896 – 1904.
- Shah, D.O. 2012. Improved oil recovery by surfactant and polymer flooding. Elsevier.
- Shandrygin, A., Shelepov, V., Ramazanov, R., Andrianov, N., Klemin, D., Nadeev, A., and Yakimchuk, I. 2015. Mechanism of Oil Displacement During WAG in Porous Media with Micro-Inhomogeneities. Presented at the SPE Russian Petroleum Technology Conference, Moscow,

- Russia, 26 – 28 October. SPE-176629-MS. <https://doi.org/10.2118/176629-MS>.
- Sharma, B., Brigham, W.E., and Castanier, L.M. 1997. A Report on CT-Imaging Techniques for Two-Phase and Three-Phase In-Situ Saturation Measurements. Prepared for US Department of Energy, Stanford University.
- Sheng, J. 2010. Modern Chemical Enhanced Oil Recovery: Theory and Practice. Gulf Professional Publishing.
- Shupe, R.D. 1981. Chemical stability of polyacrylamide polymers. *J. Pet. Technol.*, 33(8), 1513 – 1529.
- Simjoo, M. 2012. Immiscible Foam for Enhancing Oil Recovery. PhD dissertation. Delft University of Technology.
- Simjoo, M., Rezaei, T., Andrianov, A., and Zitha, P.L.J. 2013. Foam stability in the presence of oil: effect of surfactant concentration and oil type. *Coll. Surf. A*, 438, 148 – 158.
- Skauge, A., and Fotland, P. 1990. Effect of pressure and temperature on the phase behavior of microemulsions. *SPE Reserv. Eng.*, 5(4), 601 – 608.
- Skauge, A., and Stensen, J.Å. 2003. Review of WAG field experience. Presented at the Oil Recovery–2003, 1st International Conference and Exhibition, Modern Challenges in Oil Recovery, Moscow, Russia, 19 – 23 May.
- Smalley P.C., Ross B., Brown C.E., Moulds T.P., and Smith M.J. 2009. Reservoir technical limits: a framework for maximizing recovery from oil fields. *SPE Reserv. Eval. Eng.*, 12(4), 610 – 629.
- Smith, D.H. 1996. Book review: Foams: Fundamentals and Applications in the Petroleum Industry Edited by Laurier L. Schramm (Petroleum Research Institute). *Energ. Fuel.*, 10(1), 266.
- Sohrabi, M., Henderson, G.D., Tehrani, D.H., and Danesh, A. 2000. Visualisation of oil recovery by water alternating gas (WAG) injection using high pressure micromodels-water-wet system. Presented at the SPE Annual Technical Conference and Exhibition, Dallas, Texas, USA, 1 – 4 October. SPE-63000-MS. <https://doi.org/10.2118/63000-MS>.
- Solairaj, S., Britton, C., Kim, D.H., Weerasooriya, U., and Pope, G.A. 2012. Measurement and Analysis of Surfactant Retention. Presented at the SPE Improved Oil Recovery Symposium, Tulsa, Oklahoma, USA, 14 – 18 April. SPE-154247-MS. <https://doi.org/10.2118/154247-MS>.
- Song, F.Y., and Islam, M.R. 1994. Effect of salinity and rock type on sorption behaviour of surfactants as applied in cleaning of petroleum contaminants. *J. Petrol. Sci. Eng.*, 10(4), 321 – 336.
- Southwick, J.G., van den Pol, E., van Rijn, C.H.T., van Batenburg, D.W., Boersma, D.M., Svec, Y., Mastan, A.A., Shanin, G.T., and Raney, K. 2014. Ammonia as Alkali For ASP Floods – Comparison to Sodium Carbonate. Presented at the SPE Improved Oil Recovery Symposium, Tulsa, Oklahoma, USA, 12 – 16 April. SPE-169057-MS. <https://doi.org/10.2118/169057-MS>.
- Srivastava, M., Zhang, J., Nguyen, Q.P., and Pope, G.A. 2009. A systematic study of alkali surfactant gas injection as an enhanced oil recovery technique. Presented at the SPE Annual Technical Conference and Exhibition, New Orleans, Louisiana, USA, 4 – 7 October. SPE-124752-MS. <https://doi.org/10.2118/124752-MS>.
- Stahl, C.R., Gibson, M.A., and Knudsen, C.W. 1987. Thermally-enhanced oil recovery method and apparatus. U.S. Patent No. 4,694,907.
- Szlendak, S.M., Nguyen, N.M., and Nguyen, Q.P. 2013. Laboratory investigation of low-tension-gas flooding for improved oil recovery in tight formations. *SPE J.*, 18(5), 851 – 866.
- Talebian, S.H., Masoudi, R., Tan, I.M., and Zitha, P.L.J. 2014. Foam assisted CO<sub>2</sub>-EOR: A review of concept, challenges, and future prospects. *J. Pet. Sci. Eng.*, 120, 202 – 215.
- Tang, S., Tian, L., Lu, J., Wang, Z., Xie, Y., Yang, X., and Lei, X. 2014. A novel low tension foam flooding for improving post-chemical-flood in Shuanghe oilfield. Presented at the SPE Improved Oil

- Recovery Symposium, Tulsa, Oklahoma, USA, 12 – 16 April. SPE-169074-MS. <https://doi.org/10.2118/169074-MS>.
- Tang, J., Bonnieu, S.V., and Rossen, W.R. 2017. The Effect of Oil on Steady-state Foam Flow Regimes in Porous Media. Presented at the 19<sup>th</sup> European Symposium on Improved Oil Recovery, Stavanger, Norway, 24 – 27 April. EAGE.
- The EOR Alliance. 2019. Gas Foams – The EOR Alliance. Available at <https://www.eor-alliance.com/solutions/foam/> [Accessed 6 Aug. 2019].
- Thomas, S. 2008. Enhanced oil recovery-an overview. *Oil Gas Sci, Technol.- Rev. IFP*, 63(1), 9 – 19.
- Treiber, L.E., Archer, D.L., and Owens, W.W. 1972. A Laboratory Evaluation of the Wettability of Fifty Oil Producing Reservoirs. *SPE J.*, 12(6), 531 – 540.
- Turta, A.T., and Singhal, A K. 1998. Field Foam Applications in Enhanced Oil Recovery Projects: Screening and Design Aspects. Presented at the SPE International Oil and Gas Conference and Exhibition in China, Beijing, China, 2 – 6 November. SPE-48895-MS. <https://doi.org/10.2118/48895-MS>.
- Turta, A. 2013. In Situ Combustion. In: *Enhanced Oil Recovery Field Case Studies*, Chap. 18. Elsevier Inc. Chapters.
- UTCHEM Technical Documentation. 2017. UTCHEM Technical Documentation: A Three-Dimensional Chemical Flood Simulator. Volume II Documentation for UTCHEM 2017.3.
- van Dijke, M.I., Lorentzen, M., Sohrabi, M., and Sorbie, K.S. 2010. Pore-scale simulation of WAG floods in mixed-wet micromodels. *SPE J.*, 15(1), 238 – 247.
- Vizika, O. 1993. Effect of the spreading coefficient on the efficiency of oil recovery with gravity drainage. Presented at the American Chemical Society National Meeting, Denver, Colorado, USA, 28 March – 2 April. ACS.
- Vizika, O., and Lombard, J.M. 1996. Wettability and spreading: two key parameters in oil recovery with three-phase gravity drainage. *SPE Reserv. Eng.*, 11(1), 54 – 60.
- Wang, Y., Xu, H., Yu, W., Bai, B., Song, X., and Zhang, J. 2011. Surfactant induced reservoir wettability alteration: Recent theoretical and experimental advances in enhanced oil recovery. *Pet. Sci.*, 8(4), 463 – 476.
- Wasan, D.T., Shah, S.M., Aderangi, N., Chan, M.S., and McNamara, J.J. 1978. Observations on the coalescence behaviour of oil droplets and emulsion stability in enhanced oil recovery. *SPE J.*, 18(6), 409 – 417.
- Winsor, P.A. 1954. Solvent Properties of Amphiphilic Compounds. Butterworths Scientific Publications. Ltd.: London.
- Yang, Y., Yang, H., Tao, L., Yao, J., Wang, W., Zhang, K., and Luquot, L. 2019. Microscopic Determination of Remaining Oil Distribution in Sandstones With Different Permeability Scales Using Computed Tomography Scanning. *J. Energ. Resour. Technol.*, 141(9), 11 pages.
- Yeganeh, M., Hegner, J., Lewandowski, E., Mohan, A., Lake, L.W., Cherney, D., Jusufi, A., and Jaishankar, A. 2016. Capillary Desaturation Curve Fundamentals. Presented at the SPE Improved Oil Recovery Conference, Tulsa, Oklahoma, USA, 11 – 13 April. SPE-179574-MS. <https://doi.org/10.2118/179574-MS>.
- Zechner, M., Buchgraber, M., Clemens, T., Gumpenberger, T., Castanier, L.M., and Kovscek, A.R. 2013. Flow of polyacrylamide polymers in the near-wellbore-region, rheological behavior within induced fractures and near-wellbore-area. Presented at the SPE Annual Technical Conference and Exhibition, New Orleans, Louisiana, USA, 30 September – 2 October. SPE-166085-MS. <https://doi.org/10.2118/166085-MS>.

- Zhang, Y.P., Sayegh, S.G., Luo, P., and Huang, S. 2010. Experimental Investigation of Immiscible Gas Process Performance for Medium Oil. *J. Can. Pet. Technol.*, 49(2), 32 – 39.
- Zhu, T., Ogbe, D.O., and Khataniar, S. 2004. Improving the foam performance for mobility control and improved sweep efficiency in gas flooding. *Ind. Eng. Chem. Res.*, 43(15), 4413 – 4421.
- Zitha, P.L.J., Nguyen, Q.P., Currie, P.K., and Buijse, M.A. 2006. Coupling of foam drainage and viscous fingering in porous media revealed by X-ray computed tomography. *Transp. Porous Media*, 64(3), 301 – 313.
- Zitha, P.L.J., and Du, D.X. 2010. A new stochastic bubble population model for foam flow in porous media. *Transp. Porous Media*, 83(3), 603 – 621.

# Nomenclature

---

$\hat{C}_3$	Absorbed concentration of surfactant [moles/L]
$\dot{C}_3$	Total surfactant concentration [moles/L]
$C_{I3}$	Concentration of phase I solubilized in phase 3 [moles/L]
$C_{33}$	Concentration of surfactant solubilized in phase 3 [moles/L]
$C_s$	Surfactant concentration [wt.%]
$C_s^*$	Critical surfactant concentration [wt.%]
$C_s$	Spreading coefficient [N/m]
$C_{SE}$	Effective salinity [mEq/mL]
$CT$	Computed-tomography response of the core [Hounsfield units]
$CT_{air}$	Computed-tomography response of the gas phase [Hounsfield units]
$CT_{brine}$	Computed-tomography response of the water phase [Hounsfield units]
$CT_{dry}$	Computed-tomography response of the dry core [Hounsfield units]
$CT_o$	Computed-tomography response of the oil-saturated core [Hounsfield units]
$CT_{oil}$	Computed-tomography response of the oil phase [Hounsfield units]
$CT_{wet}$	Computed-tomography response of the brine-saturated core [Hounsfield units]
$D_p$	Average grain diameter [m]
$E_D$	Displacement efficiency [-]
$E_V$	Volumetric sweep efficiency [-]
$f_a$	Fractional flow of phase a [-]
$f_g$	Foam quality [-]
$f_g^*$	Critical foam quality [-]
$g$	Gravitational acceleration [ $m/s^2$ ]
$k$	Permeability [ $m^2$ ]
$k_{ref}$	Reference permeability [ $m^2$ ]
$k_{ra}$	Relative permeability to phase a [-]
$k_{ra}^0$	End-point relative permeability of phase a [-]
$k_{rg}^f$	Effective gas relative permeability modified for the presence of foam [-]
$L$	Core length [m]
$M$	Mobility ratio [-]
$M^0$	End-point mobility ratio [-]
$MRF$	Foam mobility reduction factor [-]
$MMP$	Minimum miscibility pressure [Pa]
$N_b$	Bond number [-]
$N_c$	Capillary number [-]
$N_g^0$	End-point gravity number [-]
$R$	Gas mobility reduction factor [-]
$R_{I3}$	Solubilisation ratio of phase I to phase 3 [-]
$R_{ref}$	Reference gas mobility reduction factor [-]
$R_F$	Recovery factor [-]
$R_{FCEOR}$	Recovery factor to chemical flooding [-]
$R_{FGF}$	Recovery factor to gas flooding [-]
$R_{FWF}$	Recovery factor to water flooding [-]
$S_g$	Saturation of the gas phase [-]
$S_{gf}$	Free gas saturation [-]
$S_{gt}$	Trapped gas saturation [-]
$S_h$	Upper limit for the critical water saturation [-]
$S_l$	Lower limit for the critical water saturation [-]
$S_o$	Saturation of the oil phase [-]

$S_o^*$	Critical oil saturation [-]
$S_{oi}$	Initial oil saturation [-]
$S_{or}$	Residual oil saturation [-]
$S_{or\_CEOR}$	Residual oil saturation to chemical flooding [-]
$S_{or\_GF}$	Residual oil saturation to gas flooding [-]
$S_{or\_WF}$	Residual oil saturation to water flooding [-]
$S_w$	Water saturation [-]
$S_w^*$	Critical water saturation [-]
$S_{wc}$	Connate water saturation [-]
$t_{1/2}$	Foam half-decay time [min]
$u_g$	Gas superficial velocity [m/s]
$u_{g,ref}$	Reference gas velocity [m/s]
$u_t$	Total superficial velocity [m/s]
$u_w$	Water superficial velocity [m/s]
$x_{Di}$	Dimensionless distance in x-direction of cell / [-]
$\epsilon$	Water saturation tolerance parameter [-]
$\phi$	Porosity [-]
$\Delta P$	Pressure difference [Pa]
$\Delta \rho$	Density difference [ $\text{kg}/\text{m}^3$ ]
$\sigma_{go}$	Gas-oil interfacial tension [N/m]
$\sigma_{gw}$	Gas-water interfacial tension [N/m]
$\sigma_{ow}$	Oil-water interfacial tension [N/m]
$\lambda_g$	Mobility of the gas phase [ $\text{m}^2/(\text{Pa}\cdot\text{s})$ ]
$\lambda_o$	Mobility of the oil phase [ $\text{m}^2/(\text{Pa}\cdot\text{s})$ ]
$\lambda_w$	Mobility of the water phase [ $\text{m}^2/(\text{Pa}\cdot\text{s})$ ]
$\mu_{app}$	Apparent viscosity of foam [Pa·s]
$\mu_g$	Viscosity of the gas phase [Pa·s]
$\mu_o$	Viscosity of the oil phase [Pa·s]
$\mu_w$	Viscosity of the water phase [Pa·s]

# Summary

---

Foam-assisted chemical flooding (*FACF*) is a novel enhanced oil recovery (*EOR*) methodology that combines the injection of a surfactant slug, to mobilize previously trapped residual oil, with foam generation for drive mobility control, thus displacing the mobilized banked oil. The main goal of this study concerns the understanding of oil mobilization and displacement mechanisms that take place in a *FACF* process. At first, in order to promote understanding of the incremental benefits *FACF* can provide one with, we get ourselves familiar with immiscible gas flooding and water-alternating-gas (*WAG*) injection. Subsequently, we study the effect of aqueous phase salinity, drive foam quality, and method of drive foam injection, on the oil mobilization and displacement processes in *FACF*, at both model-like conditions and in a reservoir setting. We present novel insights, on the dynamic physical processes that take place within the porous media during *FACF*, which could only be obtained through the assistance of a medical CT scanner. Moreover, in order to identify the main controlling parameters that determine incremental oil recovery in *WAG* and *FACF*, we develop several mechanistic models for the aid of history-matching laboratory observations.

Initially, we conduct an experimental base case study which scrutinizes oil displacement mechanisms that are responsible for oil recovery during immiscible continuous gas injection and *WAG*, as they form the basis for understanding the incremental effect of *FACF* (**Chapter 2**). Dedicated core-flood experiments are performed in Bentheimer sandstones where nitrogen is injected in a continuous manner, at initial oil saturation and at residual oil to waterflood, and in a *WAG* mode. Our experimental observations, and corresponding analysis, indicate that *WAG* is able to lower the residual oil saturation further, compared to the continuous injection schemes studied, as a result of the establishment of a trapped gas saturation. Furthermore, our laboratory results are consistent with the rationale that an increment in oil recovery arises mainly from the fact that the residual oil to gas flooding is lower under three-phase flow conditions compared to two-phase flow. By constructing ternary saturation diagrams, we find that the injection of nitrogen at residual oil to waterflood reveals a saturation path consisting of two segments. First, oil displacement follows a path of roughly constant oil saturation; here mainly water is produced. Eventually, the injected nitrogen is displacing the oil at a fairly constant water saturation, which is slightly higher than its connate saturation.

Once we have an understanding about the main mechanisms that play a predominant role in oil recovery through immiscible gas injection and *WAG*, we shift our attention to *FACF*. **Chapter 3** presents a laboratory investigation on *FACF* at model-like conditions, where we study the effect of drive foam quality on oil bank propagation at under-optimum salinity conditions. After optimizing the chemical surfactant slug formulation, by performing bulk phase behaviour tests, multiple CT-assisted core-flood experiments are conducted to get insight in the main mechanisms for oil mobilization and its displacement by a foam drive. We are able to clearly visualize, and quantify, the oil bank formation during surfactant slug injection. Acquired novel CT-based information shows exactly how the shape of the generated oil bank is being altered as function of injection time. The oil bank displacement, by a foam drive, proves to be most stable at the lowest drive foam quality studied. We find that the presence of oil does not necessarily imply absence of stable foam generation. On the contrary, we discover that foam generation seems to increase upon touching the oil bank, favouring its displacement.

After obtaining a clear picture regarding the effect of the drive foam quality on oil bank propagation in a *FACF* process, we investigate the effect of surfactant slug salinity on oil mobilization and displacement processes in *FACF*, applied at the same model-like conditions (**Chapter 4**). CT-assisted core-flooding results shed light on how the aqueous slug salinity affects the oil bank build-up, and whether it impacts its displacement by foam. We notice that the oil bank characteristics are strongly related to the surfactant slug salinity. Where at under-optimum salinity conditions the formed oil bank shows a highly dispersive character, once one operates at (near-)optimum salinity, the generated oil bank exhibits more uniform and elongated features. The varying aqueous phase salinity does not significantly alter the displacement of the banked oil by drive foam. Since the surfactant slug salinity directly regulates the oil-water interfacial tension, oil recoveries, in the form of clean and solubilized oil, vary as function of aqueous salinity.

Subsequent to studying *FACF* in a model-like setting, **Chapter 5** reports on an extensive experimental study that discusses the viability of *FACF* to reservoir conditions. Here we investigate the influence of drive foam strength and surfactant slug salinity on the effectiveness of *FACF* in a reservoir setting. We conduct dedicated phase behaviour and bulk foam experiments in order to optimize, and specify, the surfactant slug and drive chemical formulations. Afterwards, we perform multiple CT-assisted *FACF* core-flood experiments where we vary the drive foam strength, i.e. in-situ drive foam generation by co-injection versus injecting a pre-generated drive foam, and the salinity of the surfactant slug. Our experimental observations indicate that the designed drive formulation is able to generate excellent strong, and stable, foams in porous media, and in bulk, for all gas fractional flows studied. Injecting the specially composed surfactant slug, for the aid of oil mobilization, at both optimum and under-optimum salinity conditions, results in the creation of an unstable oil bank due to dominant gravitational forces. If we view this observation in terms of real-field conditions, we expect that the instability of the oil bank is of a considerably higher magnitude in a real reservoir due to its larger dimensions. Finally, our laboratory observations indicate that the method of drive foam injection has a bigger impact on the *FACF* efficiency than the surfactant slug salinity.

The substantial amount of experimental work performed gives us a comprehensive picture of the *FACF* process, and related physical mechanisms, both in a model-like setting and at reservoir conditions. It allows us to come up with suggestions, and proposed mechanisms, that are likely to take place during *FACF*. The final step is to develop several mechanistic models, by using a three-dimensional research simulator for multiphase and multicomponent systems, in order to history-match *WAG* and *FACF* experiments at the model-like conditions imposed (**Chapter 6**). The simulations aim to explore, and identify, main mechanisms and their controlling parameters that determine oil recovery in *WAG* and *FACF*. We are able to accurately estimate relative permeability curves for primary drainage and water flooding due to the availability of CT scan-based saturation distributions. It results in correctly modelling of the two injection stages. History-matching *WAG* injection shows us that a reduction in gas relative permeability is needed as a function of increasing *WAG* cycles. This indicates the establishment of a trapped gas saturation. Modelling of the surfactant phase behaviour, requirement for simulating *FACF*, is successfully done and is verified by effectively applying the same phase behaviour model to the two different salinity conditions studied. Mechanistic modelling of drive foam injection demonstrates to be the most challenging part. Though the simulator is a useful tool to represent complex phenomena in four-phase (i.e. water, oil, micro-emulsion, and gas) systems, its local equilibrium foam model is not capable to capture a wide range of potential foaming mechanisms.

# Samenvatting

---

Door schuim ondersteunde chemische stroming [Engels: foam-assisted chemical flooding (*FACF*)] is een nieuwe methode om meer olie uit een reservoir te verkrijgen. De methodiek combineert de injectie van een oppervlakte-actieve stof (Engels: een surfactant) opgelost in water, voor het mobiliseren van resterende olie in het reservoir, met de injectie van schuim voor het creëren van een gunstige mobiliteitsratio voor het verplaatsen van de reeds gemobiliseerde olie. In dit proefschrift onderzoeken wij de mechanismen die verantwoordelijk zijn voor de olie mobilisatie, en de verplaatsing van olie door schuim, in een *FACF* injectie proces. Aanvankelijk, om een beter inzicht te verkrijgen in de voordelen die *FACF* men kan bieden, maken we kennis met meer conventionele methoden voor verbeterde oliewinning: niet-mengbare gasstroming en alternerende injectie van water en niet-mengbaar gas [Engels: water-alternating-gas (*WAG*)]. Vervolgens bestuderen we het effect van het zoutgehalte in de waterfase, de gasfractie in het aandrijfschuim en de injectiemethode van het schuim op de olie mobilisatie- en verplaatsingsprocessen in *FACF*. Hierbij focussen we op zowel een modelachtige omgeving als realistische reservoir condities. Wij presenteren nieuwe inzichten, over de dynamische fysieke processen die plaatsvinden in poreuze media tijdens *FACF*, die alleen konden worden verkregen door de hulp van een medische CT-scanner. Tenslotte, om de belangrijkste parameters te bepalen die de incrementele oliewinning in *WAG* en *FACF* controleren, ontwikkelen wij verscheidende mechanistische modellen voor het vergelijken van laboratoriumobservaties met numerieke simulaties.

In eerste instantie voeren we een experimentele basisstudie uit waarin we olie verdringingsmechanismen onderzoeken die verantwoordelijk zijn voor oliewinning tijdens niet-mengbare gasstroming en *WAG*, aangezien deze de basis vormen voor het bevatten van het incrementele effect van *FACF* (**Hoofdstuk 2**). Toegewijde stromingsexperimenten worden uitgevoerd in Bentheimer zandstenen waarbij stikstof wordt geïnjecteerd in een continu proces, bij initiële olie saturatie en bij een resterende olie verzadiging na waterinjectie, en in een *WAG*-modus. Onze experimentele waarnemingen, en overeenkomstige analyse, geven aan dat *WAG* in staat is om de resterende olie saturatie verder te verlagen, in vergelijking tot de bestudeerde continue injectieschema's, als gevolg van de introductie van een ingesloten, niet mobiele, gas saturatie. Bovendien zijn onze laboratoriumresultaten consistent met de hypothese dat een toename in oliewinning voornamelijk voortvloeit uit het feit dat de resterende olie verzadiging na gasinjectie lager is onder driedfasige stromingsomstandigheden in vergelijking met tweefasige stroming. Door middel van het construeren van ternaire saturatiediagrammen komen wij tot de conclusie dat de injectie van niet-mengbaar stikstof, bij een restolie verzadiging na waterinjectie, een zogenoemd saturatiepad onthult dat uit twee segmenten bestaat. Allereerst volgt de verplaatsing van olie een pad van ongeveer constante olie verzadiging; in deze fase wordt voornamelijk water geproduceerd. Uiteindelijk verplaatst de geïnjecteerde stikstof de olie bij een redelijk constante water saturatie die iets hoger is dan de bijbehorende rest verzadiging.

Zodra we inzicht hebben in de belangrijkste mechanismen die een overheersende rol spelen bij oliewinning door de injectie van niet-mengbaar gas en *WAG*, verleggen we onze aandacht naar *FACF*. **Hoofdstuk 3** presenteert een laboratoriumonderzoek naar *FACF* bij modelachtige omstandigheden. Hier bestuderen we het effect van de gasfractie in het aandrijfschuim op de propagatie van de gemobiliseerde oliebank bij zoutgehaltes lager dan het optimaal zoutgehalte. Na het optimaliseren

van de chemische samenstelling van de surfactantoplossing, door het uitvoeren van bulkfase-gedragsexperimenten, worden meerdere CT-geassisteerde stromingsexperimenten uitgevoerd om inzicht te krijgen in de belangrijkste mechanismen voor olie mobilisatie en de verplaatsing ervan door schuimstroming. We zijn in staat om de formatie van de oliebank, tijdens injectie van surfactantoplossing, duidelijk te visualiseren en te kwantificeren. Verworven nieuwe CT-gebaseerde informatie laat nauwkeurig zien hoe de vorm van de gegenereerde oliebank veranderd als functie van injectietijd. De verplaatsing van de oliebank, door het geïnjecteerde schuim, blijkt het meest stabiel te zijn bij de laagste gasfractie van het schuim. We constateren dat de aanwezigheid van olie niet noodzakelijkerwijs de afwezigheid van stabiele schuimvorming impliceert. Integendeel, we observeren dat de schuimvorming lijkt toe te nemen bij het aanraken van de oliebank, waardoor de verplaatsing ervan wordt bevorderd.

Nadat we een duidelijk beeld hebben verkregen van het effect van de gasfractie in het aandrijfschuim op de voortplanting van de oliebank in een *FACF* proces, onderzoeken we het effect van het zoutgehalte van de surfactantoplossing op de olie mobilisatie- en verplaatsingsprocessen in *FACF* bij dezelfde modelachtige omstandigheden (**Hoofdstuk 4**). De resultaten van CT-geassisteerde stromingsexperimenten werpen licht op hoe het zoutgehalte van de surfactantoplossing de opbouw van de oliebank beïnvloedt, en of het invloed heeft op de verplaatsing ervan door schuim. We nemen waar dat de kenmerken van de oliebank sterk gerelateerd zijn aan het zoutgehalte van de desbetreffende surfactantoplossing. Waar de gevormde oliebank bij zoutgehaltes lager dan het optimaal zoutgehalte een zeer dispergerend karakter vertoont, toont de gegenereerde oliebank, wanneer men met een (bijna) optimaal zoutgehalte werkt, meer uniforme en langwerpige kenmerken. Het variërende zoutgehalte in de surfactantoplossing verandert de verplaatsing van de gemobiliseerde olie door het aandrijfschuim niet significant. Omdat het zoutgehalte van de surfactantoplossing direct de grensvlakspanning tussen olie en water reguleert, varieert de oliewinning, in de vorm van schone en geëmulgeerde olie, als functie van het zoutgehalte.

Volgend op het bestuderen van *FACF* in een modelachtige setting, rapporteert **Hoofdstuk 5** over een uitgebreide experimentele laboratorium studie waarin de rendabiliteit van *FACF* voor reservoiromstandigheden wordt besproken. We onderzoeken de invloed van de sterkte van het aandrijfschuim en het zoutgehalte van surfactantoplossing op de effectiviteit van *FACF* in een reservoiromgeving. We voeren specifieke fasegedrag- en bulkschuimexperimenten uit om de surfactantoplossingen, die gebruikt worden om restolie te mobiliseren en om schuim te genereren in poreuze media, te optimaliseren en te specificeren. Naderhand voeren we meerdere CT-geassisteerde *FACF* stromingsexperimenten uit waarbij we ook de sterkte van het aandrijfschuim variëren, d.w.z. in-situ schuimvorming door co-injectie versus het injecteren van een vooraf gegenereerd aandrijfschuim, in aanvulling op het zoutgehalte van de surfactantoplossing. Onze experimentele waarnemingen geven aan dat de ontworpen surfactantoplossing, voor het genereren van schuim, in staat is om uitstekende stabiele schuimen te produceren in poreuze media en in bulk. Het injecteren van de speciaal samengestelde surfactantoplossing, voor de mobilisatie van olie, resulteert in de vorming van een onstabiele oliebank, door dominante zwaartekrachten, bij zowel optimale als onder-optimale zoutgehaltes. Als we deze observatie bekijken in het licht van reële veldomstandigheden, verwachten we dat de instabiliteit van de oliebank in een echt reservoir aanzienlijk groter is vanwege de grotere afmetingen. Ten slotte geven onze laboratoriumwaarnemingen aan dat de methode van injectie van het schuim een grotere impact heeft op de *FACF* efficiëntie dan het zoutgehalte van de surfactantoplossing.

De aanzienlijke hoeveelheid uitgevoerd experimenteel werk geeft ons een uitgebreid beeld van het *FACF* proces en gerelateerde fysieke mechanismen, zowel in een modelachtige setting als bij reservoiromstandigheden. Het stelt ons in staat om potentiële mechanismen te bedenken die waarschijnlijk tijdens *FACF* zullen plaatsvinden. De laatste stap is het ontwikkelen van verschillende mechanistische modellen, met behulp van een driedimensionale simulator voor meerfase- en multicomponentensystemen, om laboratorium observaties tijdens *WAG* en *FACF* experimenten, onder de opgelegde modelachtige omstandigheden, te reproduceren (**Hoofdstuk 6**). De simulaties zijn gericht op het verkennen en identificeren van hoofdmechanismen, en hun controleparameters, die de oliewinning in *WAG* en *FACF* bepalen. We zijn in staat om de relatieve permeabiliteitscurves voor primaire drainage en waterinjectie nauwkeurig te schatten vanwege de beschikbaarheid van op CT-scan gebaseerde saturatie verdelingen. Het resulteert in een correcte modellering van de twee injectiefasen. Om de experimentele data gerelateerd aan *WAG* injectie te reproduceren met het geconstrueerde model zijn we genoodzaakt om de relatieve permeabiliteit van gas te verlagen als functie van toenemende *WAG* cycli. Dit duidt op het ontstaan van een ingesloten, niet mobiele, gas saturatie. Het modelleren van het fasegedrag van de surfactantoplossing, vereiste voor het simuleren van *FACF*, is met succes uitgevoerd en wordt geverifieerd door hetzelfde fasegedragsmodel effectief toe te passen op de twee verschillende bestudeerde zoutgehaltenes. Mechanistische modellering van schuiminjectie blijkt het meest uitdagende onderdeel te zijn. Hoewel de simulator een handig hulpmiddel is om complexe fenomenen in systemen weer te geven die bestaan uit vier fasen (d.w.z. water, olie, micro-emulsie en gas), het lokaal evenwicht schuimmodel is niet in staat een breed scala aan potentiële mechanismen van schuimvorming in poreuze media te voorspellen.



# Scientific contributions

---

## Journal articles:

- **Janssen, M.T.G.**, Pilus, R.M., and Zitha, P.L.J. 2019. A Comparative Study of Gas Flooding and Foam-Assisted Chemical Flooding in Bentheimer Sandstones. *Transport in Porous Media*. DOI: 10.1007/s11242-018-01225-3.
- **Janssen, M.T.G.**, Zitha, P.L.J., and Pilus, R.M. 2019. Oil Recovery by Alkaline/Surfactant/Foam Flooding: Effect of Drive-Foam Quality on Oil-Bank Propagation. *SPE Journal*. DOI: 10.2118/190235-PA.
- **Janssen, M.T.G.**, Mutawa, A.S., Pilus, R.M., and Zitha, P.L.J. 2019. Foam-Assisted Chemical Flooding for Enhanced Oil Recovery: Effects of Slug Salinity and Drive Foam Strength. *Energy & Fuels*, 33(6), 4951 – 4963.
- **Janssen, M.T.G.**, Torres Mendez, F.A., and Zitha, P.L.J. Mechanistic Modelling of Water-Alternating-Gas Injection and Foam-Assisted Chemical Flooding for Enhanced Oil Recovery. *Submitted to Industrial and Engineering Chemistry Research*.

## Conference papers:

- **Janssen, M.T.G.**, Azimi, F., and Zitha, P.L.J. 2018. Immiscible Nitrogen Flooding in Bentheimer Sandstones: Comparing Gas Injection Schemes for Enhanced Oil Recovery. Society of Petroleum Engineers. DOI: 10.2118/190285-MS.
- **Janssen, M.T.G.**, Zitha, P.L.J., and Pilus, R.M. 2018. Oil Recovery by Alkaline-Surfactant-Foam (ASF) Flooding: Effect of Drive Foam Quality on Oil Bank Propagation. Society of Petroleum Engineers. DOI:10.2118/190235-MS.
- **Janssen, M.T.G.**, Mutawa, A.S., Pilus, R.M., and Zitha, P.L.J. 2019. Evaluation of Foam-Assisted Surfactant Flooding at Reservoir Conditions. Society of Petroleum Engineers. DOI:10.2118/195481-MS.

## Conference talks:

- **Janssen, M.T.G.**, Azimi, F., and Zitha, P.L.J. 2017. Immiscible N<sub>2</sub> Injection for EOR: An Experimental Comparison Study. International Conference on Improved/Enhanced Oil and Gas Recovery, 22-24 April 2017, Tehran, Iran.

- **Janssen, M.T.G.**, Azimi, F., and Zitha, P.L.J. 2018. Immiscible Nitrogen Flooding in Bentheimer Sandstones: Comparing Gas Injection Schemes for Enhanced Oil Recovery. SPE Improved Oil Recovery Conference, 14-18 April 2018, Tulsa, United States.
- **Janssen, M.T.G.**, Zitha, P.L.J., and Pilus, R.M. 2018. Oil Recovery by Alkaline-Surfactant-Foam (ASF) Flooding: Effect of Drive Foam Quality on Oil Bank Propagation. SPE Improved Oil Recovery Conference, 14-18 April 2018, Tulsa, United States.
- **Janssen, M.T.G.**, Mutawa, A.S., Pilus, R.M., and Zitha, P.L.J. 2019. Evaluation of Foam-Assisted Surfactant Flooding at Reservoir Conditions. SPE Europec featured at 81st EAGE Conference and Exhibition, 3-6 June 2019, London, England.

# Acknowledgements

---

First and foremost I want to thank my promotor Prof. Dr. **Pacelli Zitha**. The past four years have been an incredible journey for me and I could not wish for a better supervisor to guide me through this process than you. You gave me the opportunity to conduct this research project and you always believed in me. Your commitment and encouragement inspired and motivated me when I needed it. Your input and suggestions helped me significantly in performing, and setting up, my research. Thank you **Pacelli** for creating a warm and comfortable atmosphere in our group. Your knowledge on conducting experimental work on flow through porous media is astonishing and was a crucial aspect for successful completion of this project. I truly appreciate the fact that you offered me to present one of our conference papers at the SPE Improved Oil Recovery Conference 2018 in Tulsa, USA, when we had two technical papers accepted for presentation. I am really grateful that you gave me the chance to be part of the organizing committee, together with Mohsen, for the workshop on “CO<sub>2</sub> Management and Utilization in Brazilian Pre-Salt Oilfields” held in Rio de Janeiro, Brazil, 2018. Near the end of my PhD you gave me the opportunity to conduct a three month research visit at Harvard University within the group of Prof. Dr. David Weitz. It was one of the best experiences in my life and I will be forever thankful to you that you supported every aspect of it.

Prof. Dr. **David Weitz**, I would like to gratefully thank you for hosting me as a visiting PhD student at the Harvard John A. Paulson School of Engineering and Applied Sciences (SEAS). This three month research visit was an amazing journey and it provided me with a broader, multi-disciplinary, view on the topic. It was an experience to hold onto forever.

A special thank you to my doctoral defence committee – Prof. Dr. **Bill Rossen**, Prof. Dr. **Erik Schlangen**, Prof. Dr. **Majid Hassanizadeh**, Dr. **Denis Voskov**, Dr. **Fred Vermolen**, and Dr. **Jeroen Groenenboom** – for reviewing my PhD dissertation and providing valuable comments.

The PhD project was a collaboration between Delft University of Technology, Universiti Teknologi Petronas, Petronas, and Shell. I am grateful to Petronas and Shell for funding the project. I thank Petronas for the supply of materials and data. I also would like to show my appreciation to Dr. **Jeroen Groenenboom**, **Erik van der Weerd**, Dr. **Rashidah Pilus**, and Prof. **Mariyamni Awang** for their useful input.

In addition, I also would like to thank the Center for Petroleum and Geosystems Engineering at the University of Texas at Austin for allowing me to use their chemical simulator: UTCHEM.

I sincerely thank all technical staff members of the Dietz laboratory in the Department of Geoscience and Engineering within Delft University of Technology. **Marc Friebe**, **Jolanda van Haagen**, **Jens van den Berg**, **Wim Verwaal**, **Joost van Meel**, and **Karel Heller** are gratefully acknowledged for their technical support and useful advice. Special thanks go to **Michiel Slob** for assisting me in building the experimental apparatus and for providing me with technical advice and support. **Ellen Meijvogel-de Koning** is thanked for the assistance required when performing CT-assisted core-flood experiments. I would also like to thank Dr. **Karl-Heinz Wolf** for the several fruitful discussions we had over the past four years.

I greatly thank **Hilbert Van der Linde** from Shell Global Solutions for his technical support when performing ultralow interfacial tension measurements using the spinning-drop tensiometer in Shell's Rock and Fluids laboratory in Rijswijk.

I also thank **Margot Bosselaar-Perk, Ralf Haak, Lydia Broekhuijsen-Bentvelzen, Marlijn Ammerlaan, Marja Roep-Van der Klis,** and **Marijke Schillemans-Van Tuijl** for their administrative assistance and overall support during my PhD studies. In addition, I would like to express my appreciation to all of my friends and colleagues within the department: **Anna Peksa, Bander Alquaimi, Baptiste Lepillier, Durgesh Kawale, Eduardo Barros, Elisa Battistutta, Faisal Al Saadi, Guanqun Yu, Jakolien van der Meer, Jiakun Gong, Jinyu Tang, Kai Li, Kiarash Mansour Pour, Mark Khait, Matei Tene, Matteo Cusini, Mojtaba Hosseini-Nasab, Nikita Lenchenkov, Rafael de Moraes, Rodrigo Salazar, Sian Jones, Siamak Abolhassani, Siavash Kahrobaei, Wesam Al Muttawa, Xiaocong Lyu and Yang Wang. Ahmed Hussain and Swej Shah,** I truly enjoyed working together with you on the same project and spending time together during our sponsor visit in Malaysia. **Mohsen Mirzaie Yegane,** it was a pleasure working closely together with you as part of the organizing committee of the workshop we organized in Rio de Janeiro. Thanks to all of you, working on the PhD study did not feel like work at all. I will always look back on this period in time with lots of joy and pleasure.

Special thanks to my MSc students: **Fardin Azimi, Abdulaziz Al Mutawa, Maazen Saarig, and Fabian Torres Mendez.** You all were fantastic students to work with and I learnt a lot from all of you. I feel honoured that you decided to work on my project for your MSc thesis.

**Guanqun Yu, Swej Shah, Mohsen Mirzaie Yegane, and Kiarash Mansour Pour,** thank you for creating the fun evenings, with plenty of exciting stories, we had together in Delft. It were these joyful evenings that turned colleagues into close friends. **Swej Shah,** not only had I an amazing time with you during our business trips to Malaysia, United States of America, and England, every time we meet is a relaxing and joyful experience. Thank you for being such a good and close friend. **Guus Pilzecker, Danny Roelofs, and Ritchie Gerrits,** it is an honour for me to call all of you my best friends since secondary school. Knowing that this friendship will last, no matter where our individual careers will take us, is a wonderful feeling.

I feel blessed that I met my beloved partner **Gulbin Uysal** during my time in Delft. Dear **Gulbin,** you can make any situation a joyful experience through your optimism, great sense of humor, enthusiasm, and empathy skills. Thank you for always being there for me, listening to my daily stories, and supporting me in everything I do. I look forward to our next journey together.

Finally, I want to express my deepest appreciation to my parents, **Theo Janssen** and **Helma Janssen-Joosten,** and my two brothers, **Jeroen Janssen** and **Bas Janssen.** I am thankful for the close relationship I have with my brothers. In addition to just being brothers, you are my closest friends. I am extremely thankful for the unconditional love and support of my parents. Although it was not always easy dealing with me in the last couple of years, I always felt your love and blessings. I appreciate everything you have done for me during my PhD studies and before that. Both of you make perfect role models.

# About the author

---

Martijn Janssen was born on November 18<sup>th</sup>, 1990, in Arnhem, The Netherlands. In September 2013 he obtained his BSc degree from Wageningen University by successfully completing the BSc programme Soil, Water, Atmosphere. In September 2015 he obtained his MSc degree from Utrecht University in Geophysics. During his MSc study he completed an internship at EBN B.V., Utrecht, The Netherlands. In October 2015 he started his PhD study at Delft University of Technology under the supervision of Prof. Dr. Pacelli Zitha. His research was part of a collaboration between Delft University of Technology, Universiti Teknologi Petronas, Petronas, and Shell. In 2018, he was part of the organizing committee of the 1<sup>st</sup> workshop on “CO<sub>2</sub> Management and Utilization in Brazilian Pre-Salt Oilfields” held in Rio de Janeiro, Brazil. In 2019, he conducted a three month research visit at Harvard University, USA, where he worked in the Experimental Soft Condensed Matter Group of Prof. Dr. David Weitz. Since October 2019, he started as a Postdoctoral Researcher at Delft University of Technology in the section of Applied Geophysics and Petrophysics within the faculty of Civil Engineering and Geosciences.



